Author:
Amoruso, Giordano

Title:
Ultrafast photoinduced bimolecular proton, electron and energy transfer

Ultrafast photoinduced bimolecular proton, electron and energy transfer

Giordano Amoruso

A dissertation submitted to the University of Bristol
in accordance with the requirements for award of the degree of

Doctor of Philosophy

in the School of Chemistry, Faculty of Science

July 2021

Word count: ~34,000

Wir müssen uns daran erinnern, daß das, was wir beobachten,
nicht die Natur selbst ist, sondern Natur,
die unserer Art der Fragestellung ausgesetzt ist.
"Die Kopenhagener Deutung der Quantentheorie" - Werner Heisenberg

Se comprendere è impossibile, conoscere è necessario.
"Se questo è un uomo" - Primo Levi

The theory of quantum electrodynamics describes Nature as absurd
from the point of view of common sense.
And it agrees fully with experiment.
So, I hope you accept Nature as She is — absurd.
"QED: The Strange Theory of Light and Matter" - Richard Feynman

Cet état de l'absurde, il s'agit d'y vivre.
"Le mythe de Sisyphe" - Albert Camus

Abstract

Bimolecular processes are ubiquitous in liquid-phase chemistry. A detailed understanding of their dynamics is pivotal to control and tune the reaction outcome, which, in turn, is essential to develop novel methodologies. Photochemically activated bimolecular reactions constitute an ideal field of study for ultrafast time-resolved spectroscopies, and this thesis demonstrates their successful application to three very different examples of reactions, that occur on vastly different timescales.

The dynamics of an excited-state proton transfer (ESPT) reaction between a coumarin derivative and a methyl-imidazole model system were definitively and unequivocally characterized using ultrafast transient-absorption (TA) and time-resolved infrared (TRIR) spectroscopies. Density functional theory calculations were used to assign the observed spectroscopic features. The timescale for the ESPT was found to be ~1 ps.

The early steps of an hydrocarboxylation reaction making direct use of CO_2 with styrenes have been studied with TA spectroscopy. The reaction relied on using a catalyst species, *p*-terphenyl (pTP), that was photoexcited and accepted an electron from a sacrificial amine electron donor. After having observed and clarified that pTP relaxation involves the release of torsional strain in the excited state on a timescale of several picoseconds, the electron-transfer reaction in ethanol was found to be diffusion limited, returning a rate constant of $7.80(\pm 1.99)\times10^{9}$ $M^{-1}s^{-1}$ and occurring at a contact radius of 0.68 ± 0.17 nm.

A novel artificial biohybrid system was synthesised and investigated with time-resolved spectroscopies to prove electronic energy transfer occurred between constituent quantum-dots (QDs) nanocrystals and a genetically modified mutant (3Hβ) of photosynthetic bacterial reaction-centre (RC) moieties. In such materials, where QDs act as an assembly hub and as artificial light harvesters, and RCs performs efficient charge-separation, energy transfer from the dots to the protein was found to occur with a time constant of 26.6 ± 0.1 ns and an efficiency of 0.75 ± 0.01.

Acknowledgements

I disagree with the trend of adding acknowledgements on personal life in professional documents publicly available. Those can be found elsewhere: a private version of the thesis, letters and conversations. However, it is my duty to acknowledge those who supported me during my research, without whom the experiments and the writing of this thesis would have never happened.

I would like to thank my supervisor, Dr. Thomas A. A. Oliver, for his constant presence throughout these four years in the labs as well in providing feedback, along all the projects presented in this thesis. As a scientist, he has always been inquisitive, critical, and careful of any detail, but also a passionate and creative mind in the lab and planning the research ahead. But a scientist is also a human being and, beyond his work ethic, Tom also has a great sense of duty and respect in the workplace and has more than once proven his will to fight against sexism, to despise any form of discrimination, to provide support on wellbeing and mental health issues. Vocally and firmly, he has always put everyone's good before any individual's or his own. I would be content knowing I have absorbed even a small fraction of his values.

At the same time, I would like to thank Professor Michael R. Jones, for his support and help for my second PhD project, on bio-engineering and nano-conjugation of *Rhodobacter sphaeroides* reaction centres. A critical and sarcastic mind, practical and able to isolate what is essential. His patience, calm and confidence have always provided the safest environment to make mistakes, explore, and learn a tiny amount of a discipline, microbiology, that I would have otherwise never appreciated.

Special acknowledgments must go to the members of the Oliver's group that I have met and worked with. You have provided, in years, a friendly, open-minded and inclusive working environment, where confrontation has never blurred into competition or asking questions has always been encouraged, and where solid bonds for reasons other than simple work have been established. This extends to all the people I have been close to in the Bristol Laser and Dynamics group.

Finally, I am grateful to the staff and people that work in the School of Chemistry, to the University of Bristol and those who financially sustained my studies and, differently from other realities, believe research is fundamental for a better world.

Author’s Declaration

I declare that the work in this dissertation was carried out in accordance with the requirements of the University's *Regulations and Code of Practice for Research Degree Programmes* and that it has not been submitted for any other academic award. Except where indicated by specific reference in the text, the work is the candidate's own work. Work done in collaboration with, or with the assistance of, others, is indicated as such. Any views expressed in the dissertation are those of the author.

SIGNATURE: _____

DATE: _____

Table of Contents

1. Introduction **1**

1.1. Overview 1

1.2. General Photochemistry 2

1.2.1. The Quantum Nature of Molecules 2

1.2.2. Absorption to an Excited State 4

1.2.3. The Fate of Excited States 7

1.2.4. Relaxation of Photoexcited Species in Solution 10

1.2.5. Non-linear Perturbation Theory 12

1.3. Bimolecular Photochemistry 14

1.3.1. General Phenomena in Liquid Phase 14

1.3.2. Electronic Energy Transfer 17

1.3.3. Electron and Proton Transfer 19

1.4. Spectroscopic Techniques for Photochemistry 22

1.4.1. Time-Correlated Single Photon Counting Spectroscopy 22

1.4.2. Pump-Probe Spectroscopy 24

1.5. Thesis Topics 27

References 30

2. Ultrafast Bimolecular Excited State Proton Transfer in a Hydroxycoumarin-Imidazole Derivatives System **35**

2.1. Introduction 35

2.2. Experimental and Theoretical Methods 37

2.2.1. Sample Preparation and Steady-State Experiments 37

2.2.2. Transient Absorption and Time-Resolved Infrared Spectroscopies 38

2.2.3. Computational Methods 40

2.3. Results and Discussion 40

2.3.1. Ground State Association Equilibrium Characterization 40

2.3.2. Time Resolved Infrared Spectroscopy 47

2.3.3. Transient Absorption Spectroscopy 55

2.3.4. General Discussion 61

2.4. Conclusions 63
References 64
2.5. Appendix 68

3. Investigation of Diffusion-Limited Electron Transfer between para-Terphenyl and an Amine Donor 85
3.1. Introduction 85
3.2. Experimental Methods 87
3.3. Results and Discussion 90
3.3.1. Steady-State Spectroscopy and Cyclic-Voltammetry 90
3.3.2. Transient Absorption Spectroscopy of pTP in Ethanol Solutions 93
3.3.3. Transient Absorption Spectroscopy of pTP–DCHMA Mixtures 98
3.4. Conclusions 105
References 106
3.5. Appendix 109

4. Excitation Energy Transfer in Biohybrid Quantum Dot–Bacterial Reaction Centre Nanoconjugates 113
4.1. Introduction 113
4.2. Experimental Methods 116
4.2.1. 3Hβ RC Engineering and Nanoconjugates Preparation 116
4.2.2. Transient Absorption Spectroscopy 117
4.2.3. Time-Correlated Single Photon Counting (TCSPC) 121
4.3. Results and Discussion 123
4.3.1. 3Hβ RCs Characterization 123
4.3.2. FRET in the Nanoconjugates 127
4.3.3. FRET Efficiency and Distance and its Role in the Nanoconjugates 135
4.4. Conclusions 137
References 138

5. Conclusions and Future Work 143

1. Introduction

1.1. Overview

In Chemistry, most reactions are bimolecular: at the foundation of the transformation of a molecule lies the encounter and the interaction with different molecular entities.

Bimolecular processes are pervasive. They occur in every state of matter over orders of magnitude in terms of space and time. The atmosphere is a gas-phase cauldron of molecules reacting together; most homogeneously catalysed synthetical procedures are carried out in the liquid phase; natural biological reactions relevant for life, spanning solar energy transduction to enzymatic catalysis happen in protein environments tailored by centuries of evolution.

Among these few examples, bimolecular reactions in solution constitute a challenging field of investigation. In liquids, phenomena as solvation, diffusion, solute-solute interactions enormously impact the equilibrium properties and the reactivity of a chemical reaction. Furthermore, reactions such as electronic energy transfer and charge-separation can occur on extremely fast timescales, requiring advanced techniques for their investigation. Knowledge on how these factors impact the kinetics of a reaction is key to direct the design of more efficient and selective synthetic procedures or to create man-made systems capable of mimicking or surpassing natural processes.

The aim of this thesis is to characterize three ultrafast photoinduced bimolecular processes that, beyond fundamental reasons, have applications in modern scientific challenges in the quest for light-harvesting substrates and novel solar energy transduction materials, or mitigation of climate change by utilisation of carbon dioxide in chemical synthesis. Furthermore, this thesis aims to show that ultrafast spectroscopies provide an insightful tool that can be successfully adapted to investigate a variety of reactions spanning several fields. To do so, concepts regarding the quantum nature of molecules, light-matter interaction and ultrafast spectroscopic techniques will be introduced.

1.2. General Photochemistry

1.2.1 The Quantum Nature of Molecules

For any photochemical reaction to occur, light and matter must interact. For the purpose of the thesis, light-matter interactions will be described using the semiclassical approximation, treating chemical species quantum mechanically and light classically.[1] The fundamental laws governing the world of the infinitely small are briefly introduced in this Section, referring to the vast literature for an in-depth conceptualization and formalization of quantum-mechanics.[2,3] For atoms and molecules to be described quantum-mechanically, the Schrödinger equation must apply:

$$\hat{H}\psi(\vec{r}) = E\psi(\vec{r}) \tag{1.1}$$

where $\psi(\vec{r})$ is the wavefunction, a function describing the particle at the coordinates $\vec{r}$ (where the arrow indicates it is a vector quantity) and its square modulus returning the probability of finding the particle in a region of space. $\hat{H}$ is the Hamiltonian operator, that includes all the possible contributions required to determine the energy of the particle (*i.e.*, kinetic and potential energy). Equation 1.1 is an eigenvalue equation that returns the energy, E, of the particle when in a stationary state, with $\psi(\vec{r})$ its solution. More formally, $\psi(\vec{r})$ lies in Hilbert space – an infinite-dimensional vector space. A wavefunction can always be projected onto a basis set spanning the Hilbert space and represented as a vector; operators mapping vectors in the Hilbert space can be represented with matrices.

A general result of Equation 1.1 is that for a particle in a potential well, the associated energy levels are quantized, and each energy value E_n has an associated wavefunction ψ_n. Knowledge of the wavefunction allows for the estimation of the physical observable properties of the particle.

The time-evolution of the wavefunction is described by the time-dependent Schrödinger equation (TDSE):

$$i\hbar\frac{\partial}{\partial t}\Psi(\vec{r}) = \hat{H}(\vec{r},t)\psi(\vec{r}) \tag{1.2}$$

Equation 1.2 is particularly useful when describing time-dependent light-matter interactions in a semiclassical regime: as the strength of interaction is small, it merely perturbs the energy

of the states of the particle. Equation 1.2 constitutes the basis to describe transitions between states of the particle induced by electromagnetic radiation.

For molecules, the Hamiltonian in Equation 1.1 includes contribution from the kinetic energy operator ($\hat{T}$) of the nuclei and the electrons, and Coulombic repulsion and inter-particle attraction potentials ($\hat{V}$):

$$\hat{H} = \hat{T}_n(\vec{R}) + \hat{T}_e(\vec{r}) + \hat{V}_{ee}(\vec{r}) + \hat{V}_{nn}(\vec{R}) + \hat{V}_{en}(\vec{r}, \vec{R}) \quad (1.3)$$

In Equation 1.3, nuclear coordinates are expressed by $\vec{R}$ and electron coordinates by $\vec{r}$. For completeness, Equation 1.3 should also include relativistic terms to account for spin. Notably, the electron-nuclei attraction potential energy operator, $\hat{V}_{en}(\vec{r}, \vec{R})$, is the only term that is dependent on both the nuclear and the electron set of coordinates, complicating enormously the solution of the Schrödinger equation. It is clear that solving the Schrödinger equation and its time-dependent equivalent for a molecule is an extremely challenging task that requires approximation.

The Born-Oppenheimer (BO) approximation is a fundamental tool to help solve the Schrödinger equation. Considering that an electron is ~10^3 lighter than a proton or a neutron, the motion of electrons can be approximated to be instantaneous with respect to the nuclei. As a consequence, the wavefunction can be factorised in two different terms and the Schrödinger equation can be solved separately for electrons and nuclei. The wavefunction becomes:

$$\psi(\vec{r}, \vec{R}) = \varphi_{el}(\vec{r}, \vec{R})\chi_{vib}(\vec{R}) \quad (1.4)$$

In Equation 1.4, χ_{vib} is the vibrational wavefunction, that is independent on the electronic coordinates. φ_{el} is the electronic wavefunction of the molecule, that is evaluated at a specific set of nuclear coordinates: φ_{el} is still dependent on $\vec{R}$, but as a parameter rather than a variable. Then, once φ_{el} is obtained, the process is repeated by varying parametrically $\vec{R}$ to generate potential energy surfaces (PES) or curves, a set of multidimensional energy maps, one for each electronic state, that vary as a function of all nuclear coordinates. The concept of PES provides a direct and intuitive picture for chemical changes a molecule can undergo.

The topology of each surface is vast and contains many local minima, or saddle points associated with energy barriers.

Although powerful, the BO approximation comes with the price of losing validity in regions of the multidimensional energy-coordinate space where two surfaces come close to one another or intersect. At such points, electronic and nuclear motion are no longer necessarily decoupled, and the energy surfaces interact with each other, resulting in alterations in their topology.[4]

For example, in polyatomic molecules, two energy surfaces can get close to each other and couple without intersecting in a region of avoided-crossing. The interaction potential perturbing the energy of the initial and final states i and f, $|V_{if}|^2$, dictates the extent of the coupling, and is given by the off-diagonal matrix element:

$$|V_{if}|^2 = |\langle \psi_f | \hat{V} | \psi_i \rangle|^2 \qquad (1.5)$$

In Equation 1.5, $\hat{V}$ is the interaction potential operator that describes the perturbation applied onto the system. Alternatively, two energy surfaces can cross, at a specific point of singularity in the phase space known as a conical intersection (CI). More generally this can be a seam of intersection. Both CIs and seams of intersection provide an effective way to move quickly from one PES to another. The probability of crossing is dependent on the value of $|V_{ij}|^2$ and on the difference between the gradients of the potential of the two states in the region close to the CI: the steeper the potential, the faster the movement along a nuclear coordinate, typically resulting in an ultrafast sub-picoseconds interconversion of the nuclear momentum into the crossing point.

1.2.2 Absorption to an Excited State

Having defined the concept of PES, it is now possible to describe photon absorption by a molecule. Absorption of light is a process by which energy of an electromagnetic radiation is transferred to a chemical species, causing the molecule to transition from an initial state, i, to a final state, f. Absorption occurs only when the frequency of the electromagnetic radiation is resonant with the frequency of the molecular transition between

i and f ($\omega = \omega_{if}$). This is immediately justified by imagining that, if the potential due to the charge distribution of nuclei and electrons in a molecule is expressed to a first approximation as a dipole, and if the molecular dipole oscillates harmonically, then, coupling with the electromagnetic radiation and energy transfer can only occur under the resonance condition. After the absorption event, the molecule in the state f will then evolve in time according to the TDSE.

This condition applies equally to transitions across the whole electromagnetic spectrum from electronic to rotational, and general rules governing the probability of the transitions can be outlined. In the semiclassical limit, the Hamiltonian for the TDSE is described by:

$$\hat{H} = \hat{H}_0 + \hat{V}(t) = \hat{H}_0 - \vec{\mu}_{el} \cdot \vec{E}(t) \tag{1.6}$$

Where $\hat{H}_0$ is the Hamiltonian for the time-independent problem as expressed in Equation 1.3, and $\hat{V}(t)$ is a time-dependent perturbation operator: as the interaction is treated classically, the potential is a scalar field resulting from the product between the electric dipole of the molecule and the electromagnetic field, as expressed by the second identity. In Equation 1.6 and in the rest of the discussion, only the electric component of the electromagnetic field is considered. The perturbation couples the states of the molecule, its matrix representation resulting in non-null off-diagonal terms. By recognizing that the electric field does not operate onto the molecular coordinates, the transition dipole moment, μ_{if}, can be defined as:

$$\mu_{if} = \langle \psi_f | \hat{\mu} | \psi_i \rangle \tag{1.7}$$

The square modulus of the transition dipole moment, $|\mu_{if}|^2$, returns the probability associated with the transition from i to f. On the basis of symmetry arguments, it is possible to say whether Equation 1.7 will be non-null and establish selection rules that allows to determine *a priori* whether a transition is allowed or forbidden, depending on the nature of the involved states. Beyond symmetry requirements, recalling classically the electric dipole is the sum of all the displacement vectors between the N charges in a molecule

($\vec{\mu}_{el} = \sum_i^N q_i \vec{r}_i$), $|\mu_{if}|^2$ is large when the charge distribution associated to the final state is similar to that of the initial state after displacement under the dipole operator. This explains why, for example, in aromatic molecules π*←π electronic transitions are particularly bright, or why direct charge separation upon photoexcitation is not observed.

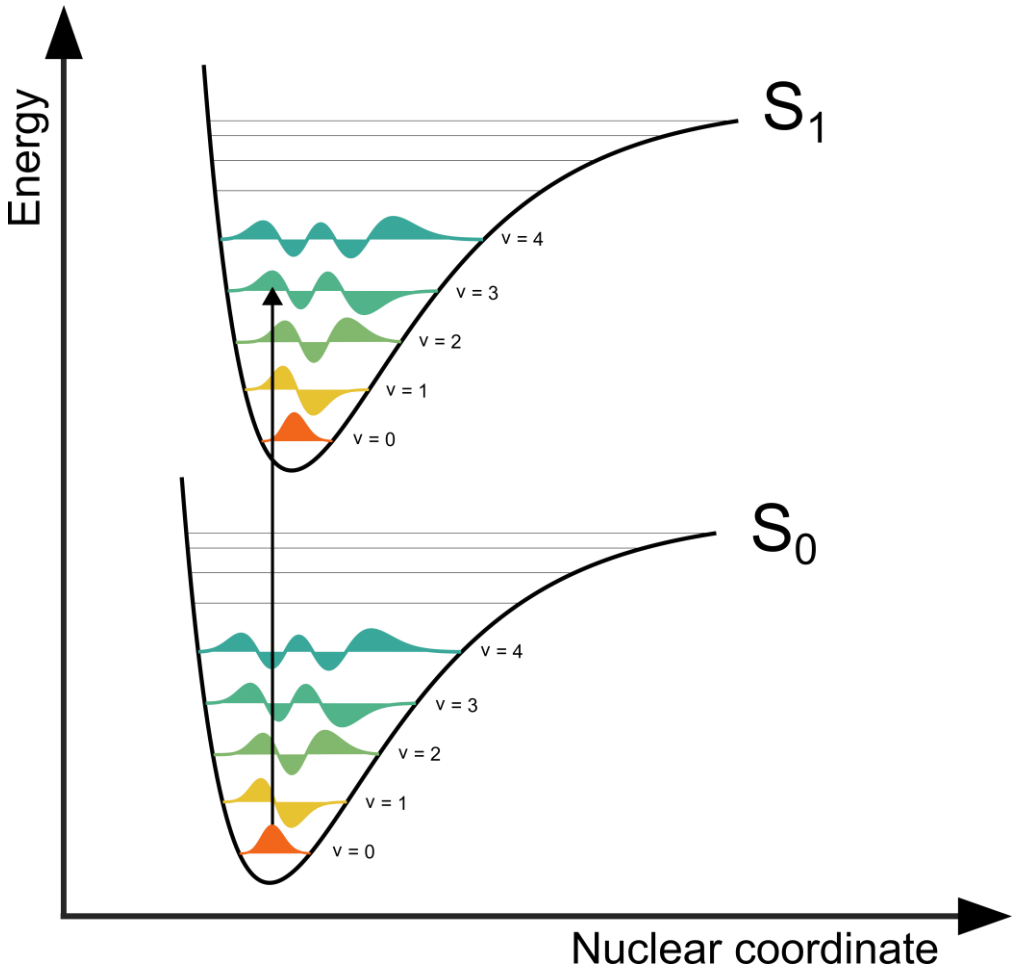

Figure 1.1. Potential energy curves for a single nuclear coordinate for the singlet ground and first excited state of a generic molecule, depicting vibrational wavefunctions in a Morse potential. The most probable transition occurs from the lowest vibrational state in S_0 to the third sublevel in S_1 as dictated by Franck-Condon principle.

Having discussed absorption in general, the specific case of electronic transitions is of interest for the experiments discussed in this thesis. Under the BO approximation, an optical transition leading to population of an excited state from the ground state occurs vertically between two energy surfaces (Franck-Condon principle) and may be accompanied by a change in vibrational state. An example is given in Figure 1.1 for a S_1←S_0 transition,

in a simplified picture of the PES where only one nuclear degree of freedom has been accounted for. Starting from the bottom of the S_0 PES, the molecule is in the lowest possible vibrational state ($v = 0$). The vibrational wavefunction describing this state is labelled as χ_0^0, where the subscript and the superscript refer to vibrational and electronic states, respectively. If the nuclear coordinates of the S_1 PES are displaced compared to those of the ground state, the lowest energy vibrational wavefunction of S_0, χ_0^0, will overlap not only with χ_0^1, but also with some higher vibrational levels χ_n^1 of S_1. Therefore, for a single molecule, it is most probable that excitation to S_1 will bring the molecule to a vibrationally excited level different from $v = 0$; for a statistical ensemble, the intensity of the absorption spectrum from a statistical ensemble of several molecules will be modulated by a factor equal to the overlap of the vibrational wavefunctions. In mathematical terms, partitioning the wavefunction in Equation 1.7 and recalling the electric dipole operator acts on electron coordinates only, for the specific case of the $S_1 \leftarrow S_0$ transition where S_0 is the initial state i and S_1 is the final state f, the square modulus of the transition dipole moment yields:

$$|\mu_{01}|^2 = |\langle\phi_1|\hat{\mu}|\phi_0\rangle|^2 |\langle\chi_m^1|\chi_n^0\rangle|^2 = \left|\mu_{01}^{el}\right|^2 |\langle\chi_m^1|\chi_n^0\rangle|^2 \qquad (1.8)$$

As introduced above, χ_m^1 is the m-th vibrational level of the S_1 state, χ_n^0 is the n-th vibrational level of the S_0 state; $\left|\mu_{01}^{el}\right|^2$ is the square modulus of the $S_1 \leftarrow S_0$ electronic transition dipole moment. The expression $|\langle\chi_m^1|\chi_n^0\rangle|^2$ is known as Franck-Condon factor and expresses the relative intensity of a vibronic progression associated with an electronic transition for a single vibrational mode. Equation 1.8 is valid for a PES defined over only one nuclear coordinate, as in Figure 1.1, but it can be generalized to polyatomic molecules considering all nuclear coordinates defining the PES. The Franck-Condon principle is the simplest justification to the emergence of vibronic progressions in absorption and in fluorescence (see Section 1.2.3).

1.2.3 The Fate of Excited States

Immediately after photon absorption, electrons and nuclei find themselves in an out-of-equilibrium state. Eventually, the species in the excited state will decay back to the ground state via several possible decay pathways.[5]

The Jablonski diagram is a schematic way to summarize the possible deactivation pathways for excited molecules (Figure 1.2); the diagram depicts states without reference to potential energy surface, so the only meaningful coordinate is the energy axis.

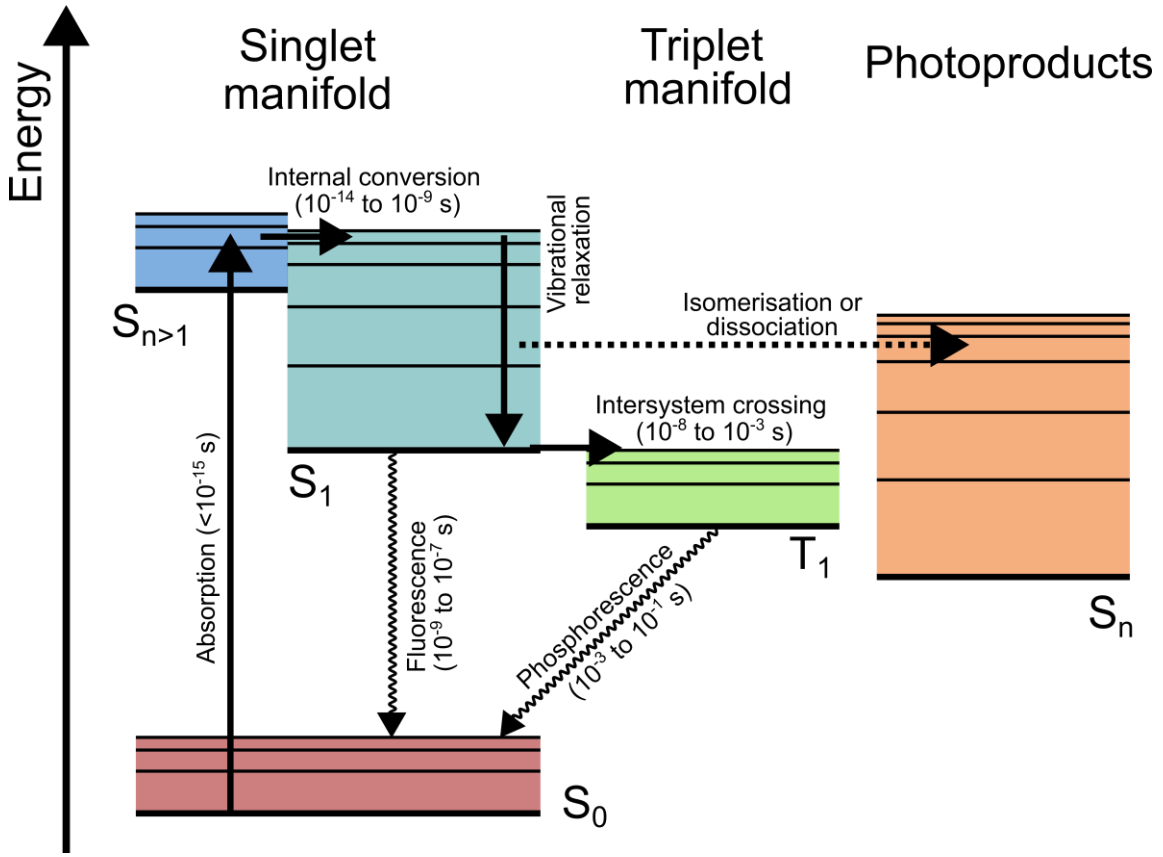

Figure 1.2. Jablonski diagram for a generic chromophore in solution, indicating states, processes and relative timescales involved in molecular relaxation.

Typically, absorption of a photon populates the S_1 excited state, from which relaxation occurs. However, it is also possible that the molecule is excited to a state $S_{n>1}$, (as depicted in Figure 1.2) for example if the $S_1 \leftarrow S_0$ transition is forbidden, or simply if the photon energy is resonant with a transition to higher excited state. If this is the case, it is generally observed that molecules in an $S_{n>1}$ state interconvert quickly to S_1 prior to any other relaxation process to the ground state (Kasha's rule).

Relaxation from S_1 to S_0 can happen spontaneously (fluorescence) with emission of a photon, or as a consequence of the presence of photon (stimulated emission). For a single molecule, for a vertical transition that populates a vibrationally excited level with probability given by the Franck-Condon factor, the vibrationally hot molecule equilibrates to the bottom

of the first excited state PES prior to radiative relaxation, provided a mechanism for dissipation of vibrational energy is available. For example, in gases, collisions between molecules can provide a route for transfer of vibrational energy from the photoexcited molecule, while in condensed phase, coupling with solvent modes is the prominent mechanism. In solution, vibrational relaxation (VR) typically occurs on a picosecond timescale.[6]

In absence of external fields, the only radiative decay pathway allowed from S_1 is fluorescence. A measure of the probability of a photon being re-emitted via fluorescence per absorbed photon is given by the fluorescence quantum yield (Φ_f). Φ_f is linked to excited state decay rates: the faster fluorescence compared to competitive non-radiative relaxation pathways, the higher the number of emission photons detected. Moreover, it should be highlighted that, as quantum-mechanics return statistical rather than deterministic information on the property of a system, the evaluation of the transition dipole moment from S_1 to S_0 only returns a probability value: in absence of external fields that trigger the transition, fluorescence of a single molecule is by nature a probabilistic event. Therefore, a fluorescence lifetime characteristic of a chemical species has meaning only when a statistically relevant ensemble of molecules is interrogated or a relevant number of observations on a single molecule are probed. Fluorescence timescales are typically found in the order of picoseconds to nanoseconds. In terms of energetics, fluorescence dominantly occurs from the bottom of the S_1 PES in presence of VR. Hence, if the $S_0 \leftarrow S_1$ transition is accompanied by a change in vibrational state, the fluorescence will be observed at wavelength longer than the absorption and will exhibit the vibronic progression as found in absorption. Under these circumstances, the fluorescence spectrum of the molecule is the mirror image of the absorption spectrum, and the energy difference between the maxima of the two spectra is called Stokes shift, which accounts for energy contributions associated with solvent molecules rearranging around the chromophore after the transition (see Section 1.2.3 for a more detailed discussion).

Non-radiative decay pathways can lead to molecular de-excitation, also. As for relaxation form higher excited states to S_1, internal conversion (IC) can be an effective non-radiative decay pathway also for the $S_0 \leftarrow S_1$ transition, for example in the presence of CI. On longer timescales, from 10^{-8} to 10^{-3} s, intersystem crossing (ISC), *i.e.*, change in spin multiplicity from singlet usually to triplet state, can compete with fluorescence. Eventually,

$T_1 \rightarrow S_0$ relaxation occurs with emission of a photon, a process known as phosphorescence. Phosphorescence often takes milliseconds to seconds due to the slow process of spin interconversion during the transition and is observed at wavelength longer than fluorescence, occurring from the bottom of the T_1 PES.

A final route of depletion of excited-state population is to form photoproduct species. This can be the case if the molecule is photoexcited to a dissociative S_n state or if after photoexcitation the S_n state couples to another PES. The nature of the dissociative state or the alternative PES may vary, from single well potentials that lead nuclei along a given coordinate to break a bond,[7,8] to potentials that simply lead to form a stable isomer of the initial molecule.[9,10]

1.2.3 Relaxation of Photoexcited Species in Solution

The photophysical events described so far have general validity. In liquids, other phenomena are concomitant with the relaxation processes outlined in Section 1.2.2, as a result of the molecule interacting with the environment.

In the gas phase, spectroscopic transitions typically appear as sharp, resolved peaks; their bandwidth is dictated by the natural lifetime for the transition. In liquids, the most evident proof of system-bath interaction is spectroscopic broadening of transitions. This can be distinguished in two different contributions. *In primis*, in the liquid phase, chromophores are not isolated and couple to a quasi-continuum of solvent states surrounding the solute. As a consequence, the natural lifetime for a transition is reduced, thus increasing the linewidth. As the phenomenon is experienced in the same way by each molecule, it is known as homogeneous broadening. However, different arrangements of solvent molecules and their dipoles around the chromophores means solute molecules experience locally different potentials, thus resulting in alterations of their ground and excited states and in turn slightly different excitation energies. As the environment around the solute is different from molecule to molecule, this source of broadening is labelled as inhomogeneous. Inhomogeneous broadening arises from a statistical ensemble of molecules, and therefore can be viewed as the sum of many different homogeneously broadened lineshapes. Together, homogeneous and inhomogeneous broadening provide a connection between system-bath

dynamics and observed lineshapes evident in absorption spectra.[11] A similar reasoning can be used to justify spectral broadening in pigment-protein complexes.

Furthermore, macroscopically, the presence of solvent changes the equilibrium properties of the molecule, in first approximation behaving as a collection of dipoles that exerts a mean electric field on the solute; in terms of dynamics, it has an influence on the stability of transition states, or changes properties associated to statistical ensemble of molecules, as diffusion. But it is more than tuning pre-existing properties of a chromophore: solvent molecules can cage solute molecules and prevent a reaction in favour of another, or directly react with solute molecules, or act as catalyst; solvent makes possible charge separation reactions and can mediate electron, proton, and energy transfer.

Effects of the solvent on the reaction dynamics change from system to system. A general phenomenon is of particular interest for photo-relaxation processes: solvation dynamics around a solute molecule. As mentioned previously, the Stokes shift accounts for the energy release associated with solvent dipole realignment around a chromophore undergoing a transition. As solvent molecules are associated with molecular dipoles, the dipoles themselves will have to respond to changes in the charge density distribution of the solute upon photoexcitation by rotating and realignment (see for example Figure 1.3). Solvent molecular rotation is not instantaneous: immediately after photoexcitation, the solvent configuration is the same as for the S_0 equilibrium. Therefore, solvent equilibration and full adaption to the charge distributions of the excited state PES is a time-dependent process. Ultrafast time-resolved experiments are able to interrogate dynamically the Stokes shift, following its evolution in time until a new equilibrium is reached, when no further spectral shifting of the fluorescence spectrum is observed.[12,13]

A treatment of solvent that fully accounts at a quantum-mechanical level for solvent granularity and addresses its microscopic role as well as macroscopic properties is an extremely complicated task.[14,15] In computation, inclusion of solvent in the Schrödinger equation is typically limited to few molecules, if necessary to investigate their role in a reaction, to then move to molecular mechanics or mean-field approaches in regions away from the solute of interest.

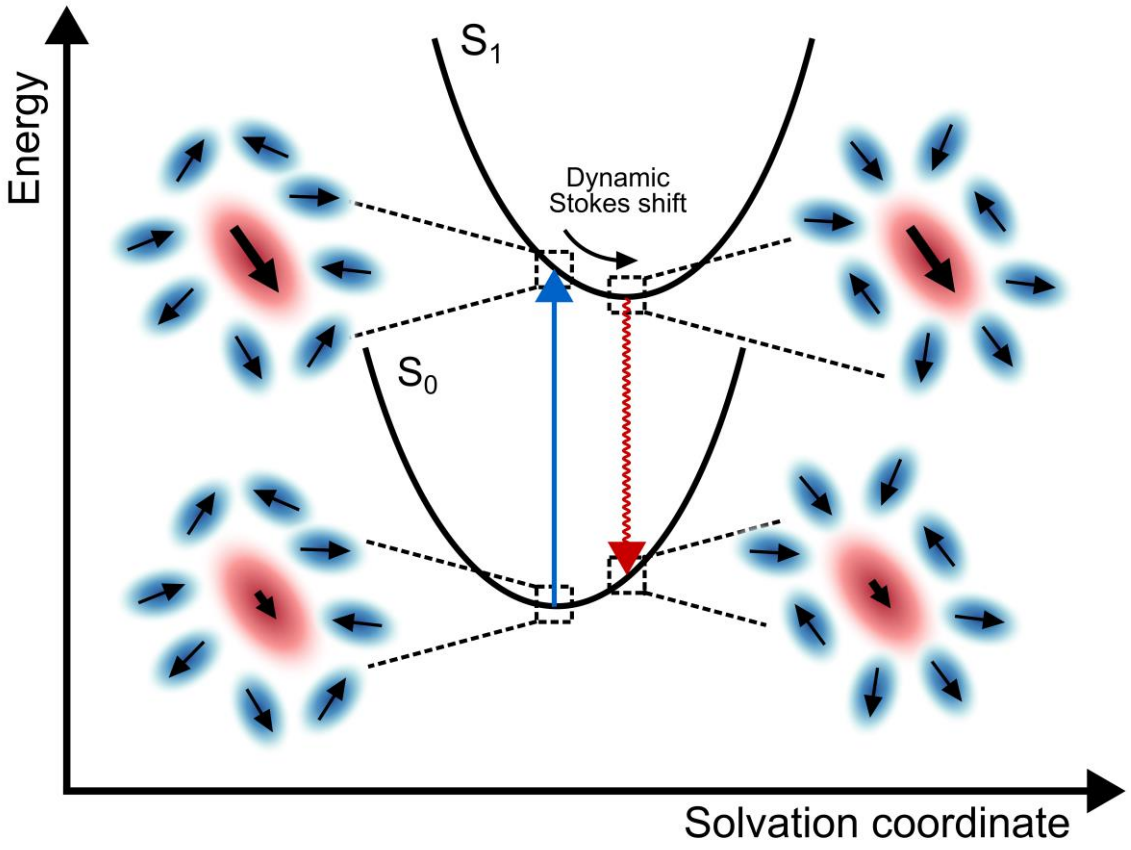

Figure 1.3. Realignment of dipoles of solvent molecules around a chromophore with little or no permanent dipole moment in the ground state and large dipole moment in the excited state. In this case, polar solvents stabilize the excited state better than apolar solvents, resulting in larger Stokes shift.

1.2.4 Non-linear Perturbation Theory

So far, the discussion has been limited to treat phenomena for which matter response to light perturbation was linear in the intensity of the incident field. However, in general, light can interact more than once with a molecule, causing a non-linear response by the material – typically ultrafast pulsed lasers with high peak power intensities are required to achieve such non-linearities. Macroscopically, non-linear optics can be described with Maxwell's equations as wave-mixing between multiple electric fields acting on a medium.[16] Non-linear optics are at the foundation of many spectroscopic techniques, where the output of a laser source often requires manipulation before running an experiment, from frequency mixing to optical parametrical amplification.[17]

In bulk, the material response to the electric field is expressed by the polarization, that, for a lossless, dispersionless and non-ferroelectric material, can be expanded in power series to include non-linearities in light-matter interaction:

$$\vec{P}(t) = \sum_i \vec{P}^{(i)}(t) = \varepsilon_0 \chi^{(1)} \vec{E}(t) + \varepsilon_0 \chi^{(2)} \vec{E}(t)\vec{E}(t) + \cdots \quad (1.9)$$

In Equation 1.9 $\vec{P}^{(i)}$ is the i-th order of the polarization signal, ε_0 is the vacuum dielectric constant, and $\chi^{(i)}$ is the dielectric permittivity for the i-th order, in general a tensor of rank equal to the order of the perturbation. Each term of the polarization signal depicts phenomena that are observable only with a number of interactions between the field and the material equal to the order term and can be interrogated with specific spectroscopic techniques. Energy and momentum conservation (phase-matching condition) laws apply to Equation 1.9.

Three non-linear phenomena of interest for this thesis can be described in terms of Equation 1.9. Briefly, second harmonic generation (SHG) is the generation of a pulse with a frequency equivalent to the double of the incoming pulse ($\omega_{out} = 2\omega_{in}$, by energy conservation). This is achieved by focussing laser light into a bi-refringent material to respect the phase matching condition ($\vec{k}_{out} = 2\vec{k}_{in}$);[16] for SHG to occur, the incoming pulse needs to be intense enough for the second term of the power series expansion in Equation 1.9 to be significant. Similar to SHG, third-harmonic generation (THG) is a process where three fields with the same energy are mixed, to obtain photons with frequency $\omega_{out} = 3\omega_{in}$. Finally, a non-collinear optical parametrical amplifier (NOPA) relies on mixing a high frequency and high intensity beam, acting as a pump pulse, with a lower frequency and weak intensity seed. Together they generate an amplified seed beam (the signal) and an idler beam as a result of the interaction. In non-collinear configurations, broadband pulses can be obtained, necessary for the generation of pulses with a duration of few femtoseconds.[17]

1.3. Bimolecular Photochemistry

1.3.1. General Phenomena in Liquid Phase

The presence of more than one reactant in liquid environment is associated to a plethora of reactive events that go beyond isomerization or dissociation reactions. Whilst in general bimolecular events can occur on the ground as well as on the excited PES, bimolecular photochemistry pertains to chemical reactions that are triggered by photon absorption by a reactant. The presence of another reagent alters the energy landscape of the chromophore and new product states are accessed when the rate of the bimolecular event outcompetes the photorelaxation pathways. Electronic energy, electron and proton transfer reactions are discussed in greater detail in Sections 1.3.2 and 1.3.3, respectively.

For a diffusive bimolecular reaction to occur, the reagents need to get sufficiently close to each other and encounter. In the liquid phase, where reactants are free to move, the encounter probability and intermolecular forces that bring molecules together or force them apart are key to determine the rate of a bimolecular event. Diffusion events directly impact the rate when reactant encounter is slower than or comparable to the reactive event. Predicting an encounter timescale in liquid is not as straightforward as in the gas phase, rather requiring an empirical measurement of diffusion coefficients: beyond the simple collisions among particles, solute-solvent interaction can accelerate or slow random-walks in the condensed phase. Moreover, solute-solute intermolecular forces determine the existence and the extent of pre-associated reactants or formation of aggregates that can be described via equilibria; in the excited state, formation of excimers or exciplexes can also impact the outcome of a reaction.

Having provided a general description of these phenomena, a more detailed discussion of diffusion relevant to the interpretation of the data shown in this thesis is provided. Diffusion reactions have been thoroughly investigated, providing both mathematical descriptive tools at different layers of complexity and scientific experimental methodologies to access its influence on chemical dynamics,[18–25] with direct application to time-resolved techniques used to interrogate them. Generally, a bimolecular reaction of the type $A + B \rightarrow P$ is described by a system of coupled differential equations dictated by classical chemical kinetics plus terms due to diffusion. The derivation can be obtained starting from Fick's law of diffusion.[14,26,27] Eventually, Equation 1.10 is obtained:

$$\begin{cases} \frac{\partial [A]}{\partial t} = D_A \nabla^2 [A] - k(t)[A][B] \\ \frac{\partial [B]}{\partial t} = D_B \nabla^2 [B] - k(t)[A][B] \end{cases} \quad (1.10)$$

where k is the rate constant of the bimolecular reaction between A and B, D_A and D_B are the diffusion coefficients of the species involved, and $[A]$ and $[B]$ are the reactant concentrations, which depend on time and on the square-term of the gradient, given by $\nabla = \frac{\partial}{\partial x} + \frac{\partial}{\partial y} + \frac{\partial}{\partial z}$. Notably, Equation 1.10 reduces to the expression for classical chemical kinetics only in case of an activation-controlled reaction, while for extremely fast bimolecular reactive events, the rate limiting step is the encounter of the two reactants with one another (diffusion-controlled reaction). In theory, solving for all reactants and products provides a full description of the dynamics of a bimolecular reaction. For specific classes of reactions, the rate of reaction can be estimated independently, and used as a known parameter to model the reactants concentration profiles of the kinetics (*e.g.*, electron or electronic energy transfer).

Analytical solutions for Equation 1.10 are available for uncoupled equations with specific boundary conditions or using a different coordinate system; alternatively, numerical simulations are necessary. In cases where the concentration of one of the two reactants is in large excess, a key approximation can be made: in a random walk in the solvent, the molecule at low concentration is not likely to encounter a replica of itself, meaning it is far more probable it encounters a molecule of the species in excess. Under these conditions, it is mathematically simpler to solve the diffusion equation by fixing the cartesian coordinates on one of the molecules at low concentration, the target, and describe the diffusive event of the molecules in excess in relative terms. Additionally requiring at time-zero only the reactants are present, and that their reaction happens infinitely faster than the time necessary for them to diffuse at a distance smaller or equal to a, the contact radius, an expression for the rate of reaction can be written as:

$$k(t) = 4\pi N_A a D \left(1 + \frac{a}{\sqrt{\pi D t}}\right) \quad (1.11)$$

In Equation 1.11, N_A is Avogadro's number and D is the sum of the diffusion coefficients of the two species. It is also common to assemble the pre-factors and define the diffusion rate constant:

$$k_D = 4\pi N_A a D \tag{1.12}$$

that accounts for the purely diffusive contribution to the rate constant, representing the long-time limit, once a stationary regime is reached. This formulation was firstly presented by von Smoluchowski and it represents the case of diffusion-limited reactions.[18,19,28] Many refinements to this description have been proposed, from models that account for on-contact reaction with a rate non-infinitely faster than diffusion (*e.g.*, proton transfer) in the Collins-Kimball approximation,[20,29] to cases when reaction rates are dependent on the reactants separation distance (*e.g.*, electron and energy transfer).[23]

Equation 1.11 can be adapted to describe the time-resolved intensity signals of spectroscopic techniques able to interrogate the dependence on diffusion of bimolecular reactions, such in the case of time-correlated single-photon counting (TCSPC) spectroscopy or transient-absorption (TA) spectroscopy.[30–34] It can be shown that in these experiments the signal intensity, I, associated with a molecule where a unimolecular decay process (*e.g.* fluorescence) competes with quenching by diffusion can be modelled via:

$$I = e^{-c_0 k_D\left(t+\frac{2a\sqrt{t}}{\sqrt{\pi D}}\right)} e^{-k_R t} \tag{1.13}$$

In Equation 1.13, k_R is the rate constant for any decay process competing with diffusion and c_0 is the initial concentration of the excess reactant, which remains roughly constant as the bimolecular reaction consumes it by a negligible amount.

The von Smoluchowski model is the simplest way of describing diffusion in a bimolecular reaction. Equation 1.12 was used in the investigation of excited-state proton transfer reaction to estimate an upper limit for diffusion step in the system under study (Chapter 2). Equation 1.13 was used to describe and model the kinetics of a diffusion-limited electron transfer reaction and accounted for excited state radiative decay of the reactants (Chapter 3).

1.3.2. Electronic Energy Transfer

In a system containing two chromophores, an additional pathway to dissipate the excess energy is available for a molecule in the excited state. The excited chromophore can act as a donor and transfer its energy to its partner moiety, provided the acceptor molecule has an energetic transition that meets the resonance condition. Electronic energy transfer (EET) has been extensively investigated and modelled in condensed phase, from liquid solutions to proteins to crystals.[35] Two limiting cases can be distinguished, one of weakly interacting molecules, typical of chromophores in solution,[36,37] and that of atoms and molecules in a crystal lattice interacting strongly.[38]

For the purpose of this thesis only the weakly interacting regime will be discussed, where the electronic states of the donor-acceptor (D-A) pair are not significantly different from those of the isolated components, as confirmed by the absorption and fluorescence spectra. The chromophores are treated as a pair of resonant dipoles, in a so-called Förster resonance energy transfer (FRET) process.[35] In this picture, two approximations are made: solvent equilibration around the donor molecule after its excitation is fast compared to the FRET timescale and the energy required to reorganise the solvent dipole is larger than the donor-acceptor coupling term. As a result of chromophores interacting, the energies of their electronic states are weakly perturbed due to the potential they exert onto each other. The perturbation is approximated with a dipole-dipole interaction potential:[35]

$$V_{DA} = \frac{1}{4\pi\varepsilon_0}\frac{1}{n^2}\left(\frac{\vec{\mu}_D\cdot\vec{\mu}_A}{{r_{DA}}^3} - \frac{3(\vec{\mu}_D\cdot\vec{r})(\vec{\mu}_A\cdot\vec{r})}{{r_{DA}}^5}\right) \tag{1.14}$$

In Equation 1.14 the potential between the two dipoles, V_{DA}, has a pre-factor resembling the Coulombic interaction potential where ε_0 is the electric permittivity in the vacuum and n is the refractive index of the host medium of donor and acceptor. The potential is proportional to the inverse of the third power of the distance r_{DA} separating the donor and the acceptor dipole moments, $\vec{\mu}_D$ and $\vec{\mu}_A$ respectively. Evaluating the transition probability for the bimolecular process $D^* + A \longrightarrow D + A^*$ under the potential in Equation 1.14 leads to an expression for the FRET rate:

$$k_{EET}(r_{DA}) = \frac{\Phi_D}{\tau_D}\frac{\kappa^2 I(\lambda)}{N_A n^4}\frac{9000(\ln 10)}{128\pi^5}\frac{1}{r^6} = \frac{1}{\tau_D}\left(\frac{R_0}{r_{DA}}\right)^6 \tag{1.15}$$

In Equation 1.15 N_A is Avogadro's number, Φ_D and τ_D are the fluorescence quantum yield and the fluorescence lifetime of the isolated donor. κ is the dipole orientation factor resulting from the relative alignment of the dipoles; in isotropic medium where the dipoles are assumed to freely rotate, integrating over all the possible dipole pair directions leads to a value of κ^2 of 2/3, typically adopted when evaluating Equation 1.15. The remaining quantity $I(\lambda)$:

$$I(\lambda) = \int_0^\infty F_D(\lambda)\lambda^4\varepsilon_A(\lambda)\, d\lambda \tag{1.16}$$

is the Förster spectral overlap integral, given by the intersection of the donor absorption spectrum and normalized acceptor fluorescence spectrum. Finally, R_0 is the Förster distance and groups all the known terms; this quantity has a physical meaning related to the efficiency of the FRET process (*vide infra*). The rate is dependent on the lifetime and the fluorescence quantum yield of the donor molecule: energy transfer is more likely if the donor excited state lives for longer and if the non-radiative decay pathways are ineffective. Moreover, for dipole orientations at which coupling is zero and for low overlaps FRET cannot occur.

The efficiency of FRET, E_{FRET}, competing with the donor radiative decay pathway is defined as:

$$E_{FRET} = \frac{k_{FRET}}{{\tau_D}^{-1}+k_{FRET}} = \frac{{R_0}^6}{{r_{DA}}^6+{R_0}^6} \tag{1.17}$$

The second part of Equation 1.17 can be obtained by substituting k_{FRET} with the second identity in Equation 1.15. This formulation is useful to interpret R_0 as the distance at which FRET efficiency is 50%.

Typically, knowledge of the donor-acceptor distance from independent microscopy measurements on nanoparticles or proteins allows for an estimation of the FRET timescale. Equation 1.17 can also be rearranged and used to estimate the average donor-acceptor distance, by determining the FRET rate constant from time-resolved emission measurements.[35]

1.3.3. Electron and Proton Transfer

Electron transfer (ET) reactions have been thoroughly studied and formalized on the principles of quantum-mechanics.[39–42] The first comprehensive treatment of ET from a reducing donor to an oxidising acceptor species ($D + A \rightarrow D^+ + A^-$) was by Marcus. Generically, the rate of a reaction is related to the energy barrier to surpass when moving from reactants and products states, as expressed by Eyring's equation within the frame of transition-state theory:

$$k = Ae^{-\frac{\Delta G^{\ddagger}}{k_B T}} \tag{1.18}$$

In Equation 1.18 k_B is the Boltzmann constant, T is the temperature, A a pre-exponential factor that depends on the coupling between the reactant and product states (*vide infra*). For the forward reaction from the reactants to the product, the rate k depends exponentially on the free energy difference between the reactant state and the transition state $\Delta G^{\ddagger}$, the activation free energy. In Marcus theory, the activation free energy is related quadratically to the standard free energy of reaction, providing a link between a kinetic and a thermodynamical parameter:

$$\Delta G^{\ddagger} = \frac{\lambda}{4}\left(1 + \frac{\Delta G^{\ominus}}{\lambda}\right)^2 \tag{1.19}$$

In Equation 1.19, the reorganisation energy λ also appears. For an electron donor-acceptor pair, λ is the energy required to rearrange all the nuclei and the solvent dipoles around them from the configuration of the reactant to that of the products without transferring an electron. Equation 1.19 is effective in describing different ET regimes. In the normal region, where $-\Delta G^{\ominus} > \lambda$, $\Delta G^{\ddagger}$ decreases and the rate of ET increases in agreement with common intuition that the larger the thermodynamic driving force, the faster a reaction will result (Figure 1.4(a)). However, the rate of the electron transfer does not grow indefinitely with the increase of the thermodynamic drive $-\Delta G^{\ominus}$, rather has a maximum at $-\Delta G^{\ominus} = \lambda$, when the energy released from the process compensates exactly that necessary to reorganise the nuclei and solvent dipoles (Figure 1.4(b)), in the barrierless regime ($\Delta G^{\ddagger} = 0$). After this point, at $-\Delta G^{\ominus} < \lambda$, Equation 1.19 correctly predicts the existence of the so-called inverted

region of ET, where further increase in $-\Delta G^{\ominus}$ decelerates the rate of reaction (Figure 1.4(c)) as $\Delta G^{\ddagger}$ is non-zero and a barrier is re-introduced.

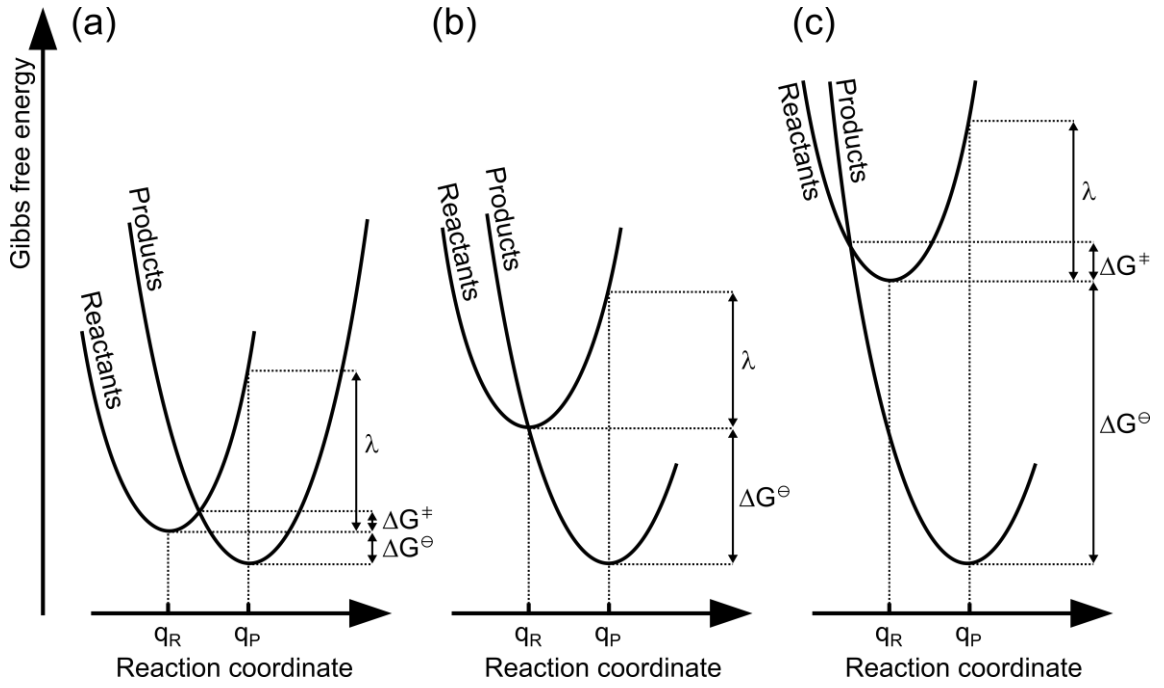

Figure 1.4. Energy-reaction coordinate diagrams for three cases individuated by Marcus equation: (a) $-\Delta G^{\ominus} > \lambda$ in the normal region of ET, with a positive value of $\Delta G^{\ddagger}$, (b) $-\Delta G^{\ominus} = \lambda$ when the ET rate is maximum as $\Delta G^{\ddagger}$ is zero, (c) $-\Delta G^{\ominus} < \lambda$ in the inverted region, where $\Delta G^{\ddagger}$ is positive again.

As a consequence, both internal degrees of freedom rearrangement and solvation contribute to the total reorganisation energy, λ can be further expressed as a sum of λ_{in}, an inner sphere one (displacement of nuclear coordinates in the solute), and λ_{out}, an outer sphere contribution (realignment of solvent dipoles around the solute). Starting with λ_{in} this can be expressed as the sum over all the possible j coordinates of the harmonic potentials associated to the displacement between the reactant coordinate ${q_j}^R$ and the product coordinate ${q_j}^P$, as directly derived by Marcus:[39]

$$\lambda_{in} = \frac{1}{2}\sum_j \omega_j ({q_j}^R - {q_j}^P)^2 \qquad (1.20)$$

In Equation 1.20, ω_j is the oscillation frequency over the j-th vibrational coordinate. The solvent contribution can be obtained from purely electrostatic considerations, evaluating the

energy necessary to create a cavity in an ensemble of solvent dipoles to accommodate a solute molecule in it and the energy released from favourable solute-solvent interaction. The contributions from the donor and the acceptor can be expressed as a function of their separation distance r_{DA}:

$$\lambda_{out} = \frac{(\Delta e)^2}{4\pi\varepsilon_0}\left(\frac{1}{2a_D} + \frac{1}{2a_A} - \frac{1}{r_{DA}}\right)\left(\frac{1}{n^2} - \frac{1}{\varepsilon}\right) \tag{1.21}$$

where Δe is the amount of charge exchanged during the ET, a_D and a_A are the solvation radius of the donor and acceptor species respectively, n is the refractive index and ε the relative dielectric constant of the medium.

An expression for the pre-exponential coefficient in Equation 1.18 can be obtained by calculation of the coupling of the donor-acceptor PES. According to the approximations made to include the vibrational sub-levels on the PES, different expressions can be obtained.[40,41] When a single vibrational mode is accounted for and solvent relaxation is assumed to respond rapidly to the change in the electronic structure of reactants and products, Equation 1.18 assumes the following form:

$$k_{ET} = \frac{2\pi}{\hbar}\left|V_{rp}\right|^2 \frac{1}{\sqrt{4\lambda k_B T}} e^{-\frac{\left(\lambda + \Delta G^{\ominus}\right)^2}{4\lambda k_B T}} \tag{1.22}$$

Where $\left|V_{rp}\right|^2$ is the coupling term between the reactant and product PES, and in the derivation is assumed to be extremely smaller than thermal fluctuations in the order of $k_B T$. The equation shows that the reactant and product PES need to couple for the electron transfer to occur. Also, it can be shown that the ET is dependent on distance, the rate of the transfer decaying exponentially with the distance between the donor-acceptor pair – evidence necessary to be accounted for when treating ET between donor and acceptor molecules free to diffuse.

The Marcus treatment of ET prompts an extension for another charge-transfer reaction, proton transfer (PT).[43] For this class of reaction a Marcus bond-order bond-energy semiempirical correlation has been used to predict and rationalize the rate of intermolecular and intramolecular PT following molecular photoexcitation.[44–46] However so far no

experiments have managed to interrogate systems that lie in a predicted inverted region for PT. Finally, further research has been done in the field of proton-coupled electron transfer reactions, where the ET and the PT occurs at the same timescales if not simultaneously, a class of reaction that tests to an extreme the validity of BO approximation.[47]

1.4. Spectroscopic Techniques for Photochemistry

1.4.1. Time-Correlated Single Photon Counting Spectroscopy

Time-Correlated Single Photon Counting (TCSPC) spectroscopy is a time-resolved fluorescence technique suitable to investigate the time-resolved decay profile of fluorescent molecules.[48] As summarized by Figure 1.5, a molecule is excited with a high-repetition laser source and every time the molecule emits, a fluorescence photon is registered by a detector, that is transduced into an electrical signal. As an electrical signal is produced by the detector, a time-to-digital converter (TDC) card registers the signal, and a photon is counted. At the same time, the TDC registers pulses associated with the excitation source, either by electronical synchronisation or by sending a portion of the excitation light onto a second detector prior to sample excitation. At each optical cycle of the laser, the excitation pulse read by the detector acts as a start clock and triggers the TDC to start a time-interval measurement. As soon as a fluorescence photon is counted, the clock is stopped, and the time-interval associated to the emission event is registered and stored. The procedure is repeated at each optical cycle of the laser, sampling the statistics of the probabilistic spontaneous emission event, and binning every registered time-interval in a histogram, until the time-resolved decay profile is obtained. The bin width determines the sampling resolution of the technique.

TCSPC is an extremely sensitive technique, as current technology in detector manufacturing allows for detection of very low photon fluxes; this is particularly useful when working at concentrations approaching single molecules, or when the fluorescence quantum yield of the sample is extremely low. Sensitivity, detection wavelength range, dead-times, and dark count-rates are specific to each kind of detector, which are chosen according with the experimental needs. All TCSPC detectors are based on the same principle that arrival of a photon on a light-sensitive material triggers an electron cascade process and

thus an electric signal is produced; photo-multiplier tubes and avalanche photodiodes are the most common types of detectors.

There are two main limitations of TCSPC. The first is clearly related to the set of molecules that can be investigated, which are required to fluoresce. The second is related to the time-resolution of the technique. In principle, the shortest recordable excitation-emission time-interval is limited by a series of factors all convolved together: the time width of the excitation pulse acting as a start clock, the temporal uncertainty between the arrival of a photon at the detector and the generation of the electrical signal determining the error on the stop clock, the jitter associated to the electronics component of the TDC in the digitalization.

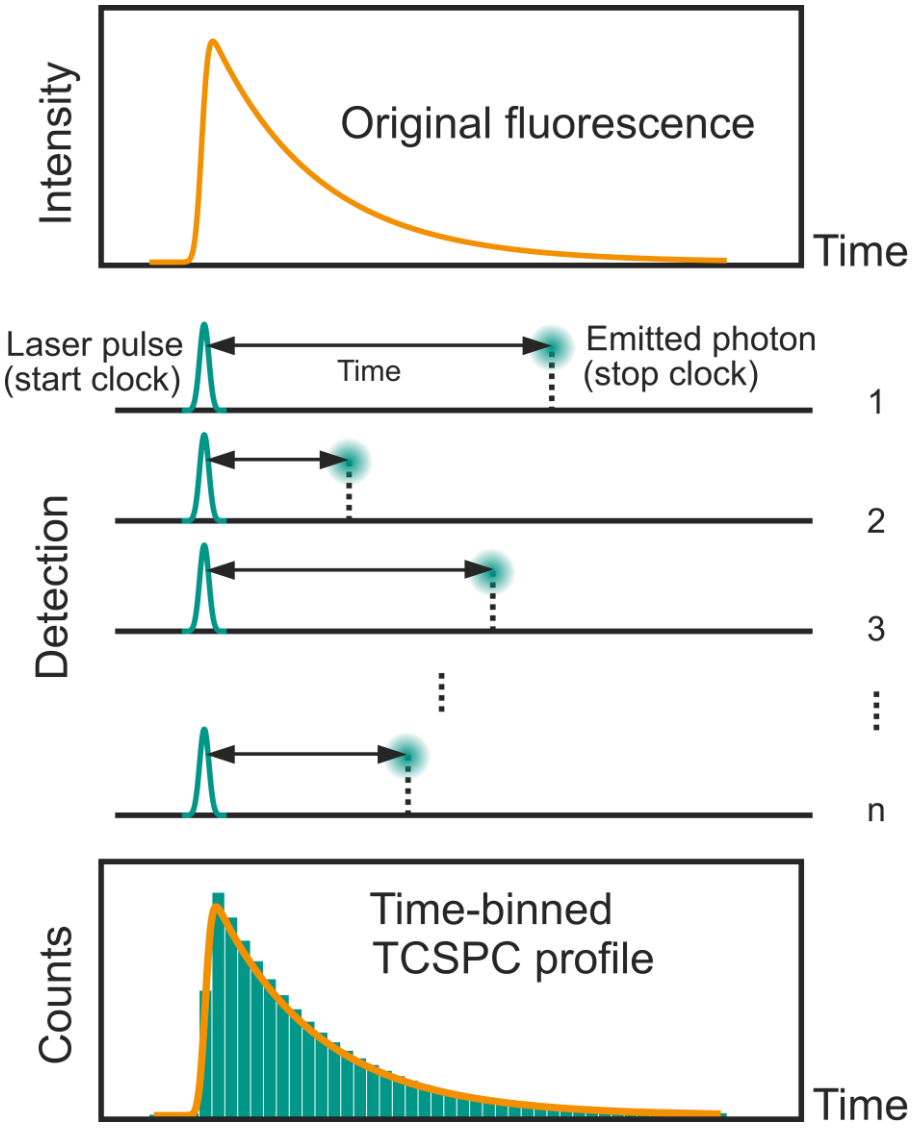

Figure 1.5. Schematic working principle of TCSPC. To recover the time-resolved decay profile of a chemical species, the time interval between the excitation and the fluorescence of a molecule is repeatedly measured and binned to obtain a histogram.

In practice, the use of lasers with ultrashort pulses and the optimization of TDC cards limits the time-resolution to the intrinsic uncertainty in the electron cascade photogeneration event and start-stop timing jitter. According to the detectors, the time-resolution could be reduced to as much as ~4 ps, but it is more commonly found to be in the order of hundreds of picoseconds due to jitter. Measurement of the overall instrument-response function (IRF) of the technique can be determined by simple scattering experiments.

A solution to access the kinetics of photochemical reactions lying in a sub-picoseconds time regime, is offered by fluorescence up-conversion (FLUP) spectroscopy. In this ultrafast technique, the fluorescence signal of a sample is mixed in a non-linear crystal with a gate laser pulse. The gate time delay is scanned and the sum-frequency generated signal is recorded. Time-resolution is no longer dictated by the electronics of the detecting system, rather by the length of the gate pulse. However powerful, FLUP spectroscopy cannot access the dynamics of dark states; for such issue, pump-probe experiments are required.

1.4.2. Pump-Probe Spectroscopy

Pump-probe spectroscopy is a versatile solution to the problem of investigating timescales faster than those limited by electronics timing and is applicable to non-fluorescent species. In this experiment, illustrated in Figure 1.6, time-resolved differential absorbance measurements of the excited and the ground state absorption spectra are recorded. Initially, a pump pulse is focussed into a sample to excite molecules. Then, a broadband probe pulse is sent in the sample, overlapping it in space and time with the pump pulse; after it is transmitted through the sample, the probe pulse and collinear signal are dispersed with a grating and imaged onto a detector, resulting in a transient (pump-on) spectrum. Subsequently, the pump beam is blocked, typically with an optical chopper: only the probe pulse is incident on the sample, collecting a simple ground state (pump-off) absorption spectrum. The recorded spectra are then subtracted from each other according to Equation 1.23 to produce a differential signal $\Delta A(\lambda, t)$:

$$\Delta A(\lambda, t) = -log \frac{I_{pump\ on}}{I_{pump\ off}} \tag{1.23}$$

In Equation 1.23, ΔA is the differential absorbance and I is the intensity, respectively, in presence or absence of the pump pulse. The procedure is repeated at many different pump-probe time-delays, to record a transient differential absorption signal.

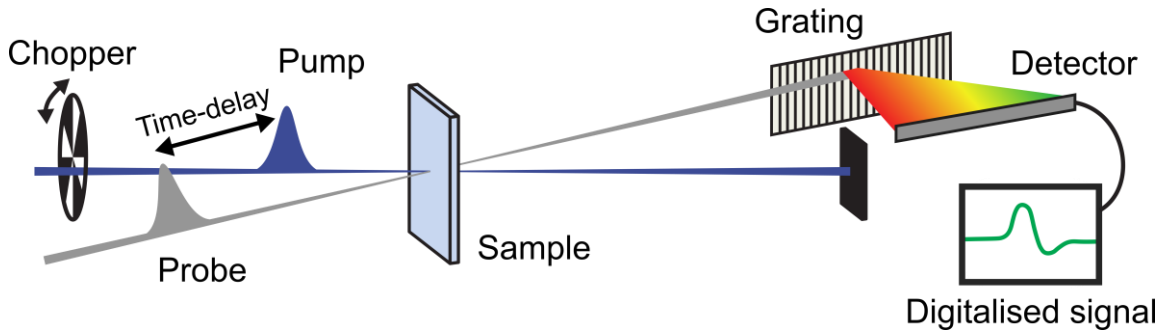

Figure 1.6. Pump-probe spectroscopy working principle. A pump laser is sent on the sample to excite it, followed by a probe pulse imaged with a grating onto a detector. Difference spectra are obtained by blocking every other pump pulse with a chopper, and the transient dynamics are accessed varying the pump-probe time delay.

As a consequence of Equation 1.23, the total pump-probe signal is the sum of different positive and negative contributions. Ground-state bleaching (GSB) is a negative feature appearing at wavelength corresponding to ground state absorption: as the pump pulses excite the sample, the ground state population is depleted; thus, on the arrival of the probe pulse, the sample will transmit more light at these wavelengths ($A_{on} < A_{off}$) resulting in more photons transmitted to the detector at these wavelengths. The probe pulse can also be responsible for stimulated emission (SE): again, the detector counts more photons than in absence of the pump, resulting in a negative feature resembling the steady state fluorescence spectrum; in cases of small Stokes shift, GSB and SE signal overlap in a single band. Positive signals can arise from excited-state absorption (ESA) contributions: molecules in the excited state can further absorb photons resonant with $S_n \leftarrow S_1$ transitions, resulting in less probe light transmitted at the corresponding wavelengths in the presence of the pump. Finally, a fourth contribution, positive in signal, can arise from photoproduct absorption: regardless the state they are formed in, by absorbing probe light they will contribute to an increased absorbance after pump excitation.

Typically, these features overlap with one another, complicating the interpretation of pump-probe spectra.[49] Dynamical solvation effects concomitant with the evolution of TA features can lead to frequency shifts. To address such sources of complexities, one resorts

to spectral deconvolution techniques to isolate the different contribution, and relies on independent experiments to assign them (*e.g.*, FLUP spectroscopy, to interrogate the emission selectively), and analyses their kinetics independently.

Advantages of pump-probe technique resides in a relatively simple setup when compared to other ultrafast techniques, providing both spectral and temporal insights on the excited state and only requiring the molecule to absorb. Furthermore, it can be easily adapted to explore different regions of the electromagnetic spectrum, employing visible broadband probe pulses to interrogate higher electronic transitions as in TA spectroscopy, or infrared probe pulses in TRIR spectroscopy to gain insights on the vibrational modes of the ground and excited state. There are limitations too. Pump-probe spectroscopy is not a background-free technique as fluorescence is, and thus far higher signal-to-noise ratios are obtained with TCSPC. Furthermore, in common setups, the use of optical choppers sets an upper limit for the repetition rate of the pump pulses and thus on how fast data can be collected; similarly, achieving pump-probe time-delays longer than 10 nanoseconds requires more specialised instrumentation. More fundamentally, as in steady-state absorption spectroscopy, TA and TRIR do not resolve homogeneous from inhomogeneous broadening with few insights gained for solute-environment interactions.

To address these limitations, multidimensional techniques have been developed, at the cost of increased complexity in the experiment. In two-dimensional (2D) spectroscopies, ultrashort broadband pulses are used to obtain frequency-frequency correlation maps at different time delays and have been used to interrogate both molecular vibrations in the infrared (2DIR) and optical transitions as electronic spectroscopies (2DES). Recent advances have also been implemented to access the mixed electronic-vibrational regime (2DEV).[50]

In ultrafast experiments, the length of the pump pulses determines the time resolution of the techniques and is theoretically limited only by the time-bandwidth product. Nevertheless, set up and data interpretation is more complicated for sub-picoseconds experiments that requires careful manipulation of laser pulses; for some experiments of this class the accessible time-window is limited; some others, as FLUP spectroscopy, require the sample to fluoresce. Ultimately, it is the sample and the scientific questions about it that dictate whether the insights gained from a technique outcompetes its complexity, in a range of choices often complementary to each other.

1.5. Thesis Topics

In this thesis, two chemical systems and a biohybrid nanomaterial that undergo three different types of bimolecular photochemical reactions will be presented and discussed, demonstrating that ultrafast spectroscopies can be successfully applied to a broad set of different problems to unveil the complexities associated with bimolecular events in the condensed phase.

In Chapter 2, the investigation of an excited-state proton transfer (ESPT) reaction between a coumarin derivative and 1-methylimidazole will be presented. ESPT is a proton-transfer reaction that occurs once a chromophore molecule is in the excited state. At a fundamental level, after photoexcitation to the excited state and rearrangement of the electron density, proton-transfer involves the breaking of a bond, exploring regions of the PES where the BO approximation does not hold; experimental evidence obtained from the analysis of this system can be used to foster research on novel theoretical methodologies. Furthermore, ESPT is a reaction relevant in biology. In plants coumarin derivatives reaction upon irradiation is supposed to oppose to bacterial and fungal infections.[51] Green-fluorescent protein radiative mechanism is based on an ESPT reaction where residues of the protein are involved in accepting a proton from the chromophore;[52,53] hence 1-methylimidazole was chosen as an ideal model proton-acceptor, able to mimic the role of protein residues. Finally, the reaction explored in Chapter 2 is one of the few examples in literature exploring intermolecular ESPT without involvement of solvent, and, therefore, constitutes an ideal model system for gaining understanding on the dynamics of this class of reactions.

In Chapter 3, the early steps of a photocatalytic cycle encompassing *p*-terphenyl and sacrificial amine electron donor for the activation and direct utilization of CO_2 in a hydrocarboxylation reaction on styrenes will be presented. CO_2 emissions by combustion of fossil fuels has systematically and dramatically increased in the last century. Its effect as a greenhouse-gas have raised concerns to limit the concentration of CO_2 to 400 ppm in the atmosphere, a threshold supposed to contain global warming within 1.5 and 2.0 °C. Beyond the limit of 2.0 °C, climate changes are believed by most of the scientific community to result unpredictable and uncontrollable.[54] To date, the safety threshold for carbon dioxide concentration has already been surpassed and is around 420 ppm, urging for action at different levels, from science and technology to legislation and politics.[55,56] In the Chemistry

community, alongside with research on carbon-free energy sources, the focus has recently moved to developing reactions and technologies for carbon-neutral combustion of fossil fuels via flue-gases carbon capture, for negative emissions through direct-air capture, for direct incorporation of CO_2 into chemicals via heterogeneous or homogeneous catalysis, either photo- or electro-chemically based, with the aim of transforming it into an asset for fine chemicals market.[57–64] In Chapter 3, the reaction recently developed by Seo *et al.*[65] has been investigated, focussing on the ET step that reduces *p*-terphenyl, a photocatalyst which has been shown to activate carbon dioxide.

In Chapter 4 the dynamics of energy transfer within a nanoconjugate biohybrid material will be investigated. The constituents of the material are quantum-dots (QDs) nanoparticles and photosynthetic bacterial reaction centre (RC) protein complexes. In nature, photosynthesis is a complex and nuanced process, that has been optimised by centuries of evolution to efficiently harvest solar photons while minimizing photodamage. Aiming to study, isolate or artificially reproduce the biological components and processes responsible for solar energy collection and conversion, organisms with simple photosynthetic apparatus, as the purple bacterium *Rhodobacter sphaeroides*, are ideal candidates. The photosynthetic apparatus of *Rba. sphaeroides* consists of three different transmembrane proteins: two light-harvesting antenna complexes (LH1 and LH2) embedding bacteriochlorophylls as chromophores and a reaction centre. Reaction centre is responsible for a reaction of charge-separation that starts the electron-transfer reactions ultimately driving photosynthesis. As shown in Figure 1.7(a), RCs are found in the protein cavity of LH1, while LH2 surrounds the supramolecular complex formed by the LH1-RC pair;[66–69] energy transfer within and between light harvesting complexes is extremely fast, from hundreds of femtoseconds to few picoseconds.[70] RCs can be characterized separately from light-harvesting complexes: its structure reveals it is constituted by three different subunits, L (light), M (medium) and H (heavy), mostly located in the hydrophobic membrane environment, embedding the chromophores responsible for charge-separation (Figure 1.7(b)). Interest in the scientific community focuses on isolated and purified RCs, able to perform almost unitary-efficient charge-separation; moreover, *Rba. sphaeroides* genome can be altered to obtain tailor-made mutant RCs for specific studies or uses. However, the wild-type RCs absorption spectrum spans the visible region but does not harvest solar photons in the 450-700 nm region (Figure 1.7(c)). While retaining LH1 and

LH2 extends photon collection in the 450-500 nm region, the majority of the photons are still unused. Therefore, biohybrid materials as QD-RC nanoconjugates have been developed: modifying the genome of RCs to provide them with a histidine tag, they can be assembled onto QDs nanocrystals, simplifying the synthetic procedure. QDs can work both as an assembly hub and an artificial light harvester, collecting visible light and transferring energy to RCs. In Chapter 4, the study of a biohybrid nanoconjugate encompassing a mutant RC able to fluoresce has been synthesised to investigate the timescale and the efficiency of the energy transfer from the QDs to the RCs.

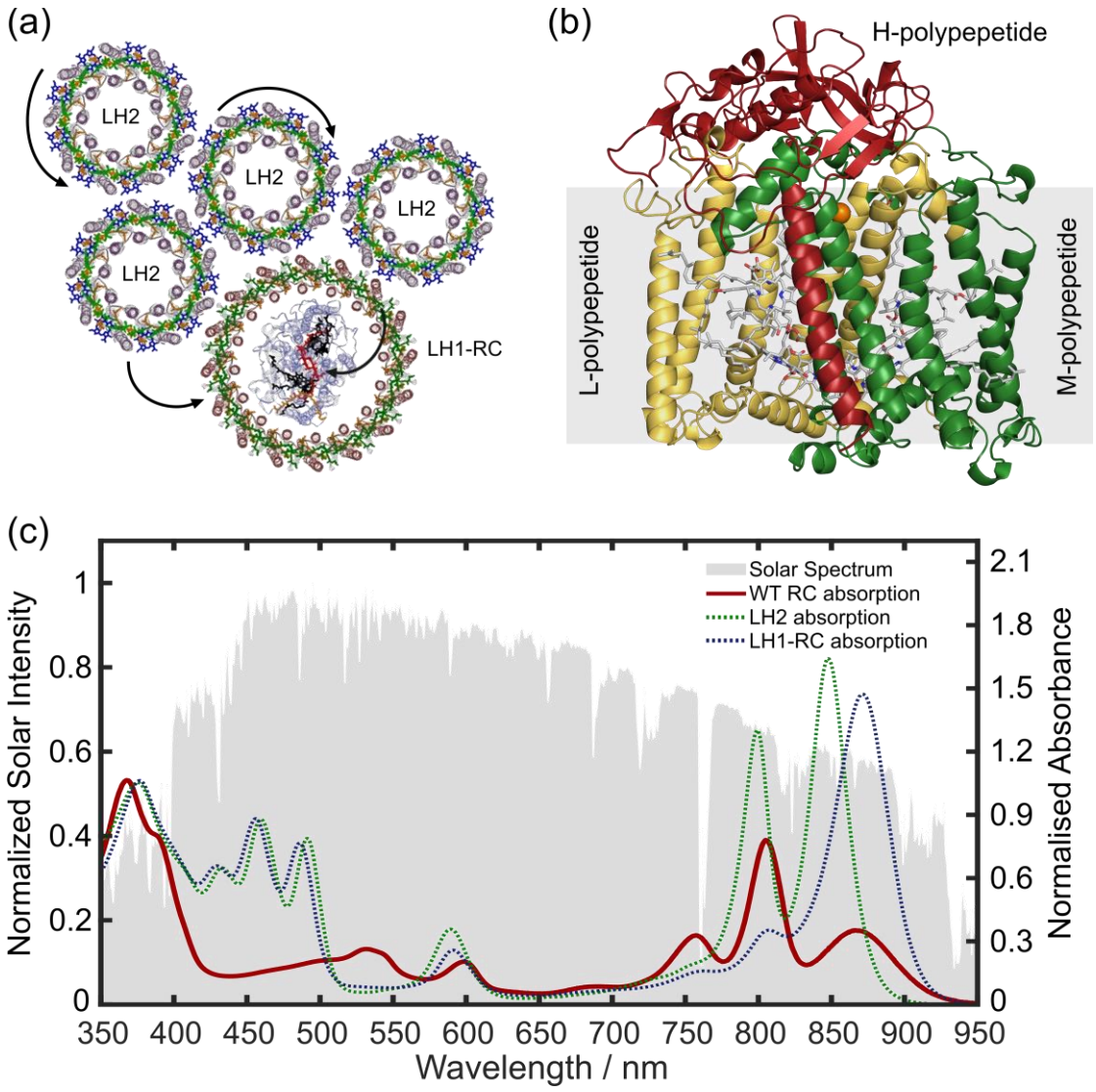

Figure 1.7. (a) The photosynthetic apparatus of photosynthetic bacteria schematically indicating the direction of the energy flow from LH2 to LH1 and to RC. Figure adapted from references.[67] (b) Side view of the RC protein, including its three subunits and the chromophores active in charge-separation. (c) Overlay of solar spectrum and absorption spectra of the constituents of *Rba. sphaeroides* photosynthetic apparatus, normalised to the Soret band at ~380 nm.

References

(1) L. Valkunas, D. Abramavicius, T. Mančal. *Molecular Excitation Dynamics and Relaxation*. Wiley: Weinheim, Germany, 2013.

(2) P. Atkins, R. Friedman. *Molecular Quantum Mechanics*. Oxford University Press: New York, NY, 2005.

(3) D. A. McQuarrie, J. D. Simons. *Physical Chemistry: A Molecular Approach*. University Science Books: Sausalito, CA, 1997.

(4) M. Brouard, C. Vallance. *Tutorials in Molecular Reaction Dynamics*; The Royal Society of Chemistry, 2012.

(5) K. K. Rohatgi-Mukherjee. *Fundamentals of Photochemistry*. Wiley: New Delhi, India, 1978.

(6) T. Elsaesser, W. Kaiser. Vibrational and Vibronic Relaxation of Large Polyatomic Molecules in Liquids. *Annu. Rev. Phys. Chem.* **1991**, *42* (1), 83–107.

(7) T. A. A. Oliver, G. A. King, D. P. Tew, R. N. Dixon, M. N. R. Ashfold. Controlling Electronic Product Branching at Conical Intersections in the UV Photolysis of Para-Substituted Thiophenols. *J. Phys. Chem. A* **2012**, *116* (51), 12444–12459.

(8) Y. Zhang, T. A. A. Oliver, M. N. R. Ashfold, S. E. Bradforth. Contrasting the Excited State Reaction Pathways of Phenol and Para-Methylthiophenol in the Gas and Liquid Phases. *Faraday Discuss.* **2012**, *157*, 141–163.

(9) D. Polli, P. Altoè, O. Weingart, K. M. Spillane, C. Manzoni, D. Brida, G. Tomasello, G. Orlandi, P. Kukura, R. A. Mathies, M. Garavelli, G. Cerullo. Conical Intersection Dynamics of the Primary Photoisomerization Event in Vision. *Nature* **2010**, *467* (7314), 440–443.

(10) H. Kandori, Y. Shichida, T. Yoshizawa. Review: Photoisomerization in Rhodopsin. *Biokhimiya* **2001**, *66* (11), 1483–1498.

(11) M. Cho. *Two-Dimensional Optical Spectroscopy*. CRC Press, 2009.

(12) M. L. Horng, J. A. Gardecki, A. Papazyan, M. Maroncelli. Subpicosecond Measurements of Polar Solvation Dynamics: Coumarin 153 Revisited. *J. Phys. Chem.* **1995**, *99* (48), 17311–17337.

(13) R. M. Stratt, M. Maroncelli. Nonreactive Dynamics in Solution: The Emerging Molecular View of Solvation Dynamics and Vibrational Relaxation. *J. Phys. Chem.* **1996**, *100* (31), 12981–12996.

(14) A. Nitzan. *Chemical Dynamics in Condensed Phases*. Oxford University Press: Oxford, UK, 2006.

(15) A. M. Kelley. *Condensed-Phase Molecular Spectroscopy and Photophysics*. Wiley: Hoboken, NJ, 2012.

(16) R. W. Boyd. *Nonlinear Optics*. Academic Press: New York, NY, 2007.

(17) G. Cerullo, S. De Silvestri. Ultrafast Optical Parametric Amplifiers. *Rev. Sci. Instrum.* **2003**, *74* (1), 1–18.

(18) M. v. Smoluchowski. Drei Vorträge Über Diffusion, Brownsche Molekularbewegung Und Koagulation von Kolloidteilchen. *Phys. Z.* **1916**, *17*, 530–594.

(19) M. v. Smoluchowski. Grundriß Der Koagulationskinetik Kolloider Lösungen. *Kolloid-Zeitschrift* **1917**, *21* (3), 98–104.

(20) F. C. Collins, G. E. Kimball. Diffusion-Controlled Reaction Rates. *J. Colloid Sci.* **1949**, *4* (4), 425–437.

(21) A. Szabo. Theory of Diffusion-Influenced Fluorescence Quenching. *J. Phys. Chem.* **1989**, *93* (19), 6929–6939.

(22) C. F. Shannon, D. D. Eads. Diffusion-Controlled Electron Transfer Reactions: Subpicosecond Fluorescence Measurements of Coumarin 1 Quenched by Aniline and N,N-Dimethylaniline. *J. Chem. Phys.* **1995**, *103* (13), 5208–5223.

(23) G. Angulo, A. Rosspeintner. Bimolecular Photo-Induced Electron Transfer Enlightened by Diffusion. *J. Chem. Phys.* **2020**, *153* (4), 040902.

(24) A. Rosspeintner, E. Vauthey. Bimolecular Photoinduced Electron Transfer Reactions in Liquids under the Gaze of Ultrafast Spectroscopy. *Phys. Chem. Chem. Phys.* **2014**, *16* (47), 25741–25754.
(25) A. Rosspeintner, G. Angulo, E. Vauthey. Bimolecular Photoinduced Electron Transfer beyond the Diffusion Limit: The Rehm-Weller Experiment Revisited with Femtosecond Time Resolution. *J. Am. Chem. Soc.* **2014**, *136* (5), 2026–2032.
(26) K. F. Riley, M. P. Hobson, S. J. Bence. *Mathematical Methods for Physics and Engineering*. Cambridge University Press: Cambridge, UK, 2006.
(27) A. J. Bard, L. R. Faulkner. *Eelctrochemical Methods: Fundamentals and Applications*. Wiley: New York, NY, 2001.
(28) M. v. Smoluchowski. The Kinetic Theory of Brownian Molecular Motion and Suspensions. *Ann. Phys.* **1906**, *21* (14), 756–780.
(29) M. Rini, D. Pines, B. Z. Magnes, E. Pines, E. T. J. Nibbering. Bimodal Proton Transfer in Acid-Base Reactions in Water. *J. Chem. Phys.* **2004**, *121* (19), 9593–9610.
(30) C. Nançoz, C. Rumble, A. Rosspeintner, E. Vauthey. Bimolecular Photoinduced Electron Transfer in Non-Polar Solvents beyond the Diffusion Limit. *J. Chem. Phys.* **2020**, *152* (24), 244501.
(31) B. Dereka, I. Fureraj, A. Rosspeintner, E. Vauthey. Halogen-Bond Assisted Photoinduced Electron Transfer. *Molecules* **2019**, *24* (23), 4361.
(32) J. S. Beckwith, B. Lang, J. Grilj, E. Vauthey. Ion-Pair Dynamics upon Photoinduced Electron Transfer Monitored by Pump-Pump-Probe Spectroscopy. *J. Phys. Chem. Lett.* **2019**, *10* (13), 3688–3693.
(33) T. Kumpulainen, B. Lang, A. Rosspeintner, E. Vauthey. Ultrafast Elementary Photochemical Processes of Organic Molecules in Liquid Solution. *Chem. Rev.* **2017**, *117* (16), 10826–10939.
(34) A. Fernández-Ramos, J. A. Miller, S. J. Klippenstein, D. G. Truhlar. Modeling the Kinetics of Bimolecular Reactions. *Chem. Rev.* **2006**, *106* (11), 4518–4584.
(35) G. D. Scholes. Long-Range Resonance Energy Transfer in Molecular Systems. *Annu. Rev. Phys. Chem.* **2003**, *54* (1), 57–87.
(36) T. Förster. Transfer Mechanisms of Electronic Excitation. *Discuss. Faraday Soc.* **1959**, *27* (10), 7–17.
(37) T. Förster. Zwischenmolekulare Energiewanderung Und Fluoreszenz. *Ann. Phys.* **1948**, *437* (1–2), 55–75.
(38) D. L. Dexter. A Theory of Sensitized Luminescence in Solids. *J. Chem. Phys.* **1953**, *21* (5), 836–850.
(39) R. A. Marcus. On the Theory of Oxidation-Reduction Reactions Involving Electron Transfer. I. *J. Chem. Phys.* **1956**, *24* (5), 966–978.
(40) V. Levich, R. Dogonadze. Theory of Non-Radiation Electron Transitions from Ion to Ion in Solutions. *Dokl. Akad. Nauk SSSR* **1959**, *124* (123).
(41) I. Rips, J. Jortner. Dynamic Solvent Effects on Outer-Sphere Electron Transfer. *J. Chem. Phys.* **1987**, *87* (4), 2090–2104.
(42) J. M. Saveant. A Simple Model for the Kinetics of Dissociative Electron Transfer in Polar Solvents. Application to the Homogeneous and Heterogeneous Reduction of Alkyl Halides. *J. Am. Chem. Soc.* **1987**, *109* (22), 6788–6795.
(43) N. Agmon. Elementary Steps in Excited-State Proton Transfer. *J. Phys. Chem. A* **2005**, *109* (1), 13–35.
(44) M. Ekimova, F. Hoffmann, G. Bekçioğlu-Neff, A. Rafferty, O. Kornilov, E. T. J. Nibbering, D. Sebastiani. Ultrafast Proton Transport between a Hydroxy Acid and a Nitrogen Base along Solvent Bridges Governed by the Hydroxide/Methoxide Transfer Mechanism. *J. Am. Chem. Soc.* **2019**, *141* (37), 14581–14592.
(45) C. Kaiser, T. Halbritter, A. Heckel, J. Wachtveitl. Proton-Transfer Dynamics of Photoacidic Merocyanines in Aqueous Solution. *Chem. A Eur. J.* **2021**, *27* (35), 9160–9173.

(46) M. Prémont-Schwarz, T. Barak, D. Pines, E. T. J. Nibbering, E. Pines. Ultrafast Excited-State Proton-Transfer Reaction of 1-Naphthol-3,6- Disulfonate and Several 5-Substituted 1-Naphthol Derivatives. *J. Phys. Chem. B* **2013**, *117* (16), 4594–4603.
(47) S. Hammes-Schiffer. Current Theoretical Challenges in Proton-Coupled Electron Transfer: Electron-Proton Nonadiabaticity, Proton Relays, and Ultrafast Dynamics. *J. Phys. Chem. Lett.* **2011**, *2* (12), 1410–1416.
(48) J. R. Lakowicz. *Principles of Fluorescence Spectroscopy*. Springer: Boston, MA, 2006.
(49) R. Berera, R. van Grondelle, J. T. M. Kennis. Ultrafast Transient Absorption Spectroscopy: Principles and Application to Photosynthetic Systems. *Photosynth. Res.* **2009**, *101* (2–3), 105–118.
(50) T. A. A. Oliver. Recent Advances in Multidimensional Ultrafast Spectroscopy. *R. Soc. Open Sci.* **2018**, *5* (1), 171425.
(51) R. Simkovitch, D. Huppert. Photoprotolytic Processes of Umbelliferone and Proposed Function in Resistance to Fungal Infection. *J. Phys. Chem. B* **2015**, *119* (46), 14683–14696.
(52) S. P. Laptenok, J. Conyard, P. C. B. Page, Y. Chan, M. You, S. R. Jaffrey, S. R. Meech. Photoacid Behaviour in a Fluorinated Green Fluorescent Protein Chromophore: Ultrafast Formation of Anion and Zwitterion States. *Chem. Sci.* **2016**, *7* (9), 5747–5752.
(53) S. R. Meech. Excited State Reactions in Fluorescent Proteins. *Chem. Soc. Rev.* **2009**, *38* (10), 2922–2934.
(54) The Intergovernmental Panel on Climate Change. URL: https://www.ipcc.ch/.
(55) N. Armaroli, V. Balzani. Solar Electricity and Solar Fuels: Status and Perspectives in the Context of the Energy Transition. *Chem. A Eur. J.* **2016**, *22* (1), 32–57.
(56) B. Obama. The Irreversible Momentum of Clean Energy. *Science* **2017**, *355* (6321), 126–129.
(57) D. W. Keith, G. Holmes, D. St. Angelo, K. Heidel. A Process for Capturing CO_2 from the Atmosphere. *Joule* **2018**, *2* (8), 1573–1594.
(58) K. Z. House, A. C. Baclig, M. Ranjan, E. A. van Nierop, J. Wilcox, H. J. Herzog. Economic and Energetic Analysis of Capturing CO_2 from Ambient Air. *Proc. Natl. Acad. Sci.* **2011**, *108* (51), 20428–20433.
(59) E. S. Sanz-Pérez, C. R. Murdock, S. A. Didas, C. W. Jones. Direct Capture of CO_2 from Ambient Air. *Chem. Rev.* **2016**, *116* (19), 11840–11876.
(60) A. Cherubini-Celli, J. Mateos, M. Bonchio, L. Dell'Amico, X. Companyó. Transition Metal-Free CO_2 Fixation into New Carbon–Carbon Bonds. *ChemSusChem* **2018**, *11* (18), 3056–3070.
(61) N. Mac Dowell, P. S. Fennell, N. Shah, G. C. Maitland. The Role of CO_2 Capture and Utilization in Mitigating Climate Change. *Nat. Clim. Chang.* **2017**, *7* (4), 243–249.
(62) J. Qiao, Y. Liu, F. Hong, J. Zhang. A Review of Catalysts for the Electroreduction of Carbon Dioxide to Produce Low-Carbon Fuels. *Chem. Soc. Rev.* **2014**, *43* (2), 631–675.
(63) C. Oloman, H. Li. Electrochemical Processing of Carbon Dioxide. *ChemSusChem* **2008**, *1* (5), 385–391.
(64) M. Yan, Y. Kawamata, P. S. Baran. Synthetic Organic Electrochemical Methods since 2000: On the Verge of a Renaissance. *Chem. Rev.* **2017**, *117* (21), 13230–13319.
(65) H. Seo, A. Liu, T. F. Jamison. Direct β-Selective Hydrocarboxylation of Styrenes with CO_2 Enabled by Continuous Flow Photoredox Catalysis. *J. Am. Chem. Soc.* **2017**, *139* (40), 13969–13972.
(66) G. R. Fleming, R. van Grondelle. Femtosecond Spectroscopy of Photosynthetic Light-Harvesting Systems. *Curr. Opin. Struct. Biol.* **1997**, *7*, 738–748.
(67) B. R. Green, W. W. Parson. *Advances in Photosynthesis and Respiration - Light-Harversitng Antennas in Photosynthesis.* Kluwer Academic Publishers: University of Illinois, Urbana, IL, 2003.
(68) R. E. Blankenship. *Molecular Mechanisms of Photosynthesis*. Blackwell Science Ltd: Oxford, UK, 2002.

(69) R. G. Saer, R. E. Blankenship. Light Harvesting in Phototrophic Bacteria: Structure and Function. *Biochem. J.* **2017**, *474* (13), 2107–2131.
(70) F. Fassioli, R. Dinshaw, P. C. Arpin, G. D. Scholes. Photosynthetic Light Harvesting: Excitons and Coherence. *J. R. Soc. Interface* **2014**, *11* (92), 20130901.

2. Ultrafast Bimolecular Excited State Proton Transfer in a Hydroxycoumarin–Imidazole Derivatives System

The results, data and discussions presented in this chapter have been published. The reader can refer to: G. Amoruso, V. C. A. Taylor, M. Duchi, E. Goodband, T. A. A. Oliver. Following Bimolecular Excited State Proton Transfer Between Hydroxycoumarin and Imidazole Derivatives. *The Journal of Physical Chemistry B*, **2019**, 123, 22, 4745–4756.

I declare that: I collected and analysed the data; wrote the manuscript in discussion with my supervisor Dr. Thomas A. A. Oliver.

2.1. Introduction

Proton transfer is a fundamental reaction that is ubiquitous throughout biology and chemistry.[1] The transfer of a proton is the most facile method of delivering a positive charge. Yet, despite the apparent simplicity of a proton transfer,[2] it has enormous consequences for the outcome of chemical reactions, for example, catalyzing enzyme reactions,[3] or creation of trans-membrane proton gradients in photosynthesis that provide an essential driving force for ATP synthesis.[4,5]

In many cases, proton transfer is not instantaneous and requires stimulus to surmount the associated reaction barrier, which is often delivered via absorption of visible or ultraviolet light. However, the key reaction itself may occur on either ground[6] or excited[7] potential energy surface(s). The latter category of reaction is termed excited state proton transfer (ESPT), and the field has been dominated by the study of photoacids. Photoacids have larger acid dissociation constants in the excited state (p*K*a*) compared to the ground electronic state, and these differences are frequently evaluated using the Förster cycle.[8,9] Recent studies have shown a strong correlation between photoacidity and O–H stretching frequency shift for a wide range of differently substituted photoacids.[10]

ESPT can be further categorized into two subclasses; (i) intramolecular ESPT where a proton is transferred between two heteroatoms on the same molecule[11,12] resulting in tautomerization[13–18]/isomerization,[19] or (ii) bimolecular ESPT where H^+ is transferred from the photoacid to a secondary molecule which may be part of the surrounding solvent,[20–23] a base solute molecule,[24–26] or a proximal protein residue.[27–30]

The timescale of ESPT depends greatly on the reaction subclass and underpinning mechanism, spanning the extremes of instantaneous/ballistic to diffusion limited.[31,32] Most reactions, however, sit in an intermediate regime where solvent re-organization must occur and/or proximal solvent molecules play a critical role in bridging or mediating ESPT.[33–35]

From a technical perspective, ESPT reactions are challenging both theoretically and experimentally, often necessitating an even-handed quantum mechanical treatment of both proton and electrons using advanced theoretical methods,[36–38] and femtosecond temporal resolution to follow events that are commensurate to, or faster than, the solvent/environmental response.[39]

Chemical systems where the acid and base concentrations can be readily controlled and photoacidity manipulated via judicious chemical substitution provides one convenient approach to systematically explore the molecular mechanisms of ESPT. For example, functionalization of photoacids with electron withdrawing groups is known to reduce the p*K*a* via stabilization of the anion photoproduct.[40] In this study, a bimolecular ESPT reaction between two solute molecules was investigated: 7-hydroxy-4-(trifluoromethyl)-1-coumarin (CouOH) and 1-methylimidazole (MI), in the aprotic solvent chloroform-d_1 ($CDCl_3$)- see Figure 2.1 for structures.

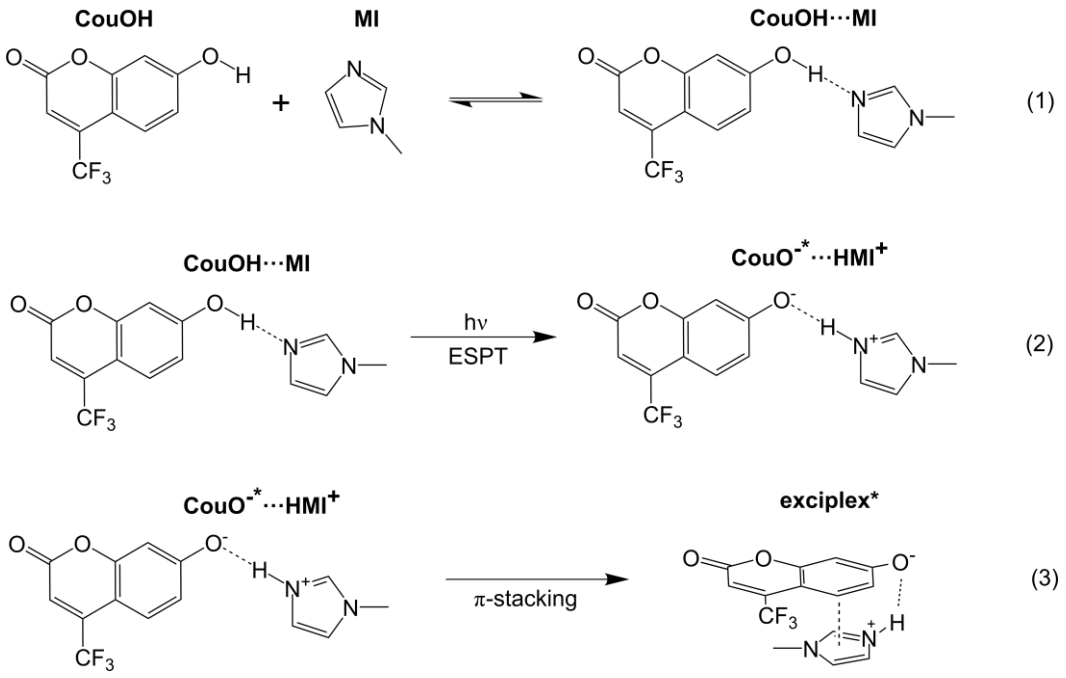

Figure 2.1. Reaction schemes for (1) ground state hydrogen-bonding equilibrium between CouOH and MI, (2) excited state proton transfer, (3) subsequent π-stacking of photoproducts to form exciplex.

The excited state acid–base reaction has previously been investigated in toluene solution by Westlake *et al.* [25,26] using coherent Raman, time-correlated single photon counting, and transient absorption spectroscopies. In these studies, the excited state dynamics were only investigated for a selected few CouOH:MI concentration ratios, where the MI base was always in excess. As part of their reaction scheme, Westlake *et al.* reported ESPT between CouOH* and MI occurred a timescale of several tens of picoseconds and the coumarin anion photoproduct subsequently tautomerized on the excited state mediated by an excess of base MI molecules. Notably, at the high concentrations used in the work by Westlake *et al.*, the probability for forming MI aggregates is significant.[41] Savarese *et al.* also studied the CouOH–MI ESPT reaction using B3LYP density functional theory calculations.[42–44] Despite these prior studies, there are numerous open questions regarding the precise timescale of ESPT for this reaction due to the limited time resolution of prior studies, the definitive identification of the nascent photoproducts and their immediate fates.

In this study, the bimolecular ESPT reaction between CouOH and MI was investigated by systematically varying the concentration ratio between the photoacid and base to reveal unequivocal spectroscopic signatures of the photogenerated products and determine the involvement of any diffusion-assisted ESPT using a combination of transient absorption (TA) and time-resolved infrared (TRIR) ultrafast spectroscopies. This approach was useful to gain insights into the earliest timescales of a prototypical biomimetic ESPT reaction and to track the fates of nascent photoproducts. Intentionally working at millimolar CouOH and MI concentrations made it possible to disentangle the photoproduct formation and rearrangement dynamics from the non-radiative relaxation dynamics of ‘free’ CouOH molecules. Under these conditions, relaxation pathways such as bimolecular diffusion-assisted ESPT or coumarin anion tautomerization in chloroform solution are excluded. The experimental findings are supported by density functional theory theoretical calculations.

2.2. Experimental and Theoretical Methods

2.2.1. Sample Preparation and Steady-State Experiments

7-hydroxy-4-(trifluoromethyl)-1-coumarin and 1-methylimidaziole were purchased from Sigma Aldrich and used without further purification. Deuterated chloroform ($CDCl_3$) solvent was used for all experiments (Sigma Aldrich, 99.8 atom % D, purity > 99.0%). The

studies explored a variety of different CouOH/MI concentration mixtures. All the samples were freshly prepared for TA and TRIR spectroscopy measurements.

Steady state ultraviolet spectra were acquired using a Thermo Scientific Genesys 10S UV-Vis Spectrophotometer. Fourier-transform infrared (FTIR) data were acquired with a Perkin Elmer Spectrum Two FTIR Spectrometer. One and two-dimensional fluorescence spectra were collected with a Perkin-Elmer LS-45 Luminescence Spectrometer. All measurements were performed at room temperature (~20 ^{o}C).

2.2.2. Transient Absorption and Time-Resolved Infrared Spectroscopies

TA and TRIR experiments were performed using an established ultrafast system, schematically summarized in Figure 2.2.[45] The fundamental output of a 5 W, 1 kHz, 800 nm, 40 fs laser system comprised of an oscillator (Coherent Vitara-S) and a Ti:Sapphire regenerative amplifier (Coherent, Legend Elite HE+) was split into three parts with a pair of beam-splitters. At first, the 800 nm fundamental was sent through a 2:98 beam-splitter using the minor portion to generate the white-light continuum probe pulses in TA spectroscopy experiments. This was achieved by focusing the 800 nm light into a rastered 3 mm thick CaF_2 window, after sending it through a polarizer and a half-wave plate to attenuate the light intensity, so to obtain a stable white-light continuum.

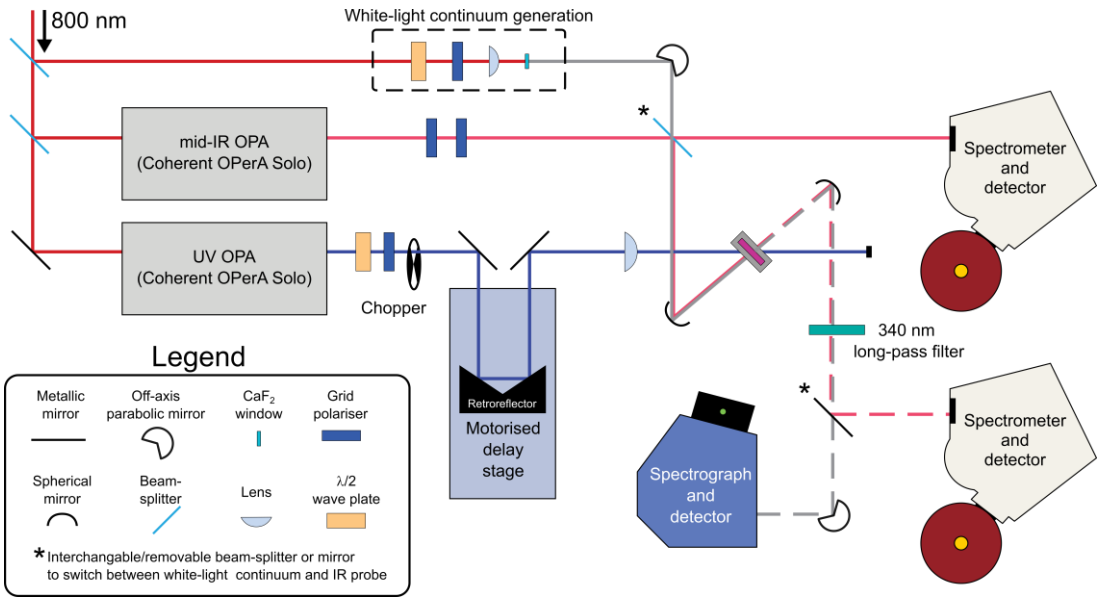

Figure 2.2. Schematic of the experimental setup used in TA and TRIR measurements to investigate the ESPT reaction between CouOH and MI derivatives.

The major portion of the 800 nm output of the laser was sent through a 50:50 beam-splitter, using the two resulting beams to seed two optical-parametric amplifiers (OPAs, Coherent OPerA Solo). The first OPA was used to generate broadband (~150 fs, ~300 cm^{-1}) mid-IR probe pulses, centered at 1380 cm^{-1} or 1460 cm^{-1} used in TRIR spectroscopy experiments. Before focusing into the sample, the mid-IR probe pulses were further split, using one of the two replicas as a reference in signal detection to account for shot-to-shot instabilities.

The second OPA was used to generate 330 nm pump laser pulses (~100 fs, 6 nm FWHM), required in both TA and TRIR experiments. The pump pulses were then sent through a polarizer and a half-wave plate pair, setting the pump polarization to magic angle (54.7°) with respect to the probe pulse and to attenuate the pump power to ~400 nJ at the sample. Subsequently, pump on/off pulses sequences required to collect transient spectra at each time delay were obtained by modulating the pump pulses at half the frequency of the laser repetition rate (500 Hz) with an optical chopper wheel (Thorlabs, MC2000). The modulated pump pulses were sent through an aluminum retroreflector (PLX) on a motorized delay stage (Thorlabs, DDS220/M), allowing to vary the time-delay between pump and probe pulses to a maximum of ~1 ns. Pump scatter was removed by inserting a 340 nm long-pass filter into the probe (and collinear signal) beam path after the sample.

Depending on the experiment, white-light continuum or mid-IR probe pulses were focused into the sample with a spherical mirror, the transmitted beam being recollimated with a second spherical mirror and sent to the detection system. For TA experiment, the probe pulses were focused onto a spectrograph (Andor, Shamrock 163) and imaged onto a 1024-pixel CCD array detector (Entwicklungsbüro Stresing) with ~1 nm resolution, using the sharp near-UV absorption spectrum of a solid film of Ho_2O_3 to calibrate the spectrograph. For TRIR experiment the signal and the reference beams were focused onto two spectrometers (iHR320, HORIBA Scientific) and frequency-dispersed onto 128-pixel HgCdTe linear array detectors (MCT-10-128, Infrared Associates Inc.) with ~2 cm^{-1} spectral resolution and cooled with liquid nitrogen at 77 K, using the mid-IR region of the absorption spectrum of stilbene to calibrate the spectrometers.

For data collection and pump on/off spectra calculation, and for control of the motorized delay-stage custom-made LabVIEW (National Instruments) software were adopted. Data were acquired at least three times for every mixture, using freshly prepared

solutions each time. Time-delays were randomized to minimize the effects of fluctuations in the intensity of laser source. Prior and during data collection, the whole experimental apparatus was purged with nitrogen, ensuring data reproducibility. All the transient data were analyzed with custom-made MATLAB (MathWorks) scripts.

Prior to the data collection, non-resonant, two-color two-photon absorption experiments in $CDCl_3$ were carried out to determine the instrument-response function (IRF), which was found to be ~200 fs.[45,46] Pump and probe spatial (beam spots) and temporal (time-zero) overlap was optimized using a cuvette with a dye solution of Oxazine 4 in methanol for TA measurements and a solid film of Ge crystal for TRIR measurements. Throughout the experiments, samples were continuously flowed using a customized Harrick flow cell (CaF_2 windows), with 170 μm and 250 μm pathlengths for TA and TRIR measurements, respectively.

2.2.3. Computational Methods

Density functional theory (DFT) and time-dependent DFT (TD-DFT) theoretical calculations, with the ωB97XD exchange-correlation functional and a 6-31+G** basis set were used to optimize the minimum energy structures of various CouOH, MI and photoproduct structures in both ground and excited electronic states. Harmonic vibrational frequencies were calculated to verify the optimized structures obtained were true minima and to assist in the assignment of TRIR data. All calculations used a polarizable continuum model (PCM) to implicitly model the chloroform solvent, and performed in the Gaussian09 computational suite.[47] An electron–hole density analysis was performed using Multiwfn.[48]

2.3. Results and Discussion

2.3.1. Ground State Association Equilibrium Characterization

The ground state hydrogen bonding equilibrium constant between CouOH and MI molecules in deuterated chloroform solution was investigated using linear ultraviolet absorption, FTIR and fluorescence spectroscopy.

The ultraviolet linear absorption spectra for several different CouOH/MI mixtures are displayed in Figure 2.3. It is important to note that MI absorbs at far shorter wavelengths

(< 220 nm) than the displayed region. The absorption spectrum of 4 mM CouOH has a local maximum at 330 nm, which TD-DFT calculations assign to a $\pi^* \leftarrow \pi$ electronic transition.

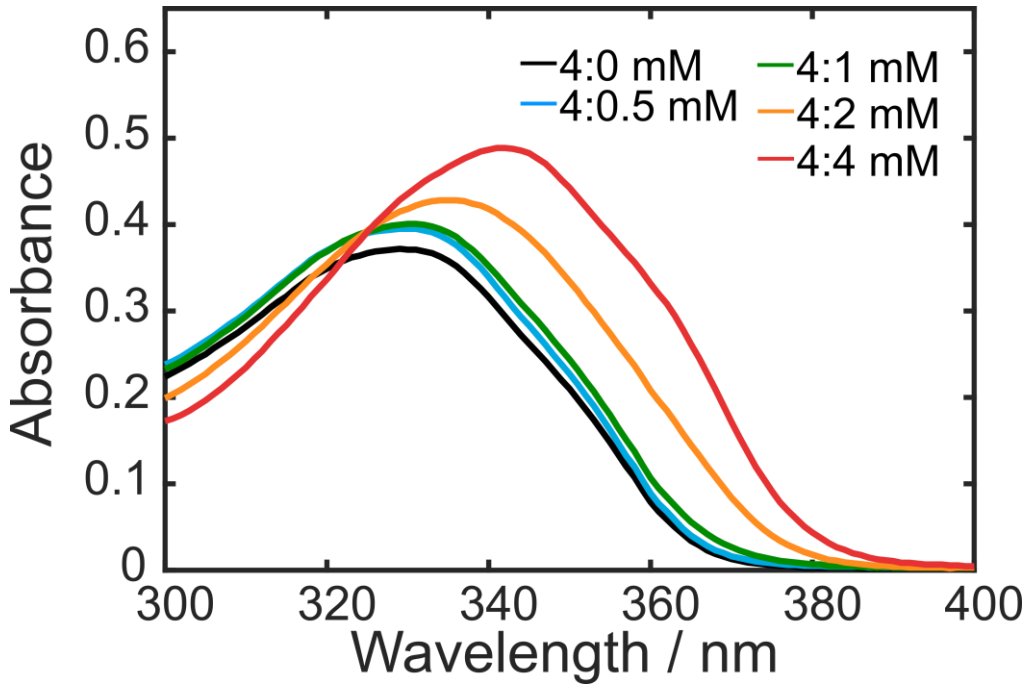

Figure 2.3. Ultraviolet absorption spectra for the specified CouOH:MI mixtures in deuterated chloroform solution (100 µm pathlength cell).

The center of this band progressively red-shifts to 342 nm upon addition of up to 4 mM MI and the maximal absorbance increases. The observed red-shift of the absorption maximum matches previous measurements reported in toluene solution.[26] The similarity in absorption maxima of CouOH in toluene and chloroform solutions is unsurprising given the very similar dielectric constants and low associated polarities of both solvents. Ground state DFT calculations found that the only significantly favorable inter-molecular interactions between CouOH and MI moieties were hydrogen-bonding structures via the O–H···N bridge, henceforth referred to as CouOH···MI. Structures including π-stacking between the aromatic rings were found to be energetically unstable in S_0 and optimized to pseudo planar H–bonded structures. TD-DFT calculations show that the observed reduced transition energy associated with the $^1\pi\pi^*$ state of the coumarin molecule in the CouOH···MI complex mainly arises due to a stabilization of the CouOH π* (LUMO), via a favorable H–bond between the CouOH hydroxyl group and the MI nitrogen lone pair. These observations are

similar to the red shifted absorption of the photoacid 1,3,6-trisdimenthylsulfonamide upon addition of hydrogen bonding acceptor molecules in aprotic chlorinated solvents.[49]

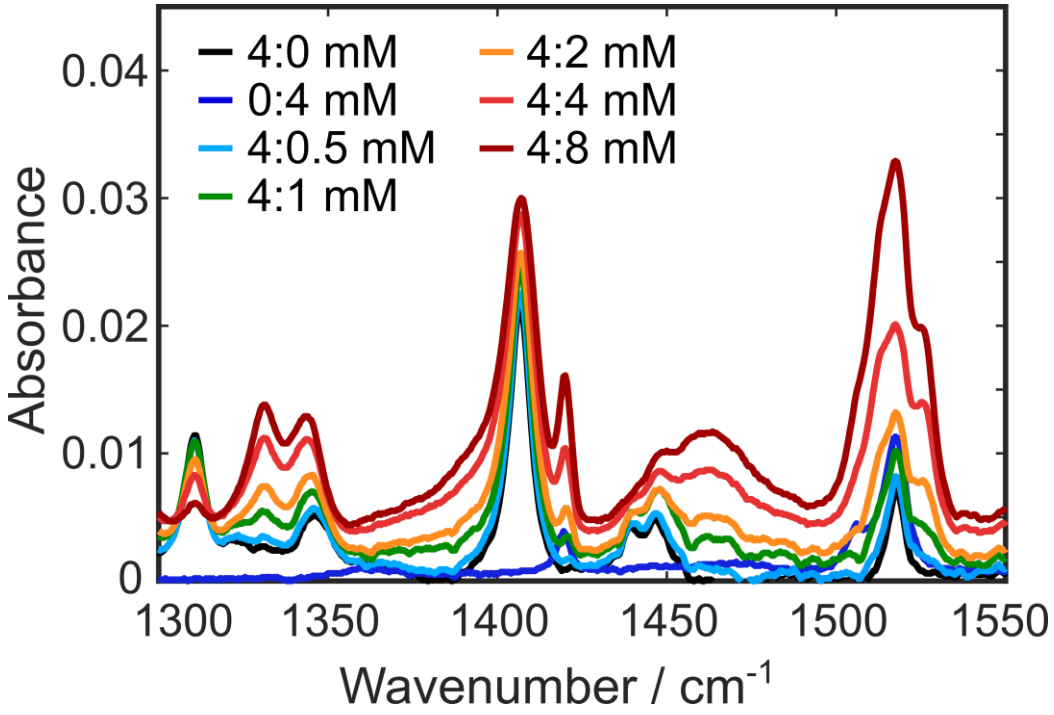

Figure 2.4. Ground state mid-IR absorption spectra for the specified CouOH:MI concentrations in $CDCl_3$.

Figure 2.4 displays the FTIR spectra for CouOH, MI and various mixtures of CouOH and MI in $CDCl_3$ solution for part of the infrared fingerprint region. The major peaks in this region were assigned using DFT calculated vibrational frequencies (see Table 2.1). In CouOH/MI mixtures two additional vibrational peaks are present at 1331 cm^{-1} and 1526 cm^{-1}. These bands have been assigned using DFT calculated frequencies to coupled CouOH and MI vibrational modes. Moreover, a broad feature at ~1463 cm^{-1} appears; although calculations did not return a clear assignment, the band is likely to be associated to modes involving the O–H···N nuclei, greatly influenced by the different configurations that the CouOH···MI species can assume, resulting in a broadening of the transition.

The association constant K_{eq} between CouOH and MI molecules in $CDCl_3$ solution was determined by utilizing the aforementioned two features in the FTIR spectrum that are unique to the hydrogen bonded CouOH···MI species.

Table 2.1. Experimentally observed and assigned calculated (DFT/ωB97XD/6-31+G**/PCM) ground state vibrational frequencies corresponding to the major peaks in Figure 2.4 and associated nuclear motions. All calculated frequencies were scaled by 0.96 to account for any anharmonicity.

Observed / cm^{-1}	Calculated / cm^{-1}	Assignment
	CouOH	
1310	1305	Symmetric C–C phenol ring breathing/O–H bend
1347	1344	Anti-symmetric C–C phenol ring breathing/O–H bend
1407	1391	Out-of-phase C–C ring breathing on both pyrone and phenol moieties
1446	1442	In-phase C–C aromatic ring breathing mode on both pyrone and phenol ring /O–H bend
1518	1510	Symmetric C–C phenol ring breathing/C–O stretch
	MI	
1421	1429	$–CH_3$ scissor
1505	1509	Anti-symmetric ring breathing
1518	1518	Symmetric ring breathing/N–CH_3 stretch
	CouOH···MI	
1331	1352	Symmetric C–C phenol stretch/C–O stretch/MI ring breath
1526	1581	CouOH ring breathing/ CouOH O–H bend/MI ring breathing

To calculate the equilibrium constant, the full second order equation was solved,[50] without introducing any approximations as per Benesi-Hildebrand linearization.[51] The equilibrium constant is given by:

$$K_{eq} = [adduct]/[CouOH]\,[MI] \qquad (2.1)$$

By substituting the equilibrium concentrations of CouOH and MI with their initial concentrations (denoted by a subscript 0) and use of the mass balance equations, it can be shown:

$$K_{eq} = [adduct]/([CouOH]_0 - [adduct])\,([MI]_0 - [adduct]) \qquad (2.2)$$

And to extract K_{eq} the following second order equation must be solved:

$$K_{eq}[adduct]^2 - \left(K_{eq}[CouOH]_0 + K_{eq}[MI]_0 + 1\right)[adduct] + K_{eq}[CouOH]_0[MI]_0 = 0 \quad (2.3)$$

It is useful to express Equation 2.3 in terms of absorbance, as it is the observable measured in FTIR. Using the Beer-Lambert law, the following equations were obtained:

$$A_0 = \varepsilon_{CouOH}[CouOH]_0 l \quad (2.4)$$

$$\begin{aligned} A &= \varepsilon_{CouOH}[CouOH]l + \varepsilon_{adduct}[adduct]l = \\ &= \varepsilon_{CouOH}([CouOH]_0 - [adduct])l + \varepsilon_{adduct}[adduct]l = \\ &= A_0 + [adduct](\varepsilon_{CouOH} - \varepsilon_{adduct})l \end{aligned} \quad (2.5)$$

Where Equation 2.4 was used to derive Equation 2.5. Upon re-arrangement, Equation 2.5 yields:

$$\Delta A = \Delta\varepsilon[adduct]l \quad (2.6)$$

Equation 2.6 provides a solution to the unknown equilibrium concentration of the adduct. Substitution of Equation 2.6 into Equation 2.3 and re-arrangement returns the following:

$$\Delta A = \frac{1}{2} l \Delta\varepsilon \left([CouOH]_0 + [MI]_0 + \frac{1}{K_{eq}} - \sqrt{\left([CouOH]_0 + [MI]_0 + \frac{1}{K_{eq}} \right)^2 - 4[CouOH]_0[MI]_0} \right) \quad (2.7)$$

Where the negative solution was chosen, as the equilibrium concentration of the adduct species cannot be greater than the sum of the initial CouOH and MI concentrations. Therefore, the association constant can be determined by monitoring the variation in ΔA as a function of the initial concentrations of MI and CouOH in solution. The features in the FTIR spectra uniquely associated with CouOH···MI species were chosen, specifically at 1331 cm^{-1} and 1518 cm^{-1} for a variety of $[MI]_0$ at fixed $[CouOH]_0$– see Figure 2.5. K_{eq} was retrieved to be 300 ± 120 M^{-1} via fitting the experimental data to Equation 2.7 and averaging over the two values returned for the different vibrational bands.

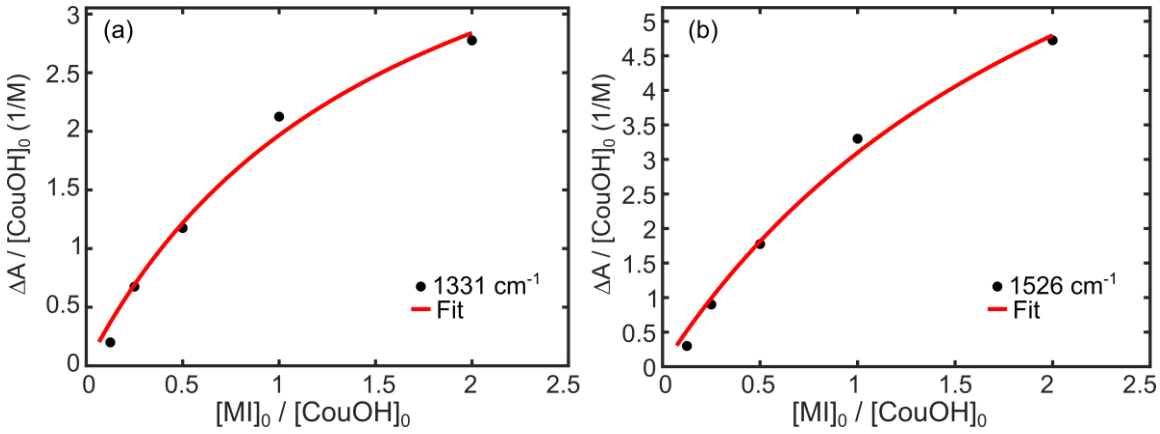

Figure 2.5. Data (black circles) and fitted curves (red line) to a re-arranged form of Equation (2.7) at two different wavenumbers indicated in the panels.

The value associated with the equilibrium constant has implications for the study: at the MI concentrations investigated (0.5–8 mM), there is a non-negligible percentage of free CouOH molecules in solution. For example, in equimolar solutions of 4 mM CouOH and MI, only ~41% of CouOH molecules are associated in the CouOH···MI form. Thus, in the ultrafast spectroscopic studies, the dynamics of CouOH and CouOH···MI are expected to contribute to the observed signals.

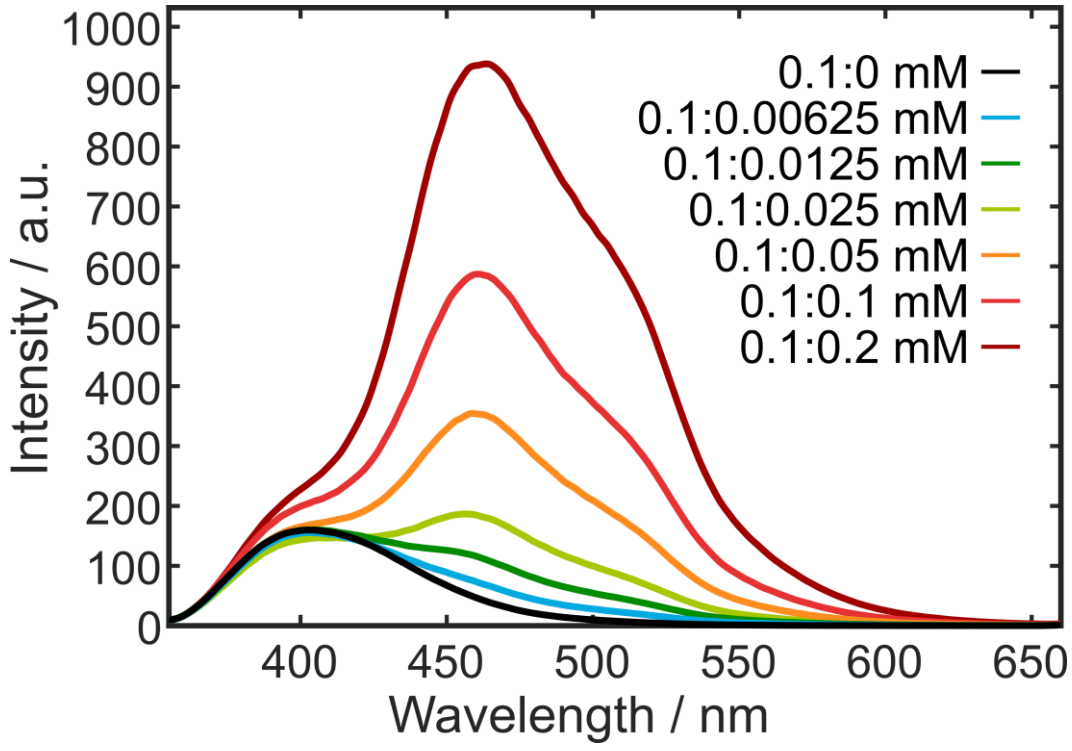

Figure 2.6. Fluorescence spectra for the specified CouOH:MI concentrations in $CDCl_3$ using 340 nm excitation.

The fluorescence spectra of CouOH and mixtures of CouOH and MI in $CDCl_3$ solution are displayed in Figure 2.6. These data were acquired with 340 nm excitation, which coincides with the maximum absorption of CouOH in CDCl, with the 0.1 mM coumarin solution dominated by a single broad feature that peaks at ~405 nm. Upon addition of MI, two additional features centered at 460 nm and 510 nm are present, and the intensity of these features is linearly proportional to the MI concentration, reminiscent of prior studies.[52] These features are assigned to fluorescent photogenerated products based on time resolved studies (*vide infra*).

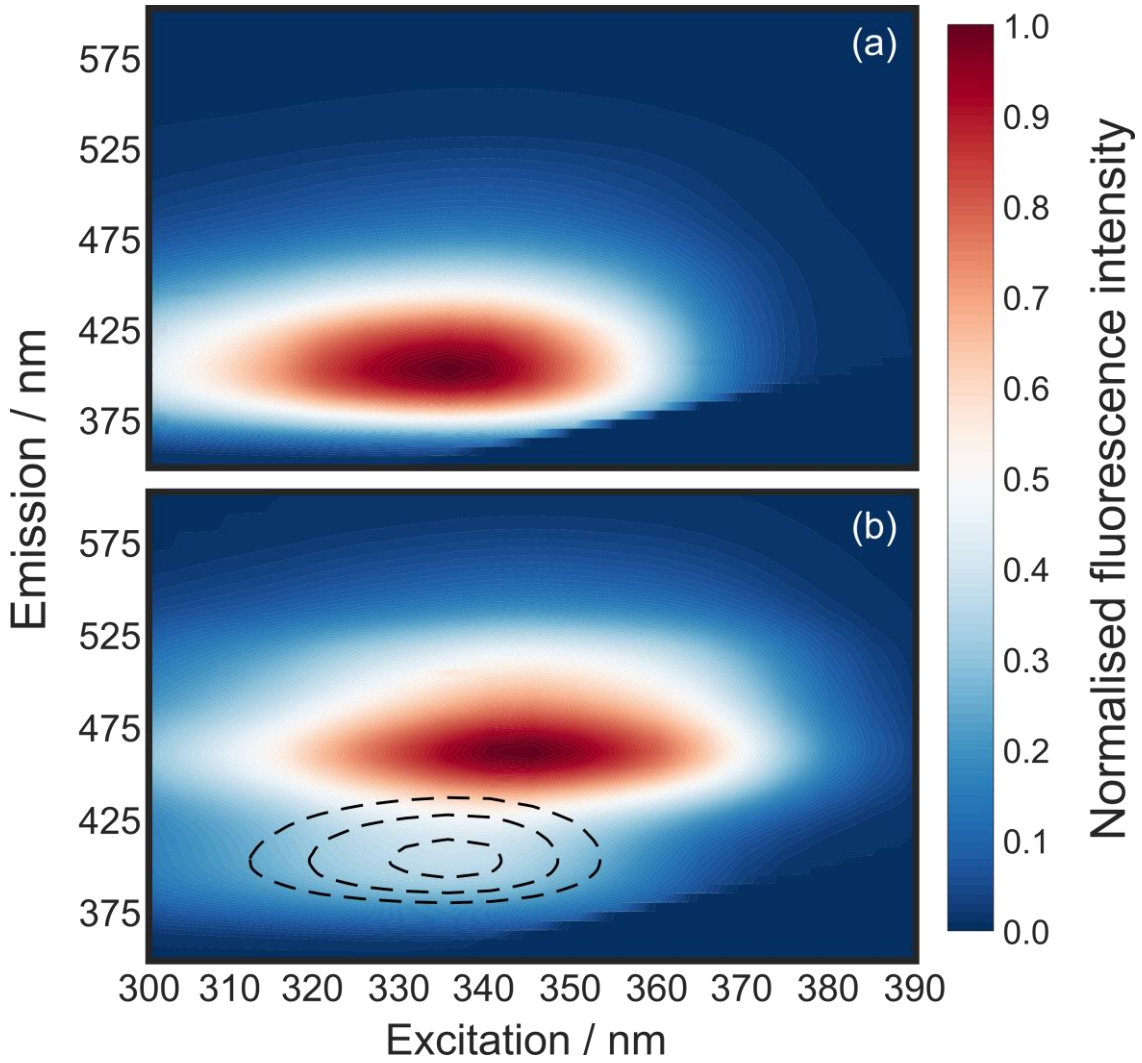

Figure 2.7. Normalized fluorescence excitation–emission correlation maps for (a) 0.1 mM CouOH in $CDCl_3$ solution and (b) 0.1 mM CouOH and 0.1 mM MI in $CDCl_3$ solution. Overlaid dashed line in panel (b) reproduces the location absorption/fluorescence for CouOH solutions.

2D fluorescence spectra reveal that these new features are strongly correlated with the red-shifted absorbance (maximum at ~345 nm– see Figure 2.7) that is only present when MI is added to CouOH. As a consequence of the value of the equilibrium constant determined through FTIR measurements, the absorption cross-section for H-bonded CouOH/MI molecules is greater than of 'free' CouOH in $CDCl_3$ solution: in the linear absorption spectrum for the 1:1 mixture, ~59% of CouOH molecules are 'free', and so 41% of hydrogen bonded CouOH molecules must be responsible for the large increase in absorption peaking at 345 nm. Along with the minor depletion of uncomplexed CouOH (evident at 310 nm), this can only be reconciled if the H-bonded species has a larger absorption cross-section than isolated CouOH.

The concentration of CouOH and MI used for fluorescence studies was far lower than for UV absorption or FTIR measurements. For the fluorescence data it is estimated that the hydrogen bonded CouOH···MI species comprised no more than ~2% of the CouOH reservoir even for solutions containing the highest MI concentrations displayed in Figure 2.6. Despite isolated CouOH molecules being the dominant form of coumarin in chloroform solutions, the photoproduct emission bands are more intense than monomeric CouOH for solutions containing > 0.025 mM MI. This implies the fluorescence quantum yield of the photoproducts must be much higher than CouOH. At this stage, this observation is partly rationalized on the basis of the low fluorescence quantum yield of isolated CouOH, which was determined to be 5 ± 1 % by referencing against a standard dye, Coumarin 153 (C153) in ethanol, with known fluorescence quantum yield of 0.53.[53,54] Finally, the relative intensity of the maxima at 460 nm and 510 nm are independent of concentration, which implies either that both bands arise from the same chemical species (*e.g.* a Franck-Condon vibronic progression), or alternatively if the bands correspond to different chemical photoproducts the relative product branching is independent of MI concentration.

2.3.2. Time Resolved Infrared Spectroscopy

TRIR studies were used to identify vibrational signatures of inter-molecular ESPT products between CouOH and MI in $CDCl_3$ solution, a selection of which are shown in Figure 2.8 (full dataset in the Appendix).

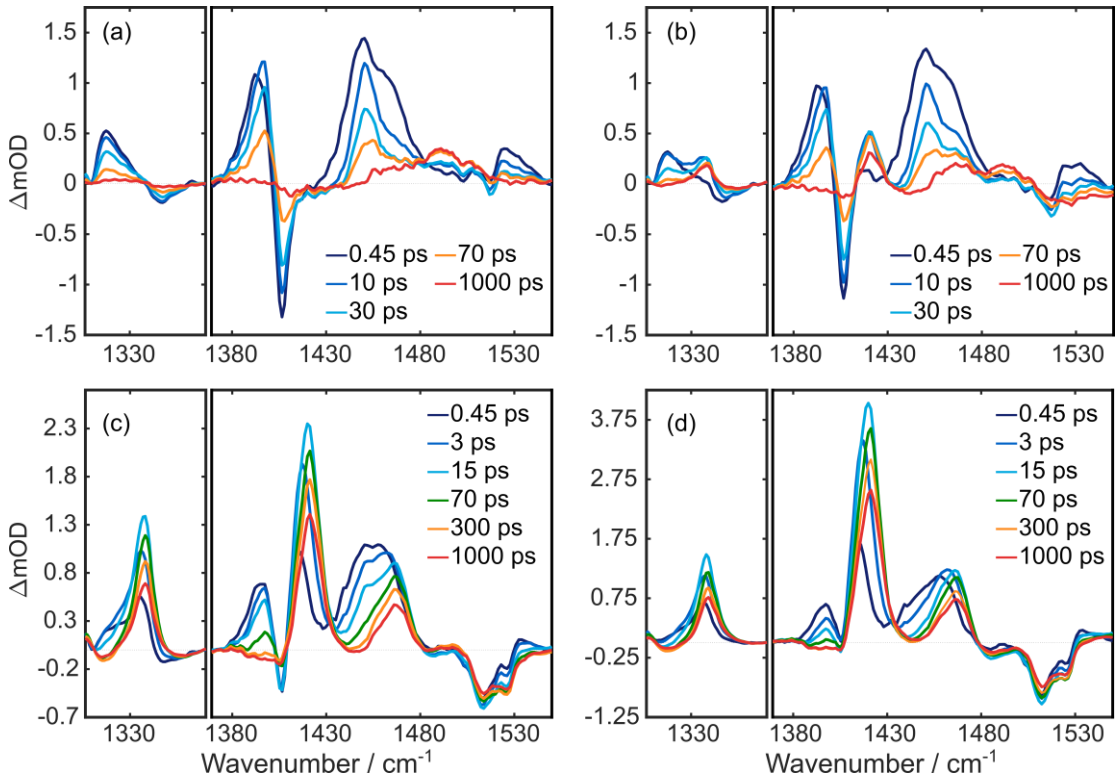

Figure 2.8. Transient infrared spectra for (a) CouOH 4 mM, (b) CouOH 4 mM and 1 mM MI, (c) CouOH 4 mM and 4 mM MI, and (d) CouOH 4 mM and 8 mM MI.

The data for 4 mM CouOH in $CDCl_3$ solution are displayed in Figure 2.8(a). Negative features in the TRIR data coincide with major features in the linear CouOH FTIR spectrum (see Figure 2.4) and correspond to loss of ground state CouOH parent molecules. The time-dependent intensity of these features reflects the percentage of molecules returned to S_0. Positive features arise from S_1 CouOH molecules or any photogenerated species. The majority of vibrational features in the TRIR data were assigned using TD-DFT calculations– see Table 2.2.

Within the first 4 ps, the feature initially centered at 1393 cm^{-1} blueshifts by ~3 cm^{-1} to 1396 cm^{-1} accompanied by a slight increase in intensity. The 1396 cm^{-1} vibrational feature is associated with a ring breathing CouOH mode. DFT and TD-DFT calculated minimum energy geometries for S_0 and S_1, respectively, reveal that the structures vary by a slight expansion of the coumarin ring, and thus the ring breathing mode is intrinsically coupled to the $\pi^* \leftarrow \pi$ electronic transition.

Table 2.2. Experimentally observed and assigned calculated (TD-DFT/ωB97XD/6-31+G**/PCM) S_1 CouOH vibrational frequencies and associated nuclear motions. All calculated frequencies were scaled by 0.96 to account for any vibrational anharmonicity.

Observed / cm^{-1}	Calculated / cm^{-1}	Assignment
	CouOH (S_1)	
1316	1321	Anti-symmetric C–C phenol ring breathing/O–H bend
1396	1387	Symmetric C–C phenol ring breathing/anti-symmetric C–C stretch on pyrone
1449–1466	1420	In-phase C–C aromatic ring breathing mode on both pyrone and phenol ring
	1455	Anti-symmetric C–C phenol ring breathing
1525	1495	In-phase C–C aromatic ring breathing mode on both pyrone and phenol ring /O–H bend)
	CouOH (T_1)	
1449–1466	1429	Out-of-phase C–C ring breathing on both pyrone and phenol moieties
	1469	In-phase C–C ring breathing on both pyrone and phenol moieties
	1482	Out-of-phase C–C ring breathing on both pyrone and phenol moieties/C–O stretch on phenol ring

Initial Franck-Condon excitation of CouOH molecules into the S_1 state places molecules out-of-equilibrium with respect to the nuclear degrees of freedom associated with this vibration. Equilibration on the S_1 state leads to a change in the force constant associated with this vibrational mode, explaining the observed vibrational Stokes' shift. The kinetics of the positive transient at ~1445 cm^{-1} are the most spectrally isolated and thus used to determine the CouOH S_1 lifetime = 51.7 ± 4.2 ps (see Figure 2.9).

At the longest pump-probe time delay accessed in this study, the majority of both positive and negative features have almost fully decayed to zero signal intensity, however, the ground state bleach recovery is incomplete at t = 1 ns. A broad peak centered at 1490 cm^{-1} rises at t > ~70 ps. DFT calculations were able to assign this vibrational feature to T_1 CouOH molecules which is assumed to be relatively long-lived. At t =1 ns, the bleach recovery is > 90% complete, and thus implying that intersystem crossing in CouOH is a relatively minor non-radiative decay pathway. Ring-opening via C–O bond cleavage on the pyran ring was excluded based on previous experiments of bare coumarin in acetonitrile,[55] and from ^{1}H-NMR experiments. 4 mM CouOH solutions were irradiated for up to five hours

and then NMR data were acquired. These spectra did not contain any additional peaks associated with the build-up of ring-opened products (see Appendix).

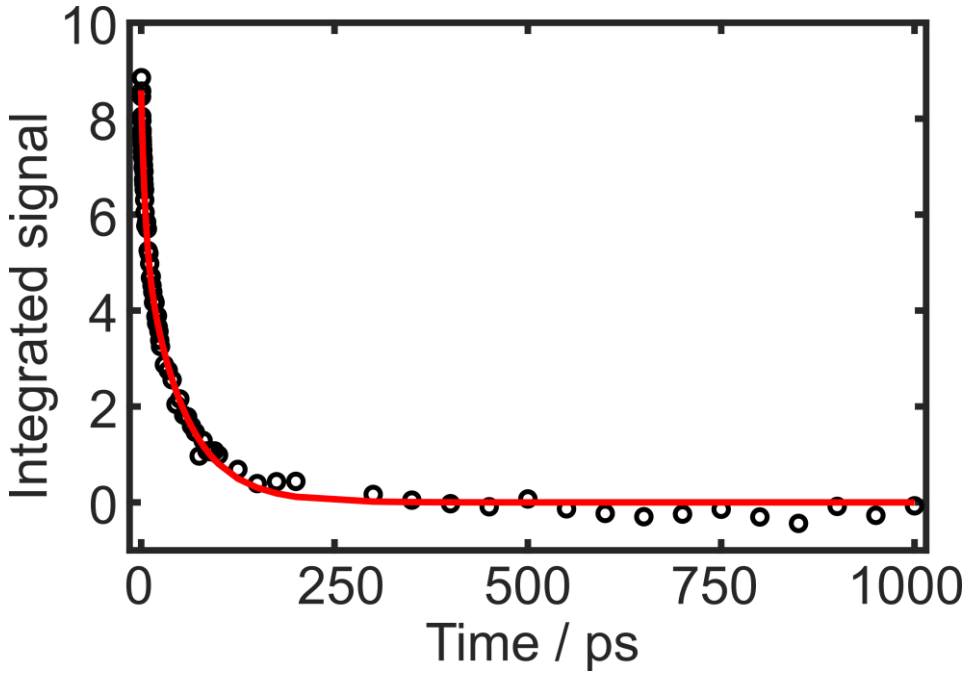

Figure 2.9. Integrated signal (open circles) of the vibrational band centred at 1445 cm^{-1} in 4 mM CouOH in $CDCl_3$ TRIR data (Figure 2.8(a)). These data were fit to a biexponential decay to obtain the S_1 lifetime. These fits returned a dominant decay constant corresponding to 51.7 ± 4.2 ps, ascribed to the S_1 lifetime, and a second low amplitude (τ > 1 ns) component which is ascribed to some triplet population. The results of the fit are in good agreement analysis of the TA data (data not shown).

Upon addition of 1 mM of MI to 4 mM CouOH solutions (Figure 2.8(b)) TRIR data contain three additional positive features centered at 1338, 1420 and 1466 cm^{-1}. The intensity of these bands increases further as the MI concentration is elevated to 8 mM (Figure 2.8(c,d)). These new transient features are far longer lived (> 1 ns) than S_1 CouOH molecules in the absence of MI base (see Figure 2.8(a)).

Aside from these three new features in CouOH/MI mixtures, there is also a bleach feature present at 1515 cm^{-1} which corresponds to a MI vibration. Although MI does not absorb at 330 nm (the pump wavelength used in this study), the bleaching of this feature is instantaneous, meaning some portion of MI S_0 molecules are depopulated within the instrument response (TRIR ~300 fs, TA ~200 fs). The proposed hypothesis is that MI acts as a H^+ or H acceptor from photoexcited CouOH molecules, via ESPT (as previously reported[26]) or excited state H atom transfer, respectively.

Table 2.3. TRIR experimental frequencies of the $CouO^{-}$*···HMI^{+} photoproducts, calculated (TD-DFT/ωB97XD/6-31+G**/PCM) excited state vibrational frequencies and associated nuclear motions. Calculated frequencies were scaled by 0.96 to account for any anharmonicity.

Observed / cm^{-1}	Calculated / cm^{-1}	Assignment
1338	1335	Out-of-phase C–C ring breathing on both pyrone and phenol moieties
1421	1370	In-phase C–C ring breathing on both pyrone and phenol moieties coupled to MI ring breathing
1466	1491	Symmetric C–C phenol ring breathing/in-phase C–O stretch coupled to N–H stretch

To discriminate between these two possible photochemical reactions, a range of ground and excited state species corresponding to possible photogenerated products from intermolecular excited state proton transfer or H atom transfer were calculated via DFT (geometries of all the calculated structures are given in the Appendix). The best agreement to the vibrational signatures in the experimental data was to the $CouO^{-}$*···HMI^{+} ESPT products (see Table 2.3). Notably, it was found that the vibrational bands mainly localized to the excited state anion were found to have higher oscillator strengths than those associated with the protonated methyl-imidazole partner. Further, the match was found to be far poorer between experiment and theory for just $CouO^{-}$*, and thus the H–bond remains intact post-ESPT.

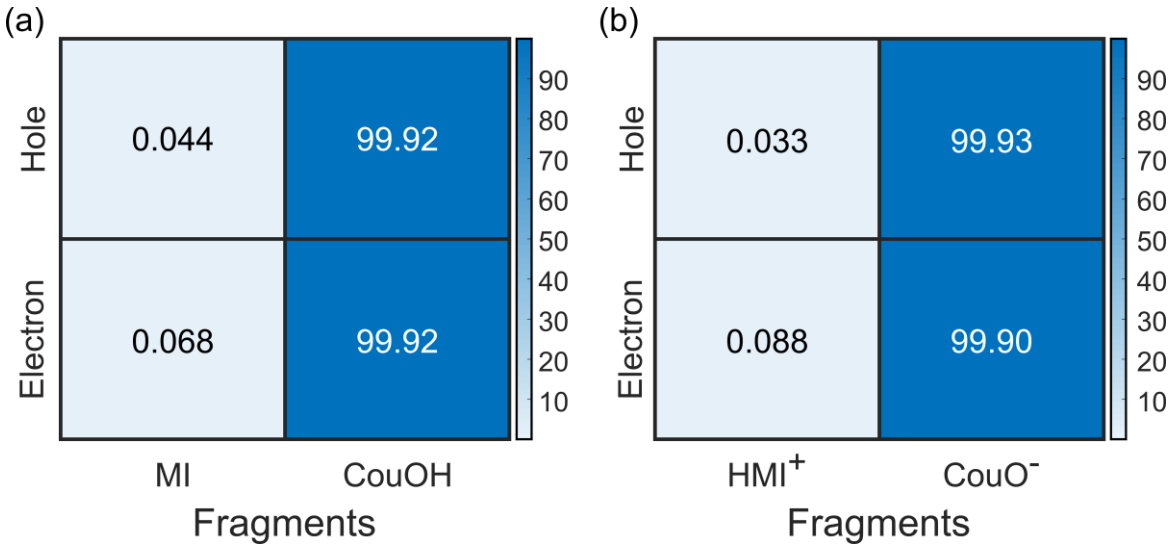

Figure 2.10. Normalized electron-hole correlation matrices (a) for the CouOH···MI S_1 minimum energy geometry, where the excitation is completely localized to the CouOH fragment, and (b) for the $CouO^{-}$···HMI^{+} S_1 minimum energy geometry, where excitation is almost completely localized to the $CouO^{-}$ fragment.

The electronic structure returned by TD-DFT calculations also support this picture; an exciton (electron-hole) analysis of the vertical excited state of CouOH*···MI and $CouO^{-}$*···HMI^{+} products showed that electron and hole remain localized on the coumarin derivative after proton transfer, a finding which is only consistent with heterolytic bond fission (*e.g.* proton transfer) instead of formation of a radical pair via H atom transfer, which presumably would occur on a $^{1}\pi\sigma^{*}$ state (see Figure 2.10(a,b)).[56,57]

Further increasing the MI concentration, data shown in Figure 2.8(c) and (d), greatly enhances the intensity associated with the inter-molecular ESPT photoproduct features over the CouOH S_1 bands. All of the ESPT vibrational bands exhibit a time-dependent vibrational Stokes' shift of ~4–6 cm^{-1} within the first 20 ps towards higher frequencies. For the 1421 cm^{-1} feature, the peak maximum shifts to higher frequencies with a time constant of 9 ps (see analysis for 4 mM CouOH and 8 mM MI solutions in Figure 2.11).

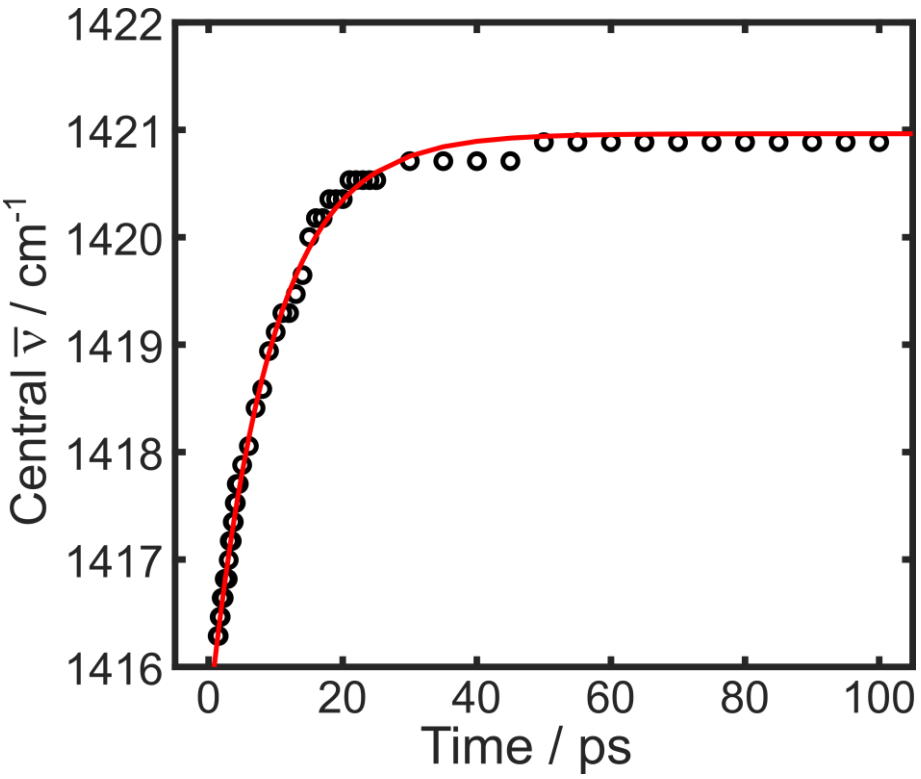

Figure 2.11. Time-dependent peak probe frequency associated with the ~1421 cm^{-1} vibrational feature for the 4 mM CouOH and 8 mM MI mixture in $CDCl_3$ solution. The data were interpolated prior to extracting the peak frequency at each pump-probe time delay. The data were then fitted to a mono-exponential function (plus offset), returning a time constant of 9.2 ± 0.3 ps.

This is far more dramatic than observed for S_1 CouOH ring breathing modes and reconciled on the basis that the degree of molecular re-arrangement associated with $S_1 \leftarrow S_0$ excitation of neutral CouOH is small compared to the loss of a proton, anion formation and subsequent re-organization.

To elucidate the dynamics of excited state proton transfer, the kinetics of the spectrally isolated 1421 cm^{-1} $CouO^{-}$* transient became the focus of the quantitative analysis. The whole peak area (1416–1425 cm^{-1}) was integrated to account for the observed shift in the peak wavenumber and growth in peak intensity and fit these data to a sum of exponentials. Analysis for two different CouOH/MI mixtures are displayed in Figure 2.12.

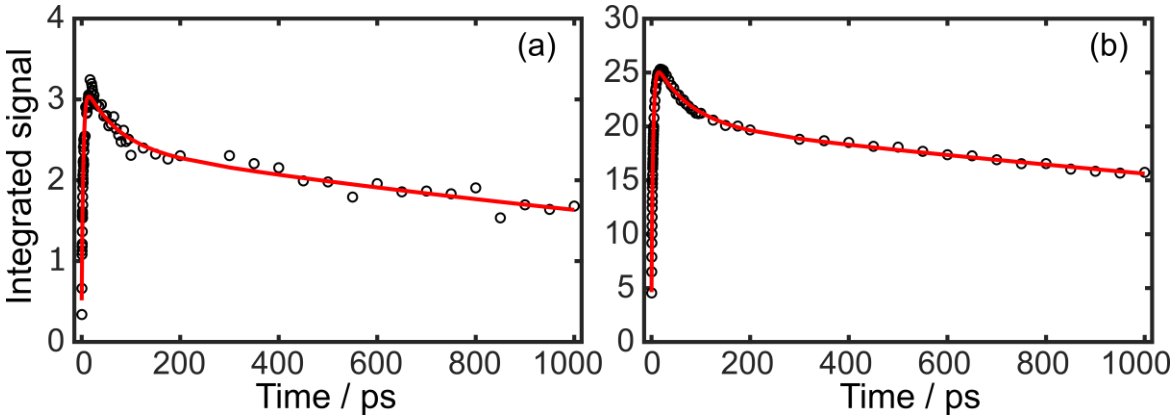

Figure 2.12. Integrated signal for the vibrational band centered at 1420 cm^{-1} (black circles) and tri-exponential fits to data (red line) for (a) 4 mM CouOH and 1 mM MI and (b) 4 mM CouOH and 8 mM MI solutions.

For all datasets, the dynamics were fitted with a tri-exponential function (one rise and two decay components, $A_1 < 0$ and $A_{2,3} > 0$, respectively). Time constants returned from these analyses are tabulated for each CouOH/MI mixture in Table 2.4.

Table 2.4. Time constants and normalized amplitudes returned from fitting the 1420 cm^{-1} photoproduct band.

CouOH:MI / mM	τ_1 / ps	τ_2 / ps	τ_3 / ns	$A_1 < 0$	$A_2 > 0$	$A_3 > 0$
4:1	3.4 ± 0.4	66 ± 38	> 1	0.46	0.14	0.40
4:2	3.3 ± 0.2	72 ± 26	> 1	0.44	0.13	0.43
4:4	3.3 ± 0.2	70 ± 16	> 1	0.44	0.14	0.42
4:8	3.3 ± 0.2	71 ± 19	> 1	0.45	0.13	0.42

The kinetics returned from fitting are independent of MI concentration within the reported errors. The S_1 lifetime of CouOH was determined to be 51.7 ± 4.2 ps, which should greatly reduce the probability of bimolecular diffusion controlled ESPT reactions between CouOH* and MI. To demonstrate the reaction diffusion is disfavored, the diffusion-controlled limiting rate was calculated. For the diffusive ESPT reaction between photoexcited CouOH* and MI base:

$$CouOH^* + MI \rightleftharpoons CouOH^* \cdots MI \rightleftharpoons CouO^{*-} \cdots HMI^+ \quad (2.8)$$

the initial encounter step between CouOH* and MI to form a reactive complex is often rate limiting, and thus the reaction is diffusion controlled. In the approximation that every collision is reactive, the Smoluchowski equation can be used to estimate the reaction rate:

$$k_D = 4\pi D N_A a \quad (2.9)$$

where N_A is Avagadro's constant, a is the contact radius at which the CouOH*···MI species is formed prior to ESPT and D is the sum of the diffusion coefficients for the reactants D_{CouOH^*} and D_{MI}. The diffusion coefficients for CouOH and MI in $CDCl_3$ were determined using DOSY ^{1}H NMR to be 1.6 × 10^{-5} cm^2 s^{-1} and 3.3 × 10^{-5} cm^2 s^{-1}, respectively; the diffusion constant for CouOH and CouOH* were assumed to be the same. Assuming a large reaction radius (a = 10 Å), the diffusion rate constant is estimated to be 3.7 × 10^{10} M^{-1} s^{-1}, which is the same order of magnitude as predicted by more refined models for photoacid–base encounters.[58] The use of the Smoluchowski equation and the associated approximations is relevant to calculate an upper limit for the diffusional rate constant between CouOH* and MI in $CDCl_3$. The contact radius of 10 Å is high, however, used to compensate for the lack of an attractive potential in the Smoluchowski equation.

The highest concentrations of photoacid and base used in this study were 4 mM CouOH and 8 mM MI. Using the equilibrium constant derived by fitting Equation 2.7, the concentrations of 'free' CouOH and MI in these solutions are 1.5 and 5.5 mM respectively. Assuming that 100% of 'free' CouOH molecules are photoexcited by a laser pulse (realistically this should be < 10% for the experimental conditions used) the concentration of reactive molecules is 3.5 mM, which yields a reaction upper limit for the reaction time

constant = 7.7 ns. This value greatly exceeds the excited state lifetime of the photoacid, precluding any diffusive ESPT. Resultantly all the observed ESPT products originate from pre-hydrogen-bonded photoacid-base molecules. Therefore, increasing the MI concentration must only affect the amount of hydrogen-bonded S_0 CouOH···MI molecules in solution prior to photoexcitation, and hence the ESPT product yield, but not the mechanism. For completeness, previous TRIR and time-resolved fluorescence studies have observed such diffusion controlled 'loose' ESPT dynamics for photoacids with longer excited state lifetimes and at orders of magnitude higher acid/base concentrations.[31,33,34,58]

Each time constant should be descriptive of a specific molecular process that occurs on the excited state. The first time constant (~3 ps) is assigned to formation of $CouO^{-}$* photoproducts far from equilibrium, which as nuclei re-arrange to the new minimum energy structure, as evident from the vibrational Stokes shift, leads to an increase in oscillator strength. Inevitably such processes greatly depend on the solvent re-organization timescale of chloroform, which is dominated by τ ~4 ps.[59]

The inter-molecular ESPT products decay biexponentially with ~70 ps and > 1 ns time constants. Based on the TRIR data alone, it is not possible to assign mechanisms to the product decay pathways and requires insights from transient absorption spectroscopy.

2.3.3. Transient Absorption Spectroscopy

Transient absorption spectroscopy measurements were conducted to probe the ESPT products fate. A selection of these data for specific pump-probe time delays are shown in Figure 2.13, alongside the kinetics associated with specific probe wavelengths (full dataset in the Appendix).

The transient absorption data for 4 mM CouOH in $CDCl_3$ solution is displayed in Figure 2.13(a) for several representative pump-probe time delays. At early time delays (t < 30 ps) transient absorption signals are dominated by three main features: a negative signal centered at ~460 nm corresponding to a stimulated emission (SE) from S_1 CouOH molecules, and two positive signals peaking at 370 nm and 625 nm corresponding to $S_n \leftarrow S_1$ excited state absorptions (ESAs). Direct comparison with the linear fluorescence spectrum (420 nm) reveals that the central frequency of the SE feature (460 nm) observed in TA experiments (Figure 2.13(a)) does not match the fluorescence m axima – see Figure 2.4.

This difference is reconciled by requiring the oppositely signed ESA signal intensity is greater than the SE in the $\lambda < 420$ nm spectral region, and the negative feature present in the TA spectrum originates from the very red edge of the SE.

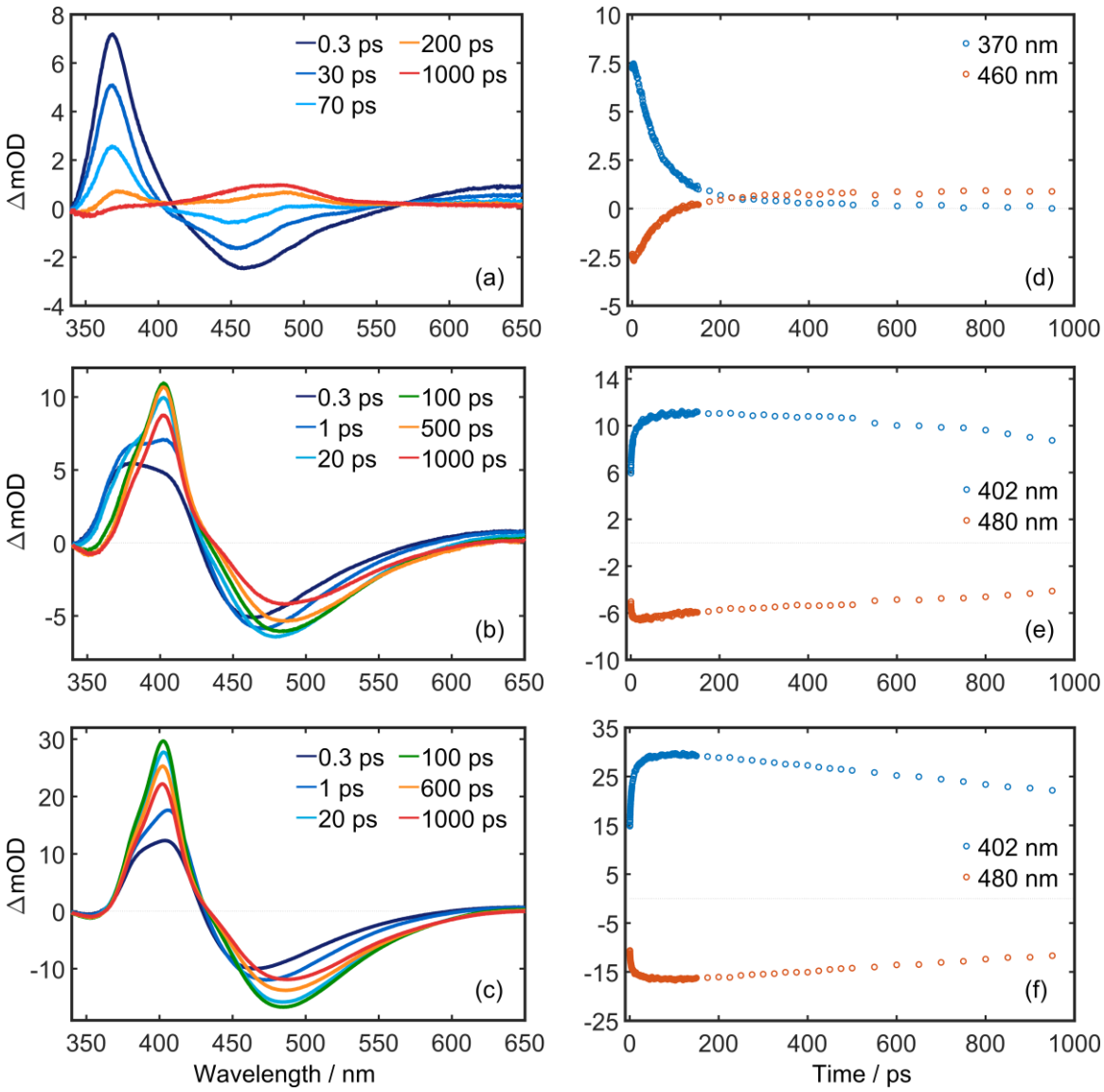

Figure 2.13. Transient absorption spectra at displayed pump-probe time delays for (a) 4 mM CouOH (b) 4 mM CouOH and 1 mM MI, (c) 4 mM CouOH and 8 mM MI solutions. (d-f) Associated kinetics for displayed probe wavelengths and respective mixtures.

At longer pump-probe time delays, (t > 150 ps) an additional positive feature centered at ~480 nm rises. On the basis of conclusions drawn from TRIR data, this was assigned to a CouOH $T_n \leftarrow T_1$ ESA transient. The kinetics associated with the main S_1

CouOH ESA (λ_{probe} = 370 nm) and overlapping CouOH S_1 SE/T_1 ESA (λ_{probe} = 460 nm) are displayed in Figure 2.13(d).

Addition of 1 mM MI to 4 mM CouOH solutions dramatically changes the TA spectral profiles and associated kinetics (see Figure 2.13(b,e)); an additional ESA feature centered at ~400 nm maximizes within the first ~100–150 ps, and the stimulated emission signal grows with intensity up to ~20 ps whilst simultaneously red-shifting by ~20 nm. The maximum of the red-shifted fluorescence (at t > 20 ps) matches the peak at 480 nm present in steady-state fluorescence data for CouOH···MI mixtures. The appearance of these new features and evolution within the first ~20 ps is rationalized in terms of excited state proton transfer reaction (*vide supra*).

When the concentration of MI is further increased (to a 1:2 CouOH:MI ratio) the TA spectra shown in Figure 2.13(c) are completely dominated by the ESA and SE signals associated to inter-molecular ESPT products. Notably, the signal intensity compared to that of isolated CouOH (Figure 2.13(a)) is ~3 times as intense. A comparison of the kinetics for 402 nm and 480 nm probe wavelengths of the 4:1 and 1:2 CouOH:MI mixtures (Figure 2.13(e,f), respectively) show the associated dynamics are concentration dependent, but at these low absolute concentrations the majority of CouOH molecules are not hydrogen bound to a MI in the ground state prior to excitation, and thus the TA spectra represent a mixture of the dynamics of 'free' CouOH molecules, and the hydrogen bound CouOH···MI ESPT reaction.

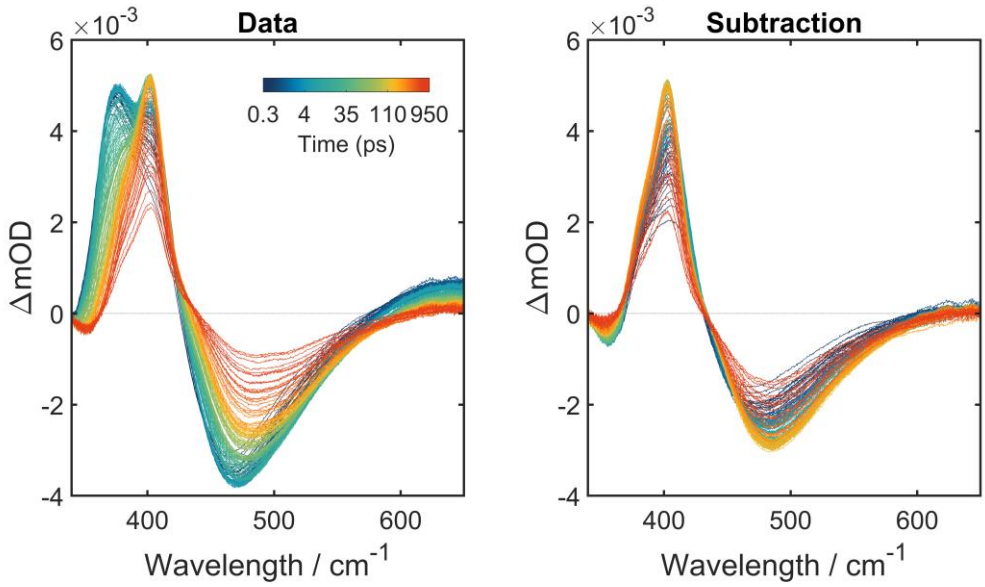

Figure 2.14. Comparison of raw TA dataset for 4 mM CouOH and 0.5 mM MI in $CDCl_3$ (left hand side) and data after subtraction of 4mM CouOH signals (right hand side).

To isolate the dynamics associated with intermolecular excited state proton transfer, the CouOH dataset (weighted) was subtracted from mixture datasets. An example of this subtraction is given in Figure 2.14. The kinetics (after subtraction) associated with integrating over the stimulated emission feature (between 460–500 nm) are shown in Figure 2.15(a,b) for two CouOH/MI mixtures, corresponding to 1 mM and 8 mM MI added to 4 mM CouOH, respectively. These data were fit to a tri-exponential function, with two components accounting for an increased negative signal ($A_{1,2} > 0$), and one for the loss of stimulated emission ($A_3 < 0$). The time constants and amplitudes returned from these analyses for 6 different CouOH/MI mixtures are tabulated in Table 2.5.

Table 2.5. Time constants and associated normalized amplitudes returned from tri-exponential fitting of SE band centered at 470 nm in TA data.

CouOH:MI / mM	τ_1 / ps	τ_2 / ps	τ_3 / ns	$A_1 > 0$	$A_2 > 0$	$A_3 < 0$
4:0.25	1.1 ± 0.3	35 ± 4.4	> 1	0.15	0.19	0.66
4:0.5	1.1 ± 0.2	34 ± 6.5	> 1	0.22	0.14	0.64
4:1	0.8 ± 0.1	30 ± 2.9	> 1	0.20	0.17	0.63
4:2	0.8 ± 0.2	27 ± 3.6	> 1	0.21	0.20	0.59
4:4	1.3 ± 0.2	41 ± 4.4	> 1	0.19	0.16	0.65
4:8	0.9 ± 0.1	28 ± 2.3	> 1	0.21	0.16	0.63

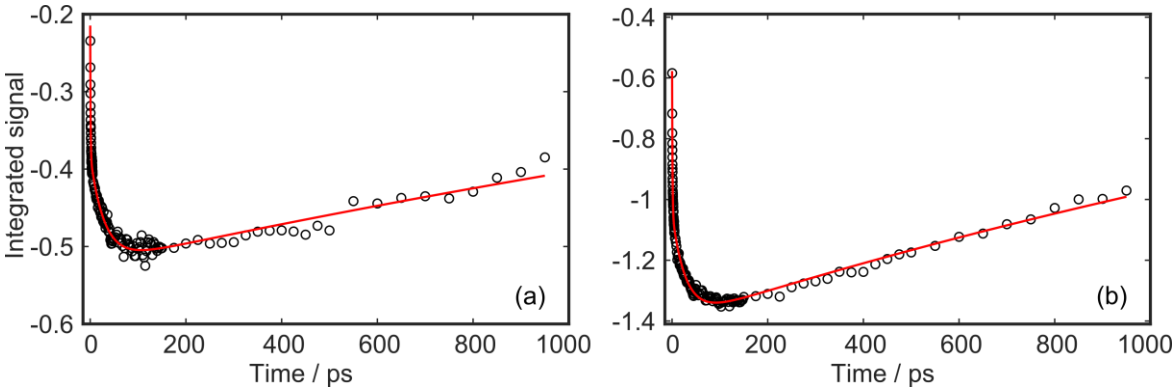

Figure 2.15. Integrated signal intensity for the stimulated emission centered at 470 nm (black circles) and triexponential fits to data (red line) for (a) 4 mM CouOH and 1 mM MI and (b) 4 mM CouOH and 8 mM MI solutions.

Similar to the TRIR studies, the time constants returned by fitting are independent of MI concentration, and therefore physical phenomena underlying the dynamics must be related to the formation, rearrangement and subsequent relaxation of the $CouO^{-}{}^{*}\cdots HMI^{+}$ of

ESPT photoproducts, once more indicating that absence of diffusion-controlled ESPT in this study. The first time constant of ~1 ps is associated with a fast increase of stimulated emission from nascent $CouO^{-}$* photoproducts, however, this is a shorter time constant than retrieved from TRIR studies. In the limit of the Born-Oppenheimer approximation, the change in electronic structure associated with transformation of CouOH* to $CouO^{-}$* is seamless compared to the slow response of the nuclei. Therefore, SE from $CouO^{-}$* in TA measurements should be more sensitive to the ultrafast proton transfer reaction than the new transients observed in TRIR measurements and thus this fast time constant is ascribed to the on-contact ESPT process. This observation agrees with the very small barrier to ESPT predicted by prior[43] and my TD-DFT calculations (see Section 2.3.4). The kinetics extracted from the TRIR data not only reflect population of photoproduct formation, but also a change in vibrational oscillator strength upon equilibration of the $CouO^{-}$* products. The time-dependent Stokes' shift[60] observed in the TA data reflects the solvation dynamics associated with anion formation – see shifting minimum of SE band plotted in Figure 2.16.

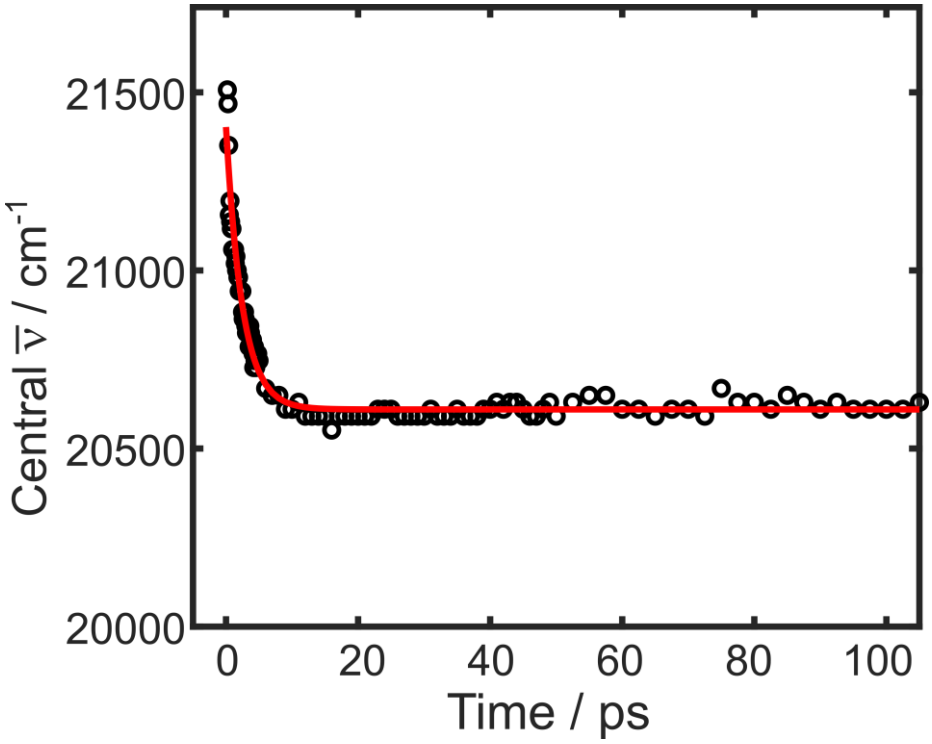

Figure 2.16. Time-dependent peak of the stimulated emission feature (~460 nm) for 4 mM CouOH and 8 mM MI data in $CDCl_3$ solution. The data were fit to a mono-exponential function (plus offset), returning a time constant of 2.5 ± 0.2 ps.

There are some similarities with the work of Pines *et al.*, who investigated the changes in hydrogen bonding network and ring geometry of a photoacid with a hydrogen bonding acceptor in the scenario where ESPT does not take place.[49] They observed a time-dependent red-shift in the SE signal, and attributed this to re-equilibration of the S_1 photoacid ring geometry and the hydrogen bonding bridge as influenced by the solvent re-organization timescale, but these data do not contain signals attributable to ESPT. As the spectral shifts in the CouOH/MI mixture solutions arise from the growth of coumarin anion photoproducts via ESPT, it is not possible to comment on the changes along the H-bonding co-ordinate immediately prior or during ESPT. The second time constant, ~33 ps, is associated with an increase in the SE signal and is also independent of MI concentration. One possible explanation for this observation is provided by TD-DFT calculations which find a π-stacked exciplex of $CouO^{-}{}^{*\cdots}HMI^{+}$ is only 0.128 eV higher in energy than the minimum energy associated with the initial ESPT products. In this structure, the ∠OHN angle becomes ~120° and maintains the $O^{-\cdots}H–N$ hydrogen bond, with the aromatic rings face-on and separated by ~3 Å. Whilst this is thermodynamically 'up-hill' for the specific calculated geometry, solvent fluctuations can easily provide the driving force for this re-arrangement. To form such species will require displacement of solvent molecules sandwiched between the two rings, and thus partially explains the induction time, alongside any barrier that must be traversed.

Such phenomena have been observed for neutral aromatic molecules that are hydrogen bonded in S_0, but π-stack in the S_1 state, *e.g.* benzene and derivatives,[61] as well as phenol.[62] Another characteristic of such process is a very strong $S_n \leftarrow S_1$ ESA signal,[62] as observed at $t > 30$ ps. The branching into this channel may be relatively minor, but the oscillator strength associated with exciplexes' ESA can be extraordinarily large, which for benzene dimer was estimated to be 76,000 M^{-1} cm^{-1}.[63] TD-DFT calculations for the minimum energy structure of the exciplex reveal that in the investigated mid-infrared probe region, the exciplex vibrational frequencies are almost indistinguishable from the precursor initial ESPT products, but have ~3× smaller associated oscillator strengths. Therefore, the ~13% decrease in TRIR signal on the order of tens of picoseconds is ascribed to a transformation of the initial ESPT photoproducts into less IR active products, which manifests as a net loss in infrared signal intensity. The third and final exponential component

is as a result of photoproducts relaxation to the ground state, which occurs on timescales longer than 1 ns.

2.3.4. General Discussion

Using a combination of TRIR and TA spectroscopy and accompanying DFT calculations, the molecular mechanism of bimolecular excited state proton transfer dynamics between 7-hydroxy-4-(trifluoromethyl)-1-coumarin and 1-methylimidazole in chloroform solution has been elucidated, as schematically illustrated in Figure 2.17.

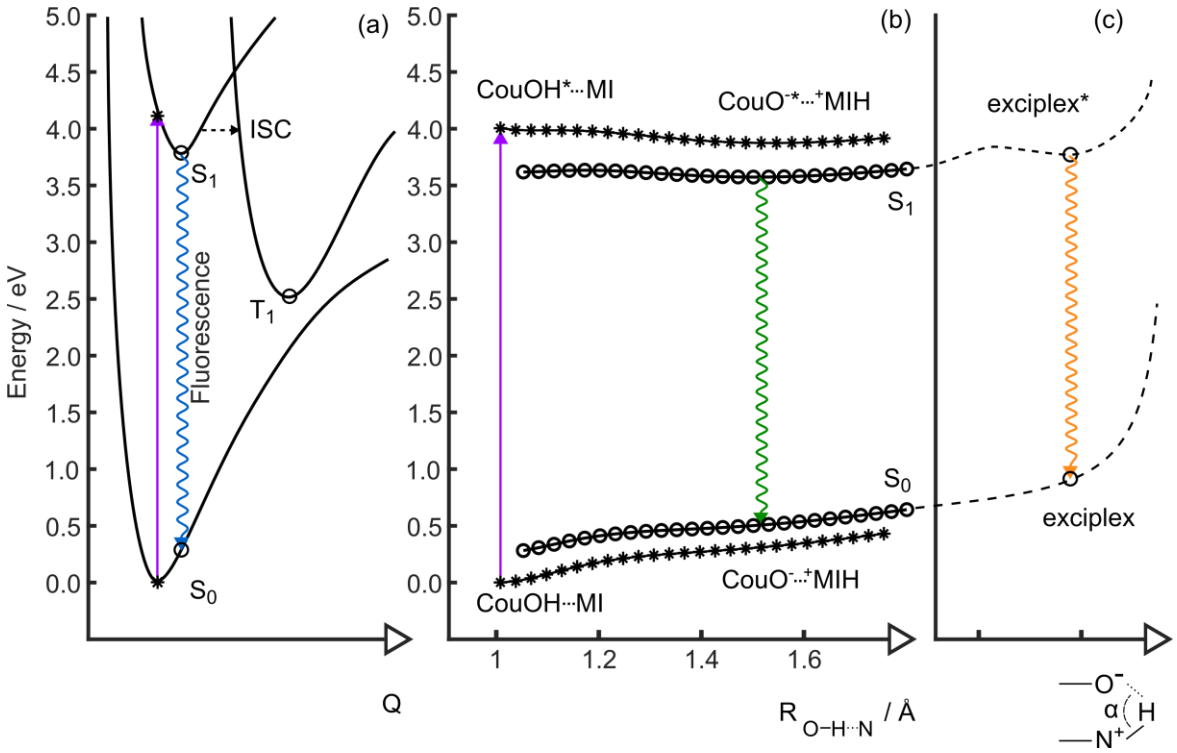

Figure 2.17. (a) Schematic potential energy surface (PECs) for CouOH based on DFT optimized structures of several key geometries (o symbols). (b) PECs associated with the O–H stretch co-ordinate of CouOH···MI. The O–H bond length was held at the displayed values and the rest of the geometry optimized for the S_1 or S_0 states, as denoted by o and ∗ symbols respectively. (c) Schematic PEC based on the exciplex S_1 minimum energy structure, and respective S_0 energy at this geometry as a function of the ∠OHN angle.

From these studies of CouOH solutions, no solute-to-solvent ESPT was discerned, as $CDCl_3$ is a very poor proton acceptor. From TRIR and TA studies, the S_1 excited state lifetime of CouOH was determined to be 51 ps, with only a minor intersystem crossing pathway (<10 %) – see Figure 2.17(a). The association constant for hydrogen bonding between CouOH

and MI in $CDCl_3$ solution was determined to be 300 M^{-1}. TRIR and TA studies of these solutions revealed direct spectroscopic signatures of inter-molecular ESPT between CouOH and MI, yielding $CouO^{-}{}^{*\cdots}HMI^{+}$. TD-DFT one-dimensional scans along the intermolecular hydrogen-bonding co-ordinate $R_{O—H\cdots N}$ are displayed in Figure 2.17(b) and show the minimum energy ESPT barrier is minimal (0.02 eV) at the TD-DFT/ωB97XD/6-31+G**/PCM level of theory.

Despite the 1D nature of the PECs in Figure 2.17(b), the potential will be shallow in the Franck-Condon region, especially in the degrees of freedom surrounding the intermolecular hydrogen bond. Therefore, not all molecules will experience the same barrier to ESPT, which in turn may be slightly higher or lower for some of the ensemble. At longer time delays, a portion of the initial $CouO^{-*\cdots}HMI^{+}$ products re-organize to form exciplexes (Figure 2.17(c)). Such products have very high ESA cross-sections, but whilst the quantum yield for the channel could not be estimated by the presented studies, it is possible to assign a rise time to this process.

Some of these findings are contrary to the prior study by Westlake *et al.*,[26] who examined ESPT between CouOH and MI in toluene solutions. They acquired TA data for two different concentrations of the photoacid and base: 1:5.9 and 1:14700 CouOH:MI ratios, which are considerably higher than those investigated in this study (maximum of 1:2). My investigation of the concentration dependence to TA data was crucial to deciphering whether any diffusional ESPT was important for 'free' CouOH molecules, in addition to the ESPT for hydrogen-bonded complexes, and isolation of the excited state reaction dynamics of uncomplexed CouOH. The reported kinetics in the prior study likely reflect a convolution of monomeric CouOH relaxation and ESPT and may explain the discrepancy between the time constants returned from the fitting (1 ps and 30 ps) and the previously observed rise times of the SE (< 1 ps and ~5–10 ps). Also, my studies utilized a shorter instrument response for TA measurements than the prior ones (200 fs *vs.* 800 fs) that were therefore unlikely to be able to resolve the < 1 ps rise time. Westlake *et al.*[26] attributed the bimodal rise in SE to immediate H^{+} transfer and delayed proton transfers, due to a sub-ensemble of molecules where the $O–H^{\cdots}N$ co-ordinate is not immediately in the correct configuration. Given the calculated minimum energy barrier to ESPT is so low, as per the calculations of Sarverse *et al.*[43], it is possible to rule out delayed proton transfer and assign the secondary rise component to exciplex formation.

Notably, at the concentrations of MI used in my studies, there is no evidence for any excited state tautomerization of Cou^{-*}, that previous experimental studies[26] and theory[43] have invoked to explain a ~300 ps red shift in the fluorescence maxima for 0.34 mM CouOH and 500 mM MI solutions via time correlated single photon counting. The mechanism provided in these studies use a hydrogen bonded network of MI molecules around the Cou^{-*} to shuttle the proton from one end of the coumarin to the other, in a net tautomerization reaction. Such a mechanism is very reminiscent of gas phase cluster studies.[64] It is reasonable to imagine that the TRIR studies would be very sensitive to this reaction, via changes in aromatic $CouO^{*-}$ vibrational frequencies, however, nor TA nor TRIR studies provided evidence for this process. This may be due to the low concentrations that were chosen for these studies, where such a multibody diffusion-controlled reaction is not accessible within a 1 ns probe window, or because the previously attributed mechanism is not operational.

2.4. Conclusions

The study investigated the bimolecular excited state proton transfer between 7-hydroxy-4-(trifluoromethyl)-1-coumarin and 1-methylimidazole in deuterated chloroform using ultrafast time-resolved infrared and transient absorption spectroscopies, accompanied by density functional theory calculations. In contrast to prior experimental studies, this system was investigated at low photoacid-base ratios to elucidate the molecular mechanism for ESPT and investigate whether there was a significant concentration dependence, *e.g.* diffusion-limited bimolecular ESPT, to the overall reaction. Through static infrared spectroscopy, the equilibrium constant for hydrogen bonding between CouOH and MI was found to be 300 M^{-1} in chloroform solution, and only molecules that are already in this configuration are primed for inter-molecular ESPT. Notably, no evidence for diffusion controlled ESPT was found, as the CouOH S_1 lifetime is 52 ps and thus much shorter than the associated bimolecular time constant for the ESPT reaction of 7.7 ns, at the low absolute concentrations of acid and base investigated. This therefore allows for an investigation of the 'contact' ESPT reaction of pre-hydrogen bonded photoacid-base molecules in isolation. With superior time resolution compared to prior studies on this photoacid-base pair,[26] the ESPT time constant was found to be ~1 ps. Time resolved infrared measurements reveal

definitive vibrational signatures of $CouO^{-*\cdots}HMI^{+}$ ESPT photoproducts. Transient absorption measurements provide complementary information on the fates of these initial ESPT products, which is proposed to subsequently re-arrange to π-stack. No evidence for the excited state tautomerization of the coumarin anion mediated via a chain of MI molecules was found. Either this is because the current study focuses on MI concentrations ≤ 8 mM, in a range that is insensitive to any multibody reaction dynamics that occur on >> 1 ns timescales or because no tautomeric species are formed in chloroform solutions. It is envisaged that such a thorough and systematic study of CouOH and MI in CouOH solution will spur on high-level dynamical theoretical calculations to investigate the earliest epoch of a computationally tractable inter-molecular ESPT reaction.

References

(1) M. Eigen. Proton Transfer, Acid-Base Catalysis, and Enzymatic Hydrolysis. Part I: Elementary Processes. *Angew. Chem.* **1964**, *3* (1), 1–19.
(2) N. Agmon. The Grotthuss Mechanism. *Chem. Phys. Lett.* **1995**, *244* (5–6), 456–462.
(3) A. J. Kirby. Efficiency of Proton Transfer Catalysis in Models and Enzymes. *Acc. Chem. Res.* **1997**, *30* (7), 290–296.
(4) P. Mitchell. Coupling of Phosphorilation to Electron and Hydrogen Transfer by a Chemi-Osmotic Type of Mechanism. *Nature* **1961**, *191* (4784), 144–148.
(5) P. D. Boyer. The Atp Synthase—a Splendid Molecular Machine. *Annu. Rev. Biochem.* **1997**, *66*, 717–749.
(6) M. M. Warren, M. Kaucikas, A. Fitzpatrick, P. Champion, J. Timothy Sage, J. J. Van Thor. Ground-State Proton Transfer in the Photoswitching Reactions of the Fluorescent Protein Dronpa. *Nat. Commun.* **2013**, *4*, 1461–1468.
(7) E. T. J. Nibbering, H. Fidder, E. Pines. Ultrafast Chemistry: Using Time-Resolved Vibrational Spectroscopy for Interrogation of Structural Dynamics. *Annu. Rev. Phys. Chem.* **2005**, *56*, 337–367.
(8) T. Förster. Fluoreszenzspektrum Und Wasserstoffionen-Konzentration. *Naturwissenschaften* **1949**, *36* (6), 186–187.
(9) L. M. Tolbert, K. M. Solntsev. Excited-State Proton Transfer: From Constrained Systems to "Super" Photoacids to Superfast Proton Transfer. *Acc. Chem. Res.* **2002**, *35* (1), 19–27.
(10) B. T. Psciuk, M. Prémont-Schwarz, B. Koeppe, S. Keinan, D. Xiao, E. T. J. Nibbering, V. S. Batista. Correlating Photoacidity to Hydrogen-Bond Structure by Using the Local O-H Stretching Probe in Hydrogen-Bonded Complexes of Aromatic Alcohols. *J. Phys. Chem. A* **2015**, *119* (20), 4800–4812.
(11) E. Driscoll, S. Sorenson, J. M. Dawlaty. Ultrafast Intramolecular Electron and Proton Transfer in Bis(Imino)Isoindole Derivatives. *J. Phys. Chem. A* **2015**, *119* (22), 5618–5625.
(12) P. Zhou, K. Han. Unraveling the Detailed Mechanism of Excited-State Proton Transfer. *Acc. Chem. Res.* **2018**, *51* (7), 1681–1690.
(13) P. K. Sengupta, M. Kasha. Excited State Proton-Transfer Spectroscopy of 3-Hydroxyflavone and Quercetin. *Chem. Phys. Lett.* **1979**, *68* (2), 382–385.
(14) P. F. Barbara, P. K. Walsh, L. E. Brus. Picosecond Kinetic and Vibrationally Resolved

Spectroscopic Studies of Intramolecular Excited-State Hydrogen Atom Transfer. *J. Phys. Chem.* **1989**, *93* (1), 29–34.

(15) C. F. Chapman, M. Maroncelli. Excited-State Tautomerization of 7-Azaindole in Water. *J. Phys. Chem.* **1992**, *96* (21), 8430–8441.

(16) C. Chudoba, E. Riedle, M. Pfeiffer, T. Elsaesser. Vibrational Coherence in Ultrafast Excited State Proton Transfer. *Chem. Phys. Lett.* **1996**, *263* (5), 622–628.

(17) Y. S. Wu, H. C. Huang, J. Y. Shen, H. W. Tseng, J. W. Ho, Y. H. Chen, P. T. Chou. Water-Catalyzed Excited-State Proton-Transfer Reactions in 7-Azaindole and Its Analogues. *J. Phys. Chem. B* **2015**, *119* (6), 2302–2309.

(18) S. Y. Park, H. B. Kim, B. K. Yoo, D. J. Jang. Direct Observation of Conformation-Dependent Pathways in the Excited-State Proton Transfer of 7-Hydroxyquinoline in Bulk Alcohols. *J. Phys. Chem. B* **2012**, *116* (48), 14153–14158.

(19) M. Moriyama, M. Kosuge, S. Tobita, H. Shizuka. Excited-State Intramolecular Proton Transfer Followed by Cis-Trans Isomerization of (1-Hydroxy-2-Naphthyl)-s-Triazine Derivatives. *Chem. Phys.* **2000**, *253* (1), 91–103.

(20) S. Takeuchi, T. Tahara. The Answer to Concerted versus Step-Wise Controversy for the Double Proton Transfer Mechanism of 7-Azaindole Dimer in Solution. *Proc. Natl. Acad. Sci.* **2007**, *104* (13), 5285–5290.

(21) L. Pinto da Silva, R. Simkovitch, D. Huppert, J. C. G. Esteves da Silva. Combined Experimental and Theoretical Study of the Photochemistry of 4- and 3-Hydroxycoumarin. *J. Photochem. Photobiol. A Chem.* **2017**, *338*, 23–36.

(22) R. Simkovitch, D. Huppert. Photoprotolytic Processes of Umbelliferone and Proposed Function in Resistance to Fungal Infection. *J. Phys. Chem. B* **2015**, *119* (46), 14683–14696.

(23) R. Simkovitch, L. Pinto da Silva, J. C. G. Esteves da Silva, D. Huppert. Comparison of the Photoprotolytic Processes of Three 7-Hydroxycoumarins. *J. Phys. Chem. B* **2016**, *120* (39), 10297–10310.

(24) W. Heo, N. Uddin, J. W. Park, Y. M. Rhee, C. H. Choi, T. Joo. Coherent Intermolecular Proton Transfer in the Acid-Base Reaction of Excited State Pyranine. *Phys. Chem. Chem. Phys.* **2017**, *19* (28), 18243–18251.

(25) B. C. Westlake, M. K. Brennaman, J. J. Concepcion, J. J. Paul, S. E. Bettis, S. D. Hampton, S. A. Miller, N. V. Lebedeva, M. D. E. Forbes, A. M. Moran, T. J. Meyer, J. M. Papanikolas. Concerted Electron-Proton Transfer in the Optical Excitation of Hydrogen-Bonded Dyes. *Proc. Natl. Acad. Sci.* **2011**, *108* (21), 8554–8558.

(26) B. C. Westlake, J. J. Paul, S. E. Bettis, S. D. Hampton, B. P. Mehl, T. J. Meyer, J. M. Papanikolas. Base-Induced Phototautomerization in 7-Hydroxy-4-(Tri-Fluoromethyl) Coumarin. *J. Phys. Chem. B* **2012**, *116*, 14886–14891.

(27) M. Chattoraj, B. A. King, G. U. Bublitz, S. G. Boxer. Ultra-Fast Excited State Dynamics in Green Fluorescent Protein: Multiple States and Proton Transfer. *Proc. Natl. Acad. Sci.* **1996**, *93* (16), 8362–8367.

(28) D. Stoner-Ma, A. A. Jaye, P. Matousek, M. Towrie, S. R. Meech, P. J. Tonge. Observation of Excited-State Proton Transfer in Green Fluorescent Protein Using Ultrafast Vibrational Spectroscopy. *J. Am. Chem. Soc.* **2005**, *127* (9), 2864–2865.

(29) M. A. Lill, V. Helms. Proton Shuttle in Green Fluorescent Protein Studied by Dynamic Simulations. *Proc. Natl. Acad. Sci.* **2002**, *99* (5), 2778–2781.

(30) E. C. Carroll, S. H. Song, M. Kumauchi, I. H. M. Van Stokkum, A. Jailaubekov, W. D. Hoff, D. S. Larsen. Subpicosecond Excited-State Proton Transfer Preceding Isomerization during the Photorecovery of Photoactive Yellow Protein. *J. Phys. Chem. Lett.* **2010**, *1* (19), 2793–2799.

(31) N. Agmon, D. Huppert, A. Masad, E. Pines. Excited-State Proton Transfer to Methanol-Water Mixtures. *J. Phys. Chem.* **1991**, *95* (25), 10407–10413.

(32) E. Pines, B. Z. Magnes, M. J. Lang, G. R. Fleming. Direct Measurement of Intrinsic Proton Transfer Rates in Diffusion-Controlled Reactions. *Chem. Phys. Lett.* **1997**, *281* (4–6), 413–420.

(33) O. F. Mohammed, D. Pines, E. Pines, E. T. J. Nibbering. Aqueous Bimolecular Proton Transfer in Acid-Base Neutralization. *Chem. Phys.* **2007**, *341*, 240–257.
(34) M. Rini, B. Z. Magnes, E. Pines, E. T. J. Nibbering. Real-Time Observation of Bimodal Proton Transfer in Acid-Base Pairs in Water. *Science* **2003**, *301* (5631), 349–352.
(35) N. Agmon. Elementary Steps in Excited-State Proton Transfer. *J. Phys. Chem. A* **2005**, *109* (1), 13–35.
(36) J. T. Hynes, T.-H. Tran-Thi, G. Granucci. Intermolecular Photochemical Proton Transfer in Solution: New Insights and Perspectives. *J. Photochem. Photobiol. A Chem.* **2002**, *154* (1), 3–11.
(37) S. Hammes-Schiffer. When Electrons and Protons Get Excited. *Proc. Natl. Acad. Sci.* **2011**, *108* (21), 8531–8532.
(38) S. Hammes-Schiffer. Current Theoretical Challenges in Proton-Coupled Electron Transfer: Electron-Proton Nonadiabaticity, Proton Relays, and Ultrafast Dynamics. *J. Phys. Chem. Lett.* **2011**, *2* (12), 1410–1416.
(39) R. Simkovitch, S. Shomer, R. Gepshtein, D. Huppert. How Fast Can a Proton-Transfer Reaction Be beyond the Solvent-Control Limit? *J. Phys. Chem. B* **2015**, *119* (6), 2253–2262.
(40) M. Prémont-Schwarz, T. Barak, D. Pines, E. T. J. Nibbering, E. Pines. Ultrafast Excited-State Proton-Transfer Reaction of 1-Naphthol-3,6- Disulfonate and Several 5-Substituted 1-Naphthol Derivatives. *J. Phys. Chem. B* **2013**, *117* (16), 4594–4603.
(41) F. Peral, E. Gallego. Self-Association of Imidazole and Its Methyl Derivatives in Aqueous Solution. A Study by Ultraviolet Spectroscopy. *J. Mol. Struct.* **1997**, *415* (1–2), 187–196.
(42) M. Savarese, P. A. Netti, C. Adamo, N. Rega, I. Ciofini. Exploring the Metric of Excited State Proton Transfer Reactions. *J. Phys. Chem. B* **2013**, *117* (50), 16165–16173.
(43) M. Savarese, P. A. Netti, N. Rega, C. Adamo, I. Ciofini. Intermolecular Proton Shuttling in Excited State Proton Transfer Reactions: Insights from Theory. *Phys. Chem. Chem. Phys.* **2014**, *16* (18), 8661–8666.
(44) U. Raucci, M. Savarese, C. Adamo, I. Ciofini, N. Rega. Intrinsic and Dynamical Reaction Pathways of an Excited State Proton Transfer. *J. Phys. Chem. B* **2015**, *119* (6), 2650–2657.
(45) K. Röttger, H. J. B. Marroux, A. F. M. Chemin, E. Elsdon, T. A. A. Oliver, S. T. G. Street, A. S. Henderson, M. C. Galan, A. J. Orr-Ewing, G. M. Roberts. Is UV-Induced Electron-Driven Proton Transfer Active in a Chemically Modified A·T DNA Base Pair? *J. Phys. Chem. B* **2017**, *121* (17), 4448–4455.
(46) G. M. Roberts, H. J. B. Marroux, M. P. Grubb, M. N. R. Ashfold, A. J. Orr-Ewing. On the Participation of Photoinduced N-H Bond Fission in Aqueous Adenine at 266 and 220 Nm: A Combined Ultrafast Transient Electronic and Vibrational Absorption Spectroscopy Study. *J. Phys. Chem. A* **2014**, *118* (47), 11211–11225.
(47) Frisch, M. J.; Trucks, G. W.; Schlegel, H. B.; Scuseria, G. E.; Robb, M. A.; Cheeseman, J. R.; Scalmani, G.; Barone, V.; Petersson, G. A.; Nakatsuji, H.; et al. Gaussian 09W, Revision D.01, Gaussian Inc, Wallingford CT. 2016.
(48) T. Lu, F. Chen. Multiwfn: A Multifunctional Wavefunction Analyzer. *J. Comput. Chem.* **2012**, *33* (5), 580–592.
(49) E. Pines, D. Pines, Y. Z. Ma, G. R. Fleming. Femtosecond Pump-Probe Measurements of Solvation by Hydrogen-Bonding Interactions. *ChemPhysChem* **2004**, *5* (9), 1315–1327.
(50) P. Thordarson. Determining Association Constants from Titration Experiments in Supramolecular Chemistry. *Chem. Soc. Rev.* **2011**, *40* (3), 1305–1323.
(51) J. J. Concepcion, M. K. Brennaman, J. R. Deyton, N. V. Lebedeva, M. D. E. Forbes, J. M. Papanikolas, T. J. Meyer. Excited-State Quenching by Proton-Coupled Electron Transfer. *J. Am. Chem. Soc.* **2007**, *129* (22), 6968–6969.
(52) D. Pines, E. Pines, W. Rettig. Dual Fluorescence and Excited-State Structural Relaxations in Donor-Acceptor Stilbenes. *J. Phys. Chem. A* **2003**, *107* (2), 236–242.
(53) A. M. Brouwer. Standards for Photoluminescence Quantum Yield Measurements in Solution (IUPAC Technical Report). *Pure Appl. Chem.* **2011**, *83* (12), 2213–2228.
(54) M. Grabolle, M. Spieles, V. Lesnyak, N. Gaponik, A. Eychmüller, U. Resch-Genger.

Determination of the Fluorescence Quantum Yield of Quantum Dots: Suitable Procedures and Achievable Uncertainties. *Anal. Chem.* **2009**, *81* (15), 6285–6294.

(55) D. Murdock, R. A. Ingle, I. V. Sazanovich, I. P. Clark, Y. Harabuchi, T. Taketsugu, S. Maeda, A. J. Orr-Ewing, M. N. R. Ashfold. Contrasting Ring-Opening Propensities in UV-Excited α-Pyrone and Coumarin. *Phys. Chem. Chem. Phys.* **2016**, *18* (4), 2629–2638.

(56) O. F. Mohammed, J. Dreyer, B. Z. Magnes, E. Pines, E. T. J. Nibbering. Solvent-Dependent Photoacidity State of Pyranine Monitored by Transient Mid-Infrared Spectroscopy. *ChemPhysChem* **2005**, *6* (4), 625–636.

(57) A. L. Sobolewski, W. Domcke. Photoinduced Electron and Proton Transfer in Phenol and Its Clusters with Water and Ammonia. *J. Phys. Chem. A* **2001**, *105* (40), 9275–9283.

(58) M. Rini, D. Pines, B. Z. Magnes, E. Pines, E. T. J. Nibbering. Bimodal Proton Transfer in Acid-Base Reactions in Water. *J. Chem. Phys.* **2004**, *121* (19), 9593–9610.

(59) M. L. Horng, J. A. Gardecki, A. Papazyan, M. Maroncelli. Subpicosecond Measurements of Polar Solvation Dynamics: Coumarin 153 Revisited. *J. Phys. Chem.* **1995**, *99* (48), 17311–17337.

(60) R. M. Stratt, M. Maroncelli. Nonreactive Dynamics in Solution: The Emerging Molecular View of Solvation Dynamics and Vibrational Relaxation. *J. Phys. Chem.* **1996**, *100* (31), 12981–12996.

(61) H. Miyasaka, H. Masuhara, N. Mataga. Picosecond Ultraviolet Multiphoton Laser Photolysis and Transient Absorption Spectroscopy of Liquid Benzenes. *J. Phys. Chem.* **1985**, *89* (9), 1631–1636.

(62) Y. Zhang, T. A. A. Oliver, M. N. R. Ashfold, S. E. Bradforth. Contrasting the Excited State Reaction Pathways of Phenol and Para-Methylthiophenol in the Gas and Liquid Phases. *Faraday Discuss.* **2012**, *157*, 141–163.

(63) R. Cooper, J. K. Thomas. Formation of Excited States in the Nanosecond-Pulse Radiolysis of Solutions of Benzene and Toluene. *J. Chem. Phys.* **1968**, *48* (11), 5097–5102.

(64) C. Tanner, C. Manca, S. Leutwyler. Hydrogen-Bonded Ammonia Wire. *Science* **2013**, *302* (5651), 1736–1740.

2.5. Appendix

2.5.1. Calculations

Table 2.6. Optimized S_0 CouOH structure (TD-DFT/ωB97XD/6-31+G**/chloroform PCM).

Atoms	Coordinate x / Å	Coordinate y / Å	Coordinate z / Å
C	0.6743940	2.4481640	0.0001840
C	-1.1298000	0.8659420	-0.0003620
C	-0.2606620	-0.2367930	0.0001780
C	1.1573020	0.0537560	0.0001070
C	1.6039980	1.3246960	0.0000610
H	-3.1492940	1.6007060	-0.0009310
C	-2.5101010	0.7261190	-0.0004850
C	-0.8405560	-1.5182730	0.0008250
H	2.6558900	1.5759350	-0.0002440
C	-2.2108340	-1.6812800	0.0007410
C	-3.0497980	-0.5544850	0.0000370
H	-0.2112990	-2.3997110	0.0013590
H	-2.6398150	-2.6777860	0.0013190
O	0.9929610	3.6157150	0.0010380
O	-0.6586150	2.1461910	-0.0009300
C	2.1586610	-1.0810790	-0.0001490
F	2.0065250	-1.8666300	-1.0844620
F	3.4257480	-0.6473020	-0.0005680
F	2.0070790	-1.8664780	1.0842470
O	-4.3965800	-0.6585010	-0.0002680
H	-4.6674030	-1.5832950	0.0000150

Table 2.7. Optimized S_0 MI structure (TD-DFT/ωB97XD/6-31+G**/chloroform PCM).

Atoms	Coordinate x / Å	Coordinate y / Å	Coordinate z / Å
C	0.1921050	1.0825110	0.0001030
C	1.5009870	-0.6057240	-0.0000790
C	0.2259320	-1.1096970	0.0000130
N	-0.6061750	-0.0155530	0.0002070
H	-0.2159540	2.0839380	0.0003760
H	2.4326500	-1.1531070	-0.0001270
H	-0.1591190	-2.1180580	0.0005440
N	1.4722000	0.7691030	-0.0001340
C	-2.0581390	-0.0334460	-0.0001710
H	-2.4308260	-0.5424710	0.8909170
H	-2.4234290	0.9939590	0.0007320
H	-2.4308020	-0.5409740	-0.8921490

Table 2.8. Optimized S_0 CouOH···MI structure (TD-DFT/ωB97XD/6-31+G**/chloroform PCM).

Atoms	Coordinate x / Å	Coordinate y / Å	Coordinate z / Å
C	4.5617230	-0.3675240	-0.7988770
C	4.4886020	-0.3543470	1.3505360
C	5.4587420	0.5384760	0.9861830
N	5.4945040	0.5193470	-0.3886080
H	4.3727720	-0.5767200	-1.8418620
H	4.1563830	-0.6219960	2.3424360
H	6.1109890	1.1733240	1.5650840
N	3.9343060	-0.9171060	0.2251670
C	6.3675160	1.3151380	-1.2368290
H	7.4120660	1.0815400	-1.0239620
H	6.1553070	1.0822640	-2.2801660
H	6.1871170	2.3775100	-1.0647840
C	-2.9101620	1.7662410	0.0697060
C	-2.9910350	0.4217290	-0.0180160
C	-1.8046730	-0.4001510	0.0117230
C	-0.5774530	0.2697980	0.1313610
C	-1.6221440	2.4311480	0.1968500
H	-2.6834190	-2.3719160	-0.1615420
H	-3.7790600	2.4094940	0.0492600
C	-1.7625390	-1.8085490	-0.0700120
C	0.6403000	-0.3935600	0.1675760
C	0.6535150	-1.7880930	0.0801910
C	-0.5666590	-2.4886740	-0.0365010
H	1.5585360	0.1736300	0.2618040
O	-0.5152240	1.6321050	0.2188910
O	-1.4595480	3.6297850	0.2813600
C	-4.3520400	-0.2248190	-0.1601600
F	-4.4414250	-0.9256790	-1.3078880
F	-5.3497370	0.6703580	-0.1666010
F	-4.5968900	-1.0829150	0.8496100
O	1.7799440	-2.5012630	0.1027460
H	2.5972680	-1.9140650	0.1571480
H	-0.5406970	-3.5705060	-0.1017790

Table 2.9. Optimized S_1 CouOH structure (TD-DFT/ωB97XD/6-31+G**/chloroform PCM).

Atoms	Coordinate x / Å	Coordinate y / Å	Coordinate z / Å
C	-0.6601980	2.4684190	0.0002210
C	1.1526600	0.8861180	0.0003070
C	0.2308650	-0.2386450	0.0000990
C	-1.1600720	0.0375440	0.0001850
C	-1.5761670	1.3918120	-0.0001230
H	3.1805090	1.5613690	0.0003350
C	2.5184620	0.7039400	0.0001730
C	0.8129600	-1.5450690	-0.0002560
H	-2.6252450	1.6561550	-0.0006030
C	2.1705750	-1.7220520	-0.0003070
C	3.0384590	-0.5921280	-0.0001030
H	0.1660720	-2.4126840	-0.0004340
H	2.5926360	-2.7215590	-0.0005260
O	-0.9076920	3.6677110	-0.0000880
O	0.7223800	2.1609060	0.0007660
C	-2.1613530	-1.0602910	-0.0000340
F	-2.0433710	-1.8810280	1.0799760
F	-3.4224510	-0.6005160	0.0007560
F	-2.0443230	-1.8797820	-1.0811190
O	4.3662740	-0.7233190	-0.0001720
H	4.6324840	-1.6516270	-0.0003210

Table 2.10. Optimized S_1 $CouO^-$ structure (TD-DFT/ωB97XD/6-31+G**/chloroform PCM).

Atoms	Coordinate x / Å	Coordinate y / Å	Coordinate z / Å
C	-0.5719890	2.4701790	-0.0000360
C	1.1986240	0.8374270	0.0004010
C	0.2838480	-0.2511040	0.0000030
C	-1.1284900	0.0520460	0.0001140
C	-1.5074300	1.4039890	-0.0002300
H	3.2232320	1.5047510	0.0006740
C	2.5586220	0.6476830	0.0003420
C	0.8488480	-1.5663830	-0.0005380
H	-2.5512810	1.6919860	-0.0006720
C	2.1990980	-1.7855770	-0.0005930
C	3.1408510	-0.6819950	-0.0002050
H	0.1770950	-2.4174620	-0.0008790
H	2.6021880	-2.7931010	-0.0009870
O	-0.8255510	3.6804260	-0.0002190
O	0.7837110	2.1439570	0.0009110
C	-2.1385050	-1.0184790	0.0001130
F	-2.0483310	-1.8594910	1.0798020
F	-3.4020600	-0.5472130	0.0005230
F	-2.0488970	-1.8590150	-1.0800130
O	4.3845260	-0.8545600	-0.0003380

Table 2.11. Optimized S_1 CouO$^{\bullet}$ (radical) structure (TD-DFT/ωB97XD/6-31+G**/chloroform PCM).

Atoms	Coordinate x / Å	Coordinate y / Å	Coordinate z / Å
C	-0.5729590	2.4533270	-0.0001340
C	1.1875820	0.8253550	0.0000810
C	0.3007530	-0.2528410	-0.0001490
C	-1.1154650	0.0731990	-0.0000530
C	-1.5293010	1.3519280	0.0001080
H	3.2275440	1.5215430	0.0003120
C	2.5711040	0.6609700	0.0001410
C	0.8471040	-1.5447830	-0.0003390
H	-2.5744240	1.6299850	0.0003230
C	2.2122860	-1.7540190	-0.0003130
C	3.0698910	-0.6366820	-0.0000650
H	0.1977060	-2.4118720	-0.0004970
H	2.6290820	-2.7529650	-0.0004650
O	-0.8598530	3.6277800	0.0007210
O	0.7538230	2.1160000	0.0002330
C	-2.1411190	-1.0391080	-0.0000800
F	-2.0041740	-1.8272240	1.0841430
F	-3.3980460	-0.5786680	0.0000930
F	-2.0043810	-1.8269950	-1.0845020
O	4.3810610	-0.8331290	-0.0000120

Table 2.12. Optimized S_1 CouOH···MI structure (TD-DFT/ωB97XD/6-31+G**/chloroform PCM).

Atoms	Coordinate x / Å	Coordinate y / Å	Coordinate z / Å
C	-4.6103780	-0.3690690	0.7878720
C	-4.4236470	-0.3545830	-1.3619160
C	-5.4674930	0.4701090	-1.0498910
N	-5.5736690	0.4501900	0.3217050
H	-4.4602990	-0.5666020	1.8390330
H	-4.0189580	-0.6011800	-2.3316060
H	-6.1286800	1.0605670	-1.6641910
N	-3.8961240	-0.8748950	-0.2033260
C	-6.5424390	1.1891800	1.1175660
H	-7.5549450	0.8768350	0.8574040
H	-6.3632280	0.9827260	2.1722320
H	-6.4287490	2.2592370	0.9382740
C	2.9524940	1.7882920	-0.0227690
C	3.0412010	0.3777320	0.0042500
C	1.8278590	-0.3693290	0.0005300
C	0.5816810	0.3566600	-0.0872910
C	1.7190350	2.4766980	-0.1094470
H	2.6445440	-2.3789470	0.1551620
H	3.8397230	2.4067630	0.0173380
C	1.7348990	-1.7963520	0.0839270
C	-0.6338570	-0.2823090	-0.0958630
C	-0.6896690	-1.6933660	-0.0179780
C	0.5283160	-2.4385160	0.0717630
H	-1.5425570	0.3035910	-0.1643600
O	0.5401230	1.7092520	-0.1732080
O	1.5409920	3.6912070	-0.1430750
C	4.3575090	-0.2968990	0.0960720
F	4.5083770	-1.0187880	1.2448900
F	5.3824480	0.5714840	0.0556590
F	4.5673980	-1.1940020	-0.9081810
O	-1.8148830	-2.3604930	-0.0237220
H	-2.6696920	-1.7485560	-0.0925570
H	0.4644610	-3.5189600	0.1324000

Table 2.13. Optimized S_1 $CouOH^{-*}\cdots HMI^{+}$ structure (TD-DFT/ωB97XD/6-31+G**/chloroform PCM).

Atoms	Coordinate x / Å	Coordinate y / Å	Coordinate z / Å
C	-4.5062700	-0.1368230	0.8013330
C	-4.8497140	-0.6429350	-1.3046330
C	-5.8515900	0.1900750	-0.9094800
N	-5.6165940	0.4967970	0.4146260
H	-4.0694310	-0.0845630	1.7859310
H	-4.6589320	-1.1089190	-2.2570530
H	-6.6985480	0.5888990	-1.4434150
N	-4.0270650	-0.8326740	-0.2220680
C	-6.4510820	1.3559150	1.2492600
H	-7.4249150	0.8876850	1.3945270
H	-5.9634290	1.4932830	2.2129880
H	-6.5704150	2.3238690	0.7628900
C	3.0532760	1.7573440	-0.0907040
C	3.1061510	0.3530080	0.0048240
C	1.8640880	-0.3666150	-0.0118190
C	0.6561630	0.3815970	-0.1801690
C	1.8422150	2.4752950	-0.2511860
H	2.6193300	-2.3840110	0.2656480
H	3.9548850	2.3551180	-0.0499650
C	1.7262840	-1.7859150	0.1299490
C	-0.5739450	-0.2229070	-0.2135460
C	-0.7065310	-1.6483560	-0.0762910
C	0.5081990	-2.4059170	0.0967270
H	-1.4573810	0.3901770	-0.3531180
O	0.6526240	1.7397380	-0.3232340
O	1.7053240	3.6967230	-0.3435690
C	4.3953260	-0.3498090	0.1630690
F	4.4953880	-1.0398980	1.3414030
F	5.4496600	0.4855770	0.1270160
F	4.6177830	-1.2926260	-0.8009440
O	-1.8421980	-2.2259230	-0.0993760
H	-3.1157820	-1.4142030	-0.1931640
H	0.4233240	-3.4817210	0.2049920

Table 2.14. Optimized S_1 $CouOH^{-*\cdots}HMI^+$ exciplex structure (TD-DFT/ωB97XD/6-31+G**/ chloroform PCM).

Atoms	Coordinate x / Å	Coordinate y / Å	Coordinate z / Å
C	-3.4893370	0.4023220	0.4617040
C	-2.0817320	-0.6348280	1.8097640
C	-1.7265680	0.6769730	1.7530420
N	-2.6223380	1.3047240	0.9109680
H	-4.2912370	0.5895670	-0.2340540
N	-3.1895500	-0.7746040	1.0087130
C	-2.6014060	2.7234380	0.5519980
H	-1.6907260	2.9463370	-0.0081850
H	-3.4705050	2.9377240	-0.0672180
H	-2.6457550	3.3191370	1.4633570
C	1.7761070	1.6363560	-0.3964250
C	2.0067570	0.2660070	-0.1959920
C	0.9194830	-0.6366020	-0.4872880
C	-0.2088270	-0.1134980	-1.1799360
C	0.6217410	2.1313700	-1.0551810
H	1.7010430	-2.4448170	0.4236980
H	2.4850770	2.3819500	-0.0585570
C	0.8535770	-2.0114080	-0.0950240
C	-1.3058750	-0.8806830	-1.4747180
C	-1.4194930	-2.2412240	-0.9926700
C	-0.2472120	-2.7865980	-0.3368210
H	-2.1398390	-0.4459040	-2.0149290
O	-0.2725650	1.1957050	-1.5815050
O	0.3132830	3.3142070	-1.2393650
C	3.2297000	-0.2024580	0.4829750
F	3.0040310	-0.6535130	1.7621590
F	4.1635760	0.7610870	0.5945730
F	3.8241490	-1.2539950	-0.1458020
O	-2.5041890	-2.8749640	-1.0771340
H	-3.5963420	-1.6573850	0.7160970
H	-0.2862930	-3.8197960	-0.0071730
H	-0.9230860	1.2124560	2.2321530
H	-1.6386350	-1.4669040	2.3301330

2.5.2 ^{1}H NMR Spectra

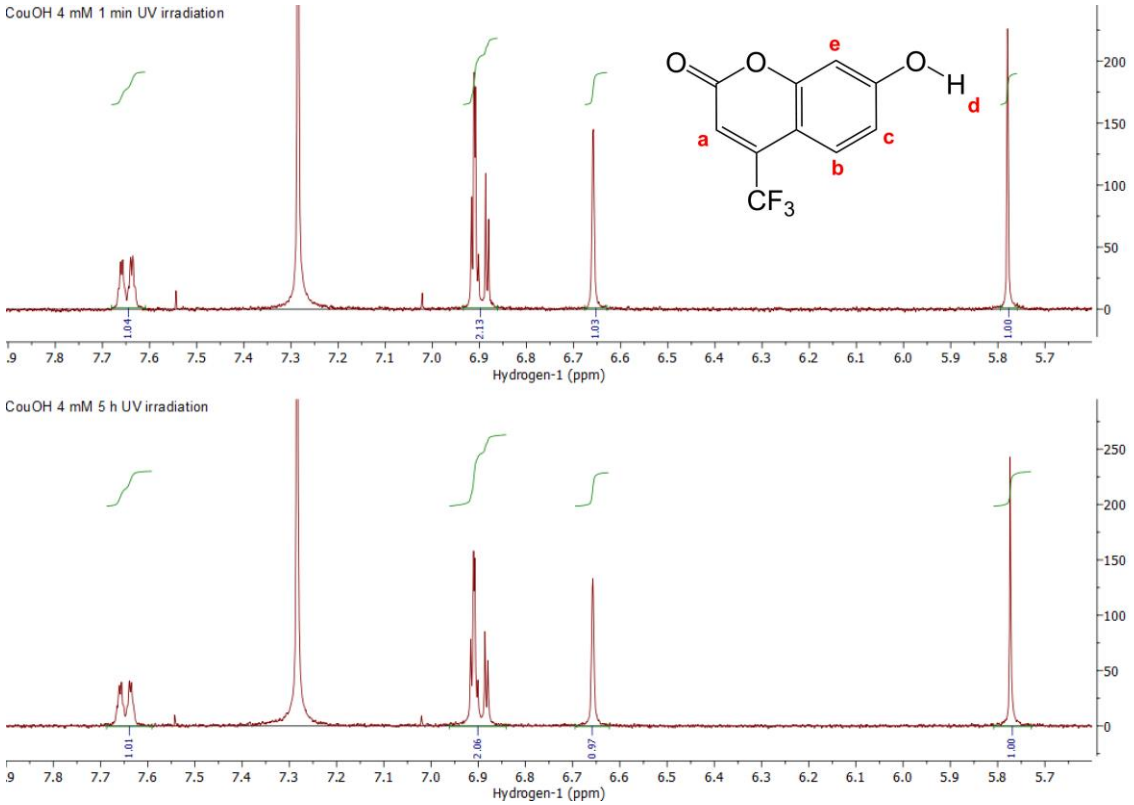

Figure 2.18. ^{1}H-NMR (400 MHz, $CDCl_3$) spectra of a 4 mM CouOH solution irradiated under UV light (power at the sample 0.415 mW, using a 254 nm light) after 1 minute (top) and after 5 hours (bottom) of irradiation. No changes are observed. Assignation: δ (ppm) = 5.78 (s,1H,H-d), 6.66 (s,1H,H-e), 6.89 – 6.91 (m,2H,H-c,H-a), 7.29 (CH_3Cl in solvent), 7.64 (m,1H,H-b).

2.5.3. Full Time-Resolved Infrared Dataset

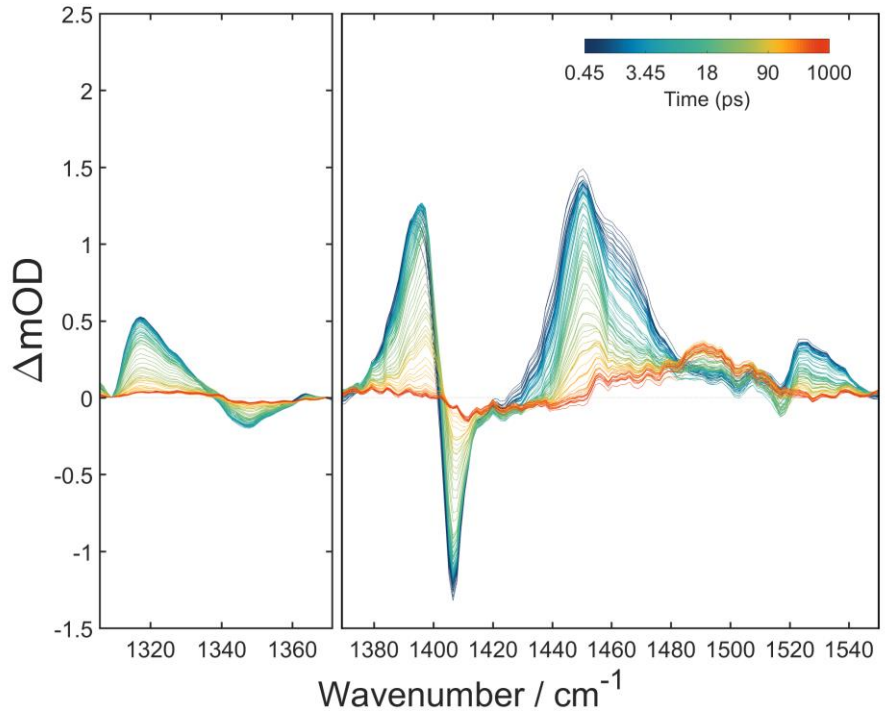

Figure 2.19. TRIR data for 4 mM CouOH in $CDCl_3$ solution.

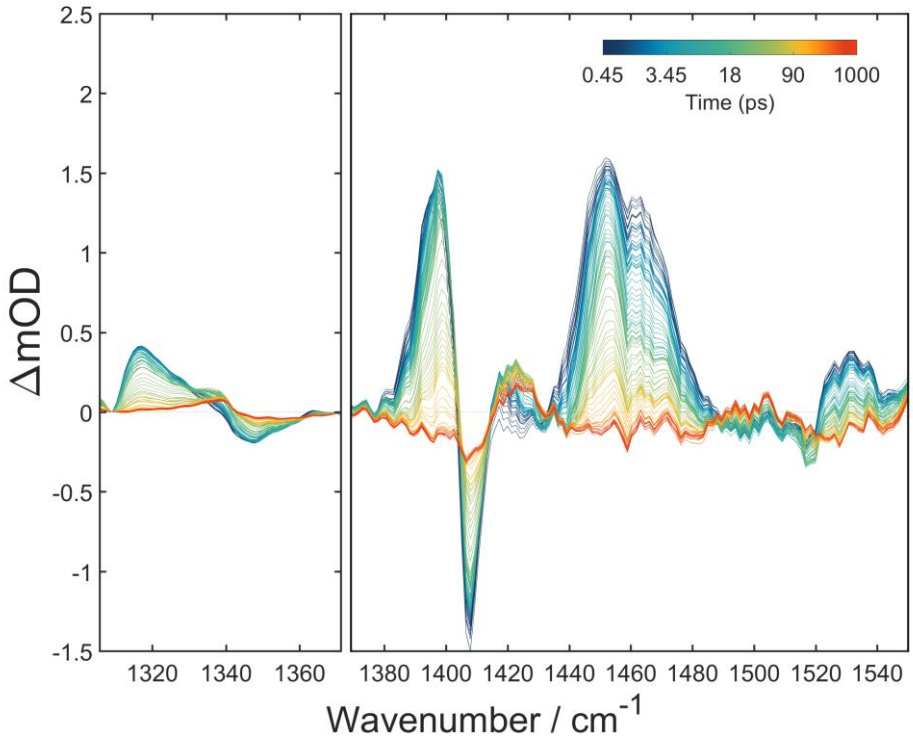

Figure 2.20. TRIR data for 4mM CouOH and 0.5 mM MI in $CDCl_3$ solution.

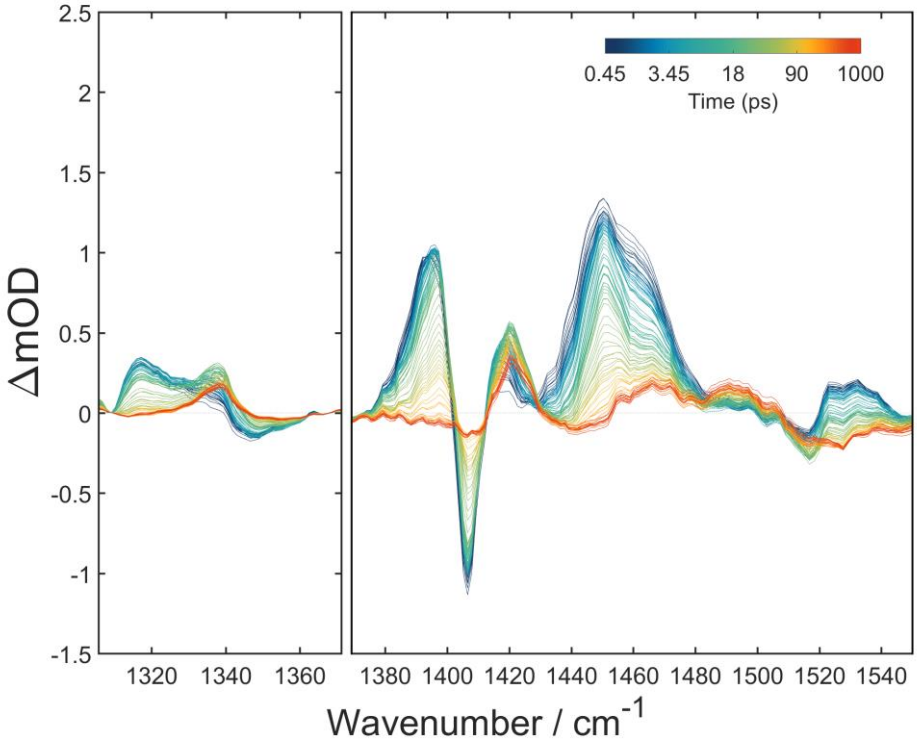

Figure 2.21. TRIR data for 4 mM CouOH and 1 mM MI in $CDCl_3$ solution.

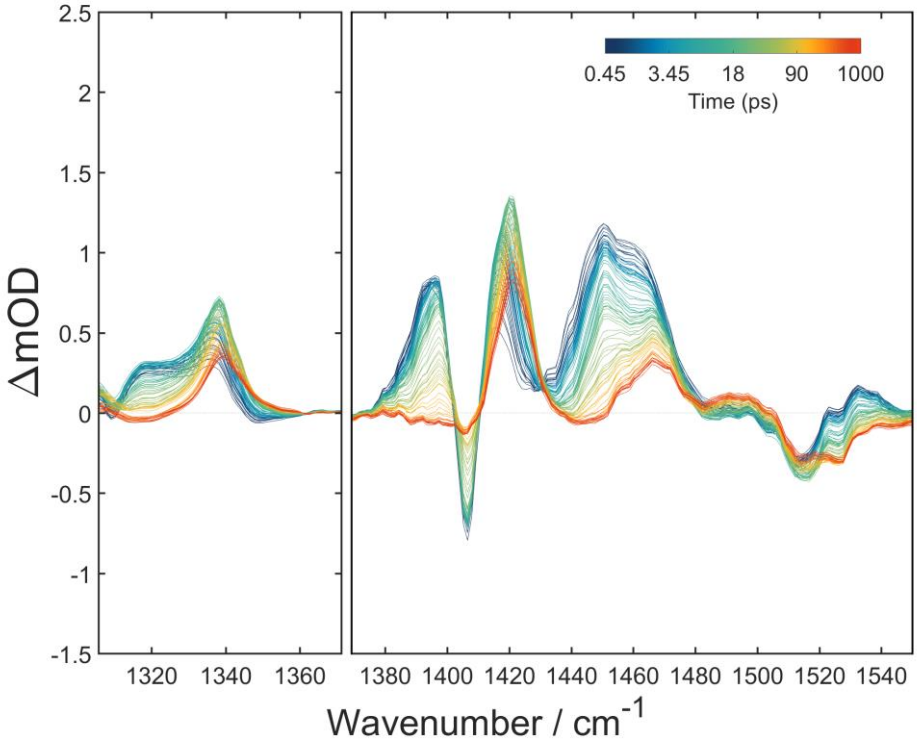

Figure 2.22. TRIR data for 4 mM CouOH and 2 mM MI in $CDCl_3$ solution.

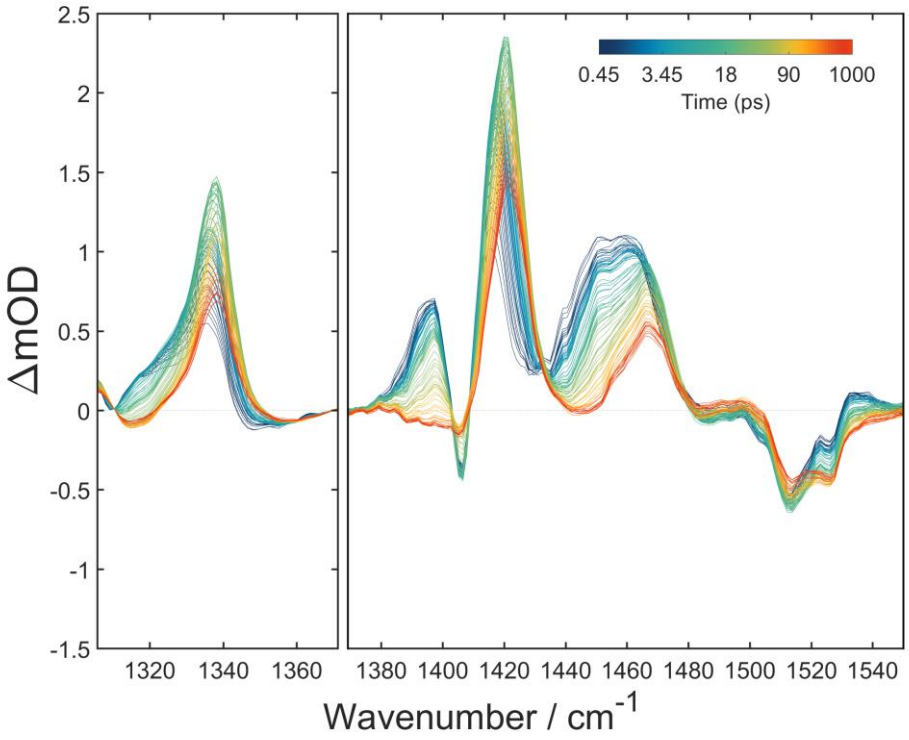

Figure 2.23. TRIR data for 4 mM CouOH and 4 mM MI in $CDCl_3$ solution.

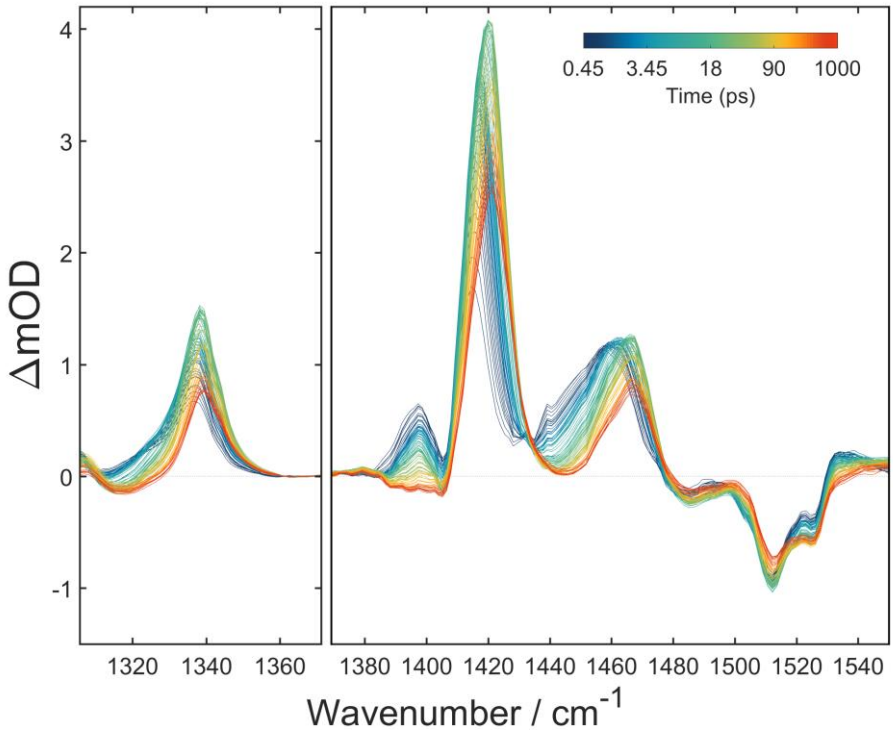

Figure 2.24. TRIR data for 4 mM CouOH and 8 mM MI in $CDCl_3$ solution.

2.5.4 Full Transient Absorption Dataset

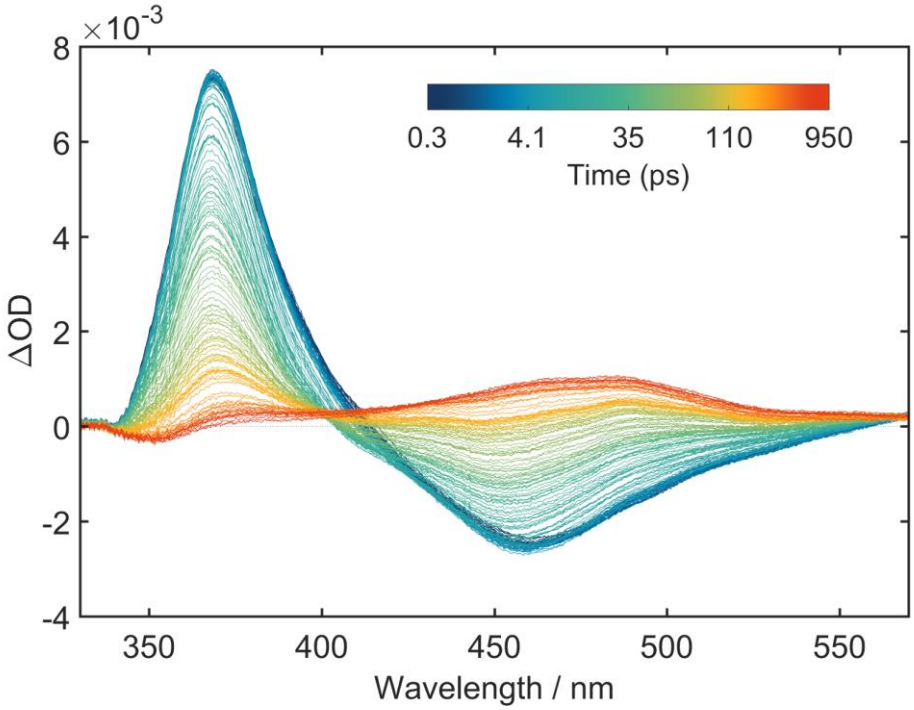

Figure 2.25. TA data for 4 mM CouOH in $CDCl_3$ solution.

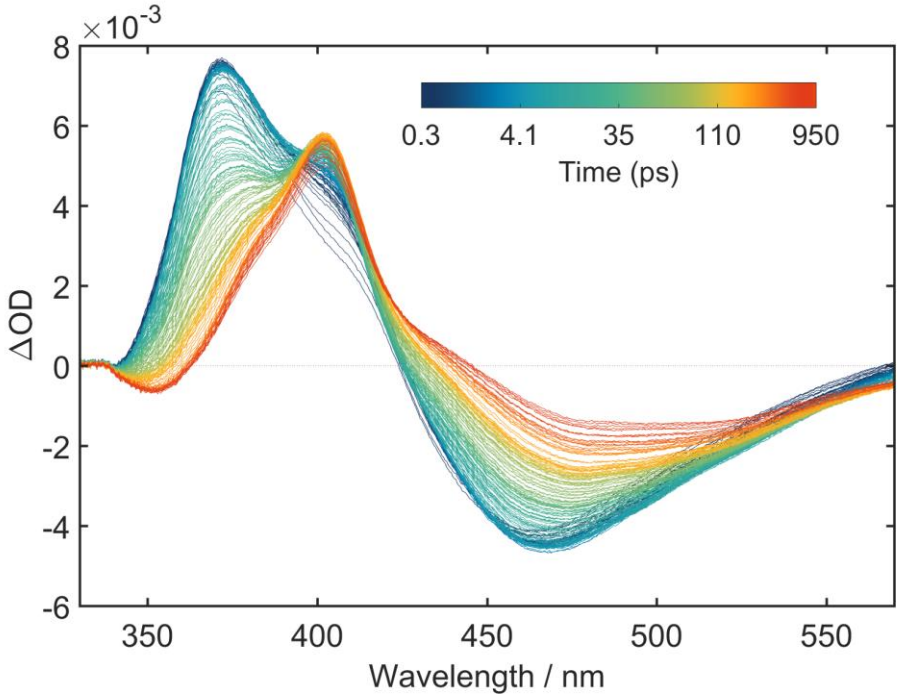

Figure 2.26. TA data for 4 mM CouOH and 0.25 mM MI in $CDCl_3$ solution.

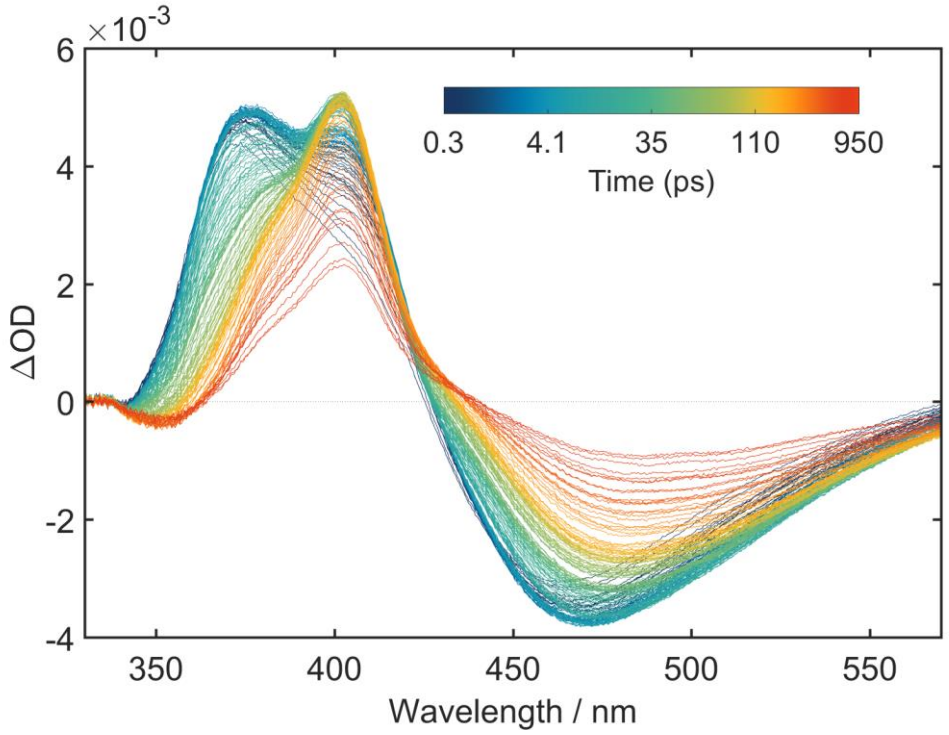

Figure 2.27. TA data for 4 mM CouOH and 0.5 mM MI in $CDCl_3$ solution.

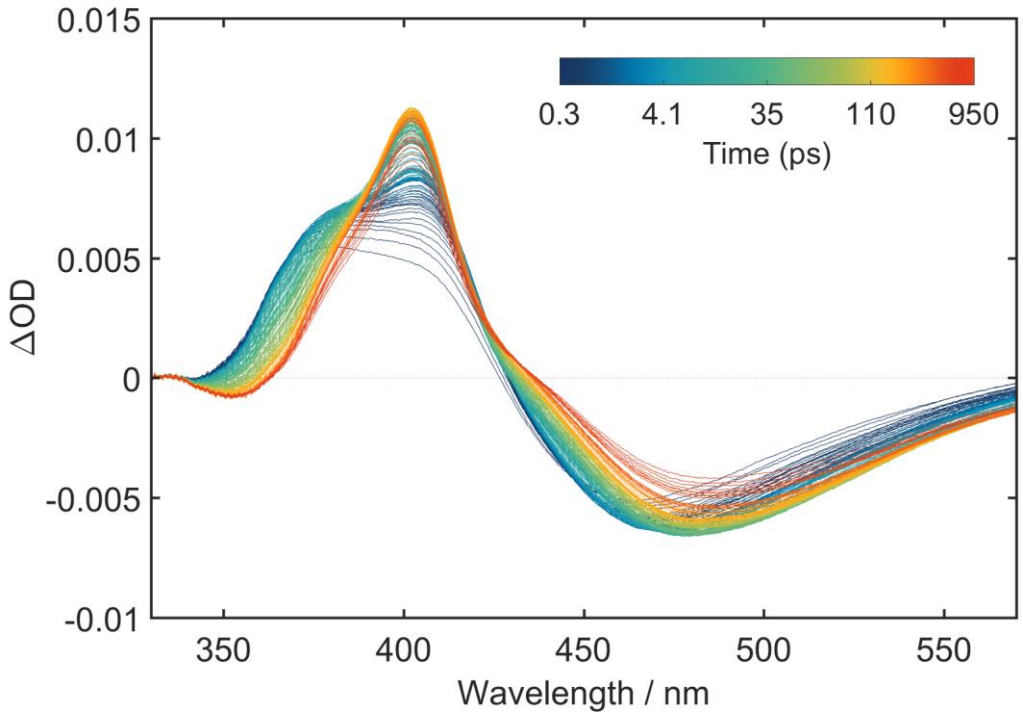

Figure 2.28. TA data for 4 mM CouOH and 1 mM MI in $CDCl_3$ solution.

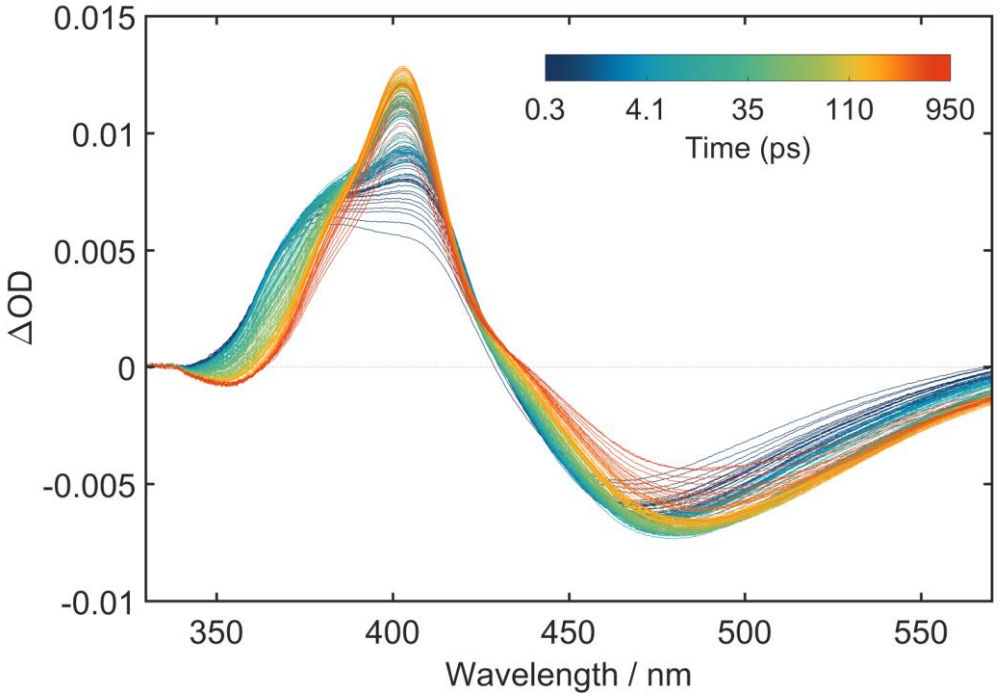

Figure 2.29. TA data for 4 mM CouOH and 2 mM MI in $CDCl_3$ solution.

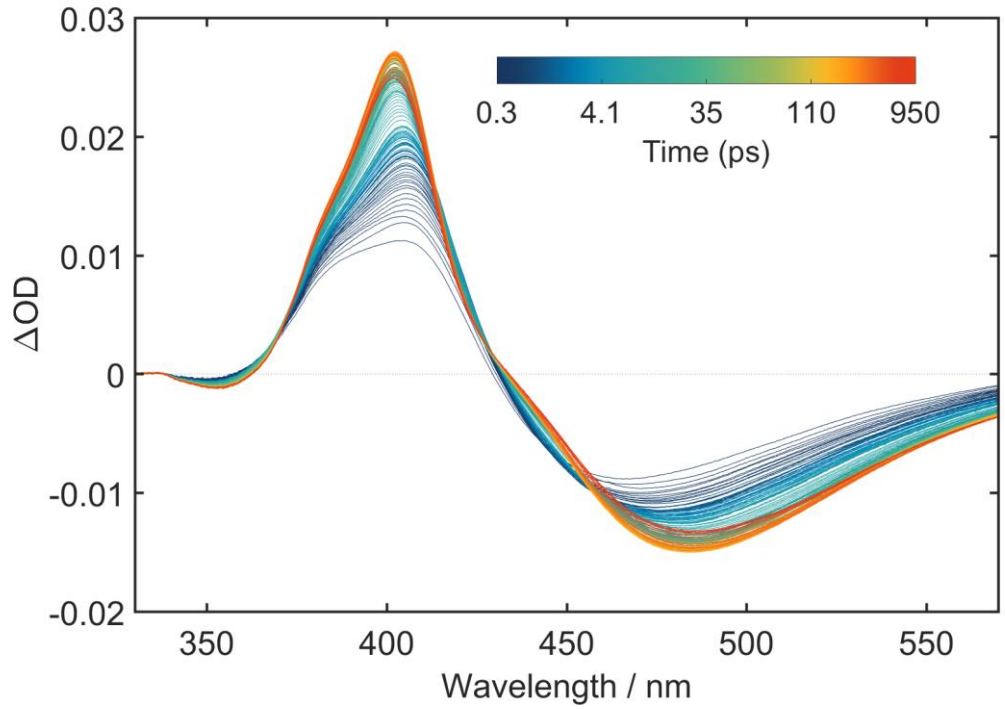

Figure 2.30. TA data for 4 mM CouOH and 4 mM MI in $CDCl_3$ solution.

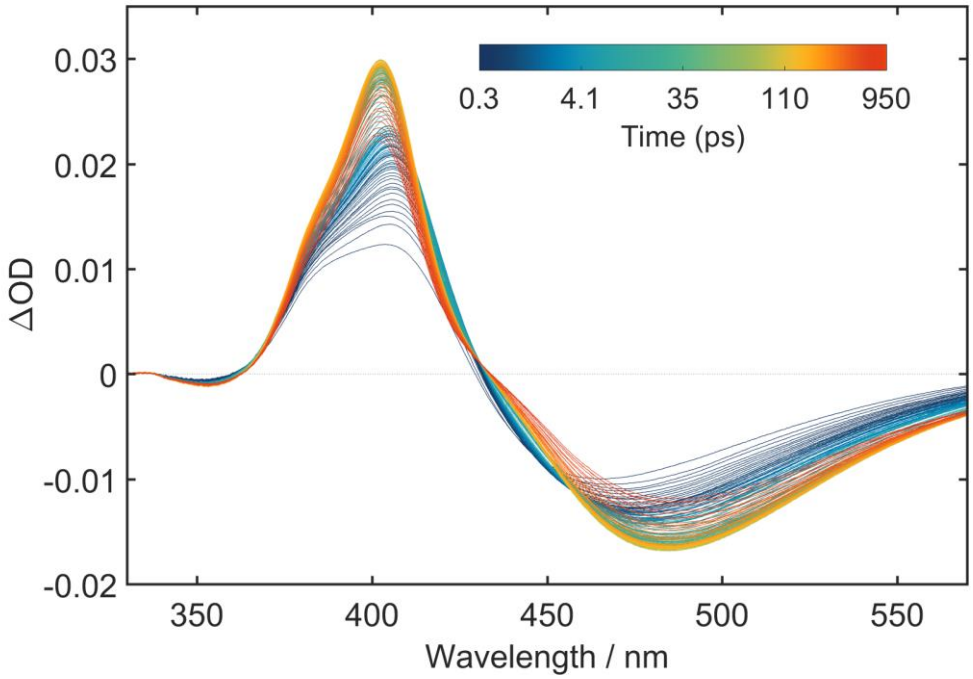

Figure 2.31. TA data for 4 mM CouOH and 8 mM MI in $CDCl_3$ solution.

3. Investigation of Diffusion-Limited Electron Transfer between *para*-Terphenyl and an Amine Donor

I declare that: cyclic voltammetry data were collected by Alexander Atkins; the DOSY ^{1}H-NMR data were collected by Teodoro Garcia Millan; I acquired and analysed.

3.1. Introduction

Light-driven chemical synthesis constitutes a promising frontier for high yield, stereo-selective reactions with low environmental impact.[1–4] In organic photoredox catalysis (OPC), the photoactivated molecule is a photocatalyst that absorbs light to generate an excited state capable of oxidation or reduction. A second electron-transfer (ET) reaction regenerates the photocatalyst, and in the process, a substrate is activated driving the synthesis of chemical products.[5–12]

The field has grown rapidly and investigations have started to focus on mechanistic aspects of OPC, with the aim of providing insights that will drive the rational design of photoactivated substrates and/or catalysts used in synthesis.[13–15] These approaches span the disciplines of electrochemistry, computation and ultrafast transient spectroscopies. Investigations are focusing on photoactivated molecules with optimal ground-state properties (*e.g.* solubility, redox-potential, pre-association with substrates) as well as determining the role of singlet and triplet excited states, and diffusional encounter steps in the dynamics.[16–21]

Whilst successful for many synthetic procedures, only recently light-driven synthesis and OPC have used carbon dioxide as a substrate in carboxylation reactions, adding -COOH functionalisation to synthetically relevant intermediates and reactants. The approach relies on a single reductive ET reaction step to convert CO_2 into its radical anion $CO_2^{\bullet -}$, bypassing multistep ET mechanisms required to produce CO or other highly reduced forms of carbon. To date, there have been few examples reporting this methodology,[22–26] as generating the radical anion of CO_2 imposes severe energetic constraints. UV absorbing photocatalysts provide an alternative route to surmount the energetic barriers necessary for CO_2 reduction. However, the height of the barrier for the first ET reduction process is

extremely high and involves rearrangement of the CO_2 nuclei from a linear ($D_{\infty h}$) to a bent geometry (C_{2v}).

Recently, Seo *et al.* reported the successful application of an OPC to convert CO_2 into valuable chemical compounds under conditions commonly used in synthetic laboratories (room temperature, 1 atm of CO_2 pressure).[23,24] The photocatalyst used in this reaction is *para*-terphenyl (pTP), which absorbs in the UV region of the electromagnetic spectrum, and undergoes reductive quenching with an amine which acts as sacrificial electron-donor, facilitating CO_2 reduction via radical single-ET reaction (see Figure 3.1). The mechanism proposed by the Seo *et al.*[23] then sees the addition of $CO_2^{\bullet -}$ to a substrate of interest, and further reduction step performed by pTP to obtain stable products. Finally, Seo *et al.*[23] optimized the scope of reaction testing several substrates, solvent conditions, and sacrificial electron donors. For example, under optimal condition the *β*-selective hydrocarboxylation of styrene had an 87% yield and a 29:1 selectivity over the *α*,*β*-di-carboxylation by-product. In particular, amines were discovered to be the most promising electron donors.

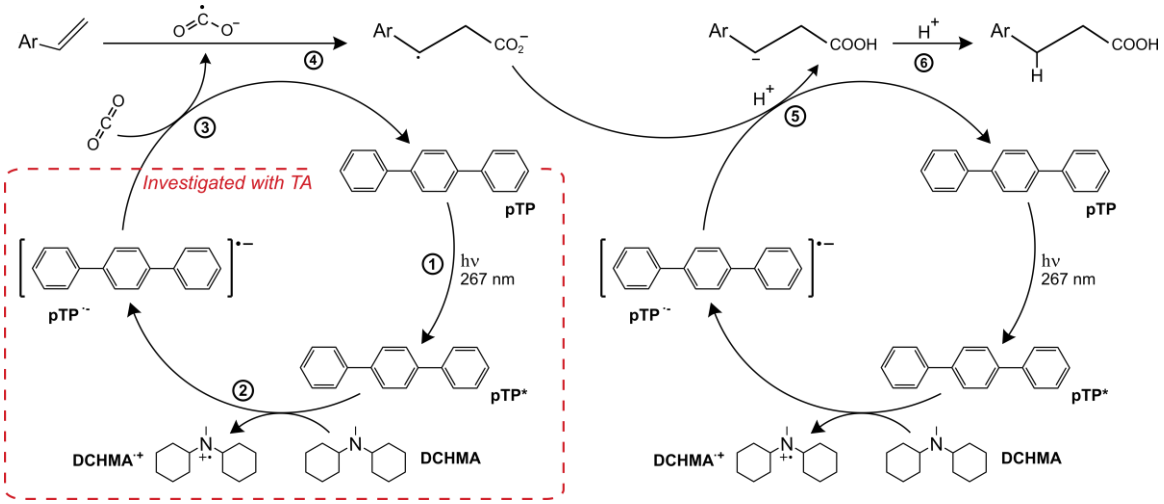

Figure 3.1. Reaction scheme proposed for the β-selective hydrocarboxylation of styrenes investigated by Seo *et al.*[27] where CO_2 is directly involved as a reactant. The OPC cycle starts with excitation of *para*-terphenyl (pTP, step 1), continues with a bimolecular redox reaction with a sacrificial electron-donor species, *N*,*N*-dicyclohexylmethylamine (DCHMA, step 2), and ends with CO_2 activation via single-ET from $pTP^{\bullet -}$ (step 3). Activated CO_2 undergoes addition to the styrene bond to form a benzyl radical (step 4) and further reduction through a second OPC cycle before forming the final carboxylic acid (stpe 6). Transient-absorption spectroscopy allowed for the investigation of the first two steps of the OPC cycle, highlighted by the red square. Figure adapted from Seo *et al.*.[27]

A thorough mechanistic investigation of the early steps of this reaction is key to further optimize yield and selectivity of this reaction, with specific attention to the timescales of the reactive encounter between pTP and the sacrificial electron-donor. It is important to also probe the deactivation pathways of pTP* and photoproducts, which will result in lower yields. The study presented here makes use of ultrafast transient absorption (TA) spectroscopy to access the picosecond to early-nanosecond regime of pTP excited state dynamics and reductive quenching with one of the amines selected by Seo *et al.*,[23] For the study, *N,N*-dicyclohexylmethylamine (DCHMA) was chosen, as it was the most stable amine under ambient conditions. Ethanol was chosen as an example of protic and polar solvent, expected to play a role in the ET reaction between pTP and DCHMA. To the best of my knowledge, no prior studies have been reported on the ultrafast transient investigation of a photocatalytic system able to make direct use of CO_2 as a reactant in a chemical synthesis. TA spectroscopy was used to investigate the bimolecular diffusive ET step of the reaction cycle, as highlighted in Figure 3.1

3.2. Experimental Methods

para-terphenyl (pTP) and *N,N*-Dicyclohexylmethylamine (DCHMA) were purchased from Sigma Aldrich and used without further purification, and dissolved in ethanol (Sigma Aldrich, HPLC, ≥99.8 % purity) for UV-absorption and TA experiments. Ethanol-d_6 (Sigma Aldrich, anhydrous, ≥99.5% D) was used for DOSY ^{1}H-NMR experiments. All measurements were performed at room temperature (~20 ºC).

Table 3.1. Summary of pTP and pTP–DCHMA mixtures investigated (filled dot) with visible and near-infrared TA experiments in ethanol.

pTP:DCHMA		visible TA	near-infrared TA
concentration / mM	ratio		
0.7:0	–	●	●
0.5:25	1:50	○	●
0.5:50	1:100	●	●
0.5:125	1:250	●	●
0.5:250	1:500	●	●
0.5:500	1:1000	●	●

In transient absorption experiments, the pTP concentration was kept fixed at 0.5 mM, a value sufficiently small to exclude pTP aggregation. The DCHMA concentration was varied and added in large excess with respect to pTP, to study the bimolecular dynamics in the pseudo-first order regime (see Table 3.1 for a summary).

Steady state ultraviolet absorption spectra were acquired using a Thermo Scientific Genesys 10S UV-Vis Spectrophotometer.

Visible and near-infrared TA measurements were collected using a home-built apparatus. A schematic of the setup is given in Figure 3.2. 40% of the fundamental output of a 1 W, 1 kHz, 800 nm, Ti:Sapphire amplifier (Coherent, Libra) was sent through a 90:10 beam splitter, to generate respectively the 267 nm pump and probe pulses necessary for the experiment.

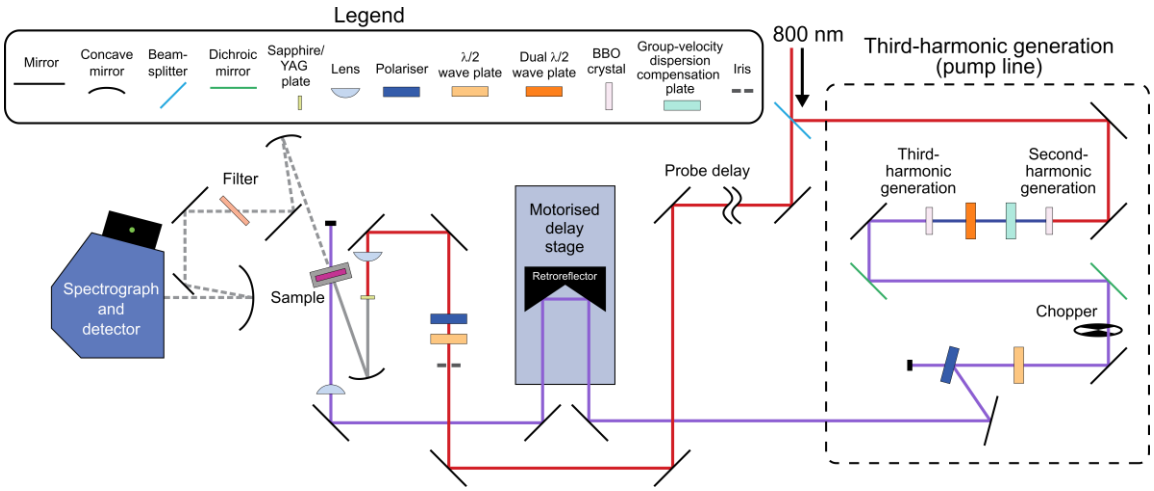

Figure 3.2. Schematic of the experimental setup used in TA measurements to investigate the ET reaction between pTP and DCHMA.

The 267 nm pump pulses were generated via third-harmonic generation (Eksma Optics THG kit, FK-800-100), which requires a frequency-doubling step and a subsequent frequency-mixing step. The 800 nm fundamental was sent through a β-barium borate crystal (BBO) to generate a 400 nm pulse via second-harmonic generation (SHG). The resulting 400 nm pulse was sent through a group-velocity dispersion compensation calcite plate to ensure temporal overlap with residual 800 nm pulses was obtained in the frequency-mixing step. As the SHG process results in 400 nm pulses polarised at 90° with respect to the 800 nm precursor, the pulses were also sent through a dual half-wave plate, to match their polarization for third-harmonic generation (THG). Eventually, THG was achieved by

mixing the temporally and spatially overlapped 400 and 800 nm pulses through a second BBO crystal, to generate 267 nm light.

The residual 800 nm and 400 nm were removed via dichroic mirrors. Subsequently, the 267 nm pump pulses were modulated at 500 Hz through an optical chopper (Thorlabs, MC2000) to generate the pump on/off sequency necessary for the TA experiment and sent through a half-wave plate and a polarizer to attenuate the power to 400 nJ at the sample position. The pump pulse was delayed relative to the probe by an aluminium retroreflector (PLX) mounted on a motorized high precision delay stage (Physik Instrumente, M-531.DG1) with maximum delay of 1.9 ns. A plano-convex lens was used to focus the pump into the sample (f = 25 cm).

Probe pulses were generated using some of the remaining 10% portion of the 0.4 W fundamental 800 nm laser output. The beam was sent through a half-wave plate and a polarizer to control the light intensity and guarantee shot-to-shot stability in the probe pulses. Subsequently, it was focused onto a sapphire or an yttrium-aluminium garnet (YAG) crystal generating, respectively, visible light to investigate the 450–700 nm region or visible and near-infrared light, which was filtered to investigate the 830–900 nm wavelength. In both cases, the probe beam was focused into the sample (f = 20 cm), recollimated with the collinear signal, and spectrally filtered to remove any residual fundamental 800 nm light. Finally, the probe pulse and the signal were focused (f = 10 cm) into a spectrograph (Shamrock 163, Andor) equipped with a linear 1024 element CCD array detector (Entwicklungsbüro Stresing).

Throughout the experiment, samples were continuously flowed using a customized Harrick flow cell (CaF_2 windows), with a 200 μm pathlength. For all the samples, TA measurements were performed using the magic angle (54.7°) condition. As outlined in Section 2.2, a custom-made LabVIEW (National Instruments) software was used for remote control of mechanical components and data acquisition. The spectrograph collected data in blocks of 200 shots, each comprised from sequential pump on/off spectrum pair, thus resulting in 100 TA spectra per block. For each block, the mean and the standard deviation were computed and only data within a standard deviation of 0.4 were retained. This procedure was applied to all the investigated pump-probe time-delays to obtain one cycle, adding a random waiting time between every time delay to account for periodic intensity fluctuations in the laser source. Every measurement was averaged over a minimum of 10 to

a maximum of 100 cycles, according to the signal-to-noise ratio of the sample. Data analysis was conducted using customised analysis codes with MATLAB (MathWorks).

The cross-correlation instrument response-function (IRF) was measured via two-photon absorption in $CHCl_3$ to be ~280 fs. The $CHCl_3$ spectra, given in Figure 3.3(a), resulted in a positively chirped signal, with two-photon absorption occurring at earlier time delays for shorter wavelengths than for longer wavelengths. This was accounted for by shifting the time axis relative to time zero at each wavelength, a process known as chirp-correction. A set of points where the signal was at the highest intensity at several different wavelengths were manually chosen and interpolated to a polynomial function; the polynomial form was then used to shift the position of time-zero. After this chirp-correction procedure, the IRF trace was extracted by averaging over all wavelengths; extrapolation of the FWHM of a Gaussian fit to the trace (Figure 3.3(b)) lead to an estimate of the IRF. As for the $CHCl_3$ spectrum, the chirp-correction procedure was applied to each of the TA datasets collected on pTP and DCHMA samples.

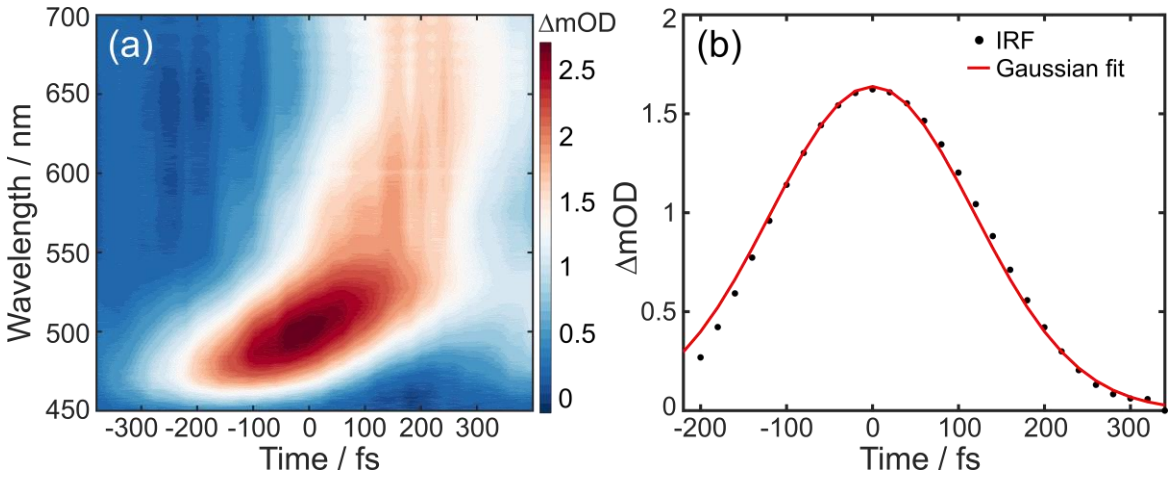

Figure 3.3. Characterization of the pump pulse length via non-resonant two-photon absorption spectroscopy in $CHCl_3$ solvent. (a) TA signal, and (b) IRF trace (black dots) obtained after chirp-correction of TA response and averaging over wavelengths and Gaussian fit (red line).

3.3. Results and Discussion

3.3.1. Steady-State Spectroscopy and Cyclic-Voltammetry

Prior to the investigation of the excited state dynamics, steady-state spectroscopy and cyclic-voltammetry studies were carried out to support the interpretation and the

modelling of the TA data. Figure 3.4 shows the UV absorption spectrum of pTP and DCHMA in ethanol, at the concentrations and path-length used in the TA studies. 267 nm irradiation of samples is predominantly absorbed by pTP, with DCHMA absorption only being relevant at concentrations as high as 500 mM. However, even in 0.5:500 mM pTP–DCHMA mixtures, the DCHMA absorbance is at least three times smaller than pTP, thus it is expected that TA spectra will be dominated by pTP absorption and its dynamics. For the photocatalytic active molecule, pTP, the $S_1 \leftarrow S_0$ feature is assigned to $\pi^* \leftarrow \pi$ electronic transition, with a characteristically high value of the absorbance even at the low concentration of 0.5 mM used in the study.[28]

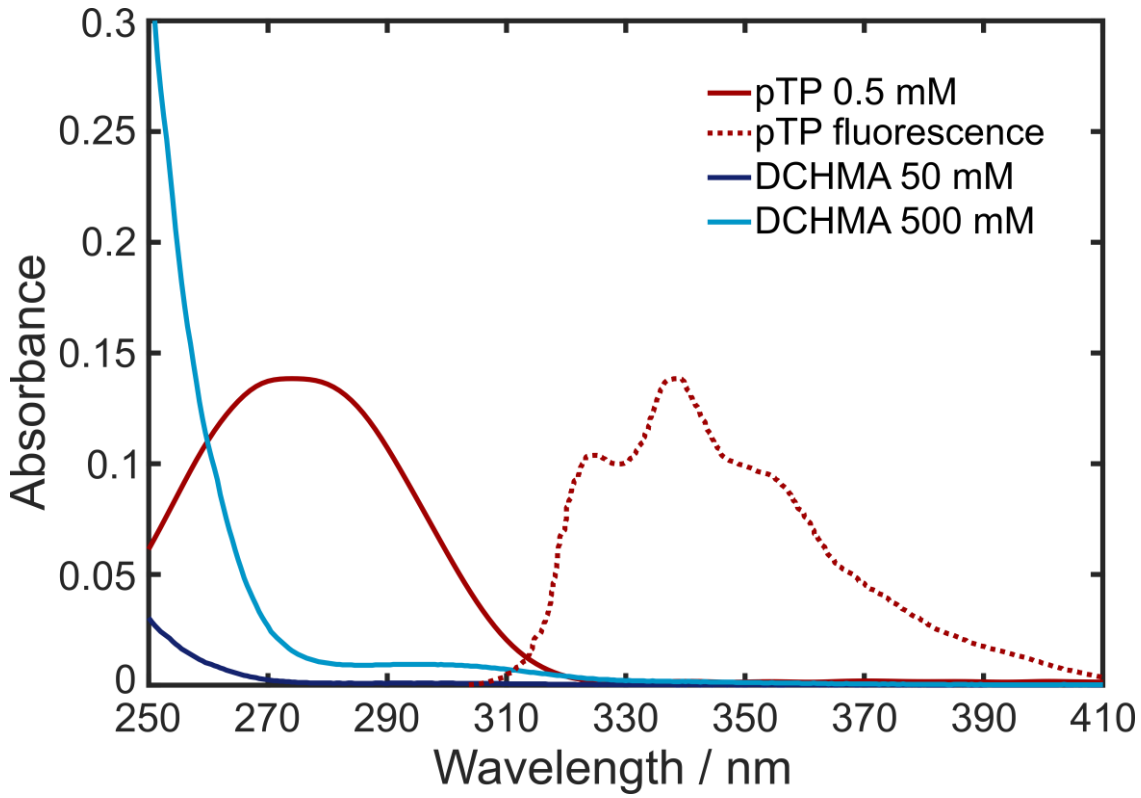

Figure 3.4. UV absorption spectrum of a 0.5 mM pTP solution (solid red line), DCHMA 50 mM (solid blue line) and 500 mM (solid light blue line) solutions in ethanol, in a 200 μm path length cell. The fluorescence spectrum of pTP in ethanol (dashed red line) is also shown, normalised to the maximum of the absorption spectrum and adapted from Lakowicz.[29]

Figure 3.4 also presents the fluorescence spectrum of pTP, normalised to the peak of UV absorption of pTP,[29] highlighting the lack of mirror symmetry between the two. Previous time-resolved fluorescence studies have highlighted the anharmonicity of the PES of electronic states of pTP, relating the S_0 state to a torsional potential and to a plethora of

rotamers associated with phenylene ring rotations along the main molecular axis (see Figure 3.5), while a planar configuration was adopted on the S_1 state in a nearly harmonic potential.[28,30] Calculations showed that the unstructured absorption band arises from the several vibrational states lying on the shallow torsional potential, each of them contributing to the broadening of the vibronic progression. Oppositely, the fluorescence spectrum preserves its vibronic progression as pTP sits in a single vibrational state on the S_1 potential, its wavefunction overlapping effectively with only one of the S_0 vibrational mode just above the torsional potential.[30]

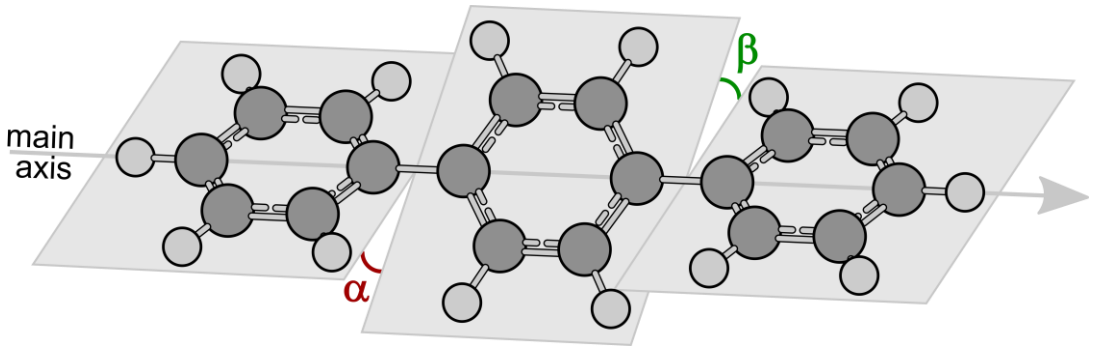

Figure 3.5. Representation of pTP, highlighting the planes onto which the phenylene rings lie and the torsional angles α and β between each plane and around the main molecular axis. Several different pTP conformers are associated to the S_0 state (α,β ≠ 0), while pTP in the S_1 state assumes a planar configuration (α = β = 0).

To confirm whether pTP in the excited state has sufficient energy to extract an electron from the amine donor, the standard reduction potential of the couple pTP/pTP$^{\bullet -}$ was measured via cyclic voltammetry (CV), as shown in Figure 3.6(a), and compared to the energy of the $S_1 \leftarrow S_0$ transition. The reduction reaction was found to be quasi-reversible, with $E^{\ominus} \approx E_{1/2}$ = -2.808 V *vs.* ferrocene in acetonitrile (MeCN), a value that agrees with prior studies when accounting for the difference in the reference electrodes.[23,31] The CV and the potential associated to the couple DCHMA$^{\bullet +}$/DCHMA were also measured (Figure 3.6(b)): the absence of a return cathodic peak demonstrates the oxidation reaction of DCHMA is irreversible, as hypothesized by Seo *et al.*,[23] with an $E^{\ominus} \approx E_{1/2}$ = 0.400 V *vs.* ferrocene in dichloromethane (DCM). Assuming similar values would be retrieved in different solvents, for the reaction in Figure 3.1 the overall electromotive force would be -3.208 V, indicating the reaction in the ground state is highly unfavoured, but photoexcitation of pTP at 267 nm (4.64 eV) would provide more than sufficient energy to satisfy the thermodynamical

requirements. These CV measurements helped to clarify whether photoexcited pTP has sufficient energy to function as an oxidant sufficiently strong to undergo multiple redox cycles. *Per contra*, the irreversibility of DCHMA ET confirms CO_2 reduction and fixation ultimately occurs at the expenses of the amine as sacrificial electron donor.

DOSY ^{1}H-NMR spectroscopy measurements were performed to extract the diffusion coefficients of pTP and DCHMA in ethanol. These data returned diffusion coefficients of 0.85×10^{-9} m^2 s^{-1} and 0.67×10^{-9} m^2 s^{-1}, respectively for pTP and DCHMA. Nevertheless, the requirement of NMR techniques to use deuterated solvents means that the diffusion coefficients obtained are not entirely correct for TA experiments: ethanol-d_6 is ~13% heavier than ethanol-h_6 and the viscosity is altered upon solvent deuteration.[32,33] As DOSY ^{1}H-NMR still provided the most accurate estimate for the diffusion coefficients without having to resort to specific and direct measurement techniques (via diaphragm cells or capillary systems), the values reported above will be used throughout the following analysis.

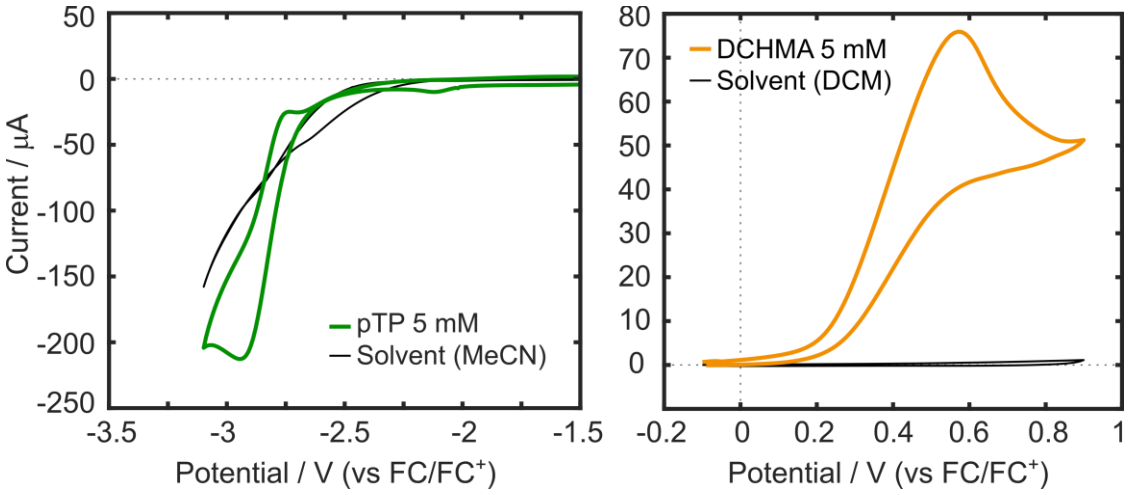

Figure 3.6. Cyclo-voltammograms of (a) a 5 mM solution of pTP in MeCN, at 0.5 V/s scan rate, and (b) of a 5 mM solution of DCHMA in DCM, at 0.1 V/s scan rate. For both reactants, a 0.1 M solution of recrystallized tetrabutylammonium hexafluorophosphate ($TBAPF_6$) was used as a supporting electrolyte, Pt was used as working and counter electrodes, Ag as pseudo-reference electrode and ferrocene was added to the solution as an internal reference; working electrode diameter was 1.6 mm.

3.3.2. Transient Absorption Spectroscopy of pTP in Ethanol Solutions

TA studies were performed to investigate the photochemistry of pTP in ethanol solution and in mixtures with DCHMA to explore the encounter dynamics and the

timescales of photoproduct generation. On the basis of previous transient absorption experiments in different solvents, features associated with the pTP radical anion were expected in the visible (450–750 nm) and in the near-infrared (830–900 nm) regions of the electromagnetic spectrum.[34,35] In the visible, signal from pTP ESA was also expected,[36] possibly complicating the spectral interpretation but also providing insights on the relaxation dynamics of parent molecules. Therefore, it was important to investigate the photochemistry of pTP alone prior to studying mixtures.

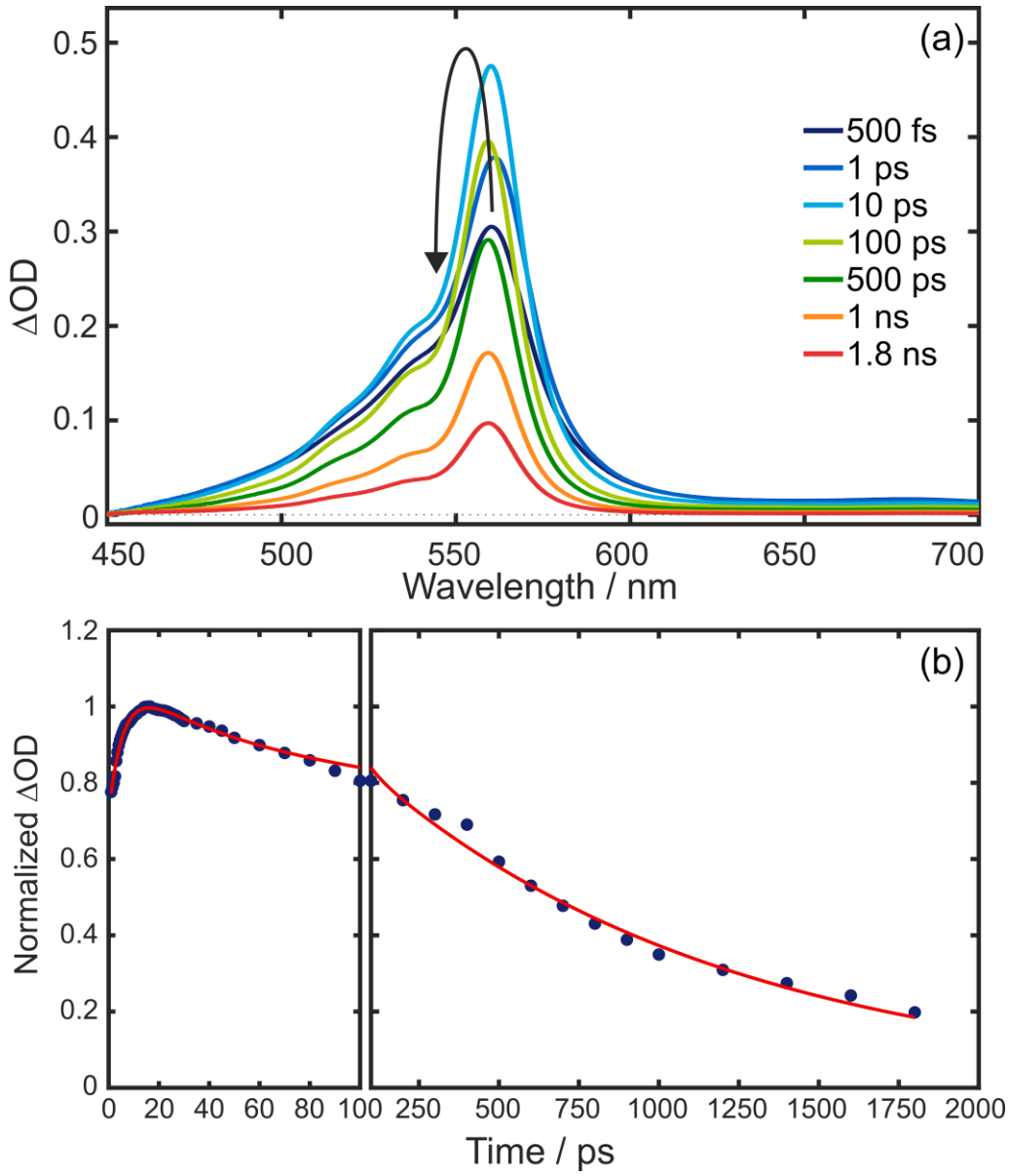

Figure 3.7. (a) Visible TA spectra in ethanol solution of pTP 0.7 mM and (b) normalized integrated signal of the ESA band centred at 560 nm. The arrow in panel (a) indicates the evolution of the parent ESA signal. Note that for these data the intensity scale is in ΔOD and not in ΔmOD.

Figure 3.7(a) displays the visible TA spectra of a 0.7 mM pTP solution in ethanol, showing a structured, positive feature peaking at ~560 nm, associated with the $S_n \leftarrow S_1$ ESA. The signal rises within the first few picoseconds, and the maximum wavelength blueshifts by ~2 nm from 561 to 559 nm; at later pump-probe time delays, the signal decays but does not completely disappear within the investigated time window. The kinetics associated with the photoexcited stated of pTP (Figure 3.7(b)) were extracted by integrating the ESA signal in the 557–563 nm region. Three exponential components were required to fit the trace,[37] according to Equation 3.1:

$$I_{pTP(560)} = A_1 e^{-k_1 t} + A_2 e^{-k_2 t} + A_3 e^{-k_3 t} \quad (3.1)$$

where I is the intensity of the signal, k_n and A_n are respectively the rate-constants and the amplitudes associated with the *n*-th component of the multiexponential decay; the first component is an exponential rise ($A_1 < 0$) while the other two were biexponential decays ($A_{2,3} > 0$).

The time constant for the exponential rise was found to be 5.7 ± 0.7 ps and was associated to a geometric rearrangement of pTP on the S_1 PES. Consistent with the interpretation given for the UV absorption and fluorescence spectra of pTP (Section 3.3.1), with reference to Figure 3.5, the vertical $S_1 \leftarrow S_0$ transition prepares pTP in a geometry that is far from the S_1 minimum. Therefore, it is proposed that the strong ESA is maximised when pTP adjusts its nuclei to the configuration of the S_1 minimum and accounting for the rise in the signal. As the phenylene rings of the molecule change from a twisted to a planar geometry,[28,30] the solvent molecules also slightly rearrange around pTP, leading to a shift in the observed peak. The timescale of the conformational rearrangements matches previous fluorescence up-conversion measurements in protic solvents with a 267 nm excitation pulse.[28]

Notably, the fluorescence up-conversion experiments conducted by a different group at 290 nm, in the red edge of the pTP UV absorption spectrum, do not show any dynamic Stoke-shift, indicating that the solvent is not involved in the relaxation processes, and pTP geometry rearrangement was proposed to occur on a sub-picosecond timescale.[38] This could be reconciled by accepting that the modes that couple to mediate the vibrational relaxation also play a role in the conformational rearrangement. Therefore, population of different

excited state vibrational modes with different excitation wavelengths, changes the observed dynamics accordingly.

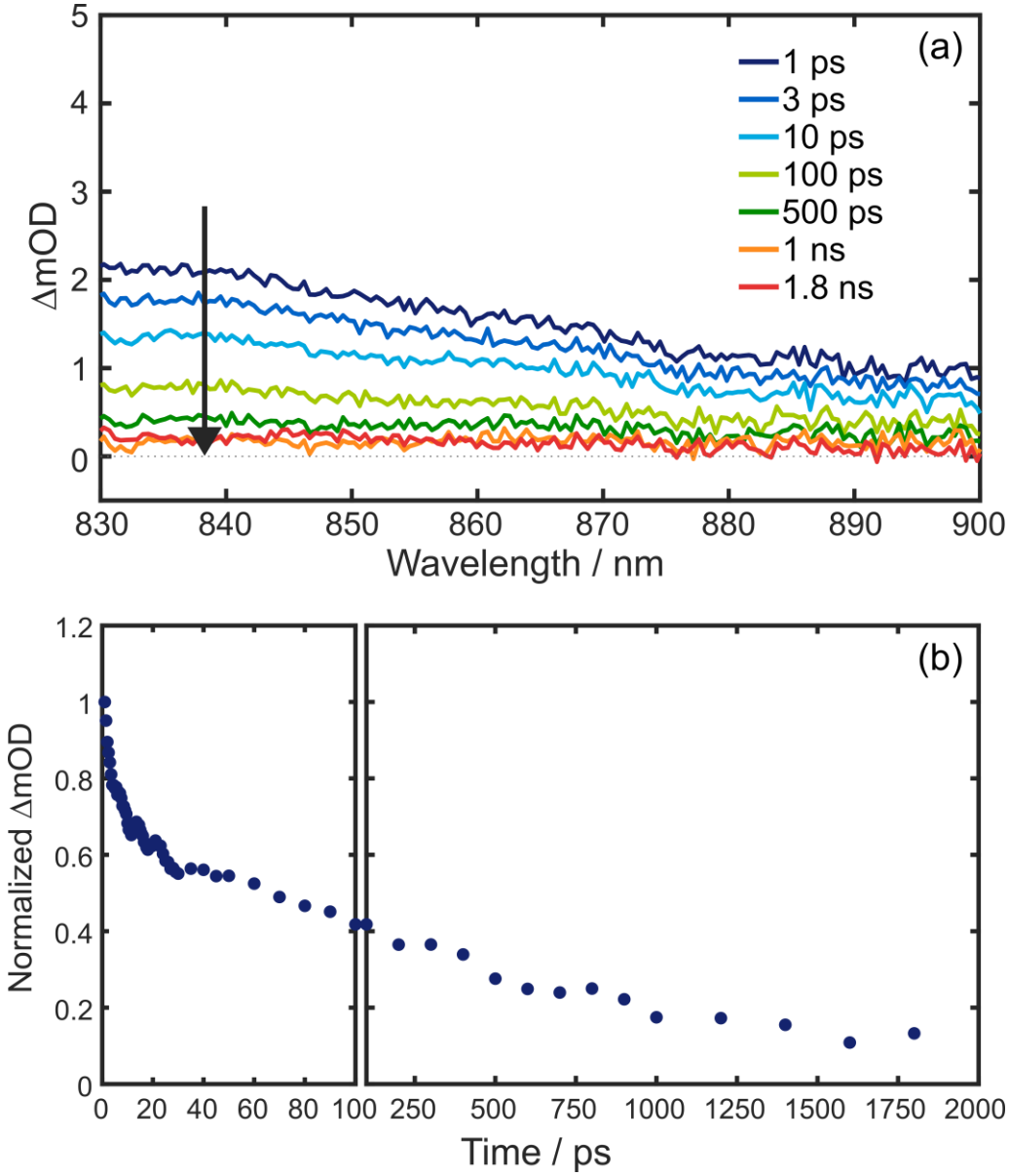

Figure 3.8. (a) Near-infrared TA spectra in ethanol solutions of pTP 0.7 mM and (b) normalized integrated signal of the ESA band centred at 860 nm. The arrow in panel (a) indicates the evolution of the parent ESA signal.

The time constants associated to the ESA decay were found to be 41.1 ± 11.7 ps and 1.14 ± 0.04 ns. Assignment was guided by previous studies. The picosecond decay component was associated to further pTP–solvent cooling *post* nuclei rearrangement, consistently with previous time-resolved Raman measurements that have shown the process

takes approximately 40 ps.[28] The long-time decay component was associated to pTP fluorescence, in agreement with TCSPC experiments that reported a fluorescence lifetime of 1.18 ± 0.01 ns for pTP in ethanol.[39] Finally, no triplet signatures are evident in the spectra nor in the kinetic traces, excluding ISC as a potential deactivation pathway.

Near-infrared TA data for pTP only solutions in ethanol were also acquired (Figure 3.8(a)), in a region of the electromagnetic spectrum where signal from $pTP^{\bullet -}$ photoproducts is expected.[34,35] The pTP near-infrared transient response shows a positive broad, structureless ESA feature peaking around 840 nm, that rises within the IRF and almost fully decays within the investigated time-window. Unlike the visible ESA, for the near-infrared ESA feature to be broad, the $S_n \leftarrow S_1$ transition may involve a shallow S_n potential, and the absence of a rise component (Figure 3.8(b)) means the molecule does not need to undergo any nuclear coordinates rearrangement prior to absorption to higher states. The near-infrared ESA dynamics were not fitted as their contribution was removed via deconvolution when investigating pTP–DCHMA mixtures.

From visible and near-infrared TA data, a schematic of the excited state photochemistry of pTP can be proposed, as summarised by Figure 3.9. The S_0 and S_1 potentials are displayed as per the prior discussion of the absorption and fluorescence spectra, highlighting the wavefunctions responsible for the breakdown of the mirror symmetry in pTP.[30] Once the molecule is excited, it finds itself in a hot vibrational state, in a conformation initially resembling one of the possible rotamer configurations of the ground state. On the S_1 state, the molecule undergoes a geometric rearrangement forming a planar conformer; fluorescence occurs dominantly from this conformation at the S_1 minimum to vibrationally hot levels of the S_0 state lying above the torsional potential. Furthermore, TA spectra shows ESA from the S_1 state lie in the visible and in the near-infrared region of the electromagnetic spectrum. Visible ESA is structured and resolved, and shows a delayed rise, associated to geometric rearrangements, so occurs from the bottom of S_1 to a S_m state. Finally, near-infrared ESA is structureless, its kinetics not showing any rising component: the transition occurs from the vibrationally hot sublevel of the S_1 state to a S_n state different from the one involved in the visible ESA.

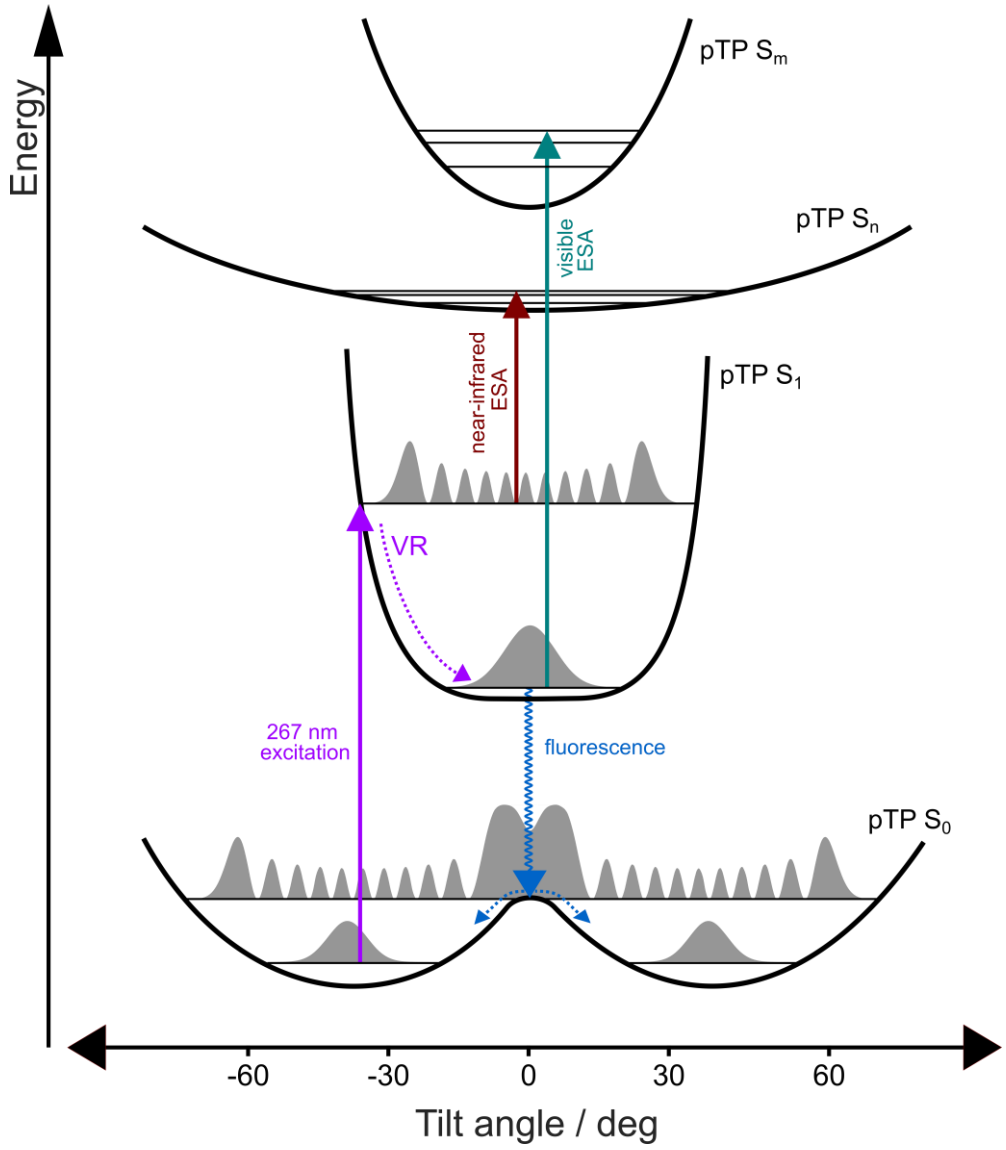

Figure 3.9. Schematic summary of the photophysical relaxation processes of pTP on the basis of visible and near-infrared TA data in ethanol. The PES diagram in the S_0 and S_1 state as a function of the tilt angle among phenyl units is adapted from Heimel *et al.*.[30] The tilt angle is defined as the angle between the plane of the central phenylene ring and the plane containing the remaining two rings (with reference to Figure 3.5 and setting $\alpha = \beta$). In the figure: VR: vibrational relaxation.

3.3.3. Transient Absorption Spectroscopy of pTP–DCHMA Mixtures

Following the investigation of pTP photochemistry, visible and near-infrared TA spectra of pTP–DCHMA mixtures in ethanol were recorded.

Upon addition of DCHMA, visible TA spectra in ethanol show an additional distinct peak at 475 nm at late pump-probe time delays, associated with $pTP^{\bullet -}$ generation (Figure 3.10(a,b)).[34,35] In conjunction with the observation that no photoproduct peaks are present

in absence of DCHMA, it follows that, subsequently to the ET, the formation of $DCHMA^{\bullet+}$ accompanies that of $pTP^{\bullet-}$. Further increases of the initial amine concentration led to a more intense photoproduct signal when compared to the parent ESA (see Figure 3.10(c,d)). The $pTP^{\bullet-}$ band rises within hundreds of picoseconds; at late time delays, for high DCHMA concentrations, the decay of the photoproduct band is also observed.

By solely analysing the pTP ESA decay dominant in the visible probe region, a complete picture of the ET event cannot be depicted. Insights on the steps and diffusion timescales of photoproduct formation require the investigation of spectroscopic features associated to $pTP^{\bullet-}$. This can be more easily achieved in the near-infrared region of the electromagnetic spectrum, where the intensity of the signal associated with the parent pTP ESA is a few ΔmOD, two orders of magnitude less than in the visible.

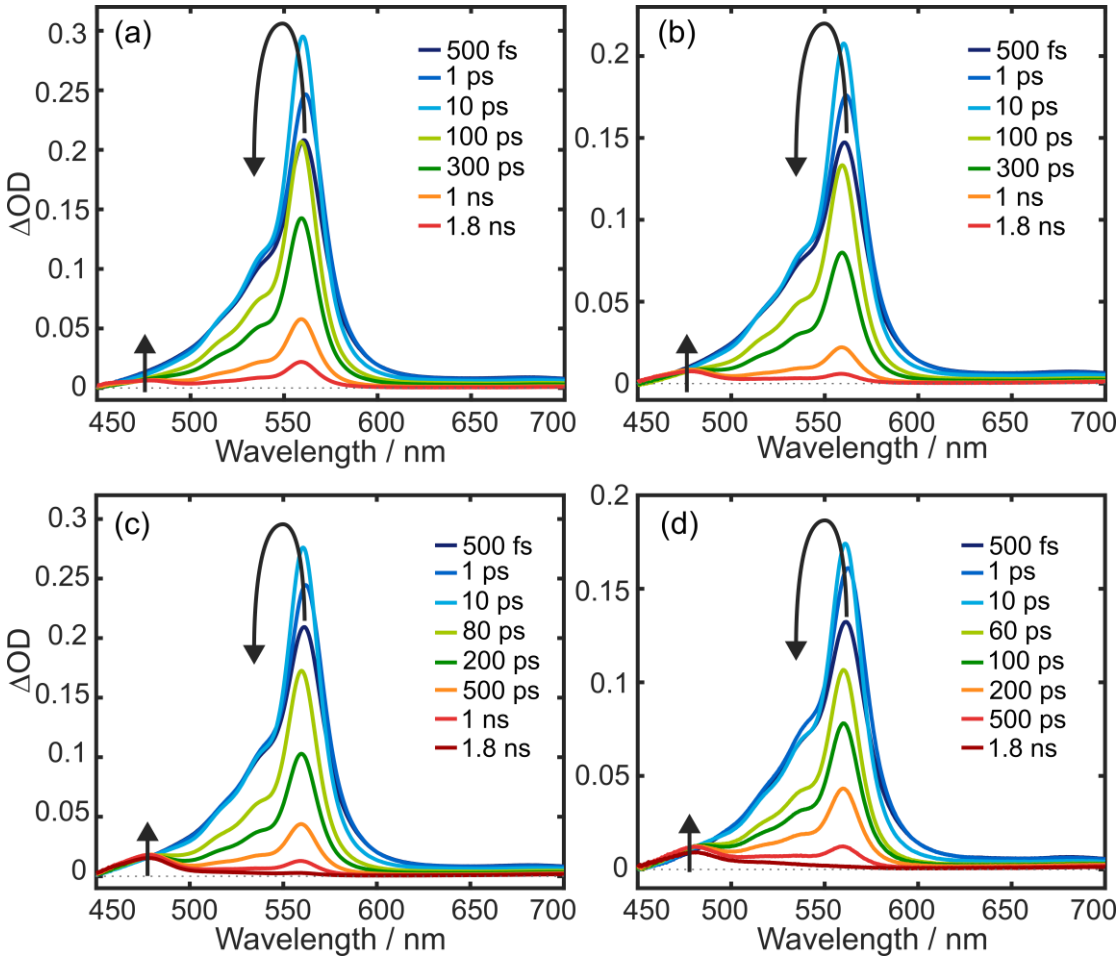

Figure 3.10. Visible TA spectra in ethanol solutions of (a) pTP:DCHMA 0.5:50 mM, (b) pTP:DCHMA 0.5:125 mM, (c) pTP:DCHMA 0.5:250 mM, (d) pTP:DCHMA 0.5:500 mM mixtures. The arrows indicate the evolution of the parent ESA signal. Note that for these data the intensity scale is in ΔOD and not in ΔmOD.

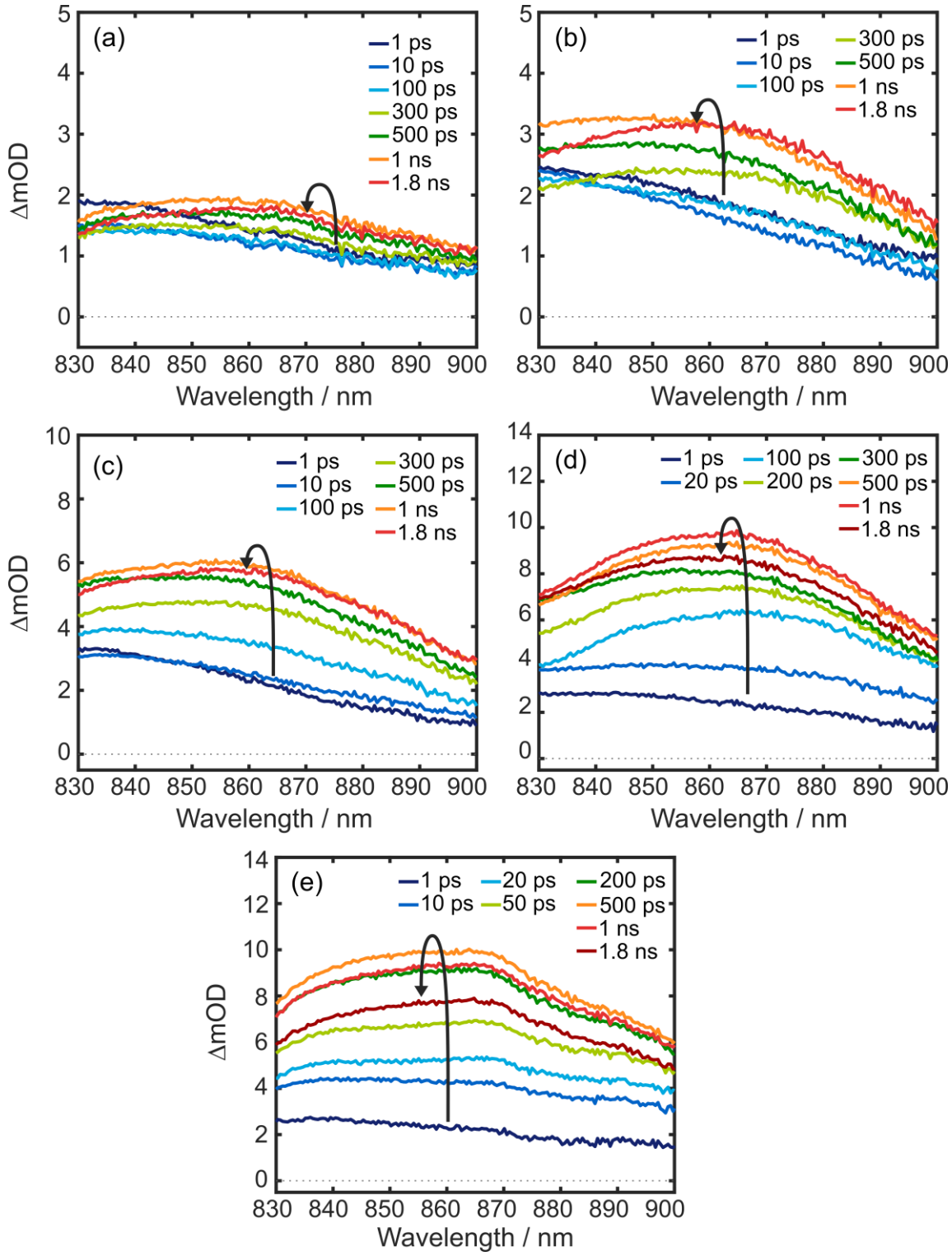

Figure 3.11. Visible TA spectra in ethanol solutions of (a) pTP 0.7 mM, (b) pTP:DCHMA 0.5:50 mM, (c) pTP:DCHMA 0.5:250 mM, (d) pTP:DCHMA 0.5:500 mM. Note only for this case the intensity scale is in ΔOD and not in ΔmOD. The arrows follow the rise and decay of parent signal evolves in time and the rise of photoproducts signal.

Near-infrared TA data for pTP:DCHMA mixtures are shown in Figure 3.11. Addition of DCHMA to pTP solutions changes the TA response, with a new band present at ~860 nm and associated with the formation of radical anion pTP species.[35] The photoproduct is long-lived and persists beyond the longest TA delay studied (Figure 3.11(a-c)). Notably, at high concentrations of DCHMA, a decay of the photoproduct signal is observed (see arrows in Figure 3.11): the higher the DCHMA concentration, the more probable a pTP–DCHMA encounter event, and the faster the rise of the $pTP^{\bullet -}$ transient. Together with the observation that photoproduct features are not already present at time-zero, it is evident the rate-determining step of the reaction is the reactants encounter, *i.e.*, the reaction is diffusion-limited. Finally, from a cursory analysis of the TA spectra, the $pTP^{\bullet -}$ rise in the near-infrared is matched by the parent decay in the visible.

As for pTP, the visible TA ESA kinetics of the mixtures around 560/565 nm were extracted by integrating the signal in the 557–563 nm region (Figure 3.12(a)) and normalised. After the initial ~10 ps rise in pTP signal independent on DCHMA concentration (inset of Figure 3.12(a)), the signal decays more rapidly in the presence of the electron donor species with a timescale of 100 to 1000 ps.

For the near-infrared data, the residual contribution due to pTP dynamics was removed via a Gaussian basis set deconvolution procedure.[40] At each pump-probe time delay the near-infrared TA spectra of pTP signal (Figure 3.8) was fitted to one Gaussian distribution with floating width, amplitude and centroid, recovering the envelope of the transient response (see Figure 3.13 in the Appendix for example traces). Subsequently, the pTP Gaussian basis set was used to model the residual pTP signal of each pTP–DCHMA mixture (Figure 3.11), allowing only the amplitude associated to pTP* decay to float. The photoproduct, $pTP^{\bullet -}$, was modelled by the sum of two Gaussians distributions (see Figure 3.14 in the Appendix for example traces). Once the photoproduct signal had been isolated, the kinetics of photoproduct formation and decay at 865 nm were extracted as for the visible ESA, integrating the signal in the 860–870 nm region (Figure 3.12(b)). The near-infrared kinetics showed even more clearly what has already been qualitatively discussed on the spectra: the timescale of $pTP^{\bullet -}$ signal rise varies greatly with DCHMA concentration and photoproduct peak is anticipated at high DCHMA concentrations (250 and 500 mM, orange and red traces in Figure 3.12(b), respectively).

For visible TA data at 560 nm (Figure 3.12(a)), the signal originated from the photoexcited parent molecule. The kinetics of pTP–DCHMA mixtures in the visible were initially modelled using a similar approach to pTP alone (see Section 3.3.2). The initial growing component and the short-time decay had similar lifetimes to those found for pTP only in ethanol (as determined in Section 3.3.2), whilst the long-time decay was altered by the presence of DCHMA, again indicating diffusion played a role for this deactivation channel.

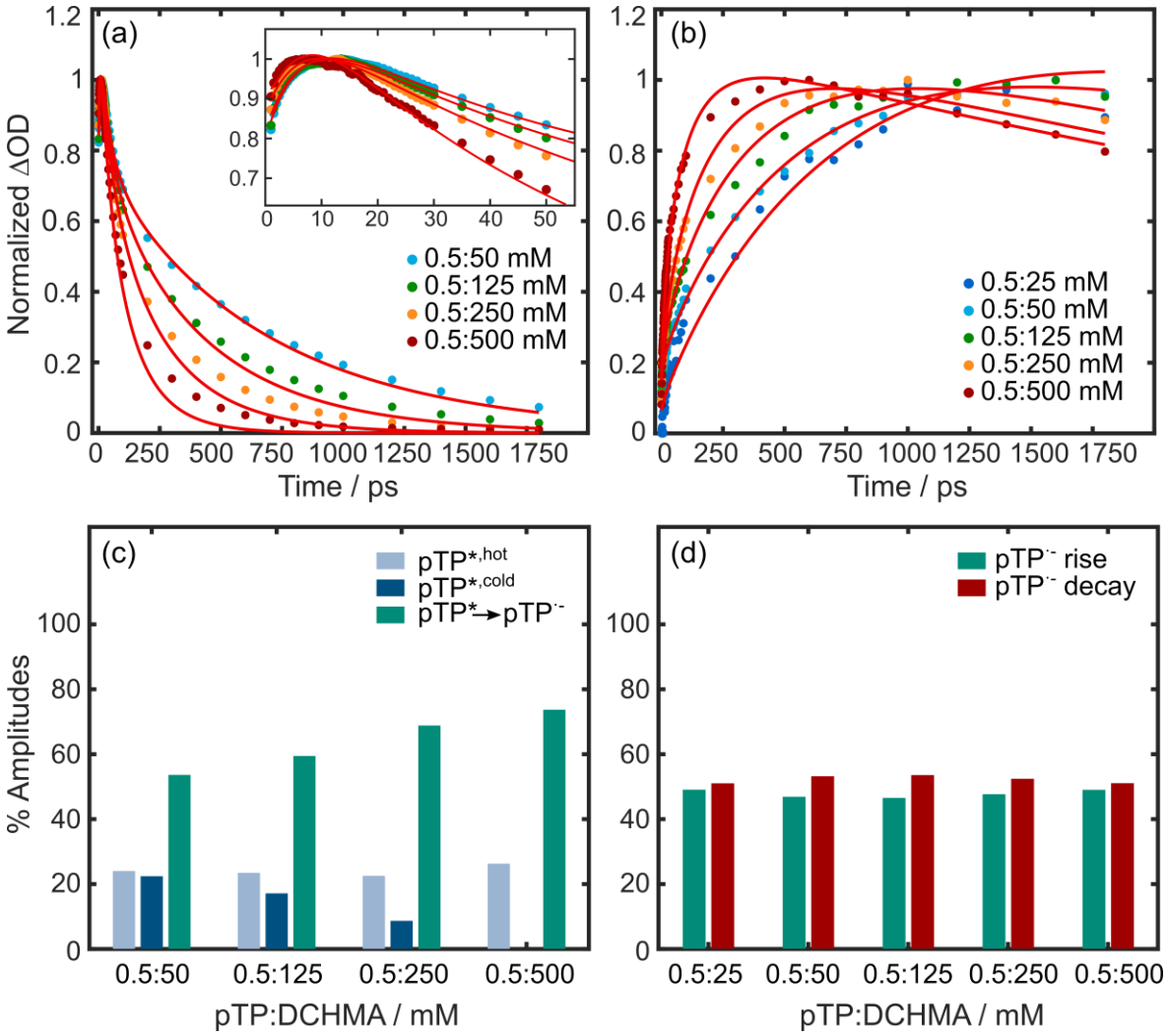

Figure 3.12. Analysis of TA data in ethanol. Normalized integrated signal of (a) the ESA band centered at 560 nm in the visible TA data (Figure 3.10) and (b) of the photoproduct band centered at 865 nm in the near-infrared TA data (Figure 3.11) for the specified pTP:DCHMA ratios, and fit to the data (red lines). Any contributions from pTP signal in the near-infrared TA kinetics was removed via a gaussian basis set deconvolution. Relative amplitudes of the fitting components contributing to the observed signal (c) for the visible traces and (d) for the near-infrared traces.

As discussed in Chapter 1, the effects of diffusion on the kinetics of reaction can be quantitatively described with a variety of models.[41–45] For a diffusion-limited reaction with one reactant is in large excess, von Smoluchowski theory can be adapted to include the effects of competitive diffusional processes that contribute to the total intensity, I, of the TA signal.[46,47] This is given by Equation 3.2:

$$I = e^{-c_0 k_D\left(t+\frac{2a\sqrt{t}}{\sqrt{\pi D}}\right)} e^{-k_R t} \tag{3.2}$$

where, c_0 is the initial concentration of the excess reactant, D is the sum of the diffusion coefficients of the two reactants, a is the contact radius – the distance at which the ET event occurs – k_R is the rate constant for any radiative decay competing with diffusion (*e.g.*, k_3 in Equation 3.4). In von Smoluchowski theory the rate of ET reaction is considered to be infinitely faster than diffusion events, making the bimolecular encounter the rate-limiting step. The reaction rate, k_D, that appears in Equation 3.2 is defined:

$$k_D = 4\pi N_A a D \tag{3.3}$$

where N_A is Avogadro's number. Therefore, the visible TA data of pTP–DCHMA were globally fitted to a function of the form:

$$I_{pTP:DCHMA\,(560)} = A_1 e^{-k_1 t} + A_2 e^{-k_2 t} + A_3 e^{-k_3 t - k_D C_0\left(t+\frac{2a\sqrt{t}}{\sqrt{\pi D}}\right)} \tag{3.4}$$

Comparing Equations 3.1 and 3.2 with Equation 3.4 it is clear that the third exponential component has been substituted with an expression that accounts for the diffusion-limited bimolecular ET.

The dynamics of photoproduct in the near-infrared region around 860 nm (Figure 3.12(b)) are similarly modelled. The signal intensity is described by two exponentials with opposite sign:

$$I_{pTP:DCHMA\,(865)} = A_4 e^{-k_3 t - k_D C_0 t\left(1+\frac{2a\sqrt{t}}{\sqrt{\pi D}}\right)} + A_5 e^{-k_4 t} \tag{3.5}$$

In Equation 3.5, $A_4 < 0$ and $A_5 > 0$, and k_4 returns the decay rate of photoproducts. Equations 3.4 and 3.5 were used to globally fit the traces in Figure 3.12(a,b) by fixing the values of k_1, k_2, and k_3 to those determined from the analysis of isolated pTP, and using the values of D determined from DOSY ^{1}H-NMR. The parameters a and k_4 were shared in fitting both near-infrared and visible probe data, while the amplitudes A_i (Figure 3.12(c,d)) were allowed to float. While the lifetime associated with the decay of photoproduct was found to be > 2 ns, so it could not be properly estimated as greater than the investigated time window (~5.6 ns from fitting), the value for the contact radius could be more accurately estimated to be 0.68 ± 0.17 nm. This is comparable to typical values around 0.5 nm.[43] Although the value is large enough not to exclude molecules of ethanol could play a role in mediating the ET, TA data and the diffusional model adopted does not provide any definitive answers regarding the role of solvent. Finally, knowledge on the contact radius allowed for an estimation of the diffusional rate constant k_D of 7.80 (± 1.99) ×10^9 $M^{-1}s^{-1}$. This is the same order of magnitude to previously reported ET reactions of other chemical systems.[43,48,49] A summary of the results of the von Smoluchowski analysis is reported in Table 3.2.

Table 3.2. Summary of fitting output from the modelling of pTP photodynamics and diffusion–limited ET in pTP–DCHMA mixtures.

Process	Timescale / ps	TA region
$pTP^{*,hot} \rightarrow pTP^*$	5.7 ± 0.7	visible
pTP–solvent *post* nuclei rearrangement	41.1 ± 11.7	visible
pTP fluorescence	1140 ± 40	visible
$pTP^{\bullet -}\cdots DCHMA^{\bullet +}$ decay	> 2000 (~5600)	near-IR
ET parameters		
contact radius a / nm	0.68 ± 0.17	
reaction rate k_D / 10^9 $M^{-1}s^{-1}$	7.80 ± 1.99	

The choice of modelling the decrease in signal associated to $pTP^{\bullet -}\cdots DCHMA^{\bullet +}$ with a simple exponentially decaying function is dictated by the experimental limitation of the investigated time window in TA. Therefore, it is not possible to assign this channel to a specific reactive step.

The relative contribution of all the pathways to the fate of the pTP–DCHMA system is given by the amplitudes of the different channels associated with Equations 3.4 and 3.5 and summarized by the bar plots in Figure 3.12(c,d). For visible TA data, the amplitude associated with visible ESA rise is constant for the different pTP:DCHMA ratios (light blue bars in Figure 3.12(c)); this is unsurprising, as the rise in pTP signal is independent of the ET event. In contrast, the DCHMA concentration alters the relative amplitudes associated with pTP decay and ET, the latter increasing at the expenses of the former whilst the number of ET-donor molecules is increased (dark blue and green bars in Figure 3.12(c)). At a DCHMA concentration of 500 mM, the signal decay is completely due to ET, identifying a regime where, in principle, the bimolecular reaction is the most effective. For the near-infrared TA traces, the amplitude associated to signal rise caused by diffusion-limited ET and the amplitude of the photoproduct decaying component in turn dependent on the ET maintain the same relative proportion (Figure 3.12(d)). This is consistent with a model comprised of steps sequential to one another, where the peak of the signal in the kinetics is governed by the DCHMA concentration, as expressed in Equation 3.5.

3.4. Conclusions

This study focussed on the photodynamics of a diffusion–limited ET reaction in a chemical system comprised from *para*-terphenyl and *N*,*N*-dicyclohexylmethylamine, relevant in carbon dioxide activation and direct utilization.[23,24] The excited state dynamics of pTP has been thoroughly investigated by means of TA spectroscopy, probing the different relaxation dynamics in ethanol, as a prototypical protic and polar solvent. It was found pTP* signal has a rise component of 5.7 ps, associated to geometric reorganisation onto the S_1 PES, and decays biexponentially, either dissipating energy via pTP–solvent coupling in 41 ps *post* nuclei rearrangement, or in the nanosecond regime via fluorescence. Addition of DCHMA influences the photodynamics of pTP by providing a new deactivation pathway. Diffusion–limited ET at the expense of DCHMA reduces pTP to its radical anion as evident from several spectral signatures and near-infrared probe region dynamics, a necessary prerequisite for carbon dioxide activation. The results of the diffusional analysis of the data in the Smoluchowski model, returned a rate constant for the ET of 7.80 (± 1.99) $\times 10^9$ $M^{-1}s^{-1}$. Ethanol was suggested to be able to mediate the ET step, contact radius of ET in the

solvent being 0.68 nm, with the effect of reducing the amount of un-reactive encounters between pTP* and DCHMA. These findings provide a fundamental basis for rational design of pTP–amine systems adopted to perform CO_2 activation and a direct, unequivocal proof of early step mechanism proposed by Seo *et al.*[23]: as a general indication a protic solvent as ethanol seems proficient in generating the radical anion $pTP^{\bullet -}$.

References

(1) M. D. Kärkäs, J. A. Porco, C. R. J. Stephenson. Photochemical Approaches to Complex Chemotypes: Applications in Natural Product Synthesis. *Chem. Rev.* **2016**, *116* (17), 9683–9747.

(2) N. J. Turro. Fun with Photons, Reactive Intermediates, and Friends. Skating on the Edge of the Paradigms of Physical Organic Chemistry, Organic Supramolecular Photochemistry, and Spin Chemistry. *J. Org. Chem.* **2011**, *76* (24), 9863–9890.

(3) T. Bach, J. P. Hehn. Photochemical Reactions as Key Steps in Natural Product Synthesis. *Angew. Chem. Int. Ed.* **2011**, *50* (5), 1000–1045.

(4) N. Hoffmann. Photochemical Reactions as Key Steps in Organic Synthesis. *Chem. Rev.* **2008**, *108* (3), 1052–1103.

(5) M. H. Shaw, J. Twilton, D. W. C. MacMillan. Photoredox Catalysis in Organic Chemistry. *J. Org. Chem.* **2016**, *81* (16), 6898–6926.

(6) J. Twilton, C. Le, P. Zhang, M. H. Shaw, R. W. Evans, D. W. C. MacMillan. The Merger of Transition Metal and Photocatalysis. *Nat. Rev. Chem.* **2017**, *1* (7), 1–18.

(7) N. A. Romero, D. A. Nicewicz. Organic Photoredox Catalysis. *Chem. Rev.* **2016**, *116* (17), 10075–10166.

(8) A. Vega-Peñaloza, J. Mateos, X. Companyó, M. Escudero-Casao, L. Dell'Amico. A Rational Approach to Organo-Photocatalysis: Novel Designs and Structure-Property Relationships. *Angew. Chem. Ed.* **2021**, *60* (3), 1082–1097.

(9) C. K. Prier, D. A. Rankic, D. W. C. MacMillan. Visible Light Photoredox Catalysis with Transition Metal Complexes: Applications in Organic Synthesis. *Chem. Rev.* **2013**, *113* (7), 5322–5363.

(10) A. Bhattacherjee, M. Sneha, L. Lewis-Borrell, G. Amoruso, T. A. A. Oliver, J. Tyler, I. P. Clark, A. J. Orr-Ewing. Singlet and Triplet Contributions to the Excited-State Activities of Dihydrophenazine, Phenoxazine, and Phenothiazine Organocatalysts Used in Atom Transfer Radical Polymerization. *J. Am. Chem. Soc.* **2021**, *143* (9), 3613–3627.

(11) Y. Du, R. M. Pearson, C. H. Lim, S. M. Sartor, M. D. Ryan, H. Yang, N. H. Damrauer, G. M. Miyake. Strongly Reducing, Visible-Light Organic Photoredox Catalysts as Sustainable Alternatives to Precious Metals. *Chem. A Eur. J.* **2017**, *23* (46), 10962–10968.

(12) M. Reckenthäler, A. G. Griesbeck. Photoredox Catalysis for Organic Syntheses. *Adv. Synth. Catal.* **2013**, *355* (14–15), 2727–2744.

(13) D. M. Arias-Rotondo, J. K. McCusker. The Photophysics of Photoredox Catalysis: A Roadmap for Catalyst Design. *Chem. Soc. Rev.* **2016**, *45* (21), 5803–5820.

(14) A. J. Orr-Ewing. Perspective: How Can Ultrafast Laser Spectroscopy Inform the Design of New Organic Photoredox Catalysts for Chemical and Materials Synthesis? *Struct. Dyn.* **2019**, *6* (1), 010901.

(15) L. Buzzetti, G. E. M. Crisenza, P. Melchiorre. Mechanistic Studies in Photocatalysis. *Angew. Chem. Ed.* **2019**, *58* (12), 3730–3747.

(16) S. M. Sartor, B. G. McCarthy, R. M. Pearson, G. M. Miyake, N. H. Damrauer. Exploiting

Charge-Transfer States for Maximizing Intersystem Crossing Yields in Organic Photoredox Catalysts. *J. Am. Chem. Soc.* **2018**, *140* (14), 4778–4781.

(17) S. P. Pitre, C. D. McTiernan, J. C. Scaiano. Understanding the Kinetics and Spectroscopy of Photoredox Catalysis and Transition-Metal-Free Alternatives. *Acc. Chem. Res.* **2016**, *49* (6), 1320–1330.

(18) M. Majek, A. Jacobi Von Wangelin. Mechanistic Perspectives on Organic Photoredox Catalysis for Aromatic Substitutions. *Acc. Chem. Res.* **2016**, *49* (10), 2316–2327.

(19) S. Jockusch, Y. Yagci. The Active Role of Excited States of Phenothiazines in Photoinduced Metal Free Atom Transfer Radical Polymerization: Singlet or Triplet Excited States? *Polym. Chem.* **2016**, *7* (39), 6039–6043.

(20) B. G. McCarthy, R. M. Pearson, C. H. Lim, S. M. Sartor, N. H. Damrauer, G. M. Miyake. Structure-Property Relationships for Tailoring Phenoxazines as Reducing Photoredox Catalysts. *J. Am. Chem. Soc.* **2018**, *140* (15), 5088–5101.

(21) M. Olivucci, F. Santoro. Chemical Selectivity through Control of Excited-State Dynamics. *Angew. Chem. Ed.* **2008**, *47* (34), 6322–6325.

(22) H. Takeda, O. Ishitani. Development of Efficient Photocatalytic Systems for CO_2 Reduction Using Mononuclear and Multinuclear Metal Complexes Based on Mechanistic Studies. *Coord. Chem. Rev.* **2010**, *254* (3–4), 346–354.

(23) H. Seo, A. Liu, T. F. Jamison. Direct β-Selective Hydrocarboxylation of Styrenes with CO_2 Enabled by Continuous Flow Photoredox Catalysis. *J. Am. Chem. Soc.* **2017**, *139* (40), 13969–13972.

(24) H. Seo, M. H. Katcher, T. F. Jamison. Photoredox Activation of Carbon Dioxide for Amino Acid Synthesis in Continuous Flow. *Nat. Chem.* **2017**, *9* (5), 453–456.

(25) Y. Masuda, N. Ishida, M. Murakami. Light-Driven Carboxylation of o-Alkylphenyl Ketones with CO_2. *J. Am. Chem. Soc.* **2015**, *137* (44), 14063–14066.

(26) A. Cherubini-Celli, J. Mateos, M. Bonchio, L. Dell'Amico, X. Companyó. Transition Metal-Free CO_2 Fixation into New Carbon–Carbon Bonds. *ChemSusChem* **2018**, *11* (18), 3056–3070.

(27) H. Seo, A. Liu, T. F. Jamison. Direct β-Selective Hydrocarboxylation of Styrenes with CO_2 Enabled by Continuous Flow Photoredox Catalysis. *J. Am. Chem. Soc.* **2017**, *139* (40), 13969–13972.

(28) K. L. Liu, Y. T. Chen, H. H. Lin, C. S. Hsu, H. W. Chang, I. C. Chen. Dynamics of the Excited States of p-Terphenyl and Tetracene: Solute-Solvent Interaction. *J. Phys. Chem. C* **2011**, *115* (45), 22578–22586.

(29) J. R. Lakowicz. *Principles of Fluorescence Spectroscopy*. Springer US: Boston, MA, 2006.

(30) G. Heimel, M. Daghofer, J. Gierschner, E. J. W. List, A. C. Grimsdale, K. Müllen, D. Beljonne, J.-L. Brédas, E. Zojer. Breakdown of the Mirror Image Symmetry in the Optical Absorption/Emission Spectra of oligo(para-Phenylene)s. *J. Chem. Phys.* **2005**, *122* (5), 054501.

(31) A. J. Bard, L. R. Faulkner. *Eelctrochemical Methods: Fundamentals and Applications*. Wiley: New York, NY, 2001.

(32) M. Holz, X. A. Mao, D. Seiferling, A. Sacco. Experimental Study of Dynamic Isotope Effects in Molecular Liquids: Detection of Translation-Rotation Coupling. *J. Chem. Phys.* **1996**, *104* (2), 669–679.

(33) E. V. Anslyn, D. A. Dougherty. *Modern Physical Organic Chemistry*; University Science Books, 2005.

(34) A. Sakamoto, T. Harada, N. Tonegawa. A New Approach to the Spectral Study of Unstable Radicals and Ions in Solution by the Use of an Inert Gas Glovebox System: Observation and Analysis of the Infrared Spectra of the Radical Anion and Dianion of p-Terphenyl. *J. Phys. Chem. A* **2008**, *112* (6), 1180–1187.

(35) X. Cai, M. Sakamoto, M. Hara, S. Tojo, K. Kawai, M. Endo, M. Fujitsuka, T. Majima. Transient Phenomena of Polyphenyls in the Higher Triplet Excited State. *J. Phys. Chem. A* **2004**, *108* (43), 9361–9364.

(36) E. Morikawa, K. Shikichi, R. Katoh, M. Kotani. Transient Photoabsorption by Singlet Excitons in p-Terphenyl Single Crystals. **1986**, *13* (3), 209–212.
(37) N. Ikeda, M. Koshioka, H. Masuhara, K. Yoshihara. Picosecond Dynamics of Excited Singlet States in Organic Microcrystals: Diffuse Reflectance Laser Photolysis Study. *Chem. Phys. Lett.* **1988**, *150* (6), 452–456.
(38) O. Braem, T. J. Penfold, A. Cannizzo, M. Chergui. A Femtosecond Fluorescence Study of Vibrational Relaxation and Cooling Dynamics of UV Dyes. *Phys. Chem. Chem. Phys.* **2012**, *14* (10), 3513–3519.
(39) K. Iwata, H. Hamaguchi. Picosecond Time-Resolved Raman Spectroscopy of S_1 p-Terphenyl and p-Terphenyl-d_{14} in Solution: Time-Dependent Changes of Raman Band Shapes. *J. Raman Spectrosc.* **1994**, *25* (7–8), 615–621.
(40) M. P. Grubb, A. J. Orr-Ewing, M. N. R. Ashfold. KOALA: A Program for the Processing and Decomposition of Transient Spectra. *Rev. Sci. Instrum.* **2014**, *85* (6), 064104.
(41) F. C. Collins, G. E. Kimball. Diffusion-Controlled Reaction Rates. *J. Colloid Sci.* **1949**, *4* (4), 425–437.
(42) G. Angulo, A. Rosspeintner. Bimolecular Photo-Induced Electron Transfer Enlightened by Diffusion. *J. Chem. Phys.* **2020**, *153* (4), 040902.
(43) C. F. Shannon, D. D. Eads. Diffusion-Controlled Electron Transfer Reactions: Subpicosecond Fluorescence Measurements of Coumarin 1 Quenched by Aniline and N,N-Dimethylaniline. *J. Chem. Phys.* **1995**, *103* (13), 5208–5223.
(44) A. Rosspeintner, E. Vauthey. Bimolecular Photoinduced Electron Transfer Reactions in Liquids under the Gaze of Ultrafast Spectroscopy. *Phys. Chem. Chem. Phys.* **2014**, *16* (47), 25741–25754.
(45) J. S. Beckwith, B. Lang, J. Grilj, E. Vauthey. Ion-Pair Dynamics upon Photoinduced Electron Transfer Monitored by Pump-Pump-Probe Spectroscopy. *J. Phys. Chem. Lett.* **2019**, *10* (13), 3688–3693.
(46) M. v. Smoluchowski. Drei Vorträge Über Diffusion, Brownsche Molekularbewegung Und Koagulation von Kolloidteilchen. *Phys. Z.* **1916**, *17*, 530–594.
(47) M. v. Smoluchowski. Grundriß Der Koagulationskinetik Kolloider Lösungen. *Kolloid-Zeitschrift* **1917**, *21* (3), 98–104.
(48) M. Rini, D. Pines, B. Z. Magnes, E. Pines, E. T. J. Nibbering. Bimodal Proton Transfer in Acid-Base Reactions in Water. *J. Chem. Phys.* **2004**, *121* (19), 9593–9610.
(49) R. C. Dorfman, M. D. Fayer. The Influence of Diffusion on Photoinduced Electron Transfer and Geminate Recombination. *J. Chem. Phys.* **1992**, *96* (10), 7410–7422.

3.5. Appendix

3.5.1. Gaussian Basis Set Deconvolution

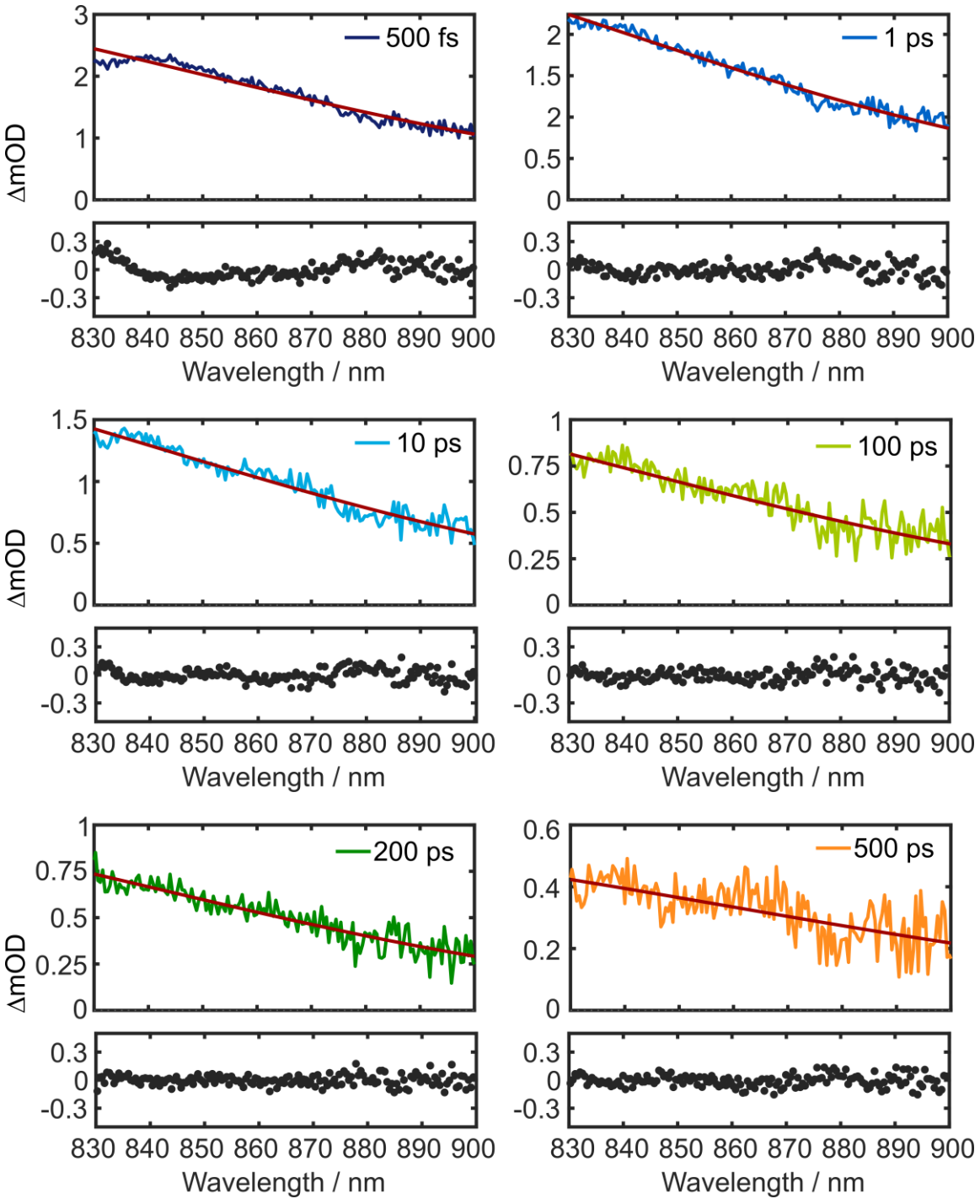

Figure 3.13. Gaussian basis set modelling of pTP near-infrared TA signal for six pump-probe time delays representative of the investigated timescales. The pTP signal (solid red lines) was modelled with one Gaussian function, allowing to float its amplitude, width and centroid. Each panel includes the residuals of the fitting.

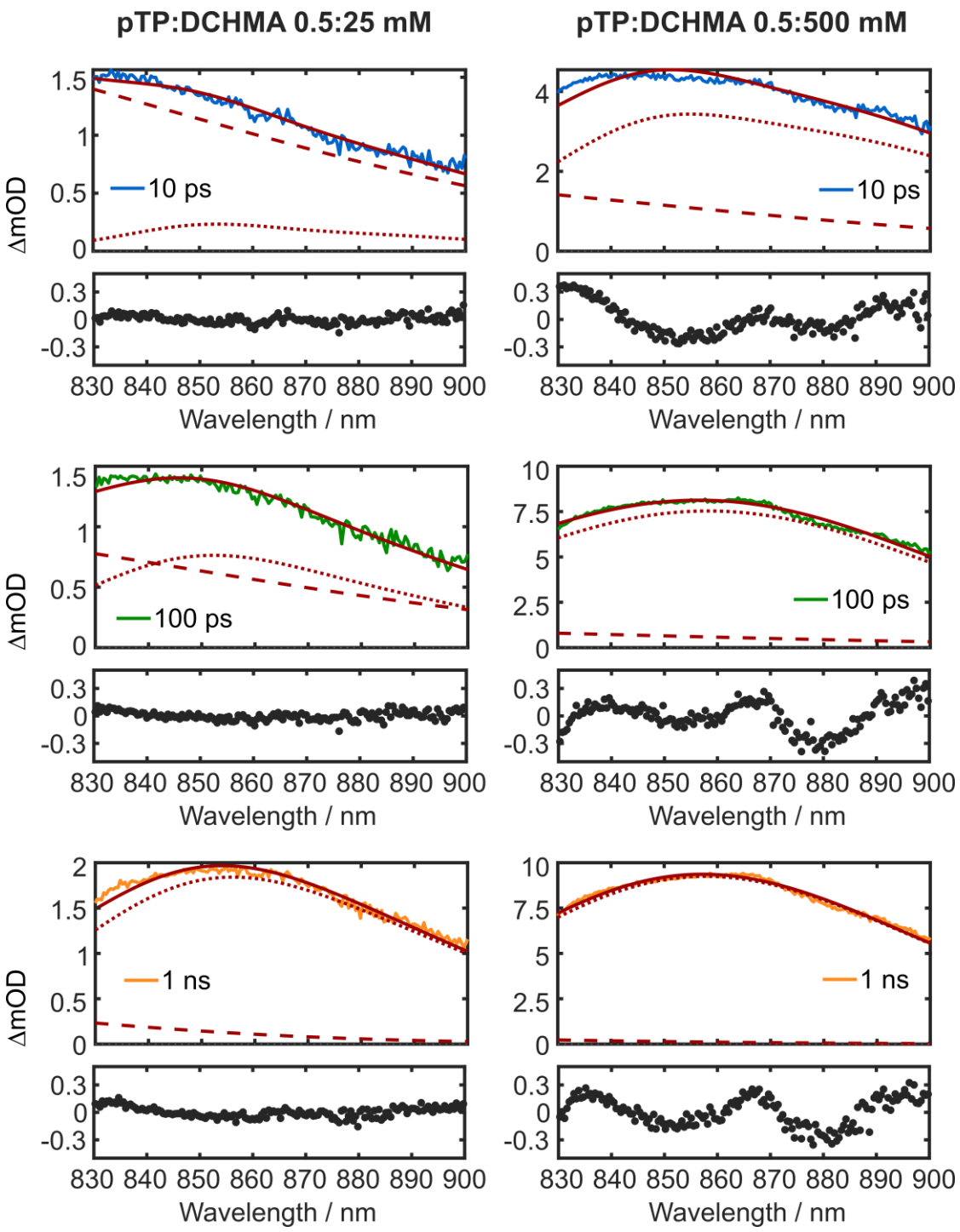

Figure 3.14. Gaussian basis set deconvolution of pTP near-infrared TA data for stated mixtures. Three pump-probe time delays representative of the investigated timescales are shown for the pTP:DCHMA 0.5:0.25 mM mixture (lowest DCHMA concentration, left column) and for the pTP:DCHMA 0.5:0.500 mM mixture (highest DCHMA concentration, right column). The pTP signal (dashed red lines) was modelled with the Gaussian basis set shown in Figure 3.13 and the width, amplitude and centroid were allowed to float. The photoproduct signal (dotted red lines) was modelled with a sum of two Gaussian functions. The pTP signal and the photoproduct signal were then summed to obtain the total mixture signal (solid red lines). Only the modelled photoproduct signal was retained to extract the kinetics at ~860 nm shown in Figure 3.12(b). Each panel includes the residuals of the fitting.

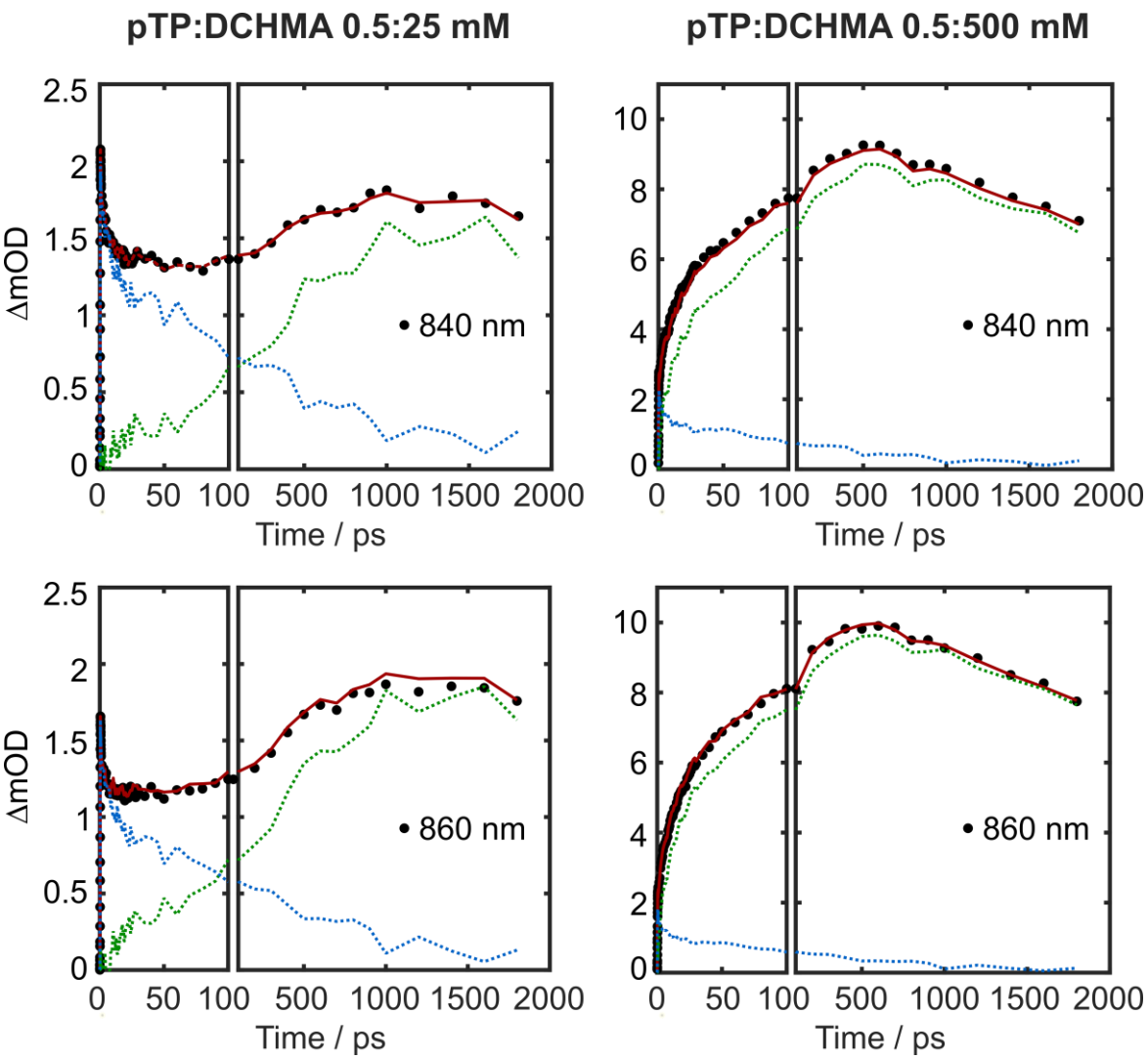

Figure 3.15. Kinetics of near-infrared TA data and of the Gaussian basis set deconvolution model at two representative probe wavelengths, 840 nm and 860 nm, for the pTP:DCHMA 0.5:0.25 mM mixture (lowest DCHMA concentration, left column) and for the pTP:DCHMA 0.5:0.500 mM mixture (highest DCHMA concentration, right column). In each plot, the deconvoluted pTP trace (blue dotted lines) and the deconvoluted photoproduct trace (green dotted lines) sums up to the total kinetic trace (red solid lines), that satisfactorily models the TA data (dots). Note that for the two stated pTP:DCHMA ratios, data are plotted on different ΔmOD axes.

4. Excitation Energy Transfer in Biohybrid Quantum Dot–Bacterial Reaction Centre Nanoconjugates

The results, data and discussions presented in this chapter have been published. The reader can refer to: G. Amoruso, J. Liu, D. W. Polak, K. Tiwari, M. R. Jones, T. A. A. Oliver. High Efficiency Excitation Energy Transfer in Biohybrid Quantum Dot–Bacterial Reaction Center Nanoconjugates. *The Journal of Physical Chemistry Letters*, **2021**, *12*, (23), 5448–5455.

I declare that: I designed, grew, purified and characterized the biological samples in collaboration with Dr. Kavita Tiwari and Dr. Michael R. Jones; I collected and analysed the data; I wrote the manuscript in discussion with Dr. Michael R. Jones and my supervisor Dr. Thomas A. A. Oliver.

4.1. Introduction

Purple bacteria such as *Rhodobacter (Rba.) sphaeroides* are among the simplest organisms capable of photosynthesis. These bacteria inhabit aquatic environments where they use pigment-protein complexes to absorb spectrally-filtered sunlight to power growth and reproduction.[1,2] To avoid competing with chlorophyll-containing oxygenic phototrophs, bacteria such as *Rba. sphaeroides* capture primarily near-infrared and blue/near-ultraviolet solar wavelengths using bacteriochlorophyll and carotenoid pigments.[1,2] In reaction center-light harvesting 1 (RC–LH1) complexes, a central RC electron transfer (ET) protein is encircled by an LH1 light harvesting pigment-protein. These RC–LH1 complexes are in turn surrounded in the membrane by peripheral LH2 light harvesting complexes.[3–5] Through sequential ultrafast electronic energy transfer (EET) steps, the initially-formed excited electronic state of LH2 or LH1 pigments is funneled to a RC where the excitation energy is used to drive rapid and efficient charge separation. The quantum yield of EET is very high because energy migration to the RC is fast (tens of picoseconds) compared to the excited state lifetime of bacteriochlorophyll (a few nanoseconds).[1,2] RCs perform the crucial energy transduction and stabilization processes of photosynthesis with a quantum yield that is near unity,[6] efficiently separating charge between a pair of bacteriochlorophylls on one side of the membrane that act as the primary electron donor (termed P), and a ubiquinone on the opposite side (see Figure 4.1(a)).[7–9]

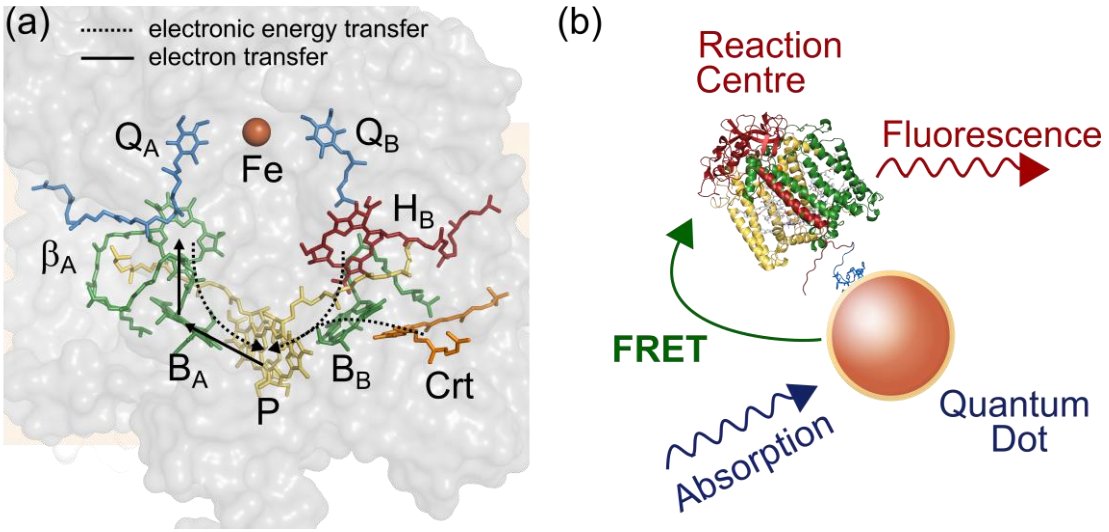

Figure 4.1. (a) Structural model of the 3Hβ RC protein (gray) highlighting the arrangement of light absorbing pigments (colored). One of the 3Hβ mutations substitutes the native A-branch bacteriopheophytin (H_A) with a bacteriochlorophyll (labelled β_A). Two different EET pathways are expected on the two sides of the RC (dashed arrows). For the B-branch (right) EET occurs between the bacteriopheophytin (H_B) or the 15 *cis-cis'* spheroidenone carotenoid (Crt) to a monomeric bacteriochlorophyll (B_B), and thence to the special pair of bacteriochlorophylls (P). Alternatively, on the A-branch (left) the EET path is from bacteriochlorophyll b_A to bacteriochlorophyll B_A, and then on to P. In the WT RC, formation of the excited singlet state of P (P*) triggers charge separation to sequentially form the radical pairs $P^+B_A^-$, $P^+H_A^-$and $P^+Q_A^-$. It is anticipated in the 3Hβ RC only a very minor percent (< 1%) undergo charge separation to form a mixed $P^+(B_A\beta_A)^-$ radical pair. (b) Schematic representation of QD-RC nanoconjugates and the energy pathways for collection, transfer, and re-emission of light.

These very high quantum efficiencies make RCs and RC–LH1 complexes attractive components for alternative solar energy conversion technologies employing environmentally-benign materials.[10] However, their limited capacity to harvest sunlight across much of the visible region of the available solar spectrum has obvious consequences for their performance in biohybrid photodevices, with relatively low external quantum efficiencies of photocurrent generation across green and red wavelengths in particular.[10–17] In addition, although highly efficient solar energy harvesting in specialized wavelength niches may be advantageous to a photosynthetic bacterium in a natural, relatively low-light habitat, the high concentrations of photo-protein required to achieve a substantive photocurrent in a biohybrid device mean that light harvesting is often saturated at these specific wavelengths where absorbance from natural pigmentation is very strong. As an illustration, the very strong absorbance band of the light harvesting bacteriochlorophylls of the RC–LH1 complex is often under-represented in action spectra of external quantum efficiency for bio-photoelectrochemical devices based on this protein.[10,13–17] One way to

address these drawbacks is to conjugate RC or RC–LH1 complexes with a non-native light harvesting system such as a synthetic quantum dot (QD),[18–24] a synthetic dye,[25–28] or a protein with complementary pigmentation.[29,30] This enables enhanced light collection over parts of the electromagnetic spectrum where the absorbance of the native RC or RC–LH1 pigmentation is weak.

Recently, J. Liu and co-workers in Prof. Michael R. Jones group (School of Biochemistry, University of Bristol) characterized a biohybrid nanoconjugate in which *Rba. sphaeroides* RCs engineered with a poly-histidine tag were tethered to the surface of water-soluble CdTe QDs (Figure 4.1(b)).[31,32] In these nanoconjugates the QDs served as both an assembly hub and an artificial light harvesting antenna for the RCs. On mixing, the His-tag bound the RCs to the surface of the QD with high affinity. Quenching of QD fluorescence upon increasing the ratio of tethered RCs per QD provided indirect proof of Förster resonance energy transfer (FRET) from the QDs to the attached RCs. As wild-type (WT) RCs are highly efficient at charge-separation, with a fluorescence quantum yield of virtually zero, a second set of nanoconjugates were constructed using a weakly fluorescent RC mutant (VL157R), that was unable to carry out charge separation due to the absence of one of the bacteriochlorophylls that make up the primary electron donor.[31] In this second set, the intensity of RC fluorescence peaking at 801 nm rose as the RC:QD ratio increased, mirroring a progressive decrease in overlapping QD fluorescence at 750 nm and providing further evidence for FRET between the QDs and the bound RCs.[31] A variety of other RC mutants were used in this prior study to explore the effect of changing the overlap integral between QD fluorescence and RC absorption on QD fluorescence quenching.

A key aspect of natural photosynthesis is the very high quantum efficiency of EET even in very extensive antenna systems. One potential way to establish the time scale and efficiency of EET in these synthetic biohybrid nanoconjugates is to use time-correlated single photon counting (TCSPC) spectroscopy.[33] This technique has previously been used to interrogate FRET dynamics between a natural plant light harvesting complex and QD hybrid.[34] However, in previous studies of WT RCs electrostatically bound to QDs it would not have been possible to apply TCSPC to the non-fluorescent WT RC energy acceptor.[18–20] Furthermore, although the VL157R RC mutant used in previous studies is fluorescent with a maximum at 801 nm,[31,35] TCSPC characterization of fluorescence changes at this wavelength caused by EET from associated QDs would be hampered by strongly

overlapping fluorescence from the 750 nm emitting QD donors. The 801 nm fluorescence in VL157R RC is from the retained three monomeric bacteriochlorophylls, this RC having lost the red-shifted absorbance at ~870 nm (and associated very weak fluorescence) from the pair of P bacteriochlorophylls normally present in the WT RC.[35]

To use TCSPC to determine the efficiency of EET in RC–QD nanoconjugates, in this study, a new RC mutant was engineered, 3Hβ (Figure 4.1(a)), that retains a normal long-wavelength primary electron donor but has a drastically-reduced quantum yield for charge separation. This was achieved by combining a triple mutation LL131H + LM160H + FM197H,[36–38] with the so-called 'β-mutation' LM214H.[39,40] The triple mutation adds three hydrogen bonds between the protein scaffold and the two bacteriochlorophylls that make up P, raising its mid-point potential for one electron oxidation by around 260 mV but without markedly affecting its absorption spectrum.[37] This has the effect of raising the free energy associated with the first radical pair formed during charge separation, $P^+B_A^-$, above that of the excited singlet state of P (P*), thus severely slowing primary charge separation (causing a ~50% decrease in quantum yield) and enhancing the fluorescence of P* through an extension of its lifetime from ~3 ps to ~50 ps.[38] The 'β-mutation' replaces the bacteriopheophytin that is the second acceptor during charge separation (H_A) with a bacteriochlorophyll (β_A) (Figure 4.1(a)).[39,40] In isolation this mutation renders the first (B_A) and second (β_A) electron acceptor isoenergetic, enabling formation of an admixture of the $P^+B_A^-$ and $P^+\beta_A^-$ radical pairs. This slows the rate of charge separation by a factor of two and lowers its quantum yield to ~60%. Formation of a mixed $P^+(B_A\beta_A)^-$ state both greatly reduces the probability of further electron transfer to the A branch quinone and strongly promotes the reverse electron transfer reaction to re-form P*.[39,40] In the combined 3Hβ mutant it is expected that the quantum yield of charge-separated species should be drastically lower than for WT RCs, and strongly enhanced P* fluorescence should be observable with a maximum at ~910 nm.[41]

4.2. Experimental Methods

4.2.1. 3Hβ RC Engineering and Nanoconjugate Preparation

The 3Hβ RC has four single point mutations. These are: (i) substitution of leucine at position 131 of the L-polypeptide with histidine (LL131H), (ii) substitution of leucine at the

position 160 of the M-polypeptide with histidine (LM160H), (iii) substitution of phenylalanine at position 197 of the M-polypeptide with histidine (FM197H), and substitution of leucine at position 214 of the M-polypeptide with histidine (LM214H). A RC with changes (i-iii) has been reported previously; each of the three histidines donates a hydrogen bond to a carbonyl group of one of the two bacteriochlorophylls that make up the primary electron donor P.[36,37,42] The fourth mutation causes replacement of the second electron acceptor bacteriopheophytin by a bacteriochlorophyll, and is often referred to as the β-mutation.[39,40] Using the QuickChange procedure (Agilent) the four mutations were introduced sequentially into plasmid pv109, which is a derivative of pUC19 containing a 1901 bp XbaI–BamHI restriction fragment encompassing the RC genes *pufLM* modified to place the protein sequence LALVPRGSSAHHHHHHHHHH at the C-terminus of the M-polypeptide.[43] The modified XbaI–BamHI restriction fragment was then shuttled into plasmid pvLMt,[43] and the resulting derivative expressed in *Rba. sphaeroides* strain DD13.[44] Bacterial growth, cell harvesting and purification of the His_{10}-tagged 3Hβ RCs was as described in detail in previous studies,[43] as was the assembly of nanoconjugates with different RC:QD molar ratios.[31,32] The latter involved mixing of RCs with water-soluble CdTe QDs that were purchased from PlasmaChem GmbH. These had an emission maximum at 750 ± 5 nm and were coated with 3-mercaptopropionic acid, with an average molecular weight of 550 kDa. For the preparation of conjugates in water buffer solution, the QD concentration was kept fixed at 0.66 μM (corresponding to an $OD_{430\ nm}$ ~1) and the RC concentration was varied with the ratios ranging from 1:1 to 10:1 RC;QD, from a minimum of 0.66 μM ($OD_{800\ nm}$ ~0.19) to a maximum of 6.6 μM ($OD_{800\ nm}$ ~1.9), using the approximation that the molar extinction coefficient of the B-band of 3Hβ mutant was the same as wild-type reaction centers (288 $mM^{-1}\ cm^{-1}$).[45]

4.2.2. Transient Absorption Spectroscopy

A schematic of the experimental setup used for TA spectroscopy is reported in Figure 4.2.[46] Part (40%) of the 800 nm fundamental laser output of a 1 W, 1 kHz, Ti:Sapphire amplifier (Coherent, Libra) was divided with a 90:10 beam splitter to generate pump and probe pulses, respectively.

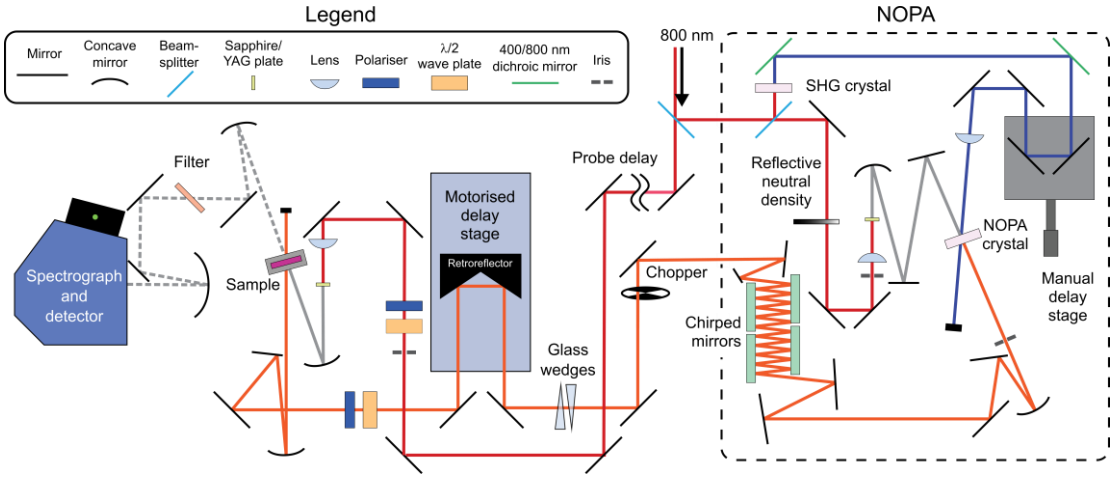

Figure 4.2. Schematic of the setup used to perform visible and near-infrared TA measurements on 3Hβ RCs. Figure adapted from references.[46]

Pump pulses were generated using a non-collinear optical parametric amplifier (NOPA).[47] The 800 nm fundamental used to pump the NOPA was divided into two portions with a 10:90 beam splitter. The low power portion was used to generate the white-light seed pulses, by using a plano-convex lens (f = 5 cm) to focus 800 nm light into a sapphire plate (2 mm, c-cut). Stability and homogeneity of the resulting white-light super-continuum were achieved by controlling the intensity of the 800 nm fundamental with a neutral density wheel and an iris. A plano-concave mirror was used to both re-collimate and focus the white light into the amplification BBO crystal (Eksma Optics, 5.0×5.0×2.0 mm crystal, θ = 31.5°, ϕ = 90°). The high power portion of the 800 nm fundamental used in the NOPA was frequency doubled by second-harmonic generation (SHG) in a BBO crystal to generate 400 nm pump pulses required in the amplification process. After removing residual 800 nm light with dichroic mirrors (CVI, BSR-48-1025), the 400 nm pulses were sent through a manual delay stage to ensure temporal overlap with white-light pulses in the NOPA crystal. The 400 nm pulses were then focused and spatially overlapped into the NOPA BBO crystal using a plano-convex lens (f = 20 cm).

The NOPA was aligned to obtain a ~50 nm broad spectrum (FWHM) centred at 595 nm, as shown in Figure 4.3. This was achieved by iteratively optimizing the spatial and temporal overlap of the white-light seed and the 400 nm pump pulses in the NOPA crystal. The inherit complexity arising from the interplay of all the parameters relevant in optimizing the NOPA resulted in a slightly bimodal spectrum (Figure 4.3) and in spatial inhomogeneity which was minimized by irising the NOPA output prior to collimation.

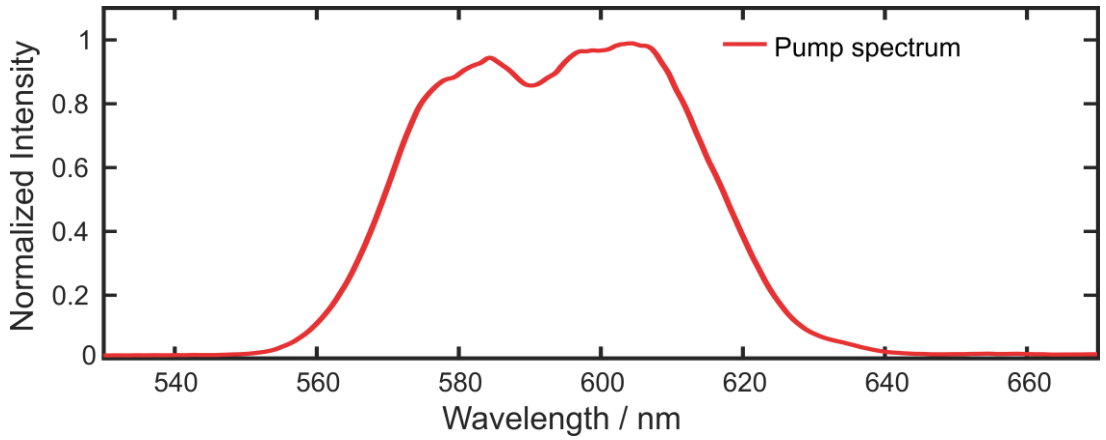

Figure 4.3. Pump spectrum used for TA experiments.

Positive second order group velocity delay (GVD) was compensated with chirped mirrors (Layertech 148545). The number of pairs of bounces on chirped mirrors coarsely controlled the GVD correction. Fine control over the chirp was achieved using thin fused silica wedges (FemtoOptics, Newport) mounted on translational stages. To characterize the pulse duration, polarization gated frequency-resolved optical gating (PG-FROG)[49,50] was used. The pulse-width for TA experiments on 3Hβ RC mutant is displayed in Figure 4.4.

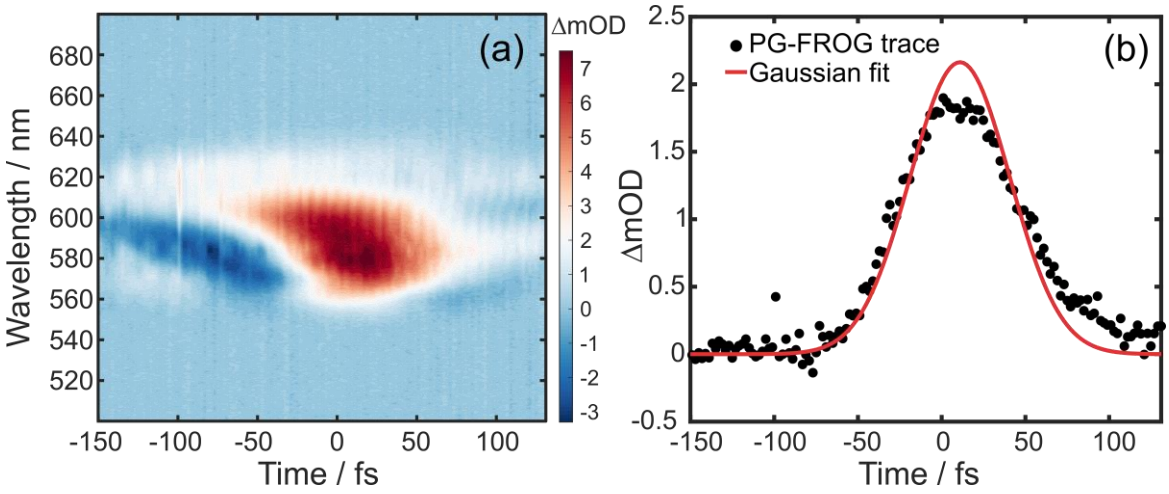

Figure 4.4. (a) PG-FROG trace of NOPA pump pulse, and (b) integrated time-trace (dots) and fit to data (red line).

In the homebuilt PG-FROG apparatus the pulse to be characterized was split into two identical replicas with a 'D'-mirror. Henceforth, one is referred to as the gate, and other as probe pulse. The probe pulse was routed via a short delay stage (Physik Instrumente, M-112.2DG) to control the relative time delay with the gate pulse. The two pulses (polarized

parallel) were then focused and spatially overlapped in a thin piece of fused silica at a tight crossing angle with a plano-concave silver mirror (f = 5 cm). The gate pulse induces a third-order non-linear optical Kerr effect, causing the fused silica to behave as a birefringent material. Therefore, when the two pulses are spatio-temporarily overlapped in the fused silica plate, the substrate acts as a waveplate and slightly rotates the polarization of the probe pulse. By scanning the gate-probe time delay, a time-dependent probe pulse polarization signal can be measured and used to determine the time duration of the original pulse. After passing through the fused silica plate, the probe pulse was collimated and passed through an achromatic polarizer. The polarizer was set orthogonal to the polarization of the unperturbed gate and probe pulses pair. The resulting PG-FROG signal was then focused into a spectrograph (Shamrock 163, Andor) and detected with a linear 1024 element CCD array detector (Entwicklungsbüro Stresing), whilst scanning the time-delay between the two pump pulse replicas. This resulted in a PG-FROG signal (Figure 4.4(b)), which could be averaged over the wavelength axis to extract a time trace (Figure 4.4(c)). The PG-FROG time-trace was then fit to a Gaussian function to estimate the pulse length, which was iteratively minimized to be 59 ± 5 fs.

For TA measurements pump pulses were modulated at 500 Hz with an optical chopper (Thorlabs, MC2000), delayed with respect to the probe via a motorized high precision delay stage (Physik Instrumente, M-531.DG1) with maximum delay of 1.9 ns, focused into the sample to a spot-size of 100 μm diameter using a plano-concave mirror (f = 20 cm). A half-wave plate and a polarizer were used to attenuate the pump fluence to ~16 nJ at the sample to obtain a power density of 2.54 GW cm^{-2}. This pump power ensured minimal multiple-exciton formation and were in line with previous RC TA studies.[48]

Probe pulse generation and TA signal detection and data acquisition were carried out as already described in Section 3.2. Briefly, a portion of the fundamental laser was focused into either a sapphire crystal for a visible detection (450 nm to 700 nm) or a YAG crystal for a near-infrared detection (860 nm to 1100 nm). The probe beam was then focused into the sample, recollimated with the collinear signal, and for visible TA measurements spectrally filtered to remove residual fundamental 800 nm light using a dichroic mirror (Thorlabs, DMSP750B). Finally, the probe and signal were focused into a spectrograph and detector apparatus described in Chapter 3.

The 3Hβ RC samples were freshly prepared and purified prior to TA measurements and diluted to obtain an absorption of 0.34 at 600 nm (1 mm path length). The sample was flowed continuously throughout measurements in a flow cell with a 1 mm path length (Starna, Type 48). TA measurements were performed under the magic angle condition. Time data were acquired using a randomized sequence of delays. Data were collected in blocks of 1000 shots. The statistics of each block were analysed and shots that deviated from the mean by a standard deviation greater than 0.6 were rejected. The retained data were averaged, and the procedure was repeated over 15 cycles for both visible and near-infrared TA measurements.

4.2.3. Time-correlated single photon counting (TCSPC)

Time-correlated single photon counting (TCSPC) measurements were recorded using a homebuilt apparatus, a schematic of the experimental setup is shown in Figure 4.5(a). The 860 nm fundamental laser output of a narrowband high-power Ti:Sapphire oscillator (3.7 W, 80 MHz, Chameleon Ultra II, Coherent) was focused with a plano-convex lens (f = 10 cm) in a 2 mm thick BBO crystal (Eksma Optics, θ = 29.2°) and frequency doubled to 430 nm. After collimation, residual near-IR fundamental light was removed using two dichroic beam splitters (Layertec, Separator 106160). To avoid re-excitation of samples, the repetition rate of the laser pulse train was reduced to 3 MHz using a pulse picker (APE cavity dumper kit).

The pulse picker kit was comprised of a quartz crystal attached to a piezoelectric transducer driven by a high power (17.5 W) radiofrequency generator. Together they act as an acousto-optic modulator (AOM). The propagation of soundwaves in the quartz crystal causes periodic and localised compression/decompression in the crystal lattice, which in turn induce localised periodic changes in the refractive index of the crystal (Figure 4.5(b)). The 430 nm pulse was focussed with a plano-convex lens (f = 7.5 cm) into the quartz crystal.

The speed and the repetition rate of the soundwave propagating in the crystal dictate whether or not at the focal point the soundwave will coincide with the optical pulse and diffract it, at an angle θ_{out} determined by Bragg's law:

$$\theta_{out} \approx \sin\theta_{out} = m\frac{\lambda}{n}\frac{1}{2\Lambda} \qquad (4.1)$$

In Equation 4.1 λ is the wavelength of the incoming pulse, Λ is the radiofrequency of the AOM, n is the refractive index of the crystal and m is an integer that expresses the order of the diffraction; the first order diffraction case is explicitly drawn in Figure 4.5(b). The appropriate choice of the repetition rate of the radiofrequency allowed for the diffraction to occur at the desired repetition rate. The intensity of the first order diffraction was maximized by tuning the crystal position.

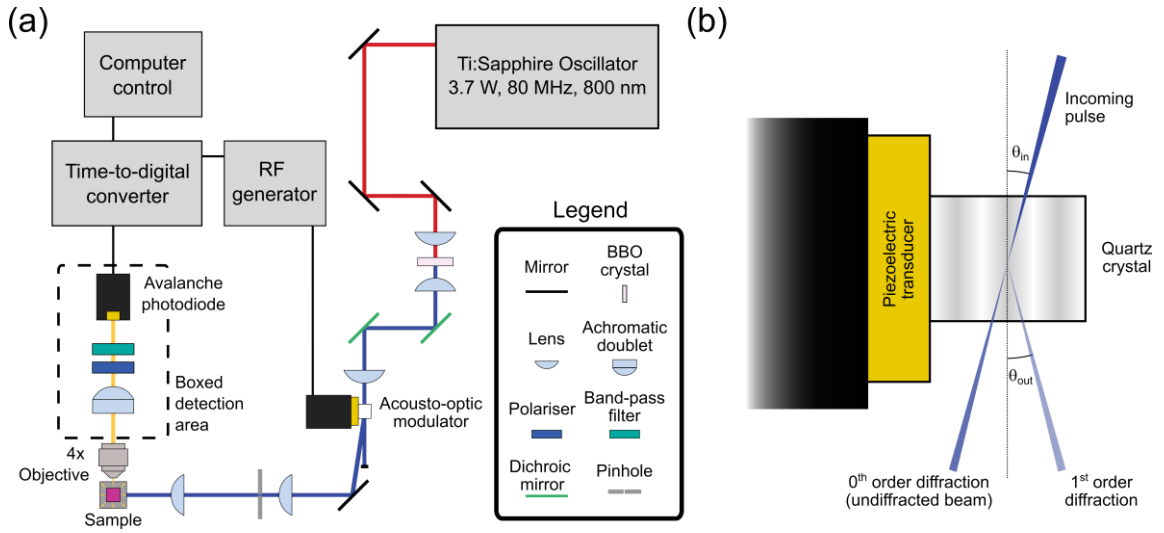

Figure 4.5. (a) Schematic of the TCSPC setup used to investigate the time-resolved fluorescence of 3Hβ RCs, CdTe QDs and QD-RC nanoconjugates and (b) schematic of the diffraction of light pulses by the acoustic waves in the AOM; only the first positive order diffraction (m = 1 in Equation 4.1) is shown, for simplicity.

The diffracted light from the AOM was subsequently collimated and focused through a 10 mm pinhole to remove any of the un-diffracted parent beam (0^{th} order). The laser light (10 mW) was subsequently collimated and focused into the sample with a second lens. Fluorescence was collected from a 1 cm pathlength sample cuvette at 90º relative to the excitation laser with an infinity corrected microscope objective (Nikon, 4×/0.2 NA Plan Apochromat). The fluorescence was filtered to remove any laser scatter and collected at 750 nm (using a 10 nm FWHM bandpass filter; Edmund Optics, 87-889) or at 905 nm (using a 25 nm FWHM bandpass filter; Thorlabs, FL905-25). A polarizer before the detector was set to magic angle relative to the excitation laser to eliminate rotational anisotropy effects. The filtered fluorescence was focused onto an avalanche-photodiode detector (IDQ, ID100-20-REG) with an achromatic doublet lens (Thorlabs, AC508-075-A). The photon counts from the detector were acquired by a time-to-digital converter (Swabian Instruments,

Time Tagger 20). This was synced to the pulse picker, using the pulse train at the repetition rate of the light diffracted by the AOM as a start clock. Every time an emission photon was recorded, the detection acted as a stop clock. The time interval between the start and the stop clock was then associated to a time-bin (10 ps width), repeating the process to build-up a histogram of the fluorescence trace. TCSPC data were acquired using customized LabVIEW software (National Instruments). The instrument response function (IRF) trace for the TCSPC experiment was acquired using a colloidal silica solution and fitted to a sum of two Gaussian functions; the FWHM of the first Gaussian was determined to be 170 ps, considered to be the lower limit for the time-resolution of the experiment. TCSPC traces were fitted in MATLAB (MathWorks) to analytical solutions of a Gaussian instrument response convoluted with two or more exponential functions.

4.3. Results and Discussion

4.3.1. 3Hβ RCs Characterization

The ground state characterization of 3Hβ RCs was performed by means of steady-state absorption spectroscopy. Bands in the spectrum of the 3Hβ RC can be assigned by reference to those associated with WT RCs and known effects of the four mutations. Figure 4.6 (solid lines) shows an overlay of absorption spectra of the 3Hβ and WT RCs, and the fluorescence spectrum of 3Hβ (dashed line). For the WT RC, the bands peaking at 360 and 390 nm are assigned to the Soret bands of the four bacteriochlorophylls and two bacteriopheophytins. The single 15 *cis-cis*' spheroidenone carotenoid contributes to a broad absorption between ~450 and ~600 nm. The sharper features in this region correspond to the Q_y bands associated with two bacteriopheophytins (between 520–550 nm) and four bacteriochlorophylls (at 600 nm). The spectrum of the 3Hβ RC showed the loss of a band at ~545 nm and the appearance of additional absorbance around 600 nm, consistent with the replacement of a bacteriopheophytin by a bacteriochlorophyll. In the WT RC, the major bands in the near-IR region are attributable to the two bacteriopheophytins (H_A/H_B, at 760 nm), the two monomeric bacteriochlorophylls (B_A/B_B, at 802 nm) and the two strongly excitonically-coupled primary electron donor bacteriochlorophylls (P, at 870 nm). As expected, the band associated with bacteriopheophytin at 760 nm was red-shifted and lowered in intensity in the spectrum of the 3Hβ RC, with the appearance of additional

absorption on the blue side of the 802 nm band. Again, this was consistent with the replacement of a bacteriopheophytin by a bacteriochlorophyll.[39,43]

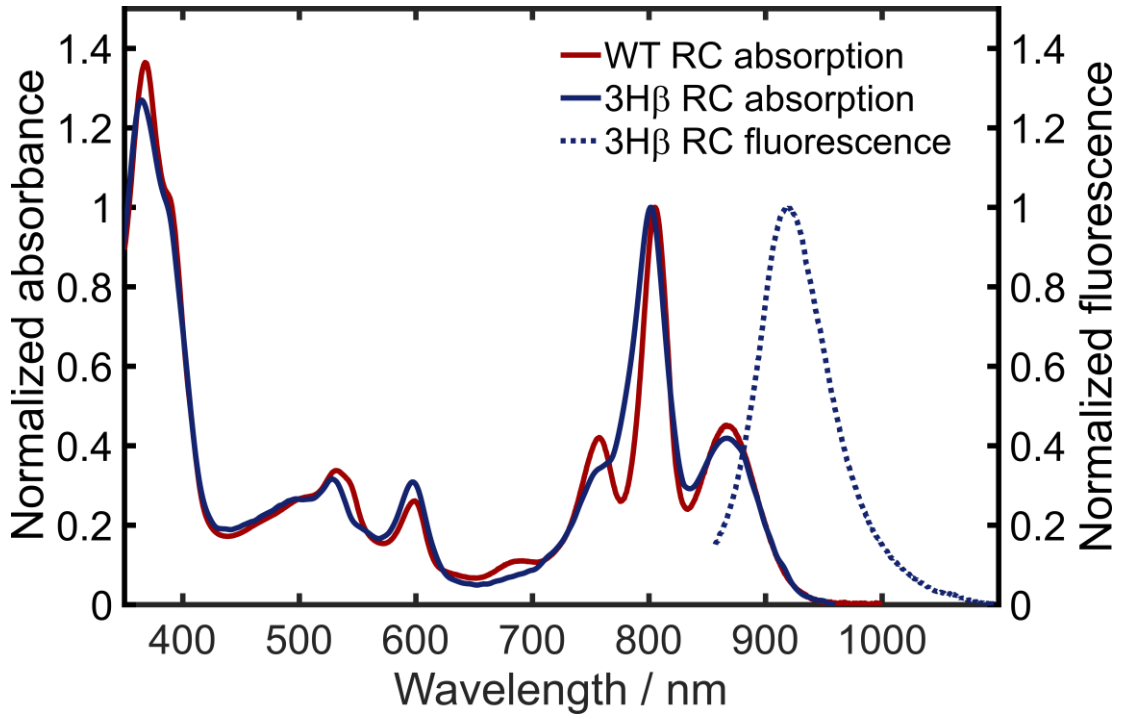

Figure 4.6. (a) Absorption spectra of wild-type RCs (solid red) and 3Hβ RCs (solid dark blue), normalized to the ~800 nm band, and fluorescence spectra of the 3Hβ RC (dashed dark blue), normalized to the maximum intensity in 700–950 nm region.

Fluorescence from the P bacteriochlorophyll pair peaked at 910 nm (dark blue dashed line in Figure 4.6) as expected after the insertion of point mutations in RCs genome. To determine the fluorescence quantum yield of 3Hβ RCs, the fluorescence of the near-infrared dye IR140 in dimethyl-sulfoxide, which has a well characterized fluorescence quantum yield, was recorded under the same excitation conditions as used to acquire the fluorescence of 3Hβ RCs. Using a previously described procedure,[51] the fluorescence quantum yield, Φ_f, of the 3Hβ RCs was determined using IR140 as a calibrant via:

$$\Phi_f(3H\beta) = \Phi_f(IR140)\frac{{n_{3H\beta}}^2}{{n_{IR140}}^2}\frac{F_{3H\beta}}{F_{IR140}}\frac{1-10^{-A(595)_{IR140}}}{1-10^{-A(595)_{3H\beta}}} \quad (4.2)$$

where F is the integrated fluorescence intensity, $A(\lambda)$ is the absorbance at excitation wavelength λ, and n is the refractive index of the solvent. Using the known fluorescence

quantum yield of 0.20 for IR140 in dimethyl-sulfoxide,[52] the fluorescence quantum yield for 3Hβ RCs was estimated to be 0.0014.

To explore whether 3Hβ RCs were capable of charge separation, ultrafast transient absorption (TA) studies of purified RCs were undertaken using 59 fs, 595 nm pump pulses and two different supercontinuum probes in the visible or near-infrared. In both measurements, pulses at 595 nm excited the strongly overlapping Q_x bands of the five bacteriochlorophylls present in the 3Hβ RC (solid dark blue line in Figure 4.6). TA data for near-IR probe wavelengths between 850 and 1100 nm are shown in Figure 4.7(a). This probe wavelength region is particularly important to track the initial steps of charge separation in RCs which, if active, will generate $P^{+}(B_A\beta_A)^{-}$ as the product of primary electron transfer. Absorbance changes at 880 nm report the electronic state of P, and bacteriochlorophyll anions have a spectrally distinct absorption band that peaks at ~1000 nm.[48,53]

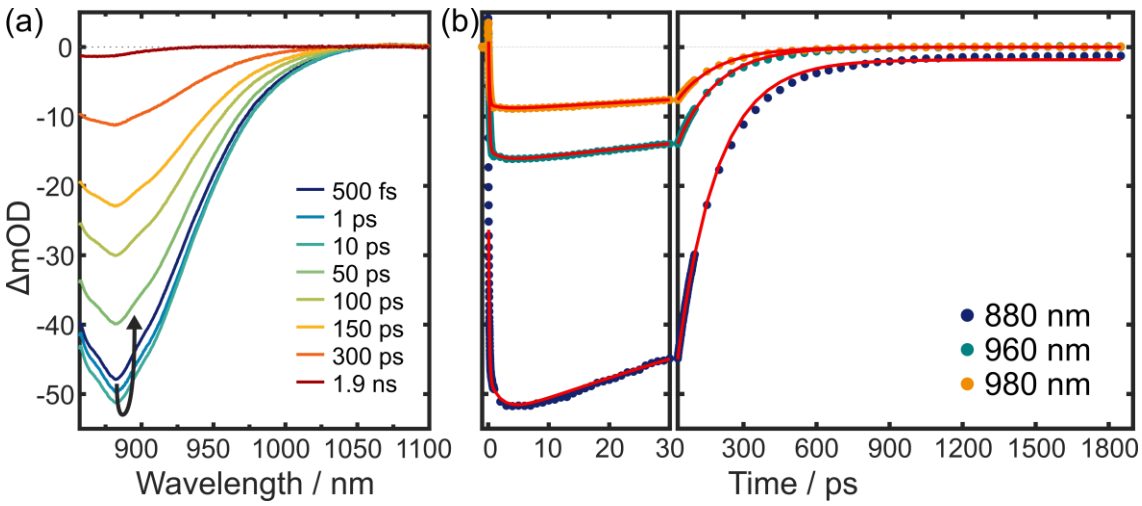

Figure 4.7. (a) Near-infrared transient absorption spectra of 3Hβ RCs for the displayed pump-probe time delays. (b) Kinetics for three different probe wavelengths and (dots) and fits to the data (solid red lines).

The spectra in Figure 4.7(a) were dominated by a negative feature at 880 nm corresponding to ground state bleaching of P, and stimulated emission from P*. This feature developed quickly in a biexponential fashion and then decayed monoexponentially. Simultaneous fits to multiple probe wavelengths in this region (Figure 4.7(b)) returned exponential rises of 140 ± 59 fs (93% amplitude) and 2.12 ± 0.49 ps (7%). As 595 nm light excited all five bacteriochlorophylls rather than just the two that form P, the fastest time constant was associated with $(B_A/B_B/\beta_A)^* \rightarrow P^*$ electronic energy transfer,[54–56] whereas the secondary

slower rise (< 7% amplitude) is attributed to a small amount of Crt* → B_B* → P* electronic energy transfer. The latter minor component was due to overlap of the ~50 nm FWHM pump pulse with the red-edge of the broad absorbance band of the single 15 *cis-cis'* spheroidenone in the RC protein,[7,57,58] as evident from carotenoid spectral signatures in the visible probe window (see Figure 4.8). P* then decayed with a time constant of 162 ± 0.2 ps via a mechanism that dominantly must have involved direct transfer back to the ground state as no discernable transient was seen, within the signal-to-noise ratio, that might be associated with formation of B_A^- or β_A^- products. These anions would be expected as a positive shoulder on the ground state bleach/stimulated emission feature at ~1000 nm. Notably, the recovery of the ground state bleach was not entirely complete within the 1.9 ns measuring window (see the kinetic trace at 880 nm in Figure 4.7(b)), with a small offset remaining. This long-lived bleach is likely a signature of a very small percentage of RCs that were able to undergo charge-separation. This combination of spectral features was consistent with the expected effects of combining the triple H-bond[36–38] and β-mutations,[39,40] very strongly reducing the quantum yield of charge separation and greatly increasing the lifetime of the P* excited state from ~3 ps to over 150 ps.

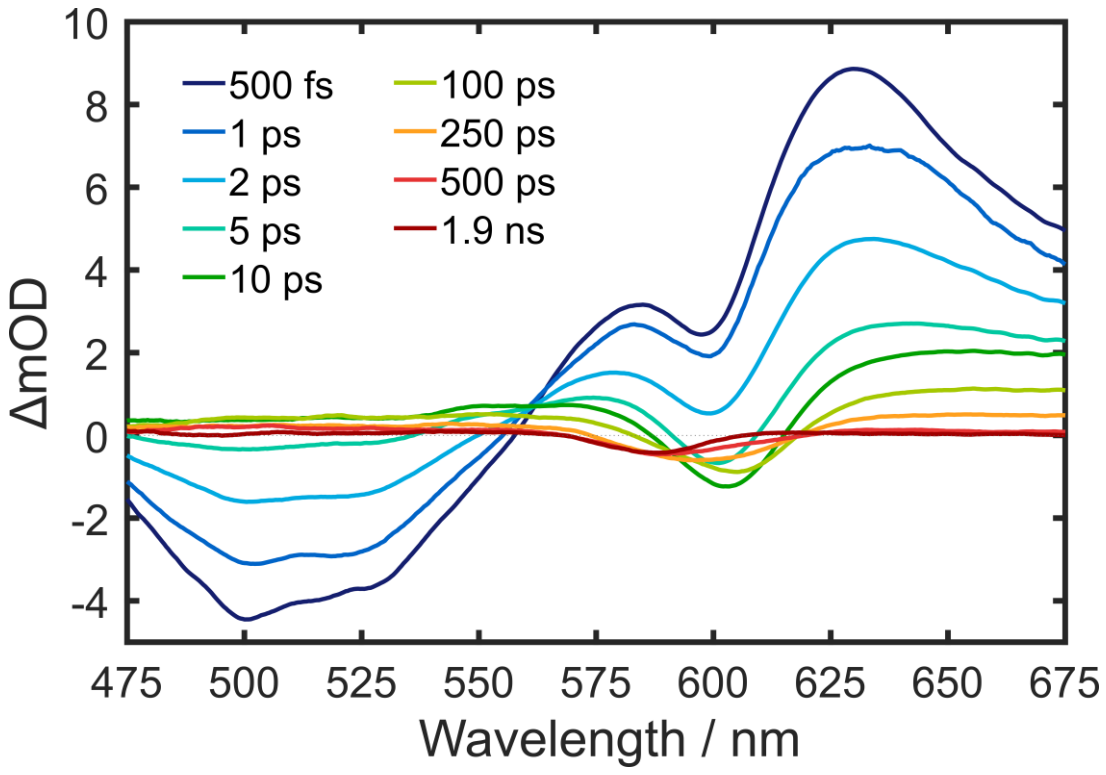

Figure 4.8. Visible transient absorption spectra of 3Hβ RCs for the displayed pump-probe time delays.

TA difference spectra for the 3Hβ RC using 595 nm excitation and a visible white light probe supercontinuum (450–720 nm) are displayed in Figure 4.8. Unlike prior measurements of R26 RCs (a *Rba. sphaeroides* RC that lacks the carotenoid cofactor) there were no obvious features associated with bacteriochlorin anions, which in this region are expected to be present at 630 and 640 nm,[48,53] and in accord with near-IR probe data shown in Figure 4.7. These results further demonstrate that the charge-transfer is greatly disfavored in the 3Hβ RC. The broad bleach between 475 and 565 nm is associated with the 15 *cis-cis*' spheroidenone, as the 595 nm (FWHM = 50 nm) excitation catches the long-wavelength tail of its absorption. The visible region TA spectrum is far more complex to decompose compared to the equivalent near-IR spectrum, due to overlapping excited state absorption bands and multiple ground state bleaches from the Q_x bacteriochlorin bands.

4.3.2. FRET in the Nanoconjugates

The absorption and emission spectra of the QDs and 3Hβ RCs used to assemble nanoconjugates are shown in Figure 4.9.

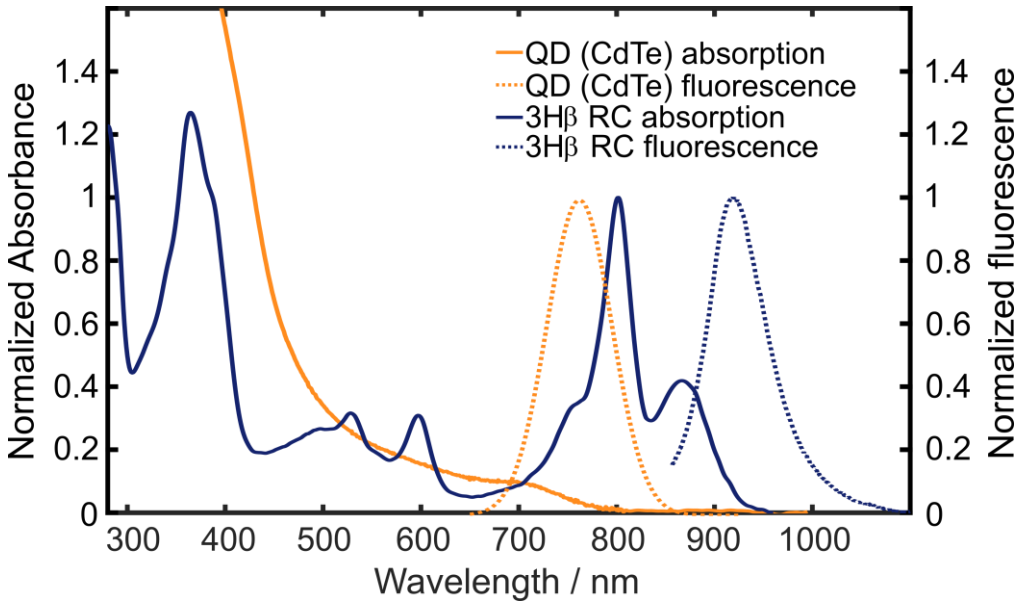

Figure 4.9. Absorption and fluorescence spectra of the 3Hβ RC and QD components of the nanoconjugates. The emission spectra and RC absorbance spectrum are normalized to the maximum intensity in 700–950 nm region. The QD absorbance spectrum is normalized at 430 nm.

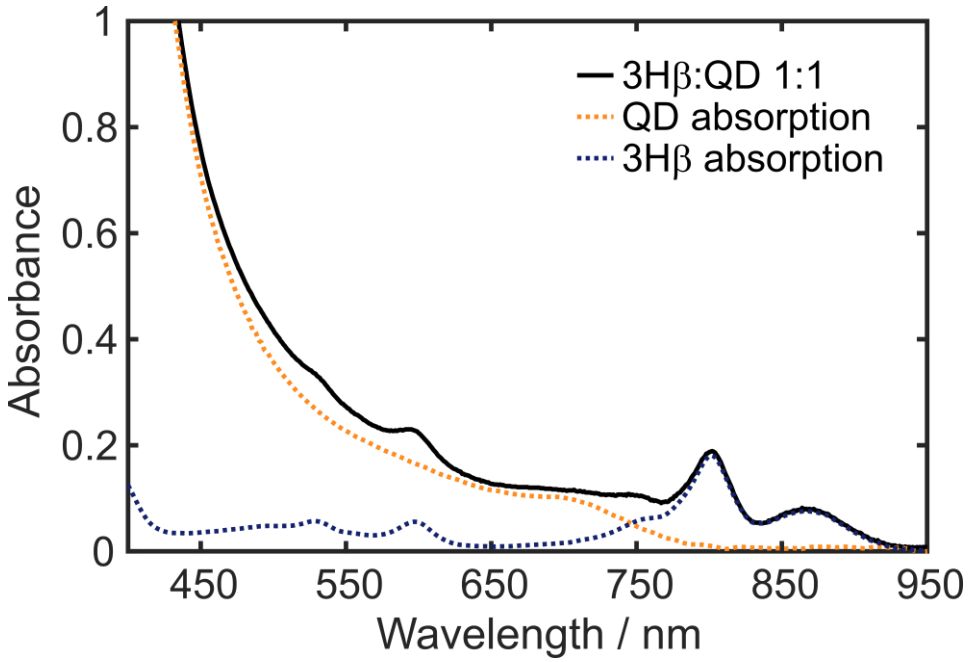

Figure 4.10. Absorption spectrum of 3Hβ RC–QD nanoconjugates for a 1:1 ratio. Dashed lines show the relative contributions of RC and QD components.

As in previous work,[31,32] water-soluble 6.5 nm diameter CdTe QDs were used in the nanoconjugates as they have broad absorbance (solid orange line in Figure 4.9) that spans the gap between the strong near-IR Q_y and near-UV Soret absorbance bands of the RC, and a fluorescence profile (dashed orange line) that overlaps well with RC absorption (solid dark blue line). Absorption spectra of the RC–QD nanoconjugates at different composition ratios were also collected. An example for RC:QD 1:1 mixture is given in Figure 4.10, showing the contributions from the constituent chromophores. The RC:QD 1:1 spectrum is in line with previous work from collaborators on similar nanoconjugate systems, confirming that the molar extinction coefficient of wild type RCs satisfactorily approximates that of the 3Hβ mutant RC.

Having characterized the energy and electron transfer dynamics in isolated 3Hβ RCs with TA spectroscopy, the excited state dynamics of QD–RC nanoconjugates were investigated using TCPSC. Fluorescence decay traces for QDs, RCs and four QD–RC biohybrid nanoconjugates with RC:QD molar ratios of between 1:1 and 10:1 are shown in Figure 4.11. Samples were excited with ~100 fs 430 nm laser pulses to preferentially excite QDs at a point where background absorbance of RCs was lowest. To achieve different RC:QD ratios the concentration of QDs was fixed and the concentration of RCs varied.

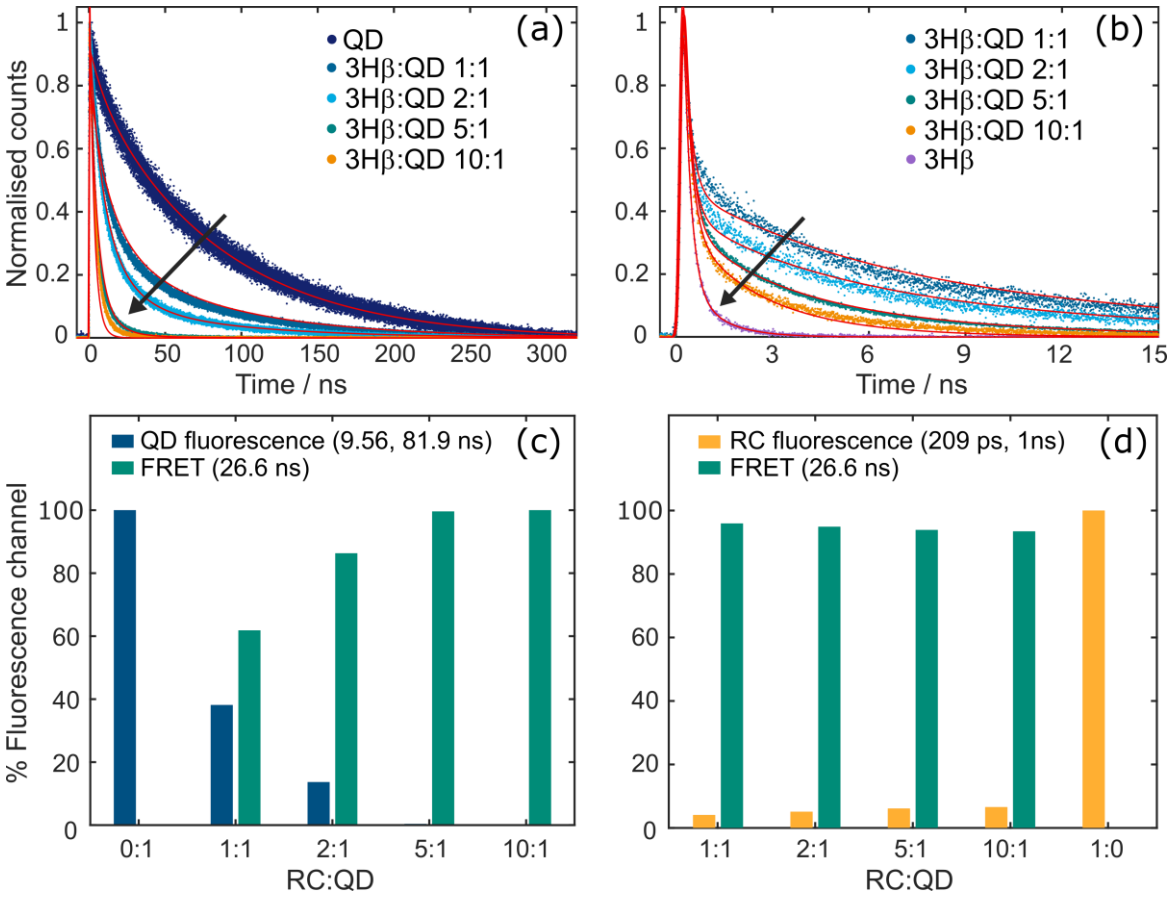

Figure 4.11. TCSPC analysis of fluorescence decay. (a) Normalized fluorescence data (scatter plots) and overlaid fits returned by global analysis (red solid lines) for QDs and RC–QD conjugates for the peak of QD fluorescence (750 nm). (b) Equivalent data for 3Hβ and RC–QD conjugates at the peak of RC P* fluorescence at 905 nm. In (a) and (b), black arrows indicate the trend upon increasing the RC:QD stoichiometry. (c) Contributions of QD fluorescence (two processes summed) and emission quenched by FRET (two channels summed) to the 750 nm signal for different RC:QD ratios; the 0:1 sample had only QDs. (d) Contributions of intrinsic RC fluorescence (two processes summed) and FRET (two channels summed) to the 905 nm signal at different RC:QD ratios; the 1:0 sample had only RCs. The amplitudes used to determine these percentage contributions are shown in Table 4.1 and Table 4.2.

Figure 4.11(a) shows the normalized TCSPC signals collected at 750 nm, which corresponds to the peak of QD fluorescence. When moving from QD-only sample (Figure 4.11(a), dark blue trace) to QD–RC conjugates (Figure 4.11(a), other colors), the time profiles showed a more rapid fluorescence decay that accelerated as the RC:QD stoichiometry increased, consistent with expectations from previous steady-state fluorescence quenching experiments.[31] These data support the hypothesis that FRET occurs between QDs and RCs in the conjugate, and that non-radiative FRET within the nanoconjugate competes with the intrinsic QDs radiative decay.

Turning to acceptor fluorescence, Figure 4.11(b) shows the normalized TCSPC signal collected at 905 nm, a wavelength where RC fluorescence was almost entirely spectrally isolated from QD emission (see Figure 4.9). For the conjugates, as the RC:QD ratio increased the fluorescence profile at 905 nm (Figure 4.11(b)) displayed the opposite trend to that observed for QD fluorescence at 750 nm (Figure 4.11(a)). The normalized fluorescence trace for the 1:1 ratio had the slowest decay, and as the RC:QD ratio was increased the rate of decay also increased. The 430 nm pulse did not exclusively excite QDs due to an appreciable absorption cross-section for the 3Hβ RC at this wavelength. As a result, assuming the hypothesis of FRET occurring between QDs and RCs is correct, the observed 905 nm fluorescence is a result of the sum of both direct excitation of RCs and FRET from associated QDs. The relative contributions of these two processes are dictated by the mixture of RC and QD in each sample, with the dynamics tending to resemble those of the RCs alone most strongly in the sample with the highest RC:QD ratio, where the relative absorbance of the RC at 430 nm was highest.

To support the interpretation FRET is operating in the nanoconjugate and quantify the rate of the process, the TCSPC traces for QDs, RCs and nanoconjugates were fitted to the analytical solution of a Gaussian instrument response function convolved with multiple exponential decays, in a model that includes the presence of a FRET channel from QDs to RCs. For the QD-only sample (Figure 4.11(a), dark blue trace), the fluorescence signal at 750 nm $I_{QDs(750)}$, was fitted with a biexponential function:

$$I_{QDs(750)} = A_1 e^{-k_{D1}t} + A_2 e^{-k_{D2}t} \quad (4.3)$$

In Equation 4.3, while k_{D1} and k_{D2} are rate constants dictating the lifetimes associated with direct and delayed fluorescence from the QD excitonic state, respectively, A_1 and A_2 are the associated amplitudes. For the sake of simplicity, Equation 4.3 and those that follow exclude the convolution function. The biexponential function comprised a short 9.56 ± 0.03 ns component attributed to fluorescence from the excitonic QD state, and a long 81.89 ± 0.03 ns component, assigned to delayed fluorescence from the QD excitonic state after de-trapping of localized surface trap states. In QDs used in this study, approximately 88% of the fluorescence originated from the delayed emission (Figure 4.11(c)), in line with previous measurements on 6.5 nm CdTe QDs.[59,60]

For 3Hβ RCs alone (Figure 4.11(b), violet trace) data were fitted with Equation 4.4 comprising a biexponential decay function, expressing the fluorescence intensity at 905 nm $I_{RCs(905)}$ as:

$$I_{RCs(905)} = A_4 e^{-k_{A1}t} + A_5 e^{-k_{A2}t} \quad (4.4)$$

where k_{A1} and k_{A2} were the rate constants, and A_4 and A_5 were the associated pre-exponential factors. The fitting returned time constants of 209 ± 4 ps and 1.00 ± 0.04 ns, the nanosecond component comprising 11% of the total fluorescence decay (Figure 4.11(d)). Guided by the near-infrared region TA data, the picosecond component was assigned to fluorescence from P* in RCs that were directly excited by the 430 nm pulse. The minor nanosecond component is assigned to delayed P* fluorescence from a small percentage of directly excited RCs that were able to undergo charge separation and slowly reformed P* through reverse electron transfer. To estimate the initial quantum yield of charge-separation for 3Hβ RCs it was assumed that all RCs able to charge-separate recombined to form P*. Combined with the estimated fluorescence quantum yield of RCs of 0.14% (*vide supra*), this returned an initial quantum yield of charge-separation of 0.02%.

For the nanoconjugates, an additional exponential decay component was required to account for the quenching of donor fluorescence at 750 nm and an additional exponential rise component was necessary to describe the lifetime increase and delay in the fluorescence signal from the acceptor fluorescence at 905 nm. However, the QD:RC stoichiometries shown in Figure 4.11(a,b) represent average compositions that do not take into account heterogeneity. As demonstrated by Liu *et al.*,[31] each mixture is more appropriately described by a probability distribution of different QD–RC$_i$ ratios (with $i \geq 0$) as determined by a dissociation constant (K_d) that describes a dynamic equilibrium between RCs bound to QDs and free in solution. Mathematical formalization of this dynamic heterogeneity resulted in a deterministic binding model that accurately predicted the RC:QD stoichiometry probability distribution for WT RCs and QDs.[31] As the 3Hβ protein still binds through to QDs via His-tags, and thus in similar way to WT RCs, it is reasonable that the same model would accurately predict the 3Hβ–QD binding distributions. With FRET operational in the nanoconjugates, the heterogeneity of the RC–QD binding has advantageous implications on the total FRET efficiency; the more RC acceptors a given QD donor binds, the increased

number of possible degenerate EET pathways, which at a macroscopic level boosts the probability of FRET *n*-fold.[61] To account for multiple possible FRET pathways, a multiplicative factor (equal to specific stoichiometry in the sum) for the FRET rate constant k_{FRET} was included for both the direct (k_{D1}) and delayed (k_{D2}) QD fluorescence donor channels (750 nm detection). Similarly, the time-resolved fluorescence of the acceptor channel at 905 nm for the nanoconjugates was modelled to include the presence of two FRET routes, and the emission from two different RCs pathways. Accounting for the heterogeneity of the binding, this yielded to an expression for the intensity of the nanoconjugate signal I_{conj}, for nanoconjugate fluorescence at 750 nm and 905 nm, respectively:

$$I_{conj(750)} = A_3 \sum_{i=0}^{15} p(i)\, e^{-(k_{D1}+ik_{FRET})t} + \frac{A_2}{A_1} A_3 \sum_{i=0}^{15} p(i)\, e^{-(k_{D2}+ik_{FRET})t} \qquad (4.5)$$

$$\begin{aligned} I_{conj(905)} = {} & A_4 e^{-k_{A1}t} + A_5 e^{-k_{A2}t} + \\ & + A_6 \sum_{i=1}^{15} p(i) \frac{k_{FRET}}{k_{A1}-k_{D1}-ik_{FRET}} \left(e^{-(k_{D1}+ik_{FRET})t} - e^{-k_{A1}t}\right) + \\ & + A_7 \sum_{i=1}^{15} p(i) \frac{k_{FRET}}{k_{A1}-k_{D2}-ik_{FRET}} \left(e^{-(k_{D2}+ik_{FRET})t} - e^{-k_{A1}t}\right) + \\ & + \frac{A_5}{A_4} A_6 \sum_{i=1}^{15} p(i) \frac{k_{FRET}}{k_{A2}-k_{D1}-ik_{FRET}} \left(e^{-(k_{D1}+ik_{FRET})t} - e^{-k_{A2}t}\right) + \\ & + \frac{A_5}{A_4} A_7 \sum_{i=1}^{15} p(i) \frac{k_{FRET}}{k_{A2}-k_{D2}-ik_{FRET}} \left(e^{-(k_{D2}+ik_{FRET})t} - e^{-k_{A2}t}\right) \end{aligned} \qquad (4.6)$$

In Equations 4.5 and 4.6, the pre-exponential terms $p(i)$ are the probabilities associated with the binding distribution at each RC:QD ratio. The kinetic model also assumed that, regardless of trapping/de-trapping in the QDs, FRET could occur only from the excitonic bright state of QD. Together with Equations 4.3 and 4.4, Equation 4.5 and 4.6 were used to globally fit the QD–RC data for the two different probe wavelengths (750 nm for QDs and 905 nm for RCs), where the binding probabilities $p(i)$, and k_{FRET} were shared parameters across all datasets. To minimize the number of free parameters, the QD and RC fluorescence lifetimes and the relative amplitudes associated with excited species decay were fixed to the values determined from QD-only and RC-only fluorescence data. Furthermore, the ratio of direct *vs.* delayed FRET was constrained to the same ratio as in QD-only data. A_3, A_6 and A_7 were allowed to float, accounting for the signal amplitude in nanoconjugate traces.

The global fitting optimized the rate constant k_{FRET} revealing a 26.6 ± 0.1 ns time constant for the QD → RC FRET process, with fits to data overlaid to TCSPC traces in Figure 4.11(a,b). Optimization of K_d in the global kinetic analysis returned a value for 3Hβ RC of 17.3 × 10^{-9} M, which was ~two-fold larger than determined for WT RCs, indicating a slightly weaker binding. Knowledge of the value of K_d implied direct determination of the pre-factors $p(i)$; the associated binding probability distributions at each investigated RC:QD ratio are given in Figure 4.12. As is evident from Figure 4.12(a), even at the lowest concentration mixtures the probability that a single QD binds multiple RCs is > 20%, meaning there will multiple degenerate QD→RC FRET pathways in each sample. Based on the calculated stoichiometry probability distributions for the mixtures studied, it is apparent that the fluorescence decay profiles need to account for a sum between 0–15 RCs as the probability of binding 15 RCs per single QD in the mixtures studied is negligible.

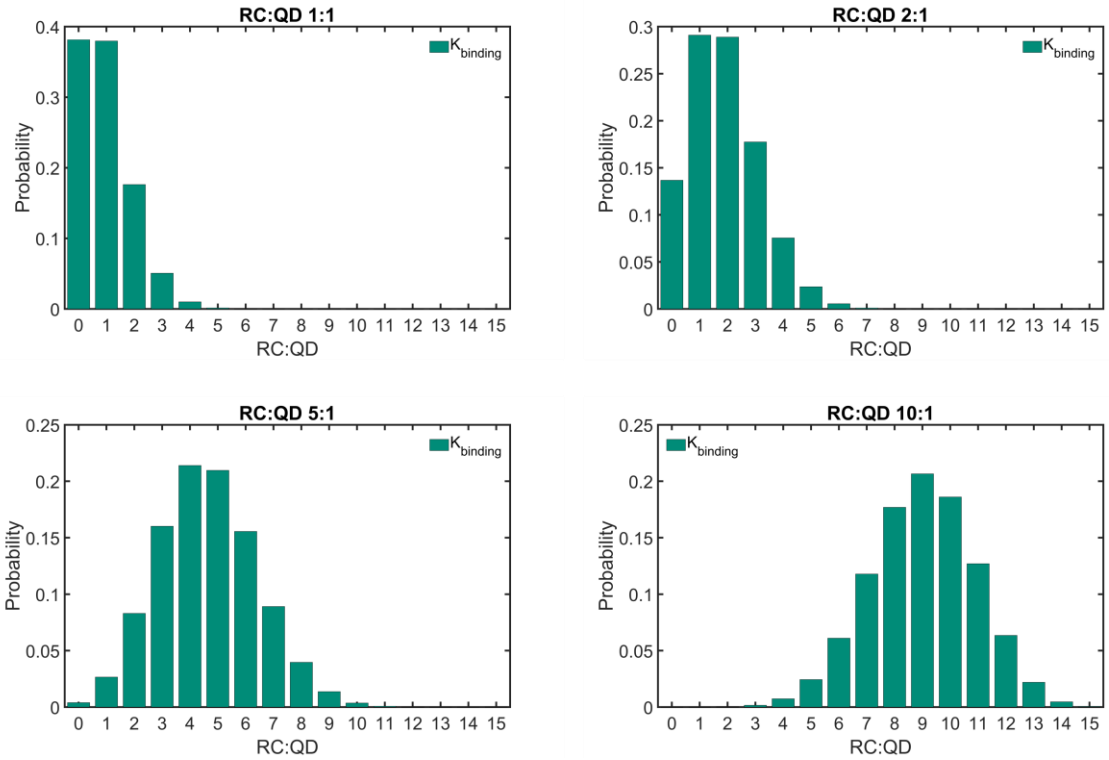

Figure 4.12. Calculated probability distributions for the RC:QD stiochiometry based on the following RC:QD mixture ratios: (a) 1:1, (b) 2:1, (c) 5:1 and (d) 10:1.

Amplitudes of the fits to data are shown in Figure 4.11(c,d) and reported in Table 4.1 and Table 4.2. For the donor channel at 750 nm, even at low RC:QD ratios the relative amplitude of the intrinsic QD fluorescence (blue bars) was outcompeted by the

corresponding FRET amplitude (green bars). This is indirect evidence of the effectiveness of the QD→RC FRET, as at stoichiometries of 1:1 or 2:1 the subpopulation of QDs with no bound RCs is still significant. Inevitably, increasing the RC:QD ratio increases the probability of FRET, and thus accounts for the observed shortening of the fluorescence decays (orange trace in Figure 4.11(a)), as slow QD emission was outcompeted by faster FRET.

Table 4.1. Amplitudes associated with the globally fit time constants for different samples at 750 nm and used to obtain the bar plot in Figure 4.11(c).

Relative amplitudes (%) for channels associated to QDs fluorescence (750 nm)				
RC:QD Ratio	$A_1p(0)$ (QDs direct τ = 9.56 ns)	$A_2p(0)$ (QDs delayed τ = 81.89 ns)	$A_3(1–p(0))$ (QDs direct + FRET τ = 9.56 + 26.6 ns)	$(A_2/A_1)A_3(1–p(0))$ (QD delayed + FRET τ = 81.89 + 26.6 ns)
0:1	12.1	87.9	—	—
1:1	4.6	33.5	7.5	54.4
2:1	1.7	12.0	10.4	75.9
5:1	0.1	0.3	12.0	87.6
10:1	0.0	0.0	12.1	87.9

Table 4.2. Amplitudes associated with the globally fit time constants for different samples at 905 nm and used to obtain the bar plot in Figure 4.11(d).

Relative amplitudes (%) for channels associated to RCs fluorescence (905 nm)						
RC:QD Ratio	A_4 (RCs direct τ = 209 ps)	A_5 (RCs delayed τ = 0.99 ns)	A_6 (FRET to P* from QDs direct)	A_7 (FRET to P* from QDs delayed	$(A_5/A_4)A_6$ (FRET to $P^+(B_A\beta_A)^-$ from QDs direct)	$(A_5/A_4)A_7$ (FRET to $P^+(B_A\beta_A)^-$ from QDs delayed)
1:0	87.2	12.8	—	—	—	—
1:1	3.5	0.5	53.1	30.6	7.8	4.5
2:1	4.5	0.6	52.5	30.3	7.7	4.4
5:1	5.3	0.8	52.0	29.9	7.6	4.4
10:1	5.7	0.8	51.7	29.8	7.6	4.4

The 26.6 ns FRET pathway dominated the decay in the 5:1 and 10:1 nanoconjugates (Figure 4.11(c), green bars), peaking at the 5:1 ratio with consequent disappearance of the QD fluorescence channels. For the acceptor channel at 905 nm, even at the lowest 1:1 stoichiometry most of the fluorescence decay was caused by RCs being excited through

FRET (Figure 4.11(d)). This percentage only slowly declined as the relative amount of RCs increased, due to an increased probability of direct excitation and subsequent fluorescence from the RCs.

4.3.3. FRET Efficiency and Distance and its Role in the Nanoconjugates

The average QD–RC donor-acceptor distance and the efficiency of the transfer were determined directly using the FRET rate constant obtained from the analysis of TCSPC data. To determine the FRET pair efficiency, the weighted average lifetime of the donor τ_D was first calculated using:

$$\tau_D = \frac{\sum \alpha_i \tau_i^2}{\sum \alpha_i \tau_i} \tag{4.7}$$

Where α_i and τ_i are the i-th amplitude and lifetime of the donor, respectively. The calculation returned an associated fluorescence rate constant of 1.24×10^7 s^{-1} for the QDs and was used together with the FRET rate constant to obtain the FRET efficiency via Equation 1.17. The analysis returned a value of E_{FRET} of 0.75 ± 0.01, which was close to a value of ~0.71 estimated in previous work by collaborators for 5:1 and 10:1 conjugates formed from RCs with the sole β-mutation.[31] Notably, the total quantum yield of FRET (<14%) was far lower than the FRET efficiency as it is limited by the ~20% QD fluorescence quantum yield, as determined by a high non-radiative relaxation quantum yield. A higher FRET quantum yield could potentially be achieved with far more fluorescent QDs, but this is not without its own issues. To increase the fluorescence quantum yield of QDs often requires surface functionalization/passivation to suppresses the number of trap states which predominantly decay non-radiatively and thus lower the fluorescence quantum yield. However, whilst this would increase the direct prompt radiative channel of QDs (9.56 ns), it would also deplete the reservoir of QDs which have delayed fluorescence from the excitonic state after de-trapping of surface states (81.89 ns). Kinetic analysis of QD–3Hβ hybrids revealed the latter channel contributes the most to FRET (τ = 26.6 ns) in the nanoconjugates (see Table 4.1), due to the more favorable competition of radiative and non-radiative lifetimes.

The FRET rate constant also allowed direct calculation of the Förster distance after rearrangement of Equation 1.15.[62] In Equation 1.15, the refractive index of the medium was chosen to be that of water buffer solution, 1.33, the fluorescence quantum yield of the isolated QD donor was taken to be 0.197 from previous work;[31] for the orientation factor, κ^2 was assumed to be 2/3 and the Förster spectral overlap integral of QD fluorescence and 3Hβ RCs absorption was calculated to be 4.61 $\times 10^{-12}$ M^{-1} cm^3 using software freely available at FluorTools.com. The calculation returned a FRET distance of 6.28 ± 0.04 nm. This was close to values of 6.4 – 6.9 nm estimated in previous studies from collaborators for a mutant RC with just the β-mutation (and therefore the same pigment composition as the 3Hβ RC).[31] The new value is more reliable, as the use of TCSPC enabled direct determination of the FRET rate constant from a global analysis of the fluorescence lifetime data, as opposed to a more complex analysis which required extrapolation.

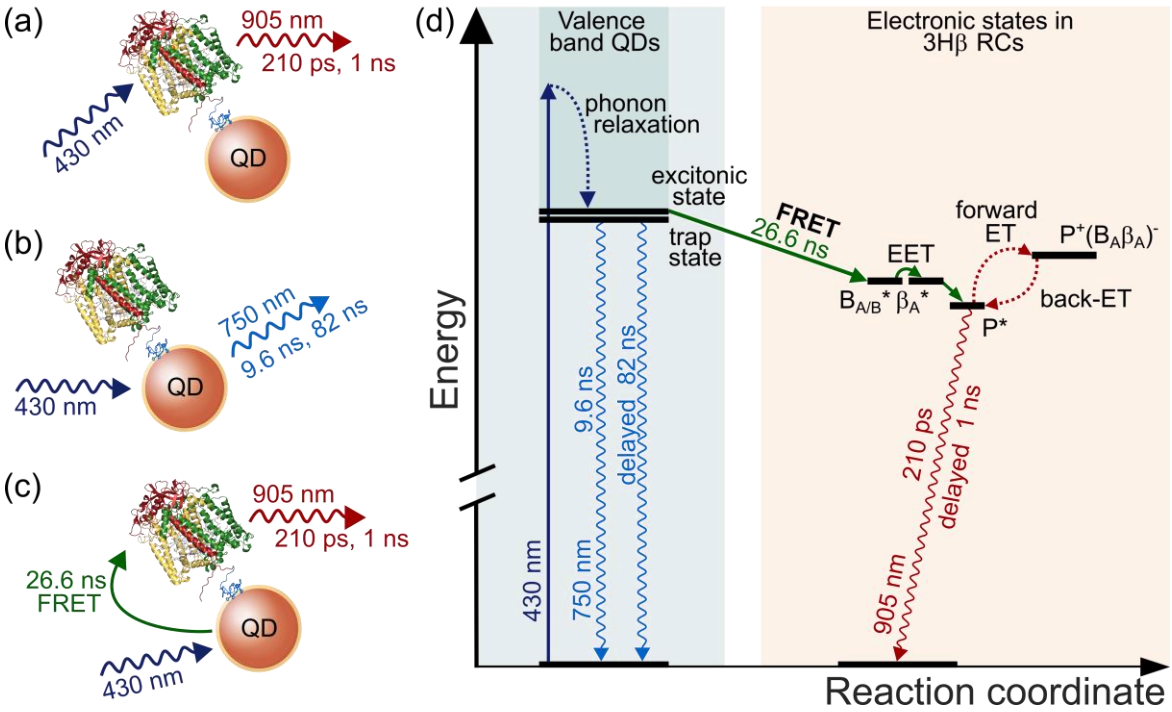

Figure 4.13. Schematic of radiative and non-radiative decay pathways in 3Hβ RC–QD nanoconjugates, indicating EET and ET components. Measurements on nanoconjugates revealed a mixture of three processes depending on the QD:RC stoichiometry: (a) direct excitation of RCs, and subsequent biexponential fluorescence; (b) excitation of QDs and the associated intrinsic radiative decay from quantum and surface trap states and (c) excitation of QDs, FRET to bound RCs, and fluorescence from those RCs. (d) Energy level diagram with the main radiative and non-radiative pathways associated with QD–3Hβ RC conjugates and their associated time constants. Note FRET to the cofactors of the RC B-branch and subsequent energy transfer to P* is omitted from (d) for the sake of clarity.

A summarizing schematic of the competing absorption, non-radiative decay and fluorescence pathways in the 3Hβ RC nanoconjugates is shown in Figure 4.13. Depending on the precise RC:QD ratio investigated, 430 nm light preferentially excited either the QD or RC components of the nanoconjugate. Direct RC excitation (Figure 4.13(a)) leads to a biphasic fluorescence decay due to minimal (~0.04%) charge separation. Excitation of the QDs can lead to direct or delayed fluorescence from the excitonic state (Figure 4.13(b)) or FRET to conjugated RCs and subsequent red-shifted 905 nm fluorescence from RCs (Figure 4.13(c)). The FRET donor–acceptor pair-wise efficiency was determined to be 0.75 ± 0.01. The high FRET efficiency allied with the high surface coverage of QDs with multiple RCs, even at 5:1 RC:QD mixtures, meant that the FRET channel dominated the radiative relaxation dynamics.

4.4. Conclusions

To explore the kinetics and efficiency of energy transfer to purple bacterial RCs from a synthetic antenna complex a RC mutant was engineered with a new combination of mutations that almost completely switches off charge separation, creating a fluorescent energy transfer acceptor. These 3Hβ RCs have a dominant excited state lifetime of 162 ± 0.2 ps, with a fluorescence maximum at 910 nm consistent with emission from the excited state of the primary electron donor. Conjugation of 3Hβ RCs to 6.5 nm diameter CdTe QDs generated an efficient FRET pair, the energy transfer dynamics of which could be directly monitored using TCSPC. FRET occurred within the nanoconjugate with a 26.6 ± 0.1 ns lifetime and a pair-wise efficiency of 0.75 ± 0.01. These parameters enabled a direct determination for the donor-acceptor distance of 6.28 ± 0.04 nm. This combination of natural and synthetic components in a nanoconjugate allows light harvesting to occur with an appreciable quantum yield from the entire visible and near-infrared spectrum. It is envisaged that the incorporation of additional light harvesting moieties could produce further enhancements in the light harvesting process, that can be characterized using this approach combining ultrafast spectroscopy with the tailoring of photoprotein properties.

References

(1) R. G. Saer, R. E. Blankenship. Light Harvesting in Phototrophic Bacteria: Structure and Function. *Biochem. J.* **2017**, *474* (13), 2107–2131.

(2) R. E. Blankenship. *Molecular Mechanisms of Photosynthesis*. Blackwell Science Ltd: Oxford, UK, 2002.

(3) S. Bahatyrova, R. N. Frese, C. A. Siebert, J. D. Olsen, K. O. Van Der Werf, R. Van Grondelle, R. A. Nlederman, P. A. Bullough, C. Otto, C. N. Hunter. The Native Architecture of a Photosynthetic Membrane. *Nature* **2004**, *430* (7003), 1058–1062.

(4) S. Scheuring. AFM Studies of the Supramolecular Assembly of Bacterial Photosynthetic Core-Complexes. *Curr. Opin. Chem. Biol.* **2006**, *10* (5), 387–393.

(5) S. Scheuring, D. Lévy, J. L. Rigaud. Watching the Components of Photosynthetic Bacterial Membranes and Their in Situ Organisation by Atomic Force Microscopy. *Biochim. Biophys. Acta Biomembr.* **2005**, *1712* (2), 109–127.

(6) C. A. Wraight, R. K. Clayton. The Absolute Quantum Efficiency of Bacteriochlorophyll Photooxidation in Reaction Centres of *Rhodopseudomonas Sphaeroides*. *Biochim. Biophys. Acta Bioenerg.* **1974**, *333* (2), 246–260.

(7) M. R. Jones. The Petite Purple Photosynthetic Powerpack. *Biochem. Soc. Trans.* **2009**, *37* (2), 400–407.

(8) G. Feher, J. P. Allen, M. Y. Okamura, D. C. Rees. Structure and Function of Bacterial Photosynthetic Reaction Centres. *Nature* **1989**, *339* (6220), 111–116.

(9) W. Zinth, J. Wachtveitl. The First Picoseconds in Bacterial Photosynthesis - Ultrafast Electron Transfer for the Efficient Conversion of Light Energy. *ChemPhysChem* **2005**, *6* (5), 871–880.

(10) L. Suresh, J. V. Vaghasiya, M. R. Jones, S. C. Tan. Biodegradable Protein-Based Photoelectrochemical Cells with Biopolymer Composite Electrodes That Enable Recovery of Valuable Metals. *ACS Sustain. Chem. Eng.* **2019**, *7* (9), 8834–8841.

(11) S. C. Tan, L. I. Crouch, M. R. Jones, M. Welland. Generation of Alternating Current in Response to Discontinuous Illumination by Photoelectrochemical Cells Based on Photosynthetic Proteins. *Angew. Chem. Int. Ed.* **2012**, *51* (27), 6667–6671.

(12) V. M. Friebe, J. D. Delgado, D. J. K. Swainsbury, J. M. Gruber, A. Chanaewa, R. Van Grondelle, E. Von Hauff, D. Millo, M. R. Jones, R. N. Frese. Plasmon-Enhanced Photocurrent of Photosynthetic Pigment Proteins on Nanoporous Silver. *Adv. Funct. Mater.* **2016**, *26* (2), 285–292.

(13) S. K. Ravi, Z. Yu, D. J. K. Swainsbury, J. Ouyang, M. R. Jones, S. C. Tan. Enhanced Output from Biohybrid Photoelectrochemical Transparent Tandem Cells Integrating Photosynthetic Proteins Genetically Modified for Expanded Solar Energy Harvesting. *Adv. Energy Mater.* **2017**, *7* (7), 1601821.

(14) V. K. Singh, S. K. Ravi, J. W. Ho, J. K. C. Wong, M. R. Jones, S. C. Tan. Biohybrid Photoprotein-Semiconductor Cells with Deep-Lying Redox Shuttles Achieve a 0.7 V Photovoltage. *Adv. Funct. Mater.* **2018**, *28* (24), 1703689.

(15) S. K. Ravi, D. J. K. Swainsbury, V. K. Singh, Y. K. Ngeow, M. R. Jones, S. C. Tan. A Mechanoresponsive Phase-Changing Electrolyte Enables Fabrication of High-Output Solid-State Photobioelectrochemical Devices from Pigment-Protein Multilayers. *Adv. Mater.* **2018**, *30* (5), 1704073.

(16) L. Suresh, J. V. Vaghasiya, D. K. Nandakumar, T. Wu, M. R. Jones, S. C. Tan. High-Performance UV Enhancer Molecules Coupled with Photosynthetic Proteins for Ultra-Low-Intensity UV Detection. *Chem* **2019**, *5* (7), 1847–1860.

(17) L. Suresh, J. V. Vaghasiya, U. P. Kannan, Y. Zhang, S. K. Ravi, N. Paul, M. R. Jones, S. C. Tan. 1200% Enhancement of Solar Energy Conversion by Engineering Three Dimensional Arrays of Flexible Biophotoelectrochemical Cells in a Fixed Footprint Encompassed by Johnson Solid Shaped Optical Well. *Nano Energy* **2021**, *79*, 105424.

(18) I. Nabiev, A. Rakovich, A. Sukhanova, E. Lukashev, V. Zagidullin, V. Pachenko, Y. P.

Rakovich, J. F. Donegan, A. B. Rubin, A. O. Govorov. Fluorescent Quantum Dots as Artificial Antennas for Enhanced Light Harvesting and Energy Transfer to Photosynthetic Reaction Centers. *Angew. Chem. Int. Ed.* **2010**, *49* (40), 7217–7221.

(19) E. G. Maksimov, E. P. Lukashev, N. K. Seifullina, G. V. Nizova, V. Z. Pashchenko. Photophysical Properties of Hybrid Complexes of Quantum Dots and Reaction Centers of Purple Photosynthetic Bacteria *Rhodobacter Sphaeroides* Adsorbed on Crystalline Mesoporous TiO_2 Films. *Nanotechnologies Russ.* **2013**, *8* (7–8), 423–431.

(20) V. De Leo, L. Catucci, A. Falqui, R. Marotta, M. Striccoli, A. Agostiano, R. Comparelli, F. Milano. Hybrid Assemblies of Fluorescent Nanocrystals and Membrane Proteins in Liposomes. *Langmuir* **2014**, *30* (6), 1599–1608.

(21) S. Y. Zaitsev, D. O. Solovyeva, I. R. Nabiev. Nanobiohybrid Structures Based on the Organized Films of Photosensitive Membrane Proteins. *Russ. Chem. Rev.* **2014**, *83* (1), 38–81.

(22) S. Y. Zaitsev, D. O. Solovyeva. Supramolecular Nanostructures Based on Bacterial Reaction Center Proteins and Quantum Dots. *Adv. Colloid Interface Sci.* **2015**, *218*, 34–47.

(23) E. P. Lukashev, P. P. Knox, I. P. Oleinikov, N. K. Seifullina, N. P. Grishanova. Investigation of Stability of Photosynthetic Reaction Center and Quantum Dot Hybrid Films. *Biochemistry* **2016**, *81* (1), 58–63.

(24) I. E. Borissevitch, E. P. Lukashev, I. P. Oleinikov, A. L. S. Pavanelli, P. J. Gonçalves, P. P. Knox. Electrostatic Interactions and Covalent Binding Effects on the Energy Transfer between Quantum Dots and Reaction Centers of Purple Bacteria. *J. Lumin.* **2019**, *207*, 129–136.

(25) P. K. Dutta, S. Lin, A. Loskutov, S. Levenberg, D. Jun, R. Saer, J. T. Beatty, Y. Liu, H. Yan, N. W. Woodbury. Reengineering the Optical Absorption Cross-Section of Photosynthetic Reaction Centers. *J. Am. Chem. Soc.* **2014**, *136* (12), 4599–4604.

(26) O. Hassan Omar, S. La Gatta, R. R. Tangorra, F. Milano, R. Ragni, A. Operamolla, R. Argazzi, C. Chiorboli, A. Agostiano, M. Trotta, G. M. Farinola. Synthetic Antenna Functioning As Light Harvester in the Whole Visible Region for Enhanced Hybrid Photosynthetic Reaction Centers. *Bioconjug. Chem.* **2016**, *27* (7), 1614–1623.

(27) S. La Gatta, F. Milano, G. M. Farinola, A. Agostiano, M. Di Donato, A. Lapini, P. Foggi, M. Trotta, R. Ragni. A Highly Efficient Heptamethine Cyanine Antenna for Photosynthetic Reaction Center: From Chemical Design to Ultrafast Energy Transfer Investigation of the Hybrid System. *Biochim. Biophys. Acta Bioenerg.* **2019**, *1860* (4), 350–359.

(28) Y. Yoneda, A. Goto, N. Takeda, H. Harada, M. Kondo, H. Miyasaka, Y. Nagasawa, T. Dewa. Ultrafast Photodynamics and Quantitative Evaluation of Biohybrid Photosynthetic Antenna and Reaction Center Complexes Generating Photocurrent. *J. Phys. Chem. C* **2020**, *124* (16), 8605–8615.

(29) K. J. Grayson, K. M. Faries, X. Huang, P. Qian, P. Dilbeck, E. C. Martin, A. Hitchcock, C. Vasilev, J. M. Yuen, D. M. Niedzwiedzki, G. J. Leggett, D. Holten, C. Kirmaier, C. N. Hunter. Augmenting Light Coverage for Photosynthesis through YFP-Enhanced Charge Separation at the *Rhodobacter Sphaeroides* Reaction Centre. *Nat. Commun.* **2017**, *8*, 13972.

(30) J. Liu, V. M. Friebe, R. N. Frese, M. R. Jones. Polychromatic Solar Energy Conversion in Pigment-Protein Chimeras That Unite the Two Kingdoms of (Bacterio)Chlorophyll-Based Photosynthesis. *Nat. Commun.* **2020**, *11*, 1542.

(31) J. Liu, J. Mantell, N. Di Bartolo, M. R. Jones. Mechanisms of Self-Assembly and Energy Harvesting in Tuneable Conjugates of Quantum Dots and Engineered Photovoltaic Proteins. *Small* **2019**, *15* (4), 1804267.

(32) J. Liu, J. Mantell, M. R. Jones. Minding the Gap between Plant and Bacterial Photosynthesis within a Self-Assembling Biohybrid Photosystem. *ACS Nano* **2020**, *14* (4), 4536–4549.

(33) Lakowicz, J. R. *Principles of Fluorescence Spectroscopy*, 3rd ed.; Lakowicz, J. R., Ed.; Springer US: Boston, MA, 2006.

(34) M. Werwie, X. Xu, M. Haase, T. Basché, H. Paulsen. Bio Serves Nano: Biological Light-Harvesting Complex as Energy Donor for Semiconductor Quantum Dots. *Langmuir* **2012**,

28 (13), 5810–5818.
(35) J. A. Jackson, S. Lin, A. K. W. Taguchi, J. A. C. Williams, J. P. Allen, N. W. Woodbury. Energy Transfer in *Rhodobacter Sphaeroides* Reaction Centers with the Initial Electron Donor Oxidized or Missing. *J. Phys. Chem. B* **1997**, *101* (29), 5747–5754.
(36) X. Lin, H. A. Murchison, V. Nagarajan, W. W. Parson, J. P. Allen, J. C. Williams. Specific Alteration of the Oxidation Potential of the Electron Donor in Reaction Centers from *Rhodobacter Sphaeroides*. *Proc. Natl. Acad. Sci.* **1994**, *91* (22), 10265–10269.
(37) N. W. Woodbury, S. Lin, X. Lin, J. M. Peloquin, A. K. W. Taguchi, J. A. C. Williams, J. P. Allen. The Role of Reaction Center Excited State Evolution during Charge Separation in a *Rb. Sphaeroides* Mutant with an Initial Electron Donor Midpoint Potential 260 mV above Wild Type. *Chem. Phys.* **1995**, *197* (3), 405–421.
(38) A. Y. Khmelnitskiy, R. A. Khatypov, A. M. Khristin, M. M. Leonova, L. G. Vasilieva, V. A. Shuvalov. Charge Separation in *Rhodobacter Sphaeroides* Mutant Reaction Centers with Increased Midpoint Potential of the Primary Electron Donor. *Biochemistry* **2013**, *78* (1), 60–67.
(39) C. Kirmaier, D. Gaul, R. DeBey, D. Holten, C. C. Schenck. Charge Separaton in a Reaction Center Incorporating Bacteriochlorophyll for Photoactive Bacteriopheophytin. *Science* **1991**, *4996* (251), 922–927.
(40) C. Kirmaier, L. Laporte, C. C. Schenck, D. Holten. Nature and Dynamics of the Charge-Separated Intermediate in Reaction Centers in Which Bacterichlorophyll Replaces the Photoactive Bacteriopheophytin. 2. The Rates and Yields of Charge Separation and Recombination. *J. Phys. Chem.* **1995**, *99* (21), 8910–8917.
(41) G. Sipka, P. Maróti. Induction and Anisotropy of Fluorescence of Reaction Center from Photosynthetic Bacterium *Rhodobacter Sphaeroides*. *Photosynth. Res.* **2016**, *127* (1), 61–68.
(42) A. G. Yakovlev, L. G. Vasilieva, A. Y. Shkuropatov, V. A. Shuvalov. Coherent Phenomena of Charge Separation in Reaction Centers of LL131H and LL131H/LM160H/FM197H Mutants of *Rhodobacter Sphaeroides*. *Biochemistry* **2011**, *76* (10), 1107–1119.
(43) D. J. K. Swainsbury, V. M. Friebe, R. N. Frese, M. R. Jones. Evaluation of a Biohybrid Photoelectrochemical Cell Employing the Purple Bacterial Reaction Centre as a Biosensor for Herbicides. *Biosens. Bioelectron.* **2014**, *58*, 172–178.
(44) M. R. Jones, G. J. S. Fowler, L. C. D. Gibson, G. G. Grief, J. D. Olsen, W. Crielaard, C. N. Hunter. Mutants of *Rhodobacter Sphaeroides* Lacking One or More Pigment-protein Complexes and Complementation with Reaction-centre, LH1, and LH2 Genes. *Mol. Microbiol.* **1992**, *6* (9), 1173–1184.
(45) S. C. Straley, W. W. Parson, D. C. Mauzerall, R. K. Clayton. Pigment Content and Molar Extinction Coefficients of Photochemical Reaction Centers from *Rhodopseudomonas Sphaeroides*. *Biochim. Biophys. Acta Bioenerg.* **1973**, *305* (3), 597–609.
(46) V. C. A. Taylor. *Ultrafast Spectroscopy of Photoactive Nanomaterials*. Ph.D. Dissertation, University of Bristol, Bristol, UK, 2020.
(47) G. Cerullo, S. De Silvestri. Ultrafast Optical Parametric Amplifiers. *Rev. Sci. Instrum.* **2003**, *74* (1), 1–18.
(48) J. Zhu, I. H. M. Van Stokkum, L. Paparelli, M. R. Jones, M. L. Groot, I. H. M. Van Stokkum, L. Paparelli, M. R. Jones, M. L. Groot. Early Bacteriopheophytin Reduction in Charge Separation in Reaction Centers of *Rhodobacter Sphaeroides*. *Biophys. J.* **2013**, *104* (11), 2493–2502.
(49) R. Trebino, K. W. DeLong, D. N. Fittinghoff, J. N. Sweetser, M. A. Krumbügel, B. A. Richman, D. J. Kane. Measuring Ultrashort Laser Pulses in the Time-Frequency Domain Using Frequency-Resolved Optical Gating. *Rev. Sci. Instrum.* **1997**, *68* (9), 3277–3295.
(50) R. Trebino. *Frequency Resolved Optical Gating: The Measurement of Ultrashort Optical Pulses*. Springer, Ed. US: Atlanta, GA, 2000.
(51) A. M. Brouwer. Standards for Photoluminescence Quantum Yield Measurements in Solution (IUPAC Technical Report). *Pure Appl. Chem.* **2011**, *83* (12), 2213–2228.
(52) S. Hatami, C. Würth, M. Kaiser, S. Leubner, S. Gabriel, L. Bahrig, V. Lesnyak, J. Pauli, N.

Gaponik, A. Eychmüller, U. Resch-Genger. Absolute Photoluminescence Quantum Yields of IR26 and IR-Emissive $Cd_{1-X}Hg_xTe$ and PbS Quantum Dots-Method- and Material-Inherent Challenges. *Nanoscale* **2015**, *7* (1), 133–143.

(53) T. Arlt, S. Schmidt, W. Kaiser, C. Lauterwasser, M. Meyer, H. Scheer, W. Zinth. The Accessory Bacteriochlorophyll: A Real Electron Carrier in Primary Photosynthesis. *Proc. Natl. Acad. Sci.* **1993**, *90* (24), 11757–11761.

(54) Y. Jia, D. M. Jonas, T. Joo, Y. Nagasawa, M. J. Lang, G. R. Fleming. Observation of Ultrafast Energy Transfer from the Accessory Bacteriochlorophylls to the Special Pair in Photosynthetic Reaction Centers. *J. Phys. Chem.* **1995**, *99* (17), 6263–6266.

(55) D. M. Jonas, M. J. Lang, Y. Nagasawa, T. Joo, G. R. Fleming. Pump-Probe Polarization Anisotropy Study of Femtosecond Energy Transfer within the Photosynthetic Reaction Center of *Rhodobacter Sphaeroides* R26. *J. Phys. Chem.* **1996**, *100* (30), 12660–12673.

(56) S. Lin, A. K. W. Taguchi, N. W. Woodbury. Excitation Wavelength Dependence of Energy Transfer and Charge Separation in Reaction Centers from *Rhodobacter Sphaeroides*: Evidence for Adiabatic Electron Transfer. *J. Phys. Chem.* **1996**, *100* (42), 17067–17078.

(57) G. R. Fleming, R. van Grondelle. Femtosecond Spectroscopy of Photosynthetic Light-Harvesting Systems. *Curr. Opin. Struct. Biol.* **1997**, *7*, 738–748.

(58) A. Niedringhaus, V. R. Policht, R. Sechrist, A. Konar, P. D. Laible, D. F. Bocian, D. Holten, C. Kirmaier, J. P. Ogilvie. Primary Processes in the Bacterial Reaction Center Probed by Two-Dimensional Electronic Spectroscopy. *Proc. Natl. Acad. Sci.* **2018**, *115* (14), 3563–3568.

(59) J. H. Blokland, V. I. Claessen, F. J. P. Wijnen, E. Groeneveld, C. de Mello Donegá, D. Vanmaekelbergh, A. Meijerink, J. C. Maan, P. C. M. Christianen. Exciton Lifetimes of CdTe Nanocrystal Quantum Dots in High Magnetic Fields. *Phys. Rev. B* **2011**, *83* (3), 035304.

(60) A. L. Rogach, T. Franzl, T. A. Klar, J. Feldmann, N. Gaponik, V. Lesnyak, A. Shavel, A. Eychmüller, Y. P. Rakovich, J. F. Donegan. Aqueous Synthesis of Thiol-Capped CdTe Nanocrystals: State-of-the-Art. *J. Phys. Chem. C* **2007**, *111* (40), 14628–14637.

(61) Á. I. Fábián, T. Rente, J. SzölloSi, L. Matyus, A. Jenei. Strength in Numbers: Effects of Acceptor Abundance on FRET Efficiency. *ChemPhysChem* **2010**, *11* (17), 3713–3721.

(62) Scholes, G. D. Long-Range Resonance Energy Transfer in Molecular Systems. *Annu. Rev. Phys. Chem.* **2003**, *54*, 57–87.

5. Conclusions and Future Work

This thesis has explored the dynamics of bimolecular photochemical processes in two chemical systems and a biohybrid nanomaterial, demonstrating the paramount importance of gaining insights into the mechanisms of bimolecular dynamics with ultrafast spectroscopies.

In Chapter 2, the bimolecular excited-state proton transfer (ESPT) reaction between a coumarin derivative (CouOH) and 1-methylimidazole (MI) in deuterated chloroform was studied using a combination of experimental ultrafast time-resolved techniques and computational calculations. The ground-state properties of the system while working at comparable concentrations of reactants were investigated to extract an equilibrium constant for the hydrogen-bonding association between CouOH and MI and determined to be 300 M^{-1}. The CouOH–MI system was then investigated with time-resolved infrared (TRIR) and transient-absorption (TA) spectroscopies. The former relied on time-dependent density functional theory calculations for the assignment of vibrational states of S_1 CouOH and of proton-transfer photoproducts, definitively identified as the $CouO^{-*}\cdots HMI^{+}$ species. Based on the characterization of the CouOH–MI ground state association equilibrium, ESPT was found to be effective only for pre-associated molecules. Contributions from photoexcited CouOH molecules freely diffusing and reacting with MI do not occur within the short CouOH excited state lifetime (52 ps) at the concentration used in this study. From transient absorption data, the on-contact ESPT timescale was found to be ~1 ps, and complementary with time-resolved infrared data, the $CouO^{-*}\cdots HMI^{+}$ pair was found to rearrange to form an exciplex via π-stacking interaction. Finally, working at low absolute concentrations did not provide any evidence of excited-state tautomerization of $CouO^{-*}$, which was excluded to be operational among the possible deactivation pathways of the system.

A direct extension of the work presented in Chapter 2 would focus attention on the investigation of the $CouO^{-*}\cdots HMI^{+}$ exciplex in the nanosecond regime, exploring its relaxation dynamics. Time-correlated single photon counting (TCSPC) spectroscopy would provide an ideal tool of investigation, given the high value of the fluorescence quantum yield of the exciplex species. Moreover, the study could be extended to the investigation of various solvents or differently functionalised coumarins, to explore whether the ESPT rate

is slowed or accelerated as a response to the different environment, whether the mechanism involves or bypasses the formation of exciplexes, to further clarify the role of excess proton-acceptor in the mechanism. Prior to any excited dynamics study, a thorough characterisation of the ground-state properties and of pre-aggregation equilibria would be required, as they directly impact the dynamics of the ESPT. Finally, high-level dynamical theoretical calculations would be necessary for a correct interpretation of TRIR and TA data, as well as determining the role solvent plays mediating the ESPT.

In Chapter 3, the early step of a photocatalytic reaction adopting *para*-terphenyl (pTP) for carbon dioxide activation and utilization was studied. In particular, the electron-transfer (ET) reaction between pTP and a sacrificial amine electron-donor species (DCHMA) in ethanol was studied with transient absorption spectroscopy. Initially, the pTP transient absorption response was investigated to clarify its photoexcitation dynamics: the molecule undergoes a fast geometric rearrangement on the S_1 PES involving torsions among its constituent phenyl rings within 5.7 ps, and then decays or via solvent coupling *post* nuclei rearrangement in 41 ps, or via fluorescence on nanosecond timescales. Subsequently, the dynamics of the pTP–DCHMA system were investigated, identifying features uniquely associated to photoproducts and assigned to the formation of the radical anion $pTP^{\bullet -}$. The ET governing the pTP–DCHMA photochemistry was found to be a diffusion-limited process, with a rate constant of 7.80 ($\pm$ 1.99)$\times 10^9$ $M^{-1}s^{-1}$, determined with an associated contact radius of 0.68 $\pm$ 0.17 nm.

Experimentally, an immediate extension of this study would require the investigation of the nanosecond transient regime, for the assignment of long-time photoproduct decay; TCSPC to study how the relaxation dynamics of pTP are affected, and nanosecond regime TRIR and TA to directly follow the evolution of photoproduced $pTP^{\bullet -}$ could be used for the purpose. Potential deactivation channels could involve back-ET in $pTP^{\bullet -}\cdots DCHMA^{\bullet +}$ to reform the parent molecules, direct reaction of $pTP^{\bullet -}$ with CO_2, or a further ET step with solvent, to clarify its role in mediating the reaction. The modelling of the data would benefit from a treatment beyond the Smoluchowski approximation, including an exponentially decaying dependence on donor-acceptor distance for the ET, as dictated by Marcus theory. To support the modelling, time-dependent density-functional theory or high level *ab initio* methods could be used to calculate the barrier to the ET step. Finally, the study could be extended to different amines and different solvents, to compare the changes in the dynamics

of the ET, and on different catalysts, as addition of phenyl groups could be of use tuning the energy of the $S_1 \leftarrow S_0$ transition. Substituent effects and comparisons with *ortho*-terphenyl or *meta*-terphenyl isomers and could offer a deeper understanding of the dynamics at a fundamental level.

In Chapter 4, the dynamics of energy transfer from quantum dot (QD) nanoparticles to reaction centre (RC) protein complexes in a biohybrid material were investigated by means of time-correlated single photon counting spectroscopy. To enable this study, a new RC mutant, 3Hβ, was designed, isolated and purified. In 3Hβ RC the charge-separation chain of events is almost completely disrupted *cf.* wild-type RC, favouring fluorescence at 910 nm. The mutant 3Hβ RC was characterized with TA spectroscopy, recovering a fluorescence timescale of 162 ± 0.2 ps. In the biohybrid material, time-resolved fluorescence from QDs was found to decrease upon conjugation, indicating energy was flowing out of QDs; in parallel, signals from RCs required an additional component to be satisfactorily fitted, with the same timescale responsible for QD fluorescence quenching. This component was assigned to Förster resonance energy transfer (FRET), with a timescale of 26.6 ± 0.1 ns, at an average distance of 6.28 ± 0.04 nm and an efficiency of 0.75 ± 0.01. These results showed biohybrid QD-RC nanoconjugate can efficiently harvest light over the entire visible and near-infrared spectrum and that time-resolved spectroscopies were able to decipher the dynamics of a bimolecular energy transfer event.

At a fundamental level, in QD-RC nanoconjugates, it would be important to study the influence of QDs radius and, consequently, of the position of the QDs fluorescence band, to completely characterise the QD-RC binding and the FRET efficiency, in terms of both spectral overlap and average amount of RCs bound per QD. Further work on QD-RC nanoconjugates would focus on incorporating additional light-harvesting moieties to further enhance photon collections in the 650–700 nm region, where QDs absorption is less effective. Genetic engineering techniques would be adopted to provide the subcomponents of histidine tags that guarantee an effective aggregation onto the QDs and providing routes for energy transfer to RCs either directly or through the QDs. With FRET operational in such materials, TCSPC would once again be effective in interrogating the dynamics of the electronic energy transfer steps among the components.

To summarise, the thesis has demonstrated the applicability of several spectroscopic time-resolved techniques to the study of three bimolecular reactions, from ultrafast excited-

state proton transfer to diffusion-limited electron transfer, to electronic energy transfer. Although bimolecular photochemistry in the condensed phase sits at the border of inherently complex field of research, from molecular computation to ensemble dynamics of solvation, to the influence of diffusion or pre-aggregation processes, time-resolved spectroscopies have proven an investigation tool versatile enough to analyse and investigate these complexities and their contributions. It is expected time-resolved spectroscopies will play a pivotal role in the study of bimolecular photochemistry and in developing a more accurate picture of the dynamics, reaction rates and the mechanisms by which they occur.